(60)

THERMIT-2: A TWO-FLUID MODEL FOR LIGHT WATER REACTOR SUBCHANNEL TRANSIENT ANALYSIS

by

J. E. Kelly, S. P. Kao and M. S. Kazimi

MIT Energy Laboratory Electric Utility Program
Report No. MIT-EL-81-014

April 1981

Energy Laboratory

and

Department of Nuclear Engineering

Massachusetts Institute of Technology
Cambridge, Mass. 02139

THERMIT-2: A TWO-FLUID MODEL FOR LIGHT WATER REACTOR SUBCHANNEL TRANSIENT ANALYSIS

by

J. E. Kelly, S. P. Kao and M. S. Kazimi

Date of Publication: April 1981

Sponsored by

Boston Edison Company
Northeast Utilities Service Company
Public Service Electric and Gas Company
Yankee Atomic Electric Company

under

MIT Energy Laboratory Electric Utility Program

Report No. MIT-EL-81-014

REPORTS IN REACTOR THERMAL HYDRAULICS RELATED TO THE MIT ENERGY LABORATORY ELECTRIC POWER PROGRAM

A. Topical Reports (For availability check Energy Laboratory Headquarters, Headquarters, Room E19-439, MIT, Cambridge, Massachusetts 02139)

A.1 General Applications
A.2 PWR Applications
A.3 BWR Applications
A.4 LMFBR Applications

A.1 J.E. Kelly, J. Loomis, L. Wolf, "LWR Core Thermal-Hydraulic Analysis--Assessment and Comparison of the Range of Applicability of the Codes COBRA-IIIC/MIT and COBRA-IV-1," MIT Energy Laboratory Report No. MIT-EL-78-026, September 1978.

M.S. Kazimi and M. Massoud, "A Condensed Review of Nuclear Reactor Thermal-Hydraulic Computer Codes for Two-Phase Flow Analysis," MIT Energy Energy Laboratory Report No. MIT-EL-79-018, February 1979.

J.E. Kelly and M.S. Kazimi, "Development and Testing of the Three Dimensional, Two-Fluid Code THERMIT for LWR Core and Subchannel Applications," MIT Energy Laboratory Report No. MIT-EL-79-046.

J.N. Loomis and W.D. Hinkle, "Reactor Core Thermal-Hydraulic Analysis--Improvement and Application of the Code COBRA-IIIC/MIT," MIT Energy Laboratory Report No. MIT-EL-80-027, September 1980.

D.P. Griggs, A.F. Henry and M.S. Kazimi, "Development of a Three-Dimensional Two-Fluid Code with Transient Neutronic Feedback for LWR Applications," MIT Energy Laboratory No. MIT-EL-81-013, April 1981.

J.E. Kelly, S.P. Kao and M.S. Kazimi, "THERMIT-2: A Two-Fluid Model for Light Water Reactor Subchannel Transient Analysis," MIT Energy Laboratory Report No. MIT-EL-81-014, April 1981.

A.2 P. Moreno, C. Chiu, R. Bowring, E. Khan, J. Liu, and N. Todreas, "Methods for Steady-State Thermal/Hydraulic Analysis of PWR Cores," MIT Energy Laboratory Report No. MIT-EL-76-006, Rev. 1, July 1977 (Orig. 3/77).

J. Liu, and N. Todreas, "Transient Thermal Analysis of PWR's by a Single Pass Procedure Using a Simplified Model Layout," MIT Energy Laboratory Report MIT-EL-77-008, Final, February 1979, (Draft, June 1977).

J. Liu, and N. Todreas, "The Comparison of Available Data on PWR Assembly Thermal Behavior with Analytic Predictions," MIT Energy Laboratory Report MIT-EL-77-009, Final, February 1979, (Draft, June 1977).

A.3 L. Guillebaud, A. Levin, W. Boyd, A. Faya, and L. Wolf, "WOSUB-A Subchannel Code for Steady-State and Transient Thermal-Hydraulic Analysis of Boiling Water Reactor Fuel Bundles," Vol. II, Users Manual, MIT-EL-78-024, July 1977.

L. Wolf, A. Faya, A. Levin, W. Boyd. L. Guillebaud, "WOSUB-A Subchannel Code for Steady-State and Transient Thermal-Hydraulic Analysis of Boiling Water Reactor Fuel Pin Bundles," Vol. III, Assessment and Comparison, MIT-EL-78-025, October 1977.

L. Wolf, A. Faya, A. Levin, L. Guillebaud, "WOSUB-A Subchannel Code for Steady-State Reactor Fuel Pin Bundles," Vol. I, Model Description, MIT-EL-78-023, September 1978.

A. Faya, L. Wolf and N. Todreas, "Development of a Method for BWR Subchannel Analysis," MIT-EL-79-027, November 1979.

A. Faya, L. Wolf and N. Todreas, "CANAL User's Manual," MIT-EL-79-028, November 1979.

A.4 W.D. Hinkle, "Water Tests for Determining Post-Voiding Behavior in the LMFBR," MIT Energy Laboratory Report MIT-EL-76-005, June 1976.

W.D. Hinkle, Ed., "LMFBR Safety and Sodium Boiling - A State of the Art Report," Draft DOE Report, June 1978.

M.R. Granziera, P. Griffith, W.D. Hinkle, M.S. Kazimi, A. Levin, M. Manahan, A. Schor, N. Todreas, G. Wilson, "Development of Computer Code for Multi-dimensional Analysis of Sodium Voiding in the LMFBR," Preliminary Draft Report, July 1979.

M. Granziera, P. Griffith, W. Hinkle (ed.), M. Kazimi, A. Levin, M. Manahan, A. Schor, N. Todreas, R. Vilim, G. Wilson, "Development of Computer Code Models for Analysis of Subassembly Voiding in the LMFBR," Interim Report of the MIT Sodium Boiling Project Covering Work Through September 30, 1979, MIT-EL-80-005.

A. Levin and P. Griffith, "Development of a Model to Predict Flow Oscillations in Low-Flow Sodium Boiling," MIT-EL-80-006, April 1980.

M.R. Granziera and M. Kazimi, "A Two-Dimensional, Two-Fluid Model for Sodium Boiling in LMFBR Assemblies," MIT-EL-80-011, May 1980.

G. Wilson and M. Kazimi, "Development of Models for the Sodium Version of the Two-Phase Three Dimensional Thermal Hydraulics Code THERMIT," MIT-EL-80-010, May 1980.

B. Papers

B.1 General Applications
B.2 PWR Applications
B.3 BWR Applications
B.4 LMFBR Application

B.1 J.E. Kelly and M.S. Kazimi, "Development of the Two-Fluid Multi-Dimensional Code THERMIT for LWR Analysis," Heat Transfer-Orlando 1980, AIChE Symposium Series 199, Vol. 76, August 1980.

J.E. Kelly and M.S. Kazimi, "THERMIT, A Three-Dimensional, Two-Fluid Code for LWR Transient Analysis," Transactions of American Nuclear Society, 34, p. 893, June 1980.

B.2 P. Moreno, J. Kiu, E. Khan, N. Todreas, "Steady State Thermal Analysis of PWR's by a Single Pass Procedure Using a Simplified Method," American Nuclear Society Transactions, Vol. 26.

P. Moreno, J. Liu, E. Khan, N. Todreas, "Steady-State Thermal Analysis of PWR's by a Single Pass Procedure Using a Simplified Nodal Layout," Nuclear Engineering and Design, Vol. 47, 1978, pp. 35-48.

C. Chiu, P. Moreno, R. Bowring, N. Todreas, "Enthalpy Transfer between PWR Fuel Assemblies in Analysis by the Lumped Subchannel Model," Nuclear Engineering and Design, Vol. 53, 1979, 165-186.

B.3 L. Wolf and A. Faya, "A BWR Subchannel Code with Drift Flux and Vapor Diffusion Transport," American Nuclear Society Transactions, Vol. 28, 1978, p. 553.

S.P. Kao and M.S. Kazimi, "CHF Predictions In Rod Bundles," Trans. ANS, 35, 766 June 1981.

B.4 W.D. Hinkle, (MIT), P.M. Tschamper (GE), M.H. Fontana (ORNL), R.E. Henry (ANL), and A. Padilla (HEDL), for U.S. Department of Energy, "LMFBR Safety & Sodium Boiling," paper presented at the ENS/ANS International Topical Meeting on Nuclear Reactor Safety, October 16-19, 1978, Brussels, Belgium.

M.I. Autruffe, G.J. Wilson, B. Stewart and M. Kazimi, "A Proposed Momentum Exchange Coefficient for Two-Phase Modeling of Sodium Boiling," Proc. Int. Meeting Fast Reactor Safety Technology, Vol. 4, 2512-2521, Seattle, Washington, August 1979.

M.R. Granziera and M.S. Kazimi, "NATOF-2D: A Two Dimensional Two-Fluid Model for Sodium Flow Transient Analysis," Trans. ANS, 33, 515, November 1979.

DEVELOPMENT OF A TWO-FLUID, TWO-PHASE MODEL FOR LIGHT WATER REACTOR SUBCHANNEL ANALYSIS

ABSTRACT

The broad effort of developing and assessing the two-fluid model computer code THERMIT for light water reactor (LWR) subchannel analysis is described. The developmental effort required a reformulation of the coolant-to-fuel rod coupling so that THERMIT is now capable of traditional coolant-centered subchannel analysis. A model that accounts for mass, momentum and energy transport between mesh cells due to turbulent mixing for two-phase conditions has also been introduced. This model is the first such attempt in a two-fluid context.

The liquid-vapor interfacial exchange terms in the two-fluid model have been modified for improved accuracy. A systematic evaluation of the exchange models has been performed. The mass and momentum exchange rates between the vapor and the liquid for pre-CHF conditions were evaluated by comparison to void fraction data in over 30 one-dimensional steady-state experiments reported in the open literature. The liquid-vapor energy exchange rate for post-CHF conditions was assessed using 15 steady-state, one-dimensional wall temperature measurements. The mixing model was tested against G.E. and Ispra BWR and PWR rod-bundle measurements. Comparisons with these measurements have shown the appropriateness of this model. The assessment of the wall-to-coolant heat transfer model involved steady-state, one-dimensional as well as transient, three-dimensional measurements.

THERMIT has been shown to accurately predict the thermal-hydraulic two-phase behavior of rod bundles. Thus, it represents the first two-fluid computer code with this proven capability.

ACKNOWLEDGEMENTS

The authors would like to express their gratitude to all those who contributed to this effort through their advice, criticism and encouragement. In particular, Professors John Meyer and Lothar Wolf and students Don Dube, Andre Schor and Mohamad Massoud deserve special mention.

This report is based on a Ph.D. thesis by the first author and on a M.S. thesis by the second author which were both submitted to the Department of Nuclear Engineering at M.I.T.

Finally, the financial support of Boston Edison Company, Consumers Power Company, Northeast Utilities Services Company, Public Service Electric and Gas Company, and Yankee Atomic Electric Company under the sponsorship of the M.I.T. Energy Laboratory is greatly appreciated.

EXECUTIVE SUMMARY

This report describes the effort involved in the development and assessment of the two-fluid computer model THERMIT for two-phase analysis of LWR rod-bundles on a subchannel basis. Extensive modifications in the original THERMIT code were undertaken to achieve this goal. The final result of this effort is that a new version, THERMIT-2, can now be utilized as an advanced tool for design and transient analysis of LWR rod bundles as well as core-wide problems. The two improvements specifically required for subchannel analysis were the expansion of the geometrical modeling capability and the addition of a two-phase mixing model. The geometrical improvements were necessary to allow both coolant-centered subchannel analysis and detailed fuel rod modeling. The addition of the two-phase mixing model was necessary to account for the inter-channel exchange processes arising from turbulent mixing and vapor diffusion. Other modifications have improved the overall predictive capabilities of THERMIT. The addition of droplet vaporization model and CHF correlations has eliminated modeling deficiencies which existed in the original version of THERMIT. The modification of the interfacial energy exchange model and the wall heat transfer logic has replaced previously simplified modeling with more realistic modeling. Hence, the modifications made in THERMIT have expanded the analytical capability to allow subchannel analysis as well as substantially improving the two-phase flow description.

The assessment effort, performed in conjunction with the developmental work, involved evaluation of the accuracy of important models in THERMIT. Since the analysis of LWR rod-bundles on a subchannel basis is the primary application of this research, the models have been assessed for conditions

which are consistent with those found in LWR rod-bundles. The method used in this assessment has been to compare experimental measurements with the code predictions. The experiments have been chosen to resemble either BWR or PWR flow conditions with the geometry being either rod-bundle or tube. The models which have been assessed include: the liquid-vapor interfacial exchange models, the two-phase mixing model and the wall heat transfer model. From this assessment effort the following conclusions can be made.

The interfacial mass exchange model has been shown to predict the proper rate of mass exchange between the liquid and vapor for both pre-CHF and post-CHF conditions. (Depressurization transients have been excluded from this assessment effort.) In the pre-CHF regime, comparisons with void fraction measurements have illustrated the appropriateness of this model for subcooled as well as saturated boiling conditions. For post-CHF conditions, THERMIT accurately predicts the amount of vapor superheat and the wall temperatures which implies that the droplet vaporization rate is properly modeled. These results show that the interfacial mass exchange model in THERMIT can accurately analyze the various types of vaporization mechanisms anticipated for LWR rod-bundle steady-state and non-depressurization transients.

Using the current formulation of the interfacial energy exchange model, the proper liquid and vapor temperature distributions are predicted to be superheated while the liquid is saturated. These results illustrate that the code can predict the appropriate temperature distributions for thermal non-equilibrium conditions.

Comparisons of the code predictions with void fraction measurements have indicated that the appropriate relative velocity is predicted. This result can be used to infer that the interfacial momentum exchange rate is

proper. It should be noted that this conlcusion is based on steady-state saturated boiling measurements. For droplet flows, very low flows, or rapidly accelerating flows, the model has not been assessed and should be used with some caution for these flow conditions. However, for steady-state and near-operational transient rod bundle analysis, the interfacial momentum exchange model should be appropriate.

A two-phase mixing model has been incorporated into THERMIT and has been assessed using a number of rod-bundle experimental measurements. One improtant result is that THERMIT can correctly predict the measured trend in the corner subchannel flow quality. This trend is that the quality is much lower than the bundle average for BWR conditions, while being near the average for PWR conditions. THERMIT accurately predicts this behavior using the same mixing model parameters in each case. Hence, the two-phase mixing model is valid over the range of pressures which are typical of BWR and PWR rod-bundle conditions.

Another important result of this assessment is that the effects of grid spacers must be carefully modeled in order to predict the correct flow distribution. The grid spacers can significantly alter the flow distribution in a non-uniform manner. Proper modeling of the grid is needed to predict the appropriate trends in the mass velocity measurements. However, the quality distribution is rather insensitive to the grid spacer modeling.

The final model to be assessed is the wall heat transfer model. Three aspects of the model have been investigated: pre-CHF correlations, post-CHF correlations and steady-state and transient CHF predictive capability. Overall, the model is able to satisfactorily predict the experimental data to which it has been compared. However, certain areas of the model may need to be improved.

For pre-CHF conditions the Chen correlation is found to underpredict the heat transfer coefficient except at low heat fluxes. Although this result leads to conservative wall temperature predictions which are probably satisfactory for many applications, the use of an alternative heat transfer correlation may be needed. Either the Thom or Jens-Lottes correlation can appropriately predict the heat transfer coefficient for all cases which have been studied. However, neither of these two correlations can calculate the heat transfer coefficient for forced convection vaporization while the Chen correlation is able to calculate this mode of heat transfer. This type of heat transfer is anticipated to be important for BWR conditions. It should also be noted that for typical BWR heat fluxes, the Chen correlation should also calculate the appropriate heat transfer coefficient. Hence, for BWR rod-bundle analysis, the Chen correlation should predict satisfactory results.

For post-CHF conditions, accurate wall temperature predictions are more dependent on the vapor temperature calculation than on the heat transfer correlation. Consequently, if the droplet vaporization model is used, accurate wall temperatures can be predicted using a single-phase vapor heat transfer coefficient. This type of modeling is currently included in THERMIT and it has been shown that the appropriate post-CHF temperature distributions are predicted.

In evaluating the CHF predictive capability of THERMIT, the W3 correlation and CISE-4 correlation were found to provide the best results for PWR and BWR steady-state conditions respectively. The CISE-4 correlation has been found to underpredict the critical heat flux (or more appropriately the critical power) in transient cases. The Biasi correlation while

underpredicting the critical heat flux for transient conditions, usually overestimates the critical heat flux for the steady-state tests which were studied. The agreement is poorest for high qualities and low heat flux cases and is probably due to the failure of the correlation to properly account for entrainment.

In summary, it can be concluded that THERMIT can now successfully analyze LWR rod bundles on a subchannel basis. The geometrical and physical modeling capability needed for this type of analysis has been added to the code. Assessment of the important models for conditions typical of LWR rod-bundles has shown that appropriate results are predicted by the code. Hence, the main objective of this research has been accomplished, since THERMIT is the first two-fluid model code which has been developed and tested for LWR subchannel applications. Specific details on the programming and usage of THERMIT may be found in Ref. 9.

TABLE OF CONTENTS

LIST OF FIGURES

LIST OF TABLES

1.0 INTRODUCTION

1.1 Background

Light water reactor safety research is ultimately aimed at ensuring that the public will not be adversely affected if any of a variety of anticipated or postulated reactor accidents should occur. This requirement is met by specifying operational design limits that are based on conservative assumptions for the behavior of the reactor. Reactor safety research is primarily concerned with validating the appropriateness of these limits as well as assessing the margins present in these limits.

In order to study the normal and abnormal transient behavior of nuclear reactors, many complex phenomena and systems need to be analyzed. One of the major areas which must be investigated is the thermal-hydraulics of the reactor system. Included here are the reactor core heat removal system, the secondary heat removal system (if present) as well as any auxiliary systems which are related to removal of heat from the reactor. Since most of the radioactive inventory is contained within the reactor core, the preservation of the core integrity is essential. Moreover, the most likely radioactivity release mechanisms result from a thermally induced failure of the fuel rod cladding. Thus, the thermal-hydraulic behavior of the core is generally the most important consideration of reactor safety analysis.

In order to meet the objective of accurately predicting the thermal-hydraulic field in the reactor core a number of analytical tools have been developed. These range from simple one equation models, used to predict a particular phenomenon, to large computer codes which attempt to analyze the entire reactor system. Typically, the most widely used

and generally the most useful tools are the thermal-hydraulic computer codes. Simply stated, these codes attempt to numerically solve the mass, momentum and energy conservation equations for a particular geometrical configuration and for the conditions of interest. Since the conservation equations must be supplemented by empirical correlations needed to describe specific phenomena, the thermal-hydraulic computer codes are engineering analysis tools which combine basic physics with empirical models.

In the past few years, the need for improved analysis of nuclear reactor safety has lead to the rapid development of advanced methods for multidimensional thermal-hydraulic analysis. These methods have become progressively more complex in order to account for the many physical phenomena which are anticipated during both steady-state and transient conditions. In particular, the modeling of two-phase flow, which is required for both BWR and PWR systems, is especially complex. In two-phase flows, both thermal and mechanical non-equilibrium between the two phases can exist. These non-equilibrium effects take the form of sub-cooled boiling, vapor superheating and relative motion of the two phases. In order to have realistic calculations, these physical phenomena must be accounted for in the numerical method.

The numerical methods must also be capable of analyzing the many flow patterns which occur in postulated transients. For example, in a loss of coolant accident (LOCA) or a severe anticipated transient without scram (ATWS), flow reversal or counter-current flow may occur in the reactor core. Elaborate solution techniques have been developed specifically to be able to describe fluid fields with no restriction on speed or direction.

Although it is improbable that a particular computer code be applicable for all transients, it is necessary that a code be able to analyze all anticipated flow conditions in problems for which the code is applied. The only practical way to realize the needed flexibility is to combine realistic physical models with unrestricitive numerical solution techniques. Hence, the trend in current thermal-hydraulic safety research is to pursue the development of such codes.

1.2 Research Objective

As discussed in the previous section, the thermal-hydraulic computer codes play a key role in LWR safety analysis. However, due to the limitations of present day computers, precise details of the thermal-hydraulic behavior can only be determined for a relatively small region of the core. The response of the entire reactor can be determined if large control volumes are used. However, within these volumes information about the temperature and flow distribution is lost. If these distributions are important for assessing the safety of the reactor, then detailed modeling is required. By using smaller control volumes, for example subchannels, sufficient temperature and flow information can be determined, but only for limited regions of the core. For instance, the largest region which might be analyzed on a subchannel basis would be one BWR 8 x 8 assembly. Nevertheless, if the limiting region of the core can be identified, then this type of detailed analysis is sufficient to evaluate the safety of the reactor.

A number of power and flow transients do require detailed subchannel modeling, particularly in the hottest part of the core. However,

previous computer codes, which have used subchannel modeling, have either lacked a realistic two-phase flow model (e.g. COBRA IV [1]) or lacked an unrestricted solution technique (e.g. COBRA-IIIC [2]). Consequently, the applicability of the previous codes is somewhat limited.

In view of the shortcomings of the previous codes, a new code which does not suffer from these deficiencies has been developed. Using the computer code THERMIT [3] as a framework, the present developmental effort has expanded the capabilities of THERMIT such that the new version of THERMIT can successfully analyze subchannel geometry [4].

THERMIT has been selected for this project due to its two-phase flow model and solution technique. The two-fluid, two-phase model which is used in THERMIT realistically allows for thermal and mechanical non-equilibrium between the phases. This feature permits description of the complex phenomena encountered during transients. The solution technique is a modification of the ICE method [5,6], and is capable of predicting the flow conditions with minimum restrictions.

The primary application of this new version is transient analysis of LWR rod bundles on a subchannel basis. Although depressurization transients (i.e. LOCA) have not been excluded as possible applications of this code, these transients are not the primary type of transient under consideration. Rather, anticipated or near-operational power and flow transients are the main focus of the present development considerations. By concentrating on non-depressurization transients, the code can be validated for several practical conditions. Furthermore, the proper analysis of a LOCA generally requires modeling the entire reactor system and THERMIT has been designed for core analysis only. Consequently, the applications for this new tool are limited to cases which can be analyzed by modeling only the

core and supplying appropriate core flow boundary conditions. Nevertheless, these cases represent a large number of problems with practical interest.

With the ability to analyze subchannels, THERMIT is the first two-fluid model code with this capability. Due to the advanced treatment of the two-phase flow and reliable solution method, this code represents a significant addition to the area of rod-bundle thermal-hydraulic analysis. Other multi-fluid codes that may be used for subchannel applications are still under development at Argonne National Laboratory (COMMIX-2 [7]) and Battle Pacific Northwest Laboratory (COBRA-TF [8]).

1.3 Development Approach

The development of this new version of THERMIT has been accomplished using the following strategy:

(1) Modify the code structure and numerical method as necessary,

(2) Verify, extend, and assess the constitutive models,

(3) Assess numerical properties of the code, and

(4) Implement improved models as necessary.

This strategy is actually iterative in nature. That is, as the need for improved models is found, code modifications and assessment are subsequently required. Hence, the above steps overlap one another.

This development can be divided into two main steps. The first step has involved modifying the original version of THERMIT so that subchannel geometry could be analyzed. This modification has affected both the geometrical modeling capability as well as the physical modeling. The geometrical modeling changes were required so that the traditional coolant-centered subchannels might be analyzed with THERMIT. The changes in the

physical modeling were necessary to account for turbulence effects in single phase and two-phase flows for rod-bundle analysis. After reviewing previous work in Chapter 2, the significant work related to this modification effort is discussed in Chapter 3.

After implementing the capability for subchannel analysis, the second step has been the validation and assessment of the code. A strategy has been adopted which allows for independent assessment of the various constitutive models using open literature experimental measurements. Measurements typical of expected subchannel conditions have been compared with the code's predictions in this effort. These comparisons are useful for both validating the predictive capability of the code as well as identifying areas which require improvement. The net result of this assessment effort is that the code can be used with confidence for subchannel applications. The results of this assessment are discussed in Chapters 4, 5, 6 and 7.

A listing of the actual computer code will not be given here due to its length. Rather, the interested reader is referred to reference 9 which contains detailed information on the usage of this new version of THERMIT. Sample problems as well as input instructions are given in this reference.

2.0 REVIEW OF PREVIOUS WORK

2.1 Introduction

Nuclear reactor thermal-hydraulic safety research encompasses both experimental and analytical investigations. The experimental research attempts to measure and identify the important variables in both single-phase and two-phase flows. The analytical research attempts to develop methods which numerically solve the equations describing the heat transfer and fluid dynamics in a reactor. Elaborate numerical methods have evolved which rely heavily on the use of digital computers. Conceivably, if all of the significant physical phenomena are considered in the computer code, then accurate predictions of the flow conditions can be obtained. These methods can also analyze conditions which could not be directly measured. The only practical limitation of these methods is the problem size which a computer can accomodate in terms of both storage and execution times.

Since this thesis has been concerned with the development of the thermal-hydraulic computer code, THERMIT, it is instructive to review the general characteristics of nuclear reactor thermal-hydraulic codes. The key features of a few of these codes are presented in Table 2.1. As discussed by Massoud [13], it is possible to classify the codes according to the criteria summarized in Table 2.2. The first major division is related to the code's capability to handle one component or the entire hydraulic loop. Loop codes analyze a number of components simultaneously and,

TABLE 2.1

Features of Some Thermal-Hydraulic Computer Codes

Computer Code	Type of Analysis	Method of Analysis	Two-Phase Flow Model	Solution Technique
COBRA IIIC [2]	Component	Subchannel	Homogeneous Equilibrium	Marching Method
COBRA IV [1]	Component	Subchannel	Homogeneous Equilibrium	Marching Method or I.C.E. Method
WOSUB [10]	Component	Subchannel	Drift Flux	Marching Method
COMMIX-2 [7]	Component	Distributed Resistance	Two-Fluid	I.C.E. Method
THERMIT [3]	Component	Distributed Resistance	Two-Fluid	I.C.E. Method
TRAC [12]	Loop	Distributed Resistance	Two-Fluid or Drift Flux	I.C.E. Method

TABLE 2.2

Thermal-Hydraulic Code Classification Criteria

1. System Analysis Capability
   - A. Loop Codes
   - B. Component Codes
     - i. Subchannel Analysis
     - ii. Distributed Resistance Analysis
     - iii. Distributed Parameter Analysis

2. Two-Phase Flow Model
   - A. Homogeneous Equilibrium Model
   - B. Drift-Flux Model
   - C. Two-Fluid Model

consequently, analysis is not as detailed as found in the individual component codes. However, the component codes must have appropriate boundary conditions supplied from external calculations. This prevents accurate modeling of the coupling between the component and the rest of the system. Naturally, loop codes do not suffer from this problem.

Component codes, specifically those intended for rod-bundle analysis, can be further classified according to their analysis method. This topic has been reviewed by Sha [14]. Three types of methods can be identified; subchannel analysis, distributed resistance analysis and distributed parameter analysis. Each of these analytical techniques has certain advantages and disadvantages relative to the other methods. Subchannel analysis techniques permit fairly detailed analysis of the flow, but are limited by inherent assumptions concerning the flow. Distributed resistance methods can analyze either large or small regions but require the accurate determination of the flow resistances. The distributed parameter analysis method gives the most detail of the flow structure, but is limited to small regions. All of the core component codes use one of these three analysis techniques.

The second major division is the type of two-phase flow model. The important types of models which have been incorporated into thermal-hydraulic codes include the homogeneous equilibrium model (HEM), the drift-flux model, and the two-fluid model. Essentially, the type of two-phase model refers to the number of conservation equations which are used to describe the two-phase flow, as summarized in Table 2.3. As the number of conservation equations increases, the number of constitutive models also increases. However, with more equations, accurate results are more likely to be predicted for severe conditions. The more general

TABLE 2.3

Summary of Two-Phase Flow Models

Two-Phase Flow Model	Conservation Equations			Constitutive Laws					Imposed Restrictions:	
	Mass	Energy	Momentum	F_W	Q_W	Γ	Q_i	F_i	Phasic Temperatures	Effective Phasic Velocities
Homogeneous	1	1	1	1	1	0	0	0	T_v and T_ℓ Equil.	Equal
Drift Flux	2	1	1	1	1	1	0	0	T_v or T_ℓ Equil.	Slip Relation
4 Equation	1	2	1	1	2	0	1	0	T_v or T_ℓ Equil.	Slip Relation
Models	1	1	2	2	1	0	0	1	T_v and T_ℓ Equil.	None
Drift Flux	2	2	1	1	2	1	1	0	None	Slip Relation
5 Equation	2	1	2	2	1	1	0	1	T_v or T_ℓ Equil.	None
Models	1	2	2	2	2	0	1	1	T_v or T_ℓ Equil.	None

TABLE 2.3 (continued)

Two-Phase Flow Model	Conservation Equations			Constitutive Laws					Imposed Restrictions:	
	Mass	Energy	Momentum	F_W	Q_W	Γ	Q_i	F_i	Phasic Temperatures	Effective Phasic Velocities
Two-Fluid	2	2	2	2	2	1	1	1	None	None
Three-Fluid (Liquid, Vapor and Liquid Drops)	3	3	3	3	3	2	2	2	None	None

equations also allow better physical modeling which is essential for the description of two-phase flow.

Since the present work is concerned with the application of the two-fluid model code THERMIT to detailed rod-bundle analysis, it is useful to discuss in detail both the type of analysis techniques and the two-phase flow models. The analysis techniques are discussed in Section 2.2 while the two-phase flow models are discussed in Section 2.3. Following this discussion, the specifics of the THERMIT computer code will be given in Section 2.4.

2.2 Rod-Bundle Analysis Techniques

As discussed in the previous section, three types of techniques are available for rod-bundle analysis. These include subchannel analysis, distributed resistance analysis and distributed parameter analysis. The distributed parameter methods are limited to very small regions and will not be discussed here. The other two methods, however, are very useful for analyzing the entire rod-bundle and are discussed in detail.

2.2.2 Subchannel Analysis

Of all the methods developed for analyzing the thermal-hydraulic behavior in complex rod-bundle geometry, the subchannel method has been found to be particularly well-suited. Weisman and Bowring [16] and Rouhani [17] have reviewed this type of analysis and present the following view of traditional subchannel analysis.

In this method, the rod-bundle cross section is subdivided into a number of parallel interacting flow subchannels. Conventionally these subchannels are defined by lines joining the fuel rod center (see Figure

2.1a). This choice is somewhat arbitrary and other choices are possible, such as the lines of zero shear stress (see figure 2.1b) [12]. This latter type of subchannel is referred to as a rod centered subchannel while the former type is called a coolant centered subchannel.

Once the radial plane has been defined, each subchannel is divided axially into a number of intervals (nodes) which are typically between 8 and 30 cm long. For each node, which can be thought of as a control volume, a set of mass, energy, axial momentum and transverse momentum conservation equations are written and solved with an iterative technique.

The main assumptions of this method are:

(1) The detailed velocity and temperature destributions within a subchannel are ignored;

(2) The transverse momentum equation is simplified due to the assumption of predominantly axial flow.

The first assumption reflects the fact that only spatially averaged parameters are contained in the conservation equations. Consequently, the distributions within the control volume can not be calculated. The second assumption means that, due to the predominance of the axial flow, the transverse momentum exchange can be crudely represented without introducing significant errors. Hence, the transverse momentum equation is usually much simpler than the axial momentum equation.

A number of computer codes have been developed which use the subchannel analysis method. Among these are included COBRA IIIC [2], COBRA-IV [1] and WOSUB [10]. These codes treat most of the important phenomena in the same way and in each code a marching type solution method is utilized. (COBRA-IV also contains a modified I.C.E. method [19] for transient analysis.) The marching method begins the

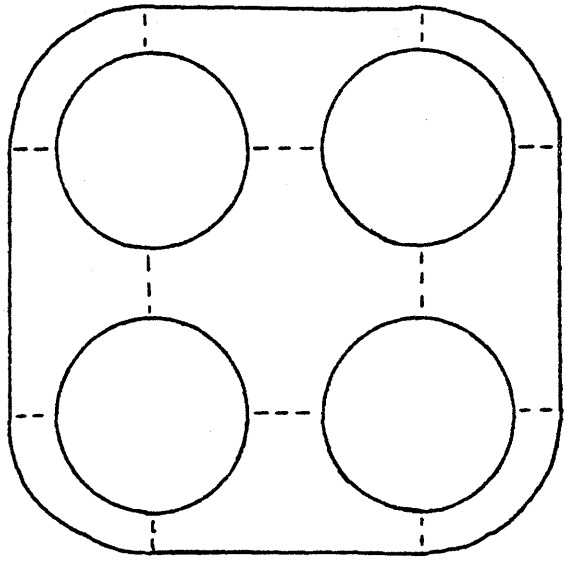

Figure 2.1a: Coolant-Centered Subchannel Layout

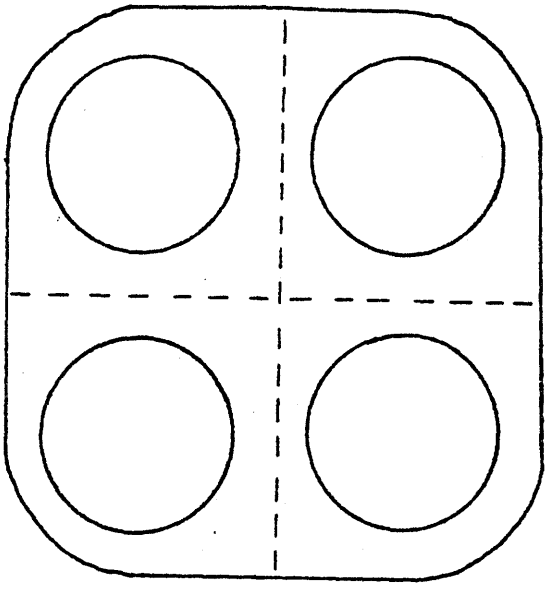

Figure 2.1b: Rod-Centered Subchannel Layout

calculation of the flow parameters at the core inlet and moves upward, in a stepwise manner, simultaneously solving the conservation equations for all subchannels, at each axial level. Typically, more than one sweep through the core will be required to obtain a converged solution. Therefore, the marching method is basically an iterative technique.

For steady-state, single-phase conditions, the subchannel codes can generally predict the correct flow distributions in rod-bundles [16]. However, for two-phase conditions or severe transients, the use of the subchannel codes may not be strictly valid. For example, comparisons of COBRA-IIIC with steady-state two-phase flow measurements have indicated that the correct flow and enthalpy distributions could not be calculated [10]. Also, if a strong perturbation causes large lateral flow, then the basic assumption in these codes is violated. Furthermore, if reverse flow should occur, then the marching type solution method will fail unless appropriately modified. Consequently, although useful for many rod-bundle problems, the subchannel codes are limited in their applications.

2.2.2 Distributed Resistance Models

In order to eliminate the assumptions and restrictions of the subchannel methods, distributed resistance models have been developed. These models also referred to as porous body models, use orthogonal coordinates and geometrically similar control volumes. The name for this method is due to the fact that frictional resistances are distributed throughout each of the control volumes. Quasi-continuum governing equations are written for the conservation of mass, energy or momentum and no simplifications of the transverse momentum equations are made. Consequently,

no restrictions are placed on the flow conditions. However, as in the case of subchannel analysis, the details of the flow structure within a control volume cannot be determined.

By employing Cartesian coordinates, the geometrical noding of the rod-bundle can be the same as for subchannel analysis (i.e., for square bundles). Hence, the information obtained by the distributed resistance method is at least as detailed as that found in subchannel methods. Of course, the governing equations in the distributed resistance methods are more general than those in subchannel analysis methods.

However, the key to successful use of this method is the correct formulation of expressions for the transport processes in the control volume (i.e., heat transfer, friction, etc.). These processes can be described for most conditions, but completely general formulations are not possible. However, these processes can usually be defined for many cases of practical interest.

A number of computer codes use the distributed resistance method. Among these are COMMIX-1 [11], TRAC [12], and THERMIT [3]. Each of these codes use some form of the I.C.E. solution technique [6]. This technique coupled to the full three-dimensional representation of the distributed resistance method allows for the calculation of flow reversal, recirculating flow and even counter-current flow in two-phase conditions. With the ability to analyze these conditions, the above codes represent powerful tools for steady-state and transient thermal-hydraulic analysis of rod-bundles.

2.3 Two-Phase Flow Models

Aside from the choice of modeling technique for the flow, the other

important feature to be defined is the two-phase flow model. A wide variety of possibilities exist for describing the two-phase flow. These range from describing the two-phase flow as a pseudo single-phase flow to a multi-component flow (e.g., liquid, vapor and droplets). The various possibilities are summarized in Table 2.3. Generally, as the two-phase flow model becomes more complex (i.e., more equations), more constitutive equations are required to represent the various interactions between the phases.

The homogeneous equilibrium model (HEM) is the simplest of these models. It assumes that the vapor and liquid are in thermal equilibrium and that there is no relative velocity between the two phases. These assumptions are clearly limiting, but may be adequate for certain flow conditions. Extensions of this model to include relative velocity (slip) and thermal non-equilibrium (subcooled boiling) effects are possible using empirical models.

The drift flux models, either the four or five equation models add some complexity to the two-phase flow description. By treating the vapor and liquid phases as separate streams still in thermal equilibrium, these methods allow for accurate velocity predictions.

In the two-fluid model, separate conservation equations are written for the vapor and liquid phases. This model allows a very general description of the two-phase flow. However, it also introduces a large number of constitutive equations. The most important relations are those which represent the transfer of mass, Γ, transfer of energy, Q_i, and transfer of momentum, F_i, across liquid-vapor interfaces. The advantages of using this model is that physically based mechanistic models can be formulated for these terms which should be valid over a wide range

of conditions.

An extension of the two-fluid model is the three-fluid model in which the three-fluid fields are the vapor, liquid and droplet fields. COBRA-TF [8] is an example of such a model. This formulation, while introducing more constitutive models, seems to contain the necessary capability to analyze complex flow situations such as the reflood stage of a LOCA.

However, for all but reflood analysis, the two-fluid model is probably general enough to describe the important non-equilibrium effects. Consequently, THERMIT which uses the two-fluid model, is expected to provide a good description of most two-phase conditions.

The complexity of the two-phase flow model is seen to depend on the assumptions concerning the non-equilibrium phenomena. Mixture models, that is either the homogeneous equilibrium or the drift flux models, contain one or more restrictions on either the thermal or mechanical non-equilibrium in the flow. Only when both phases are represented with separate conservation equations can all the non-equilibrium effects be modeled.

2.4 Description of THERMIT

2.4.1 Background

It is instructive to review the key characterisitcs of THERMIT prior to the description of the modifications involved in the present work. The characteristics include the conservation equations, finite difference equations and constitutive models.

2.4.2 General Characteristics

The thermal-hydraulic computer code, THERMIT, originally developed

at MIT under EPRI sponsorship, solves the three-dimensional, two-fluid equations describing the two-phase flow and heat transfer dynamics. This two-fluid model uses separate partial differential equations expressing conservation of mass, momentum, and energy for each individual fluid phase. By using this two-fluid model, thermal and mechanical non-equilibrium between the phases can exist, only requiring that mathematical expressions for the exchange of mass, momentum and energy be available. Such a formalism allows very general and physically reasonable modeling of relative motion of the phases and of thermal non-equilibrium.

A second important feature of the THERMIT fluid dynamics is the three-dimensional representation of flow is x-y-z geometry. Previous codes (e.g., COBRA-IIIC) have used a subchannel model which assumes predominantly axial flow. The rectangular coordinate system in THERMIT is well-suited for either core-wide or subchannel analyses. THERMIT also offers the choice of either pressure of velocity boundary conditions at the top and bottom of the core. This feature permits realistic modeling of the core boundary conditions and is important for reactor transient analysis.

A third important feature of THERMIT is the heat transfer modeling. A radial heat conduction model (with gap conductance between the fuel pellet and cladding) is used with a continuous general boiling curve describing heat transfer to the fluid both below and above the critical heat flux. The boiling curve is based on recommendations by Bjornard [20] and consists of five basic regimes: convection to liquid, nucleate boiling, transition region, stable film boiling, and convection to vapor. The heat flux is modeled as a heat transfer coefficient times a wall-fluid temperature difference in all regimes except in the transition

region, where the heat flux is computed for each phase.

The final important feature of THERMIT is the numerical method used to solve the fluid dynamics equation. A semi-implicit technique is used which is a modified version of the I.C.E. method [5,6]. As such, the method has a stability restriction in the form of a maximum allowable time step:

$$\Delta t < (\Delta z/V_k)_{min} \qquad (2.1)$$

where Δz is the mesh and V_k is the larger of the phase velocities. However, the method is not restricted by the direction or speed of the flow. Furthermore, convergence can be obtained at each time step if the time step is sufficiently small. Consequently, this numerical method is ideally suited for severe transient analysis.

Although coarse mesh sizes had originally been envisioned when using THERMIT, there is no intrinsic reason to prohibit the code's application to small mesh size problems; up to a point. From a numerical point of view, the solution method does not explicitly restrict the size of the mesh. However, due to stability considerations, a linear mesh size smaller than 0.2 mm may lead to numerical problems [21]. Since this limit is at least 30 times smaller than subchannel size, no instabilities would be expected for subchannel applications.

Overall then, it can be stated that THERMIT is a very powerful analytical tool. This code contains an advanced two-phase model and a fairly unrestricted solution technique. Also since the code is theoretically not restricted to large mesh applications, THERMIT would seem to be well-suited for subchannel applications. However, as will be discussed in Chapter 3, the original version of THERMIT had certain geo-

metrical and physical characteristics which prevented accurate subchannel analysis. Hence, the code needed to be modified to permit this type of application.

2.4.3 Two-Fluid Model Conservation Equations

The governing equations of the two-fluid model in THERMIT, which are the mass, energy, and momentum conservation equations for each phase, can be derived from local, instantaneous conservation equations. The general procedure is to average the equations over time and then average them over an arbitrary volume. The result is a set of time and space averaged conservation equations which contain a number of integral terms. Examples of this type of derivation can be found in references 22 and 23.

The THERMIT conservation equations are derived in Appendix A. This derivation begins by applying the appropriate time and space averaging operators to the local, instantaneous balance equations. The assumptions required to obtain the THERMIT equations are given and, by suitable rearrangement, the appropriate two-fluid model equations are obtained.

The major simplifying assumptions are:

(1) that viscous stress and energy dissipation can be neglected, and

(2) that the liquid and vapor pressures are assumed to be equal within any control volume.

The assumption concerning the viscous and energy dissipation terms is appropriate due to the relatively small value of these terms. The assumption of uniform pressure is also appropriate provided the size of the volume is not too large.

Following the derivation in Appendix A, one obtains the following

set of equations:

Conservation of Vapor Mass

$$\frac{\partial}{\partial t}(\alpha\rho_v) + \nabla\cdot(\alpha\rho_v\vec{V}_v) = \Gamma - W_{tv} \tag{2.2a}$$

Conservation of Liquid Mass

$$\frac{\partial}{\partial t}[(1-\alpha)\rho_\ell] + \nabla\cdot[(1-\alpha)\rho_\ell\vec{V}_\ell] = -\Gamma - W_{t\ell} \tag{2.2b}$$

Conservation of Vapor Energy

$$\frac{\partial}{\partial t}(\alpha\rho_v e_v) + \nabla\cdot(\alpha\rho_v e_v\vec{V}_v) + P\,\nabla\cdot(\alpha\vec{V}_v) + P\,\frac{\partial\alpha}{\partial t} = \tag{2.2c}$$

$$= Q_{wv} + Q_i - Q_{tv}$$

Conservation of Liquid Energy

$$\frac{\partial}{\partial t}[(1-\alpha)\rho_\ell e_\ell] + \nabla\cdot[(1-\alpha)\rho_\ell e_\ell\vec{V}_\ell] + P\,\nabla\cdot[(1-\alpha)\vec{V}_\ell] \tag{2.2d}$$

$$- P\,\frac{\partial\alpha}{\partial t} = Q_{w\ell} - Q_i - Q_{t\ell}$$

Conservation of Vapor Momentum

$$\alpha\rho_v\frac{\partial\vec{V}_v}{\partial t} + \alpha\rho_v\vec{V}_v\cdot\nabla\vec{V}_v + \alpha\nabla P = -\vec{F}_{wv} - \vec{F}_{iv} \tag{2.2e}$$

$$+ \alpha\rho_v\vec{g} - \vec{F}_{tv}$$

Conservation of Liquid Momentum

$$(1-\alpha)\rho_\ell\frac{\partial\vec{V}_\ell}{\partial t} + (1-\alpha)\rho_\ell\vec{V}_\ell\cdot\nabla\vec{V}_\ell + (1-\alpha)\nabla P = -\vec{F}_{w\ell} - \vec{F}_{i\ell} \tag{2.2f}$$

$$+ (1-\alpha)\rho_\ell\vec{g} - \vec{F}_{t\ell}$$

The notation for these equations can be found in the Nomenclature section.

A few important characteristics of these equations should be discussed. First, it is seen that all the important transport mechanisms are included. In particular, the terms describing the turbulent transport effects are included in these equations. In the original version of THERMIT, these terms had been neglected. However, for subchannel applications, as well as large fluid plena applications, it is imperative that these terms be included. The turbulent transport terms are discussed in detail in section 3.3.

A second feature of the equations concerns the representation of the interfacial heat and momentum exchange terms. As written, these terms include the effects of mass transfer between the phases. That is, the interfacial heat transfer term, Q_i, includes heat conduction between the phases as well as the heat transfer due to mass transfer (e.g., evaporation). Similarily, the interfacial momentum exchange term, F_i, includes the momentum exchange due to mass transfer. In the original version of THERMIT both of these mass transfer effects had been neglected. The absence of the momentum exchange contribution is probably appropriate due to its relatively small value for most problems. However, the energy exchange contribution is comparable with the other terms and, hence, has now been included in the present formulation. Further details on these models may be found in Chapter 4.

2.4.4 Finite Difference Equations

The finite difference equations which approximate the above conservation equations, without the newly added terms, have been presented in

reference 3. The procedure for obtaining the difference equations is to approximate the temporal and spatial derivatives by difference operators. Since a semi-implicit differencing method is used, the temporal derivatives are replaced by a forward difference operator. The other terms are treated either implicitly or explicitly depending on the term. New time variables are represented with the superscript n+1 while old time variables are superscripted with an n. Source terms are treated as implicitly as possible, but do contain some variables evaluated at the old time. Consequently, source terms are superscripted with n+1/2 to indicate their semi-implicit formulation.

The spatial discretization of the equations requires a three-dimensional grid to be overlayed on the geometrical configuration under consideration. Once this grid has been defined the locations of the variables are determined. The convention for associating the variables with a particular mesh cell is illustrated in Figure 2.2. All unknowns except the velocities are associated with cell centers. The velocity components normal to that face are defined. On cell faces, subscripts for the cell-centered quantities are i, j, and k, while on cell faces half increments are used (e.g., i+1/2, j, k). In order to simplify the following equations, only the half integral subscripts will be retained (e.g., $P_{i+1/2}$ refers to $P_{i+1/2,j,k}$).

With this background information, the finite difference equations will now be given. In the mass and energy equations control volume flux balances are used to approximate the divergence terms. With this approximation the equations are:

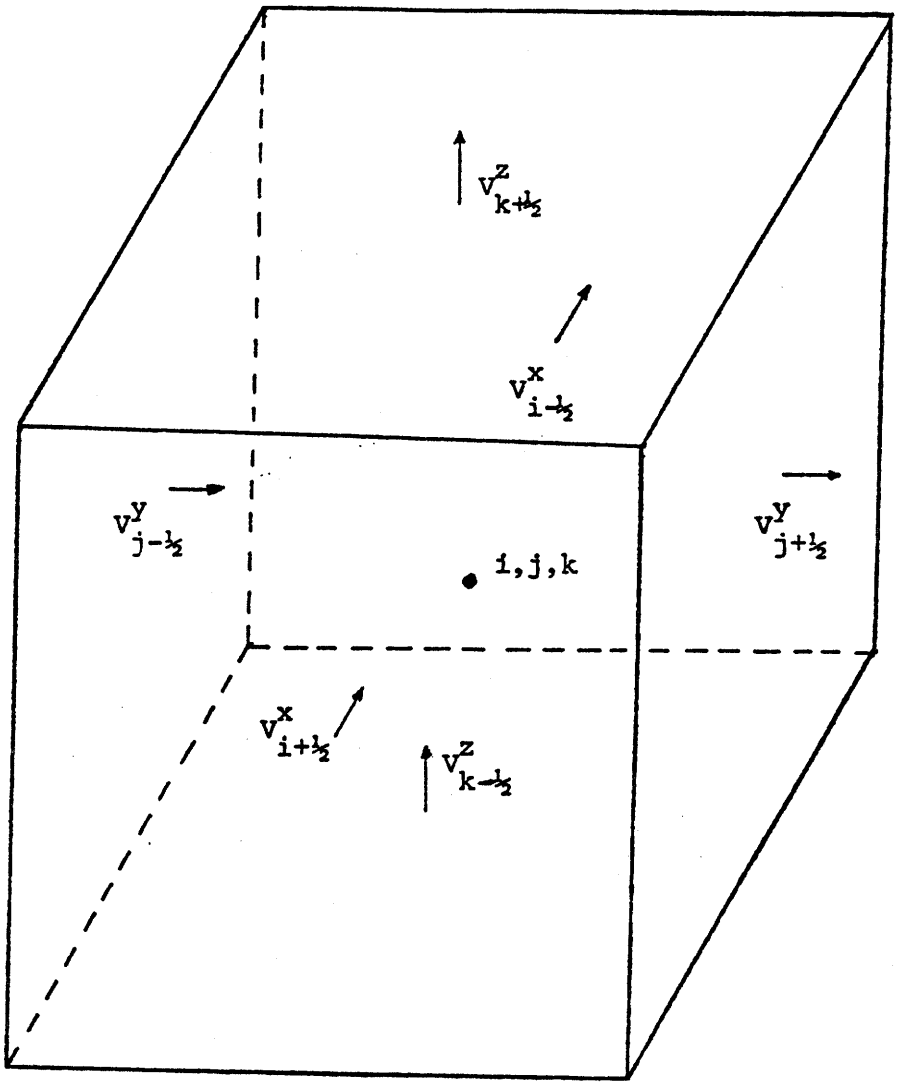

Cell Centered Quantities: P, T_v, T_ℓ, e_v, e_ℓ, ρ_v, ρ_ℓ, α,

Figure 2.2: Typical Fluid Mesh Cell Showing Locations of Variables and Subscripting Conventions

Vapor Mass

$$\frac{(\alpha\rho_v)^{n+1} - (\alpha\rho_v)^n}{\Delta t} + \frac{1}{W}\Big[[A(\alpha\rho_v)^n(V_v^x)^{n+1}]_{i+1/2} \tag{2.3a}$$

$$- [A(\alpha\rho_v)^n(V_v^x)^{n+1}]_{i-1/2} + [A(\alpha\rho_v)^n(V_v^y)^{n+1}]_{j+1/2}$$

$$- [A(\alpha\rho_v)^n(V_v^y)^{n+1}]_{j-1/2} + [A(\alpha\rho_v)^n(V_v^z)^{n+1}]_{k+1/2}$$

$$- [A(\alpha\rho_v)^n(V_v^z)^{n+1}]_{k-1/2}\Big] = \Gamma^{n+1/2} - W_{tv}^{n+1/2}$$

Liquid Mass

$$\frac{((1-\alpha)\rho_\ell)^{n+1} - ((1-\alpha)\rho_\ell)^n}{\Delta t} + \frac{1}{W}\Big[[A((1-\alpha)\rho_\ell)^n(V_\ell^x)^{n+1}]_{i+1/2} \tag{2.3b}$$

$$- [A((1-\alpha)\rho_\ell)^n(V_\ell^x)^{n+1}]_{i-1/2} + [A((1-\alpha)\rho_\ell)^n(V_\ell^y)^{n+1}]_{j+1/2}$$

$$- [A((1-\alpha)\rho_\ell)^n(V_\ell^y)^{n+1}]_{j-1/2} + [A((1-\alpha)\rho_\ell)^n(V_\ell^z)^{n+1}]_{k+1/2}$$

$$- [A((1-\alpha)\rho_\ell)^n(V_\ell^z)^{n+1}]_{k-1/2}\Big] = -\Gamma^{n+1/2} - W_{t\ell}^{n+1/2}$$

Vapor Energy

$$\frac{(\alpha\rho_v e_v)^{n+1} - (\alpha\rho_v e_v)^n}{\Delta t} + \frac{1}{W}\Big[[P^n + (\rho_v e_v)^n_{i+1/2}][A\alpha^n(V_v^x)^{n+1}]_{i+1/2}$$

$$- [P^n + (\rho_v e_v)^n_{i-1/2}][A\alpha^n(V_v^x)^{n+1}]_{i-1/2}$$

$$+ [P^n + (\rho_v e_v)^n_{j+1/2}][A\alpha^n(V_v^y)^{n+1}]_{j+1/2}$$

$$- [P^n + (\rho_v e_v)^n_{j-1/2}][A\alpha^n(V_v^y)^{n+1}]_{j-1/2} \tag{2.3c continued}$$

$$+ [P^n + (\rho_v e_v)^n_{k+1/2}][A\alpha^n (V_v^z)^{n+1}]_{k+1/2} \qquad (2.3c)$$

concluded

$$- [P^n + (\rho_v e_v)^n_{k-1/2}][A\alpha^n (V_v^z)^{n+1}]_{k-1/2} \Big]$$

$$+ P^n \frac{\alpha^{n+1} - \alpha^n}{\Delta t} = Q_{wv}^{n+1/2} + Q_i^{n+1/2} - Q_{tv}^{n+1/2}$$

Liquid Energy

$$\frac{((1-\alpha)\rho_\ell e_\ell)^{n+1} - ((1-\alpha)\rho_\ell e_\ell)^n}{\Delta t} \qquad (2.3d)$$

$$+ \frac{1}{W}\Big[[P^n + (\rho_\ell e_\ell)^n_{i+1/2}][A(1-\alpha)^n (V_\ell^x)^{n+1}]_{i+1/2}$$

$$- [P^n + (\rho_\ell e_\ell)^n_{i-1/2}][A(1-\alpha)^n (V_\ell^x)^{n+1}]_{i-1/2}$$

$$+ [P^n + (\rho_\ell e_\ell)^n_{j+1/2}][A(1-\alpha)^n (V_\ell^y)^{n+1}]_{j+1/2}$$

$$- [P^n + (\rho_\ell e_\ell)^n_{j-1/2}][A(1-\alpha)^n (V_\ell^y)^{n+1}]_{j-1/2}$$

$$+ [P^n + (\rho_\ell e_\ell)^n_{k+1/2}][A(1-\alpha)^n (V_\ell^z)^{n+1}]_{k+1/2}$$

$$- [P^n + (\rho_\ell e_\ell)^n_{k-1/2}][A(1-\alpha)^n (V_\ell^z)^{n+1}]_{k-1/2}\Big]$$

$$- P^n \left(\frac{\alpha^{n+1} - \alpha^n}{\Delta t}\right) = Q_{w\ell}^{n+1/2} - Q_i^{n+1/2} - Q_{t\ell}^{n+1/2}$$

For the momentum equations, the equation for a particular direction is differenced between the centers of the two appropriate cells. Consequently, the mesh used in the momentum equations is different than that used in the mass and energy equations. Since there are a total of six momentum equations all having the same form, only the z-direction vapor equation will be given. The other equations are found by permutation.

The vapor z-direction momentum equation is given by

$$(\alpha\rho_v)^n_{k+1/2} \frac{[(V_v^z)^{n+1} - (V_v^z)^n]_{k+1/2}}{\Delta t} + (\alpha\rho_v)^n_{k+1/2} \left[(V_v^x)_{k+1/2} (\frac{\Delta x}{\Delta x} V_v^z)_{k+1/2} \right.$$

$$\left. + (V_v^y)_{k+1/2} (\frac{\Delta y}{\Delta y} V_v^z)_{k+1/2} + (V_v^z)_{k+1/2} (\frac{\Delta z}{\Delta z} V_v^z)_{k+1/2} \right]^n$$

$$+ \alpha^n_{k+1/2} \left[\frac{P_{k+1} - P_k}{\Delta Z_{k+1/2}} \right]^{n+1} = - (F^z_{wv})^{n+1/2}_{k+1/2} - (F_{iv}{}^z)^{n+1/2}_{k+1/2}$$

$$- (\alpha\rho_v g)^n_{k+1/2} - (F_{tv})^n_{k+1/2} \qquad (2.4)$$

A few important features of these equations need to be highlighted. First of all, it is seen that values are required for the unknowns at locations other than those defined by the noding convention. For example in the mass equation, the quantity $(\alpha\rho_v)_{i+1/2}$ is required. For all such terms in the mass and energy equations the donor cell logic is used. Mathematically this can be expressed as

$$C_{i+1/2} = \begin{cases} C_{i+1} & \text{if } V_{i+1/2} < 0 \\ C_i & \text{if } V_{i+1/2} \geq 0 \end{cases} \qquad (2.5)$$

where C is the quantity of interest (i.e., α, P, ρ_v, ρ_ℓ etc.).

In the momentum equations, no such general rule exists for specifying variables at locations other than the noding convention. Instead, each required term is specified separately. The expression for $(\alpha\rho_v)_{k+1/2}$ is given by

$$(\alpha\rho_v)_{k+1/2} = \alpha_{k+1/2} (\rho_v)_{k+1/2} \qquad (2.6)$$

where

$$\alpha_{k+1/2} = \frac{\alpha_{k+1}\,\Delta Z_{k+1} + \alpha_k\,\Delta Z_k}{\Delta Z_{k+1} + \Delta Z_k} \tag{2.7}$$

and

$$(\rho_v)_{k+1/2} = \frac{(\rho_v)_{k+1}\,\Delta Z_{k+1} + (\rho_v)_k\,\Delta Z_k}{\Delta Z_{k+1} + \Delta Z_k} \tag{2.8}$$

Every velocity except $(V_v^z)_{k+1/2}$ needs to be difined since they are not at the aprior defined location. These velocities are defined by:

$$(V_v^y)_{k+1/2} = \frac{1}{4}\,[(V_v^y)_{j-1/2} + (V_v^y)_{j+1/2} + (V_v^y)_{j-1/2,\ k+1} + (V_v^y)_{j+1/2,\ k+1}] \tag{2.9}$$

$$(V_v^x)_{k+1/2} = \frac{1}{4}\,[(V_v^x)_{i-1/2} + (V_v^x)_{i+1/2} + (V_v^x)_{i-1/2,\ k+1} + (V_v^x)_{i+1/2,\ k+1}] \tag{2.10}$$

Finally for the convective operators, which use the donor cell logic, the following expressions are used:

$$\left(\frac{\Delta_x V_v^z}{\Delta X}\right)_{k+1/2} = \begin{cases} \dfrac{(V_v^z)_{i+1,\ k+1/2} - (V_v^z)_{k+1/2}}{\Delta X_{i-1/2}} & \text{if } (V_v^x)_{k+1/2} < 0 \\ \dfrac{(V_v^z)_{k+1/2} - (V_v^z)_{i-1,\ k+1/2}}{\Delta X_{i-1/2}} & \text{if } (V_v^x)_{k+1/2} \geq 0 \end{cases} \tag{2.11a}$$

$$\left(\frac{\Delta_y V_v^z}{\Delta Y}\right)_{k+1/2} = \begin{cases} \dfrac{(V_v^z)_{j+1,\,k+1/2} - (V_v^z)_{k+1/2}}{\Delta Y_{j+1/2}} & \text{if } (V_v^y)_{k+1/2} < 0 \\ \dfrac{(V_v^z)_{k+1/2} - (V_v^z)_{j-1,\,k+1/2}}{\Delta Y_{j-1/2}} & \text{if } (V_v^y)_{k+1/2} \geq 0 \end{cases} \tag{2.11b}$$

$$\left(\frac{\Delta_z V_v^z}{\Delta Z}\right)_{k+1/2} = \begin{cases} \dfrac{(V_v^z)_{k+3/2} - (V_v^z)_{k+1/2}}{\Delta Z_{k+1}} & \text{if } (V_v^z)_{k+1/2} < 0 \\ \dfrac{(V_v^z)_{k+1/2} - (V_v^z)_{k-1/2}}{\Delta Z_k} & \text{if } (V_v^z)_{k+1/2} \geq 0 \end{cases} \tag{2.11c}$$

where the mesh spacing are given by

$$(\Delta X)_{i+1/2} = \frac{(\Delta X_{i+1} + \Delta X_i)}{2} \tag{2.12a}$$

$$(\Delta Y)_{j+1/2} = \frac{(\Delta Y_{j+1} + \Delta Y_j)}{2} \tag{2.12b}$$

The second important feature of the equations is the definition of the transverse flow areas (i.e., A^x and A^y). As the rows of rods are transversed, the cross-sectional area normal to the x (or y) direction changes with x (see Figure 2.3). Since the momentum equation control volumes do not coincide with the mass and energy control volumes it is necessary to carefully define these areas. To be consistent, the cell averaged transverse flow areas must be used [3]. This requirement is the origin of the concept of a distributed resistance approach in which

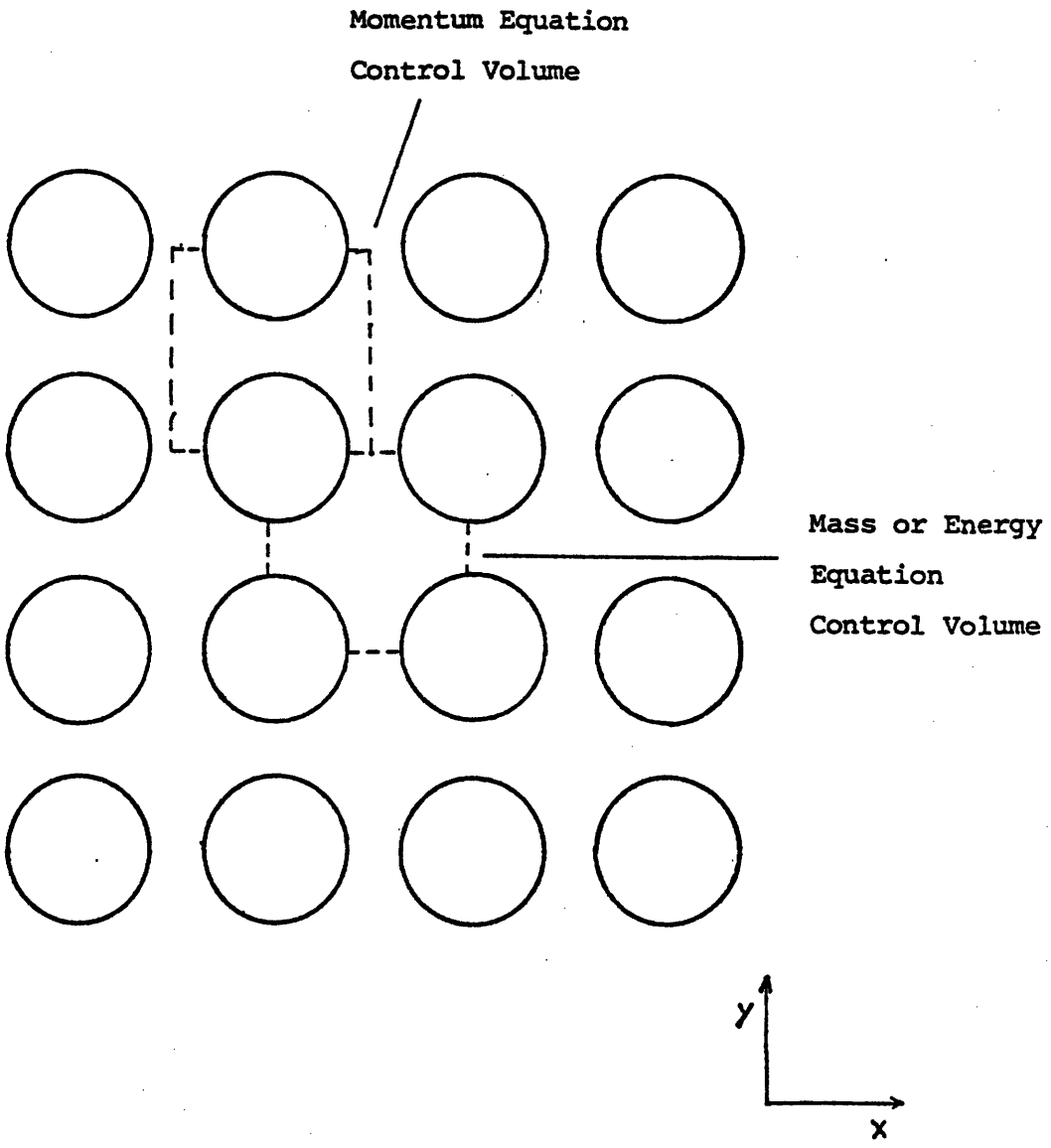

Figure 2.3: Typical Rod Arrangement in Transverse Plane

the structure and associated resistances are averaged over the control volume. By using volume averaged flow areas, the transverse velocity and flow areas are consistent so that continuity of mass and energy can be achieved.

2.4.5 Constitutive Equations

The two-fluid formulation of the conservation equations introduces terms which represent the transfer of mass, energy or momentum in a given control volume. These transport processes occur at one of the four types of interfaces found in a control volume. These interfaces include:

(1) Wall-Liquid Interfaces within cell volume

(2) Wall-Vapor Interfaces within cell volume

(3) Liquid-Vapor Interfaces within cell volume

(4) Inter-Cell Interfaces at cell boundary

Table 2.4 summarizes the transport mechanisms which occur at each interface. The wall friction and wall heat transfer terms are common to all thermal-hydraulic codes. However, for the two-fluid model, the total friction or heat transfer must be apportioned into liquid and vapor components.

A unique feature of the two-fluid equations is that the transport of mass, energy and momentum across liquid-vapor interfaces must be modeled explicitly. These interfacial exchange terms while presenting complex interactions, do allow for general modeling of phasic non-equilibrium.

Across the interchannel interfaces turbulent eddy transport leads to the transfer of mass, energy and momentum. The terms which represent these transport mechanism are referred to as the turbulent mixing terms. These terms account for the coolant-coolant interactions which occur due

TABLE 2.4

Summary of Transport Processes

Wall to Coolant

$F_{w\ell}$	-	Wall Frictional Force on the Liquid
F_{wv}	-	Wall Frictional Force on the Vapor
$Q_{w\ell}$	-	Wall Heat Transfer to the Liquid
Q_{wv}	-	Wall Heat Transfer to the Vapor

Liquid to Vapor

Γ	-	Interfacial Mass Transfer Rate
F_i	-	Interfacial Momentum Exchange Rate
Q_i	-	Interfacial Heat Exchange Rate

Inter-Cell

W_{tv}	-	Turbulent Vapor Mass Exchange Rate
$W_{t\ell}$	-	Turbulent Liquid Mass Exchange Rate
Q_{tv}	-	Turbulent Vapor Energy Exchange Rate
$Q_{t\ell}$	-	Turbulent Liquid Energy Exchange Rate
F_{tv}	-	Turbulent Vapor Momentum Exchange Rate
$F_{t\ell}$	-	Turbulent Liquid Momentum Exchange Rate

to property gradients from one channel to the next.

All of the above terms need to be specified by correlations in order to specify the variable of the two-fluid model. The specific correlations are discussed along with their assessment in Chapter 4, 5, and 6. In general, mixture model correlations are apportioned to determine the wall-coolant transport processes while mechanistic models are used to describe the interfacial and turbulent transport processes.

3.0 DEVELOPMENT OF THERMIT SUBCHANNEL ANALYSIS CAPABILITY

3.1 Introduction

While containing many capabilities for thermal-hydraulic analysis, THERMIT, as originally written, was not acceptable for analyzing subchannels for two reasons. The first was the limitation of being able to model only one fuel rod per unit cell (i.e., per coolant channel). This restriction prevented the analysis of traditional coolant centered subchannels in which up to four fuel rods per channel need to be modeled. Since many experimental measurements are based on this coolant centered geometry, for validation purposes, the code had to be able to analyze coolant centered subchannels.

The second deficiency in THERMIT was the lack of description of turbulent mixing or for that matter any coolant-coolant interactions at channel boundaries. For large control volumes, the omission of turbulent mixing is probably justified but for subchannel analysis these effects are very significant. Hence, in its original form, the use of THERMIT for subchannel analysis seemed questionable at best.

In view of the above mentioned deficiencies, a developmental effort has been undertaken to improve the capabilities of THERMIT. This effort has required a reformulation of the capability to describe the interactions of the coolant and the fuel rods. Additionally, a turbulent mixing model has been added to THERMIT. This model has been formulated to be applicable for both single and two-phase coolant conditions. With these modifications, THERMIT now contains consistent thermal-hydraulic models capable of traditional coolant-centered subchannel analysis. A detailed description of the modifications is given in this chapter.

3.2 Geometrical Modeling Capability

The original version of THERMIT permitted the modeling of only one fuel rod per coolant channel which is adequate for coarse mesh (core) analysis, where only the behavior of an average fuel rod can be determined. However, if subchannel size control volumes are used, then only rod centered subchannels can be exactly analyzed (see Figure 2.1). If coolant centered subchannels are to be analyzed then the fuel rod sections within a channel would have had to be lumped together. Clearly, this lumping causes the loss of all information about the actual clad temperature distribution. Since one of the reasons for performing subchannel analyses is to determine the clad temperature distribution, the restriction of one rod per channel is not compatible with subchannel analysis.

Furthermore, a second aspect of the geometry is related to the validation of the code. This validation relies on comparing the code predictions to experimental measurements. Many measurements in rod arrays have been made based on a coolant centered subchannel. Consequently, realistic calculations and comparisons are feasible only if the same geometry is used.

In view of these considerations, THERMIT has been modified so that coolant centered subchannels could be modeled. The first step in this reformulation has been the modification and expansion of the coupling between the coolant and fuel. This coupling occurs through the heat flux which can be written as:

$$q''^{n+1} = H^n \left(T_w^{n+1} - T_f^{n+1}\right) \qquad (3.1)$$

The heat flux couples the temperature calculations in the fuel to the thermal-hydraulic calculations in the coolant. The significant feature

of this coupling is that it is implicit in time. In order to have this implicit coupling, the special algorithm described in Appendix E of reference 3 is needed. This algorithm, outlined in Table 3.1, solves the fuel rod conduction equation in a two-step procedure. By doing this, the wall temperature is found iteratively, thus preserving the implicit coupling between the wall and the fluid temperatures.

This coupling has been maintained and expanded so that up to four fuel rods can contribute to the power input of a subchannel. The power released by the ith rod to the jth subchannel is given by

$$q_i^{n+1} = H_j^n (T_{w_i}^{n+1} - T_{f_j}^{n+1}) P_{hi} \Delta Z \qquad (3.2)$$

Where P_{hi} is the heated perimeter of the ith rod which faces the adjacent subchannel. The power input to the jth subchannel is then given by

$$\sum_{i=1}^{4} q_i^{n+1} = \sum_{i=1}^{4} H_j^n (T_{w_i}^{n+1} - T_{f_j}^{n+1}) P_{hi} \Delta Z \qquad (3.3)$$

With this modification, a given subchannel can be coupled to as much as four fuel rods, consistent with coolant centered subchannel analysis.

However, a complication is introduced with this formulation. Namely, four clad temperatures are required for each fuel rod. (Alternatively an average clad temperature for each rod could be defined, but would not be consistent with the implicit coolant-to-fuel coupling.) This requirement, while increasing the complexity of the heat transfer calculations, allows for detailed fuel rod modeling. Since accurate fuel rod temperatures are of interest, the increased complexity caused by adding this capability is certainly welcome.

This capability has resulted in a more general thermal modeling of the fuel rods. In particular, a given fuel rod does not necessarily

TABLE 3.1

Implicit Heat Transfer Algorithm

1. Calculate H^n using previous time step wall and fluid conditions.

2. Set up fuel rod conduction equation using the boundary condition

$$q'' = H^n \, (T_w^{n+1} - T_f^{n+1})$$

at this stage the assumption $T_f^{n+1} = T_f^n$ is made.

3. Forward Elimination of the rod conduction problem yields both an initial guess for new wall temperature, $T_w^{n+1,0}$ and $\partial T_w^{n+1} \; / \; \partial T_f^{n+1}$.

4. Solve the fluid dynamics equations using

$$q'' = H^n \, (T_w^{n+1,(0)} - T_f^{n+1}) + H^n \, (\partial T_w^{n+1} / \partial T_f^{n+1})(T_f^{n+1} - T_f^n)$$

5. Once T_f^{n+1} is found, T_w^{n+1} is calculated using

$$T_w^{n+1} = T_w^{n+1,(0)} + (\partial T_w / \partial T_f)^{n+1} \, (T_f^{n+1} - T_f^n)$$

6. Complete the backward substitution step of the rod conduction equation.

have to be modeled as a single rod. That is, the rod may be divided into four quarters with each quarter being analyzed separately. The only restriction of this method is that each rod section must be adjacent to only one coolant channel. Hence, as illustrated in Figure 3.1 a rod may be divided into four sections, two sections or one section. In each section, a complete heat transfer calculation is performed so that the temperature distribution throughout the section is calculated. Thus, the clad temperature for each rod section are determined as required by the expanded fuel-to-coolant coupling.

A disadvantage of this approach is that for any given rod modeled as four sections, there will be four centerline temperatures calculated which are not necessarily equal. This is not always accurate due to azimuthal heat conduction effects which are neglected here. For all cases of practical importance that have been run, negligible differences in the centerline temperature were calculated. Furthermore, uncertainties in the physical properties and voiding of the fuel near its center outweigh this numerical approximation. Another minor disadvantage is that the computational time will be increased, but this increase should not be excessive. Therefore, on the whole, the fuel pin expanded modeling together with the coolant-centered subchannel capability provide THERMIT with the geometrical flexibility required for subchannel analysis.

3.3 Two-Phase Turbulent Mixing Model

3.3.1 Background

One of the most important phenomenon that must be accounted for in subchannel analyses is the exchange or mixing of coolant between adjacent subchannels. This mixing is important as it leads to the transfer of

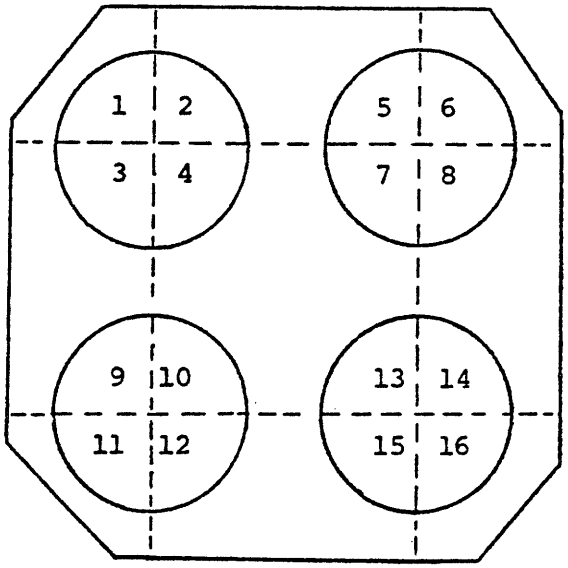

Each Rod Modeled
In 4 Sections

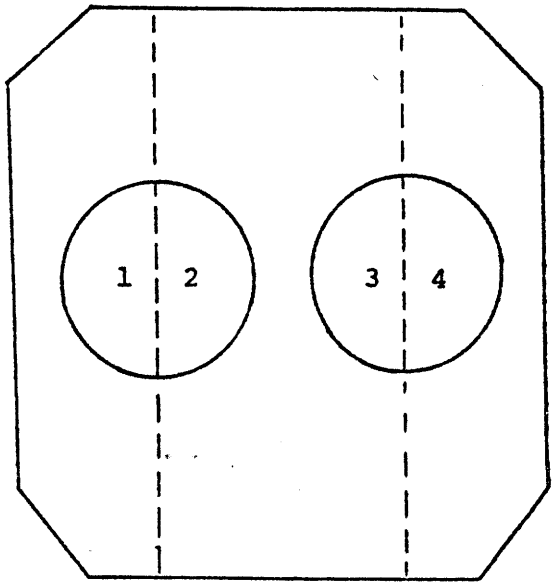

Each Rod Modeled
In 2 Sections

Figure 3.1: Illustration of Fuel Rod Modeling

mass, energy and momentum between adjacent subchannels. As discussed by Rogers and Todreas [24], who have reviewed this subject for the case of single-phase flows, this mixing can be either forced or natural. Forced mixing is caused by mechanical protuberances, such as grids or wire wrap, which either randomly break up the flow or actually divert the flow in a preferred direction. Natural mixing, which occurs in the absence of such protuberances, consists of turbulent mixing and diversion cross-flow. The main distinction between these two types of natural mixing is whether the mixing occurs with or without pressure gradients. Turbulent mixing results from the natural eddy transport between subchannels, while diversion cross-flow is caused by radial pressure gradients.

Even though these various types of mixing have been identified for single-phase flows, they will also exist in two-phase flows. However, an additional mixing phenomenon has been postulated to occur in two-phase flows. This phenomenon, known as vapor diffusion, has been postulated in order to describe the experimental measurements which could not be explained with single-phase concepts of turbulent mixing [25]. Specifically, the void fraction profile in a rod bundle geometry, referred to as the fully developed distribution, is such that the more open areas have the larger vapor (void) concentrations. In other words, the vapor tends to diffuse to unobstructed regions. This observation cannot be predicted using turbulent mixing alone. Hence, vapor diffusion must also be included as a separate type of natural mixing in two-phase flows.

Another important difference between single and two-phase flows is the mechanism for eddy transport. In single-phase flow the conventional approach is to assume equal mass exchange between two cells such that no net mass transfer occurs due to turbulent mixing. However, in two-

phase systems, the equal mass exchange model must be replaced by an equal volume exchange model in order to explain energy mixing [26]. In this latter model a volume of vapor in one channel exchanges with an equal volume of liquid in the adjacent channel. In this manner a net transfer of mass occurs. However, this mass transfer is reasonable as evidenced by experimental findings [26]. Furthermore, if one considers energy exchange in saturated boiling, then with an equal mass exchange model no energy can be transferred. On the other hand, energy is clearly transferred in the equal volume model. It should also be noted that in single-phase flows the two exchange models are essentially equivalent. Consequently, in view of its superior physical interpretation of two-phase flow, the equal volume exchange model is preferred.

If all these types of mixing are present, then they must be accounted for in the analytical model. In the original version of THERMIT, only the diversion cross-flow type of mixing has been explicitly considered. The omission of the forced mixing is justified since the use of wire-wrap of flow diverters is not common in light water reactor rod bundles. However, the absence of turbulent mixing would only be justified if the scale of the mesh size is much larger than the scale of the turbulent eddy transport in the flow. Practically, this means that the dimensions of the computational cell must be larger than the Prandtl mixing length (taken here as the scale of the turbulence). This condition is met when subassembly size cells are used. However, for subchannel applications the mixing length is on the order of the subchannel size, therefore, the effects of turbulence must be included.

3.3.2 Model Formulation

3.3.2.1 Background

In view of the need to include the effects of turbulent mixing, a model suitable for use in THERMIT has been developed. Before discussing the mathematical formulation of this model, its important physical features will be discussed. The first important feature is the two-phase flow regime dependence of the model [27]. By considering the mixing rate as a function of the flow quality, the general characteristics of the model are qualitatively described as follows. For single-phase liquid or single-phase vapor, the model naturally defaults to a single-phase turbulent mixing model appropriate for the phase present. For two-phase conditions it is found that the mixing rate is enhanced above the single-phase rate. The peak mixing rate depends on the flow regime. Near the slug-annular transition point the mixing is found to be greatest and at this point the model reaches its maximum. The approach to this maximum from the two single-phase limits is approximated with simple functions. These functions, while not exactly corresponding to measured data, do represent the observed trends in the two-phase mixing rate, as will be discussed in Chapter 5.

Aside from the flow regime dependence of the model, a second important feature is that, for two-phase conditions, the effects of both turbulent mixing and vapor diffusion are included. Although these two phenomena are different, they do share similar characteristics. Both phenomena result in the transfer of mass, energy and momentum between adjacent subchannels. Furthermore, both phenomena are postulated to occur in the absence of pressure gradients. In view of these similari-

ties the two phenomena are combined into a net two-phase mixing model.

The mathematical formulation of the two-phase mixing model has been adapted from previous work for mixture models [28,29] in order to fit into the framework of THERMIT's two-fluid model. The previous work has dealt with simpler two-phase flow models such as homogeneous or drift-flux. The extension of the semi-mechanistic models which attempt to represent the important physical processes to the two-fluid model is not unambiguous. Many possibilities exist for proportioning a given model when going from a homogeneous model to a two-fluid model. However, the one constraint which must be observed is that when the liquid and vapor portions are added together the sum is the homogeneous model result. The adaptation of these previous models is, therefore, to some extent arbitrary and the choice given here is justified by the validation with experiments discussed in Chapter 5.

Another consideration of the mathematical formulation is that the equations must not introduce any numerical instabilities. Both the numerical and physical description of a particular phenomenon are important to the overall structure of THERMIT. Since THERMIT is not fully implicit, a number of temporally explicit terms are included in the equations. These explicit terms require stability restrictions such that numerical errors do not grow with time. The inclusion of a new phenomenon, such as two-phase mixing, may introduce limits which did not previously exist. Hence, the numerical representation of any phenomenon must be done with some care.

The two-phase mixing model can be discussed in terms of its physical as well as its numerical nature. In order to simplify this description, the physical nature of the model will be given first. The salient

numerical aspects of the model will be given next.

3.3.2.2 Analytical Formulation and Discussion

The terms which represent the effects of turbulent mixing have been identified in Section 2.4. These terms, which represent the exchange of mass, energy and momentum due to turbulent interactions, can be written as follows:

$$W_{tv} = \nabla \cdot W''_{tv} = \Sigma \frac{S_{ij}}{A_i} (W''_{tv})_{ij} \tag{3.4}$$

$$W_{t\ell} = \nabla \cdot W''_{t\ell} = \Sigma \frac{S_{ij}}{A_i} (W''_{t\ell})_{ij} \tag{3.5}$$

$$Q_{tv} = \nabla \cdot q''_{tv} = \Sigma \frac{S_{ij}}{A_i} (q''_{tv})_{ij} \tag{3.6}$$

$$Q_{t\ell} = \nabla \cdot q''_{t\ell} = \Sigma \frac{S_{ij}}{A_i} (q''_{t\ell})_{ij} \tag{3.7}$$

$$F_{tv} = \nabla \cdot \tau_{tv} = \Sigma \frac{S_{ij}}{A_i} (\tau_{tv})_{ij} \tag{3.8}$$

$$F_{t\ell} = \nabla \cdot \tau_{tv} = \Sigma \frac{S_{ij}}{A_i} (\tau_{t\ell})_{ij} \tag{3.9}$$

where S_{ij} is the gap between rods. The divergence operator has also been approximated by its control.volume equivalent.

In each of these equations, there are still the terms which represent the flux of the specific property involved. In the mass equations, W''_{tv} and $W''_{t\ell}$ are the vapor and liquid mass fluxes due to mixing. The energy equation terms q''_{tv} and $q''_{t\ell}$ are the vapor and liquid heat fluxes due to mixing. Finally, in the momentum equations the terms τ_{tv} and $\tau_{t\ell}$ are the shear stresses due to mixing. It should be noted that only transverse mixing is considered which is appropriate due to the larger interaction area in the transverse direction. The set of equations which describe these terms are similar in form and, hence, only one of these terms will

be discussed in detail.

If one considers single-phase flow, then the turbulent shear stress term, also referred to as the Reynolds stress, is usually written as

$$\tau = \varepsilon\rho \frac{\partial V}{\partial x} \tag{3.10}$$

where ε is the eddy diffusivity. This term can be approximated as follows:

$$\tau \approx \frac{\varepsilon (G_i - G_j)}{\ell} \tag{3.11}$$

where ℓ is the effective mixing length. This form is convenient to use provided the term ε/ℓ can be determined. This term, which has the dimensions of a velocity and is sometimes referred to as the turbulent velocity, can be related to measured mixing through the following equation

$$\varepsilon/\ell = W'/\rho S_{ij} \tag{3.12}$$

The mixing rate, W', has been measured by a number of authors [27,30], and is usually expressed as a function of the Reynolds number. Once ε/ℓ is determined, the Reynolds stress is easily calculated.

The extension of the above equations to two-phase flow requires the addition of two physical effects. First, the vapor diffusion phenomena must be added to the model. Following the work of Lahey [25], the two-phase Reynolds stress is written as

$$\tau_{TP} = \varepsilon/\ell(G_i - G_j - (G_i - G_j)_{FD}) \tag{3.13}$$

where the subscript, FD denotes the fully-developed distribution. This form of the shear stress term accounts for both turbulent mixing and

vapor diffusion. The justification for this form is based on the experimental work of Gonzalez-Santalo and Griffith [26]. These authors have shown that the net two-phase mixing is proportional to the nonequilibrium void fraction gradient. Specifically, they have been able to correlate their vapor mixing rate data using the following equation

$$W_v' = K \rho_v [(\alpha_i - \alpha_j) - (\alpha_i - \alpha_j)_{FD}] \tag{3.14}$$

where K is an empirically determined constant. By analogy, this form can be applied to the other mixing terms so that the shear stress can be written as in Equation 3.13 [25].

The second physical effect which must be included is the dependence of the mixing rate on the flow regime. This effect is included by writing the two-phase turbulent velocity, $(\varepsilon/\ell)_{TP}$, as a function of the single-phase value, $(\varepsilon/\ell)_{SP}$. Mathematically, following the work of Beus [27], this can be expressed as

$$(\varepsilon/\ell)_{TP} = (\varepsilon/\ell)_{SP} \theta \tag{3.15}$$

where θ is a "two-phase multiplier" which depends on the quality. As indicated above, the mixing rate (and hence ε/ℓ) reaches a maximum at the slug-annular transition point. The criterion for this transition point is the Wallis model [31] which is in terms of the superficial velocities:

$$j_v^* = 0.4 + 0.6\, j_\ell^* \tag{3.16}$$

where

$$j_v^* = j_v\, \rho_v^{1/2} [(\rho_\ell - \rho_v) g\, D]^{-1/2} \tag{3.17}$$

$$j_\ell^* = j_\ell \rho_\ell^{1/2} [(\rho_\ell - \rho_v) g D]^{-1/2} \tag{3.18}$$

and

$$j_v = XG/\rho_v \tag{3.19}$$

$$j_\ell = (1-X)G/\rho_\ell \tag{3.20}$$

By rearranging Equation 3.16, an expression for the quality at the transition point can be obtained:

$$X_M = [0.4(\rho_\ell(\rho_\ell - \rho_v) g D)^{1/2}/G + 0.6]/[(\rho_\ell/\rho_v)^{1/2} + 0.6] \tag{3.21}$$

Again following Beus, the function for θ is assumed to increase linearly between $X = 0$ and $X = X_M$. For qualities greater than X_M, θ is assumed to decrease hyperbollically. At $X = X_M$, $\theta = \theta_M$ i.e., θ reaches a maximum. These conditions are expressed as follows:

$$\theta = 1 + (\theta_M - 1)\, X/X_M \qquad \text{if } X < X_M \tag{3.22}$$

$$\theta = 1 + (\theta_M - 1)\left(\frac{1 - X_o/X_M}{\frac{X}{X_M} - \frac{X_o}{X_M}}\right) \qquad \text{if } X > X_M \tag{3.23}$$

and

$$\frac{X_o}{X_M} = 0.57\ Re^{0.0417} \tag{3.24}$$

as correlated by Beus. If a value for θ_M can be prescribed, then the function describing θ is complete.

The only remaining unknown in model for $(\varepsilon/\ell)_{TP}$ is the value for $(\varepsilon/\ell)_{SP}$. As given in Equation 3.12, $(\varepsilon/\ell)_{SP}$ can be expressed as a function fo the mixing rate. The correlation for the single-phase mixing rate used in this model is that of Rogers and Rosehart [30]. By making appropriate substitutions, their correlation can be expressed as a single-phase turbulent velocity which is given by

$$(\varepsilon/\ell)_{SP} = \frac{1}{2} \lambda \, Re^{-0.1}[1 + (\frac{D_j}{D_i})^{1.5}] \frac{D_i}{D_{FS}} \frac{G_i}{\rho} \tag{3.25}$$

where

$$\lambda = 0.0058 \left(\frac{S_{ij}}{D_{FS}}\right)^{-1.46} \tag{3.26}$$

Both the Reynolds number and the density are based on the two-phase mixture and D_{FS} is the fuel rod diameter.

With this correlation, the description of the two-phase turbulent velocity is complete. It should be noted that this velocity is assumed to be the same for both vapor and liquid phases. Clearly, there may be some differences in this velocity for each phase, but within the scope of the overall model these would have small, if any, impact.

Returning to the mixing terms, by analogy these terms can be written as

$$(W''_{tv})_{ij} = \varepsilon/\ell \, [(\alpha\rho_v)_i - (\alpha\rho_v)_j - [(\alpha\rho_v)_i - (\alpha\rho_v)_j]_{FD}] \tag{3.27}$$

$$(W''_{t\ell})_{ij} = \varepsilon/\ell \, [((1-\alpha)\rho_\ell)_i - ((1-\alpha)\rho_\ell)_j - [((1-\alpha)\rho_\ell)_i - ((1-\alpha)\rho_\ell)_j]_{FD}] \tag{3.28}$$

$$(q''_{tv})_{ij} = \varepsilon/\ell \left[(\alpha\rho_v e_v)_i - (\alpha\rho_v e_v)_j - [(\alpha\rho_v e_v)_i - (\alpha\rho_v e_v)_j]_{FD}\right] \quad (3.29)$$

$$(q''_{t\ell})_{ij} = \varepsilon/\ell \left[((1-\alpha)\rho_\ell e_\ell)_i - ((1-\alpha)\rho_\ell e_\ell)_j - [((1-\alpha)\rho_\ell e_\ell)_i - ((1-\alpha)\rho_\ell e_\ell)_j]_{FD}\right] \quad (3.30)$$

$$(\tau_{tv})_{ij} = \varepsilon/\ell \left[G_{vi} - G_{vj} - [G_{vi} - G_{vj}]_{FD}\right] \quad (3.31)$$

$$(\tau_{t\ell})_{ij} = \varepsilon/\ell \left[G_{\ell i} - G_{\ell j} - [G_{\ell i} - G_{\ell j}]_{FD}\right] \quad (3.32)$$

These may be written more concisely as

$$\psi = \frac{\varepsilon}{\ell} \left[(\phi\rho)_i - (\phi\rho)_j - [(\phi\rho)_i - (\phi\rho)_j]_{FD}\right] \quad (3.33)$$

where ψ is the generalized mixing flux term and

$\phi = 1$ in the mass equations

$= e$ in the energy equations

$= V$ in the momentum equations

$\rho = \alpha\rho_v$ in the vapor equations

$= (1-\alpha)\rho_\ell$ in the liquid equations.

The only terms yet to be discussed are the fully-developed distributions. The assumption used by Lahey [25,32], is also used here as a basis for developing expressions for these terms. This assumption states that the fully-developed void fraction distribution is proportioned to the fully-developed mass velocity distribution. Mathematically this is expressed as follows:

$$(\alpha_i - \alpha_j)_{FD} = K(G_i - G_j)_{FD} \tag{3.34}$$

Physically, this equation reflects the observed trend that the void fraction is higher in the channels with higher velocity. Recently, Drew and Lahey [32] have analytically derived this expression. While the fully-developed mass velocity distribution is also not known, it is assumed that this distribution is proportional to the calculated mass velocity distribution.

By using these assumptions and extending the assumption concerning the fully-developed void fraction distribution to the other fully-developed distributions, the following set of equations are obtained.

$$((\alpha\rho_v)_i - (\alpha\rho_v)_j)_{FD} = K_M \frac{(G_i - G_j)}{(G_i + G_j)} ((\alpha\rho_v)_i - (\alpha\rho)_{vj}) \tag{3.35}$$

$$(((1-\alpha)\rho_\ell)_i - ((1-\alpha)\rho_\ell)_j)_{FD} =$$

$$= -K_M \frac{(G_i - G_j)}{(G_i + G_j)} ((\alpha\rho_\ell)_i + (\alpha\rho_\ell)_j) \tag{3.36}$$

$$((\alpha\rho_v e_v)_i - (\alpha\rho_v e_v)_j)_{FD} =$$

$$= K_M \frac{(G_i - G_j)}{(G_i + G_j)} ((\alpha\rho_v e_v)_i + (\alpha\rho_v e_v)_j) \tag{3.37}$$

$$(((1-\alpha)\rho_\ell e_\ell)_i - ((1-\alpha)\rho_\ell e_\ell)_j)_{FD} =$$

$$= -K_M \frac{(G_i - G_j)}{(G_i + G_j)} ((\alpha\rho_\ell e_\ell)_i + (\alpha\rho_\ell e_\ell)_j) \tag{3.38}$$

$$((G_v)_i - (G_v)_j)_{FD} = K_M \frac{(G_i - G_j)}{(G_i + G_j)} (G_{vi} + G_{vj}) \tag{3.39}$$

$$((G_\ell)_i - (G_\ell)_j)_{FD} =$$

$$= K_M \frac{(G_i - G_j)}{(G_i + G_j)} ((\alpha\rho_\ell V_\ell)_i + (\alpha\rho_\ell V_\ell)_j) \tag{3.40}$$

With these equations the description of the two-phase mixing model is complete except for the specification of θ_M and K_M. These two parameters are treated as constants and can be estimated from experimental measurements. For example, measured two-phase mixing rates show that θ_M can vary from 2 to 10 for typical BWR conditions [27]. The value for K_M should be approximately equal to unity [29]. Using typical values, comparisons have been made with subchannel data and recommendations for these parameters have been made as discussed in Chapter 5.

3.3.2.3 Numerical Scheme

As a final note about the two-phase mixing model, the numerical aspects of this model will be discussed. Due to the structure of the solution method in THERMIT, implicit coupling between adjacent channels is only possible through the pressure. This restriction prevents the implicit treatment of either the void fraction or internal energy for adjacent channel terms in the two-phase mixing model. Consequently, a fully implicit formulation of the two-phase mixing model is not possible with the current solution technique.

In view of this restriction, two different numerical formulations of the two-phase mixing terms have been investigated. The first attempt

has been a fully explicit formulation which may be written as

$$\psi^n = (\varepsilon/\ell)^n[(\phi\rho)_i^n - (\phi\rho)_j^n - [(\phi\rho)_i - (\phi\rho)_j]_{FD}^n] \qquad (3.41)$$

However, when this formulation was used, the code developed numerical instabilities. Apparently, the inclusion of the mixing effects introduces an additional stability limit. Hence, this formulation was unacceptable.

The above explicit formulation has been modified to be at least partially implicit. This modification consists of treating the $(\phi\rho)_i$ term in a fully implicit manner. Rewriting the generalized mixing term using this more implicit formulation one obtains:

$$\psi^{n+1/2} = (\varepsilon/\ell)^n[(\phi\rho)_i^{n+1} - (\phi\rho)_j^n - [(\phi\rho)_i - (\phi\rho)_j]_{FD}^n] \qquad (3.42)$$

It should be noted that the fully-developed distribution term is still fully explicit. This formulation is more implicit in time, but is not exactly conservative. However, this should not be a problem since long time step sizes cannot be used due to the convective stability limitation (equation 2.1). Hence, this formulation represents the most acceptable combination of implicit and explicit terms and is the current choice for the two-phase mixing model.

4.0 DEVELOPMENT AND ASSESSMENT OF THE LIQUID-VAPOR INTERFACIAL EXCHANGE MODELS

4.1 Introduction

While the two-fluid model and modified ICE solution technique contained in THERMIT are very flexible and well-suited for analyzing transient two-phase flow, the accuracy of THERMIT is strongly dependent on the choice of constitutive models. As discussed in Section 2.4.5, these models are required to represent the various transport processes which occur in the two-phase flow. Careful definition of these models is essential for the accurate prediction of the complicated non-equilibrium effects which occur in two-phase flows.

The most important non-equilibrium phenomena are subcooled boiling, vapor superheating and relative motion of the two phases (i.e., vapor slip). Both subcooled boiling and vapor slip are important for operational conditions, while vapor superheating becomes important only after the critical heat flux (CHF) has been exceeded.

In addition to modeling these non-equilibrium phenomena, accurate constitutive models are required to predict the correct two-phase flow distribution for subchannel applications. These models account for the transport of mass, energy, and momentum due to turbulent mixing and vapor diffusion.

Finally, for accurate wall temperature prediction, the wall-to-coolant heat transfer model must also be carefully developed. This model needs to account for the heat transfer mechanisms in both the pre-CHF

and post-CHF regimes.

The program for developing and validating the models in THERMIT has been undertaken with two goals:

(1) to define and develop necessary models and,

(2) to validate the predictive capabilities.

The emphasis of this effort has been on evaluating the code for subchannel applications. In particular, the liquid-vapor interfacial exchange models, the two-phase mixing model and the heat transfer model have all been carefully reviewed, modified as necessary and evaluated. The overall predictive capabilities of THERMIT have been judged primarily based on comparisons with experimental measurements.

4.2 Assessment Strategy

In order to meet the goals of this program, an orderly progression of tests and comparisons has been performed. These include comparisons with both one-dimensional and three-dimensional experimental data. The order in which these comparisons have been made is structured so that individual models could be assessed and validated in a logical manner. Ideally, this procedure consists of selecting a set of experimental data which can be used to evaluate a specific model independent of the other models. Then, once a model has been judged appropriate, it can be used with some confidence in the effort to validate the other models. In this manner the data base for the code is built up systematically.

Of course, it is not always possible to evaluate each model separately. For these cases, engineering judgement is required to interpret the results of the comparisons with experimental data. Nevertheless, the present evaluation strategy represents a viable method for validating THERMIT.

Another consideration in the effort is that experimental measurements suitable for model evaluation need to be relatively simple in order to successfully validate individual models. Consequently, the measurements used in this study are straightforward and well-documented. Simple steady-state, one-dimensional measurements as well as steady-state and transient three-dimensional data have been used. The experimental measurements and models which have been assessed are summarized in Table 4.1. It is seen that, typically, more than one model is evaluated using a given set of data. This is possible, though, due to the logical order in which the comparisons have been made.

In this systematic procedure, the initial evaluations have been performed using steady-state, one-dimensional void fraction data. The void fraction measurements of Maurer [33], Christensen [34], and Marchaterre [35] have been used in this study. These measurements are utilized to evaluate the interfacial mass exchange model, Γ, and the interfacial momentum exchange rate, F_i.

Steady-state, three-dimensional measurements have also been used in this study. These measurements include both mass velocity and quality distributions in subchannel geometry. Both the nine rod G.E. bundle data [36] and the sixteen rod Ispra bundle data [37,38] have been used. These measurements are useful for validating the two-phase mixing model.

TABLE 4.1

Summary of Assessment Program

Measurement	Constitutive Model			
	Γ	F_i	Q_w	Turbulent Mixing Model
Steady-State 1 - D Void Fraction	X	X		
Steady-State 1-D Wall Temperature	X		X	
Steady-State 3-D Mass Velocity and Quality				X
Transient 3-D CHF			X	

The final comparisons have been made with steady-state, one-dimensional wall temperature data [39] and transient three-dimensional CHF data [40]. These measurements permit both the transient capabilities as well as the heat transfer model to be assessed.

The results of the comparisons will be discussed here in terms of the individual models. That is, each model, with the exception of the two-phase mixing model already described in Section 3.3, will first be described in detail and then the results of the assessment effort will be given. The interfacial exchange models are discussed in this chapter, the two phase-mixing results are presented in Chapter 5 and the wall-to-coolant heat transfer model assessment is discussed in Chapter 6.

4.3 Interfacial Mass Exchange

4.3.1 Background

In the two-fluid model, the exchange of mass across liquid-vapor interfaces must be explicitly modeled. In reactor applications, this exchange usually takes the form of vapor generation so that the mass exchange model is also referred to as the vapor generation model. Physically, this exchange of mass is strongly dependent on the flow conditions. The mass exchange actually occurs on microscopic scales with vapor being produced at interfaces which are in constant motion. Hence, to describe this phenomenon on the microscopic scale would be virtually impossible. Fortunately, the mass exchange needed in THERMIT is the net exchange which occurs in a given control volume. Consequently, only the integral of all the microscopic effects is considered in the formulation.

However, even the integral or macroscopic vapor generation rate is difficult to define due to the various types of vaporization which can

occur. For BWR conditions at least three different vaporization regimes can be identified as illustrated in Fig. 4.1. The first is termed subcooled boiling due to the fact that vapor is generated even though the bulk liquid is subcooled. For this vaporization mechanism, vapor bubbles are formed at nucleation centers on the heater surface. These bubbles grow and detach when the bulk liquid temperature is above a certain value (referred to as the bubble departure temperature). Of course, since the liquid is subcooled, condensation of the vapor in the bulk fluid may also occur. Consequently, for subcooled boiling conditions, both the vapor generation on the heater walls as well as the vapor condensation need to be modeled.

The second type of vapor generation is referred to as saturated flow boiling. As its name implies, this type of vaporization occurs when the bulk liquid is at saturated conditions. For these conditions, a liquid film is assumed to coat the heater surface. Heat is transferred directly through the liquid film so that vaporization occurs at the liquid-vapor interface. Since both phases are assumed to be at saturation, for steady-state conditions, all of the wall heat flux produces vapor (i.e., neither phase temperature is increased). Hence, if the wall heat flux is known, then the determination of the vapor generation rate follows from an energy balance.

The third type of vapor generation is that which occurs when a superheated vapor transfers heat to liquid droplets thus evaporating the droplets. This form of vaporization primarily occurs after CHF has been exceeded. For these conditions, the liquid can no longer wet the heater surface and, therefore, the entire wall heat flux is transferred directly to the vapor. Due to the relatively low conductivity of the vapor, not

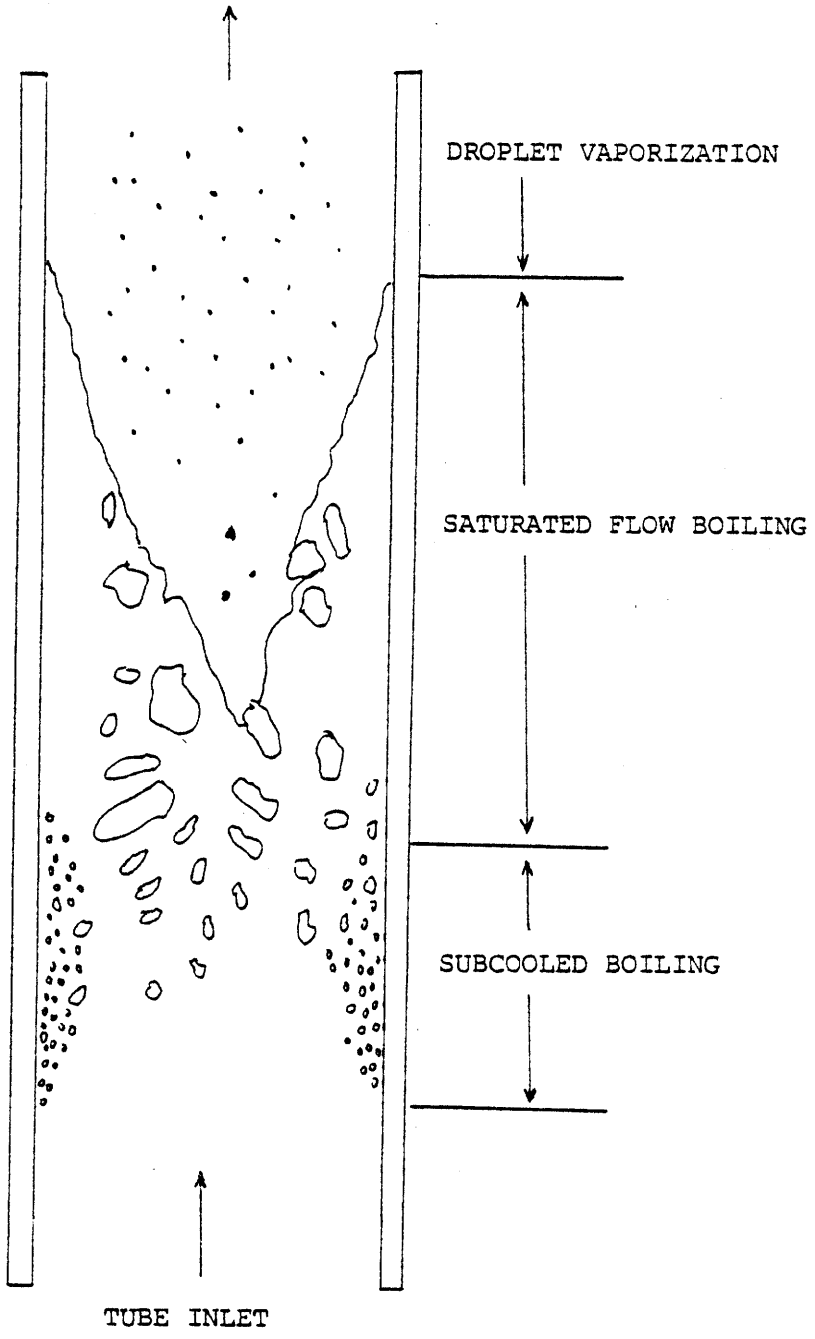

Figure 4.1: Boiling Regimes in Two-Phase Flow in a Vertical Tube with Heat Addition

all of the transferred heat will vaporize the remaining liquid (which takes the form of entrained liquid droplets). Rather, a portion of the heat flux will superheat the vapor with the remainder vaporizing the liquid droplets. This type of vaporization leads to substantial vapor superheat [41] and is clearly a non-equilibrium process.

These three types of vaporization represent the primary vapor generation regimes for steady-state and non-depressurization transient conditions. Both subcooled and saturated boiling occur for steady-state BWR conditions, while only subcooled boiling occurs for most steady-state PWR conditions. Certain transients in either reactor type may result in all three regimes.

In order to decide which regime dominates for a given set of conditions, the range of application of each must be carefully defined. As sketched in Fig. 4.2, the vapor generation rate may be considered to be a function of the equilibrium quality. It is seen that one clear dividing point is the CHF quality (X_{CHF}). For pre-CHF conditions either subcooled or saturated boiling will occur. However, for post-CHF conditions only droplet vaporization will occur. Hence, the droplet vaporization mechanism will be postulated to occur only after CHF has been exceeded.

The division between subcooled and saturated boiling is not very clear due to the gradual transition from one to the other. Hence, it is advantageous to describe both types of boiling in a single, continuous model so that the gradual transition from subcooled to saturated boiling is well represented. Furthermore, this model would be used for all pre-CHF conditions. Hence, the choice of vapor generation regime depends directly on the heat transfer regime.

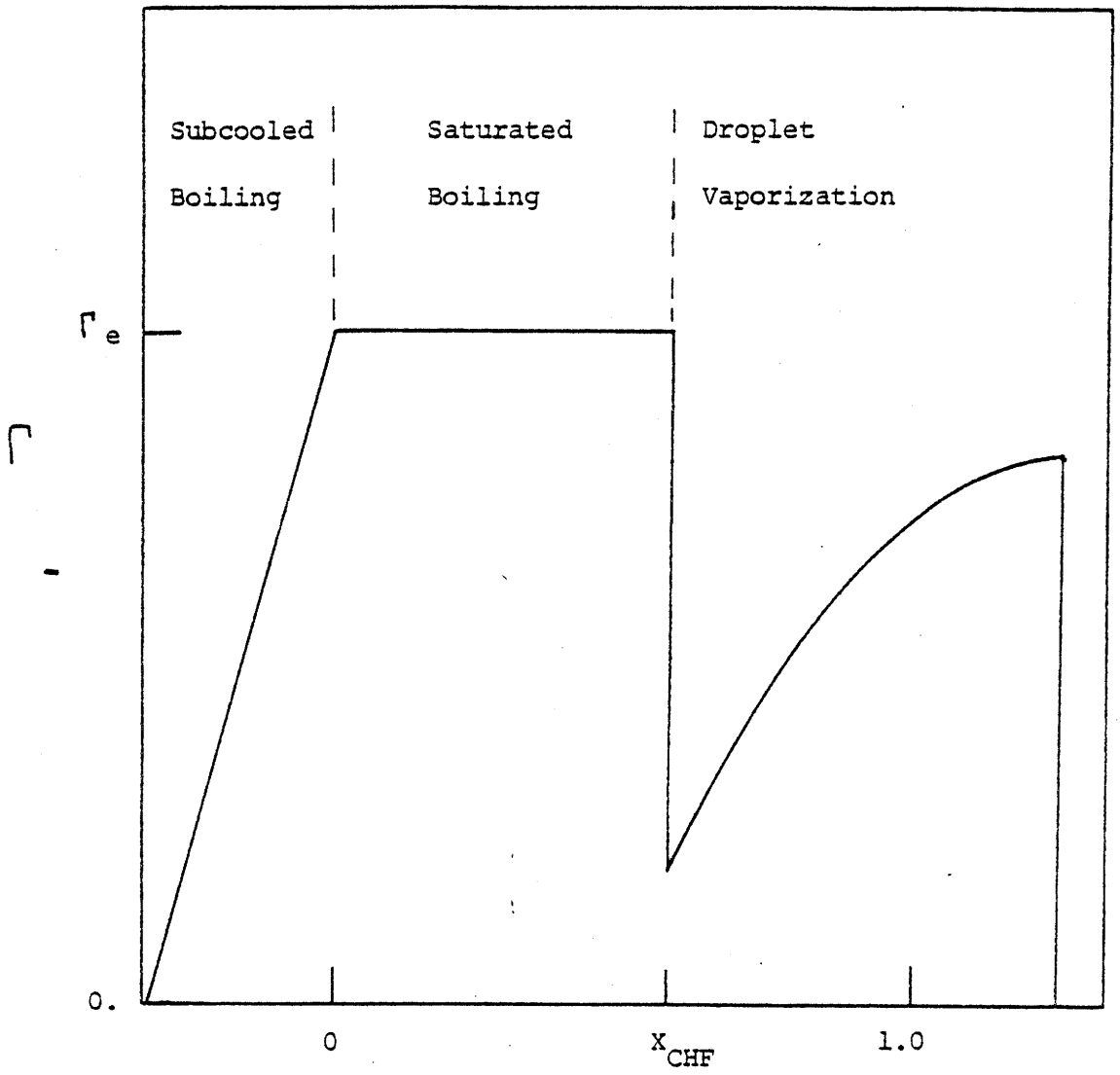

Figure 4.2: Illustration of Vapor Generation Rate, Γ , versus Equilibrium Quality, X_e. ($\Gamma_e = q_w / i_{fg}$)

This approach of using the heat transfer regime to determine the appropriate vapor generation rate has been incorporated into THERMIT. The use of this simple selection scheme eliminates the need to have a more elaborate flow regime map.

Two models are used to represent the vaporization phenomena. The first, referred to as the subcooled boiling model, is employed for all pre-CHF conditions. For the post-CHF droplet vaporization regime, the Saha [42] vapor generation model is used. In the original version of THERMIT this droplet vaporization had not been considered so that the addition of the Saha model represents a significant improvement to the code's capability. Furthermore, the subcooled boiling model was not described in the original report on THERMIT. Detailed descriptions of the physical bases as well as the results of the assessment effort are presented in the following two sections.

4.3.2 Subcooled Vapor Generation Model

The subcooled vapor generation model in THERMIT accounts for both subcooled and saturated boiling in the pre-CHF regime. Since it is relatively easy to formulate a model to describe saturated boiling, the main difficulty in formulating this model is in representing vapor generation for subcooled conditions. The difficulty is that in subcooled boiling vaporization occurs at discrete sites along the heater wall for highly non-equilibrium conditions. Furthermore, the vaporization rate is found to be strongly dependent on the bulk fluid conditions as well as the wall heat flux.

On a microscopic scale, the subcooled vapor generation can be directly related to the vapor bubble rate of growth. Vapor bubbles are

formed at nucleation sites on the heated surface as illustrated in Fig. 4.3. These nucleation sites are only activated when the wall temperature is greater than the saturation temperature. However, once the wall temperature exceeds the saturation temperature, bubbles can begin to form. The temperature distribution in the liquid permits slightly superheated liquid to exist near the wall (see Fig. 4.4). This superheated liquid is easily vaporized provided a vapor bubble site exists. As the bubble liquid temperature increases, so does the region of superheated liquid which in turn allows the bubbles to grow. The bubbles will remain attached to the wall until the bulk liquid temperature reaches the bubble departure temperature, T_d. Once T_d has been exceeded the bubbles detach and flow into the main flow stream. Hence, the bubble departure temperature (which of course is less than the saturation temperature) represents the bulk liquid temperature at which vaporization may begin.

The value for T_d is found to be strongly dependent on the heat flux. For the same bulk liquid temperature, as the heat flux is increased the region of superheated liquid near the wall increases and T_d will decrease. Hence, as the heat flux is increased, boiling will begin at higher subcoolings because the amount of superheated liquid is greater (see Fig. 4.4).

The evaluation of the bubble departure temperature is seen, then, to be very important. This parameter has been correlated by many authors [43, 44]. The correlation of Ahmad [43] has been selected for use in THERMIT. In this correlation, T_d is related to the heat flux through a heat transfer coefficient. The expression for this relationship is given by

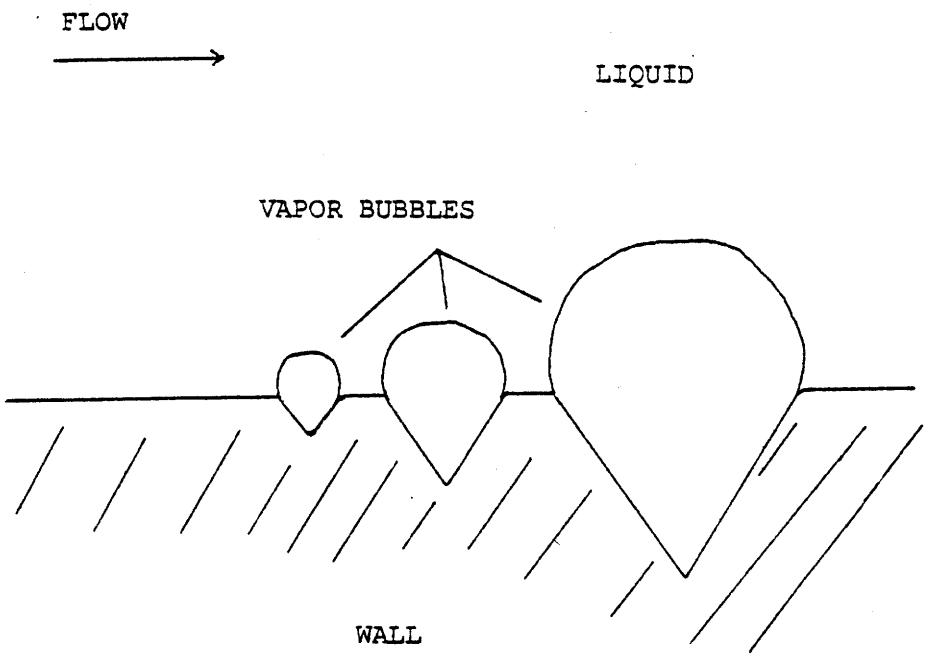

Figure 4.3: Illustration of Vapor Bubble Nucleation and Growth

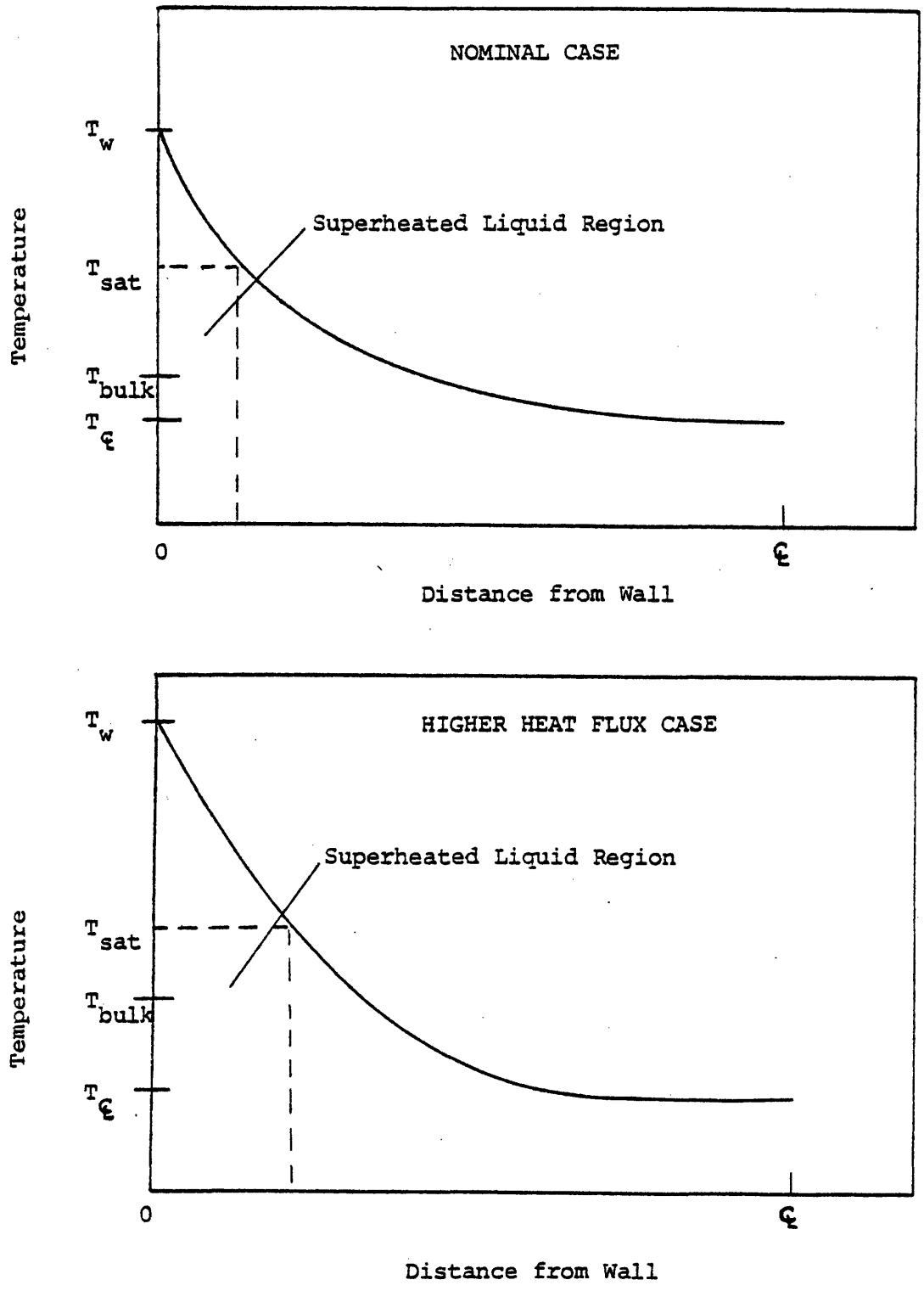

Figure 4.4: Typical Temperature Distributions in Subcooled Boiling

$$T_d = T_s - q''_w/H_A \tag{4.1}$$

The heat transfer coefficient H_A has been correlated using a large number of experimental measurements and is given by

$$H_A = \frac{k_\ell}{D}\left[2.44\ Re^{1/2}\ Pr^{1/3}\left(\frac{i_{in}}{i_f}\right)^{1/3}\left(\frac{i_{fg}}{i_f}\right)^{1/3}\right] \tag{4.2}$$

It is seen that for given flow conditions (i.e., H_A and T_s constant) if the heat flux is increased, then T_d decreases as expected. Hence, the proper trend of the microscopic picture is obtained in this correlation using bulk flow parameters.

Even though T_d is well defined by correlation, the problem of obtaining the vaporization rate based on bulk flow properties still remains. Again following Ahmad, the following physical picture can be constructed. For bulk liquid temperature below T_d, bubbles do not detach and the net vaporization rate is zero. At the other limit, that is $T_\ell = T_s$, all of the wall heat flux leads directly to vapor generation so that the equilibrium vaporization rate, Γ_e, may be written as

$$\Gamma_e = \frac{\dot{q}_w}{i_{fg}} \tag{4.3}$$

where $\dot{q}_w$ is the power transferred to the coolant and i_{fg} is the heat of vaporization. Ahmad then assumes that the vaporization rate increases linearly from T_d to T_s. With these assumptions the vapor generation rate may be written as

$$\Gamma = \begin{cases} 0 & \text{if } T_\ell \leq T_d \\ \dfrac{T_\ell - T_d}{T_s - T_d}\ \Gamma_e & \text{if } T_d < T_\ell < T_s \\ \Gamma_e & \text{if } T_\ell \geq T_s \end{cases} \tag{4.4}$$

It is seen that this model correctly defaults to the saturated boiling model once the liquid becomes saturated. Although the assumption concerning the linear increase in Γ may not be strictly valid for all cases, it is appropriate for most cases of interest. Hence, this model is able to realistically describe the vapor generation rate.

However, this model is still not complete since vapor condensation has not been included. If the bulk liquid is subcooled, some of the vapor bubbles which detach from the wall may be condensed. Hence, the loss of vapor due to condensation must be accounted for.

The model used to represent the condensation is relatively simple, but appropriate. The condensation rate, Γ_c, is modeled as a conduction term divided by the heat of vaporization. This can be written as

$$\Gamma_c = A_i H_i (T_\ell - T_v)/i_{fg} \tag{4.5}$$

The term A_i represents the interfacial area and if one assumes spherical bubbles of radius R_b then A_i may be written as

$$A_i = 3\alpha/R_b \tag{4.6}$$

Hence, if the average bubble radius can be calculated then the interfacial area is obtained. The value for R_b is given by a modified form of the Ahmad correlation [43]:

$$R_b = \begin{cases} R_{bo} & \alpha < 0.1 \\ R_{bo}\left[\dfrac{9\alpha}{1-\alpha}\right]^{1/3} & \alpha \geq 0.1 \end{cases} \tag{4.7}$$

and

$$R_{bo} = 0.45 \sqrt{\frac{\sigma}{(\rho_\ell - \rho_v)}} \left[1+1.34((1-\alpha)V_\ell)^{1/3}\right]^{-1} \tag{4.8}$$

The interfacial heat transfer coefficient, H_i, also needs to be defined. Based on the effective conductivity of the two phases, H_i is given by

$$H_i = \begin{cases} \dfrac{k_\ell}{0.15R_{bo}} & T_v \leq T_\ell \\ \dfrac{k_v k_\ell}{0.01R_{bo}\, k_\ell + 0.015R_{bo}\, k_v} & T_v > T_\ell \end{cases} \tag{4.9}$$

With these definitions, the condensation model is complete. It is seen that if one assumes the vapor to be saturated, then the driving force for condensation is the amount of liquid subcooling. It should also be noted that for subcooled conditions ($T_\ell < T_v$), Γ_c is negative as expected.

Both the vaporization and condensation terms can be combined to obtain the net vaporization rate:

$$\Gamma = \begin{cases} 0 & \text{if } T_\ell \leq T_d \\ \dfrac{T_\ell - T_d}{T_s - T_d}\Gamma_e + A_i H_i (T_\ell - T_v)/i_{fg} & \text{if } T_d < T_\ell < T_s \\ \Gamma_e & \text{if } T_\ell \geq T_s \end{cases} \tag{4.10}$$

From the previous discussion it is seen that this model is mechanistically based on the physical phenomena involved. Nevertheless the model needs to be validated by comparisons with experimental measurements. The main characteristics of the model include the boiling incipient point and the vapor generation rate for subcooled conditions.

Both of these characteristics have been assessed using steady-state, one-dimensional void fraction measurements. The boiling incipient point, which corresponds to the bubble departure temperature, can be clearly identified in the measurements which makes the assessment of this characteristic rather straightforward.

The vapor generation rate in subcooled conditions can be directly related to the void fraction if the assumption of no slip is used. This assumption will be appropriate for void fractions at low quality and high pressure. For these cases the expression for the void fraction is

$$\alpha = \frac{1}{1 + \dfrac{1-X}{X}\dfrac{\rho_v}{\rho_\ell}} \tag{4.11}$$

The quality, in turn can be related to the vapor generation rate via the vapor mass equation (simplified for one-dimensional, steady-state conditions):

$$\frac{\partial X}{\partial z} = \frac{\Gamma}{G} \tag{4.12}$$

Hence, the vapor generation rate can be assessed with one-dimensional, steady-state void fraction measurements.

In the assessment effort, over 30 void fraction comparison cases have been made. The data of Maurer [33], Marchaterre [35], and Christensen [34], have been used in this study. These data cover a wide range of flow conditions as seen in Table 4.2.

For assessing the vaporization rate, only comparisons at low qualities have been used. Excellent agreement has been found in these comparisons for both the boiling incipient point and the subcooled void fraction. Typical comparison cases, covering a range of pressures, are illustrated in Fig. 4.5 - 4.8. The point where boiling begins is seen to be well-predicted in each case. This good agreement indicates the appropriateness of using Ahmad's correlation for the bubble departure temperature. The void fraction for subcooled conditions is also well predicted by THERMIT. This result strongly supports the use of the mechanistic subcooled vapor generation model. Other comparison cases also exhibit this good agreement, even though a wide range of conditions have been considered.

In view of the above comparisons and the inherent physical attributes of the subcooled vapor generation model, it can be stated that the model satisfactorily predicts subcooled boiling. Extending this model to

TABLE 4.2

Test Conditions for One-Dimensional

Steady-State Data

Test	Pressure Range (MPa)	Hydraulic Diameter (mm)	Mass Flux Range ($kg/m^2 \cdot s$)	Heat Flux Range (kW/m^2)	Inlet Subcooling Range (kJ/kg)
Maurer	8.3-11.0	4.1	540-1220	280-1900	150-350
Christensen	2.7-6.9	17.8	630-950	190-500	9-70
Marchaterre	1.8-4.2	11.3	600-1490	45-250	9-63

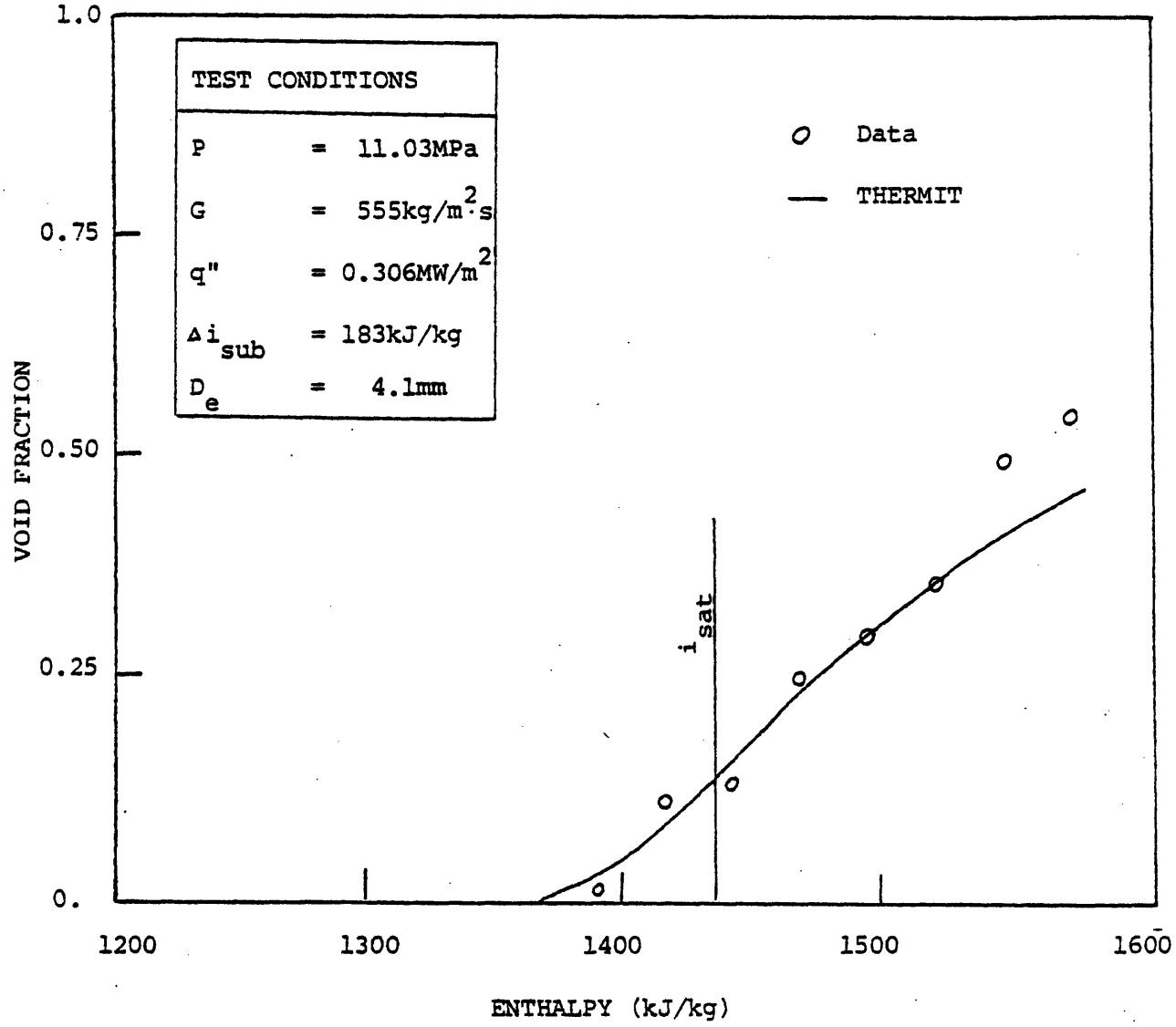

Figure 4.5: Void Fraction versus Enthalpy for Maurer Case 214-9-3

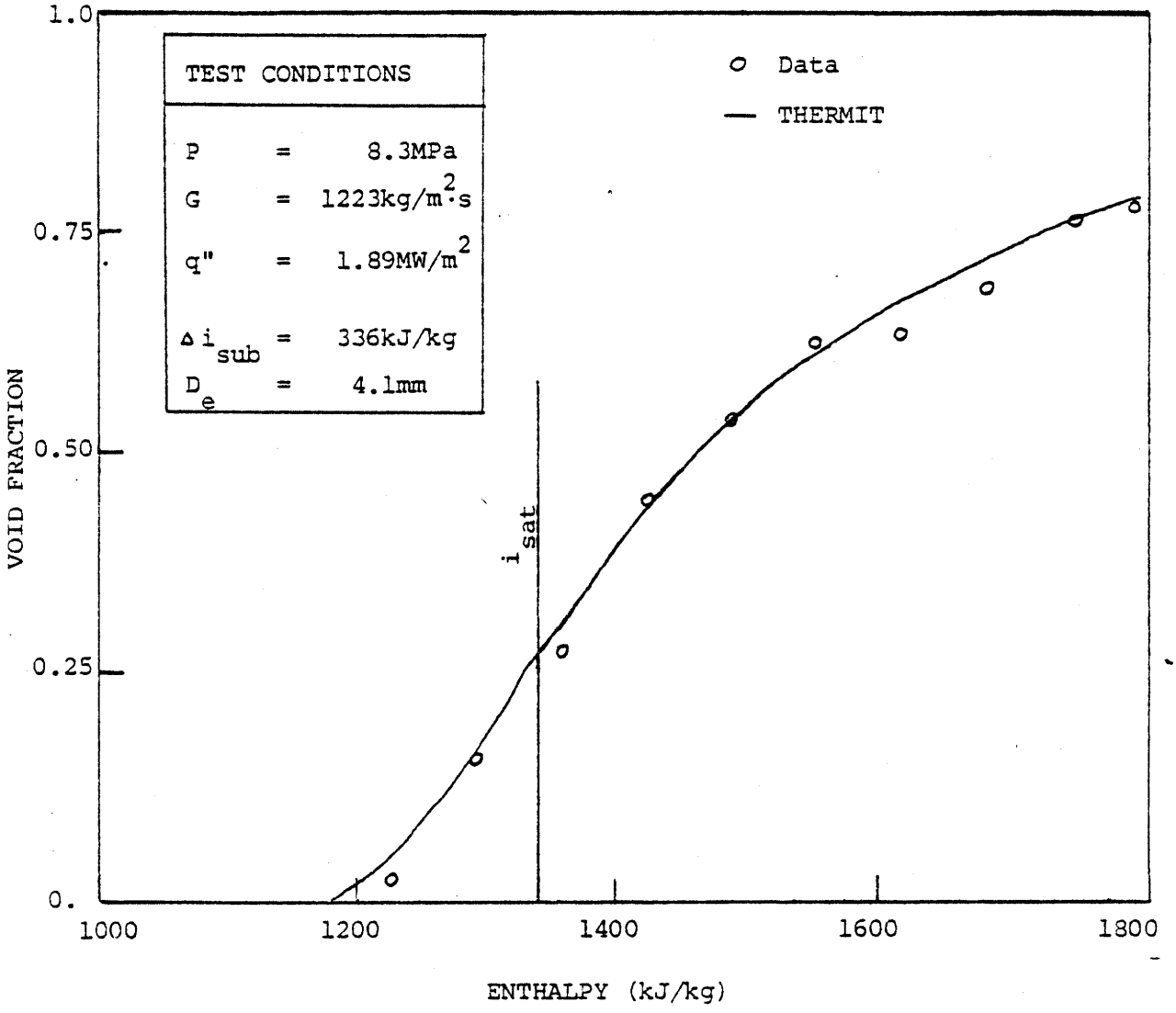

Figure 4.6: Void Fraction versus Enthalpy - Maurer Case 214-3-5

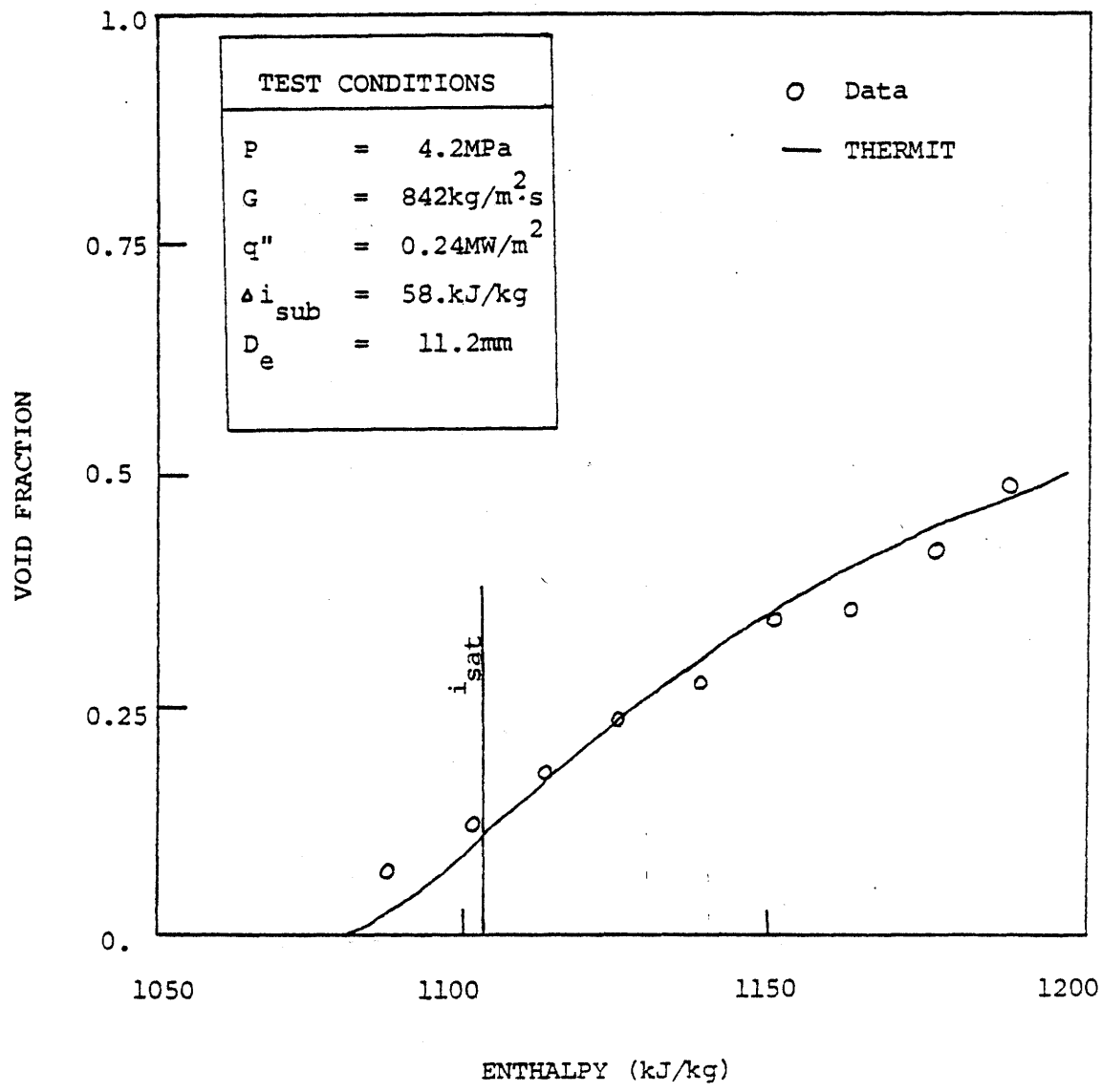

Figure 4.7: Void Fraction versus Enthalpy for Marchaterre Case 168

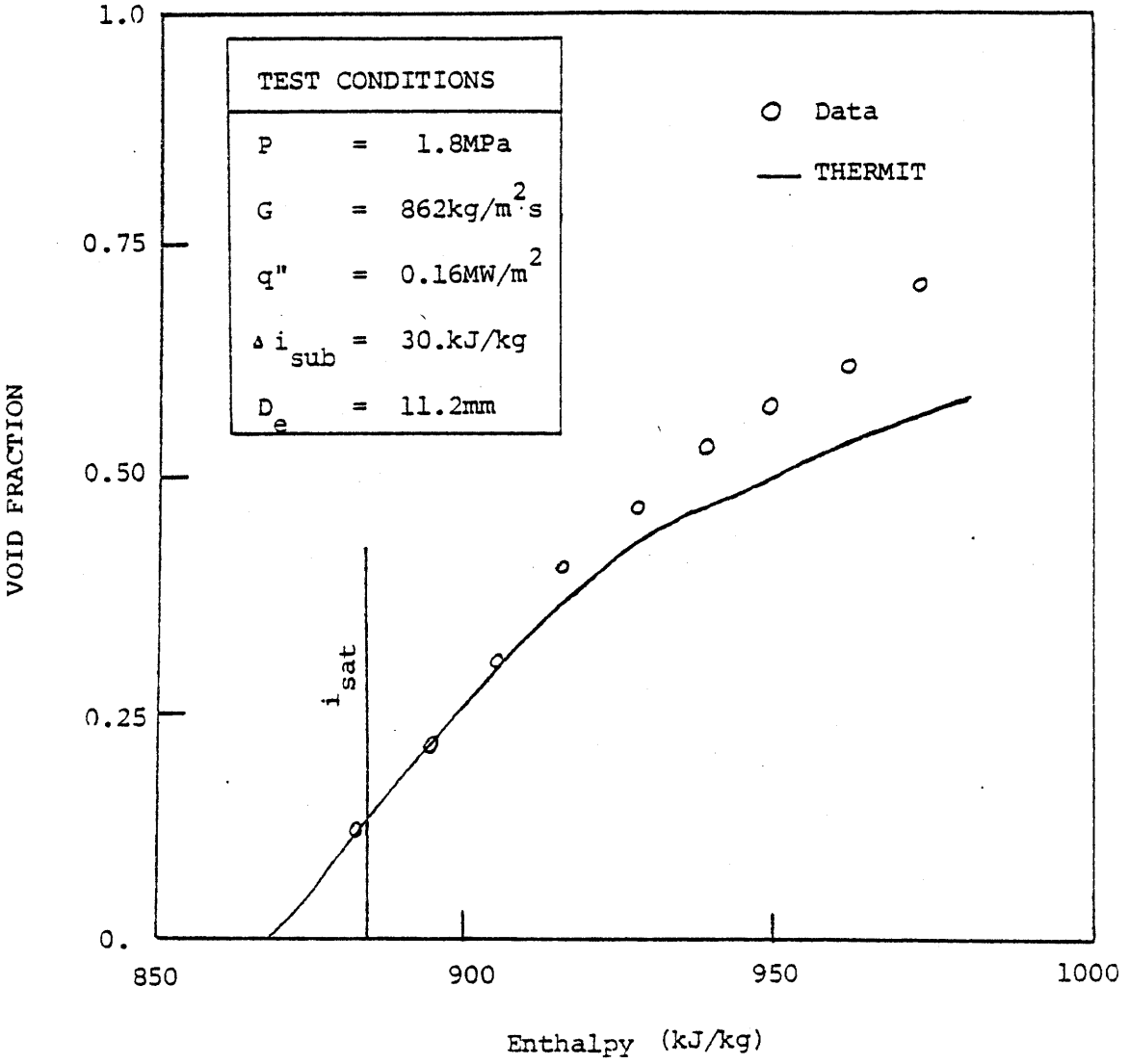

Figure 4.8: Void Fraction versus Enthalpy for Marchaterre Case 184

three-dimensional cases also seems to be appropriate due to its mechanistic nature. That is, the actual vaporization mechanism has been modeled on a local basis independent of surrounding control volumes. It should be noted that this model will approach the correct saturated boiling limit as the liquid becomes saturated. Therefore, the subcooled vapor generation model should be applicable for all pre-CHF conditions except for depressurization transients (in which flashing becomes the significant vaporization mechanism).

4.3.3 Droplet Vaporization Model

For post-CHF conditions, the predominant form of vapor generation is evaporation of entrained liquid droplets. The reason for this is that after CHF has been exceeded the wall temperature will rapidly increase and in a short period of time the minimum stable film boiling temperature, T_{msfb}, will be exceeded. Once this temperature has been attained, the liquid can no longer receive heat directly from the wall. Instead, the vapor is in contact with the wall and only by vapor-to-liquid heat transfer can the liquid be heated and evaporated. Hence, the rate of vapor generation is directly dependent on the rate of heat transfer from the vapor to the liquid. However, due to the low conductivity of the vapor, the vapor-to-liquid heat transfer is not very efficient. Consequently, the vapor becomes superheated by a significant amount (e.g., 150 °K [41]).

The key to predicting the correct vaporization rate is to carefully model the heat transfer between phases. Once this heat transfer rate is determined, the vaporization rate is found by simply dividing by the heat of vaporization:

$$\Gamma = A_i H_i \, (T_v - T_\ell) / i_{fg} \tag{4.13}$$

where A_i and H_i are the appropriate interfacial area and effective heat transfer coefficient. The interfacial area is dependent on the droplet diameter while the heat transfer coefficient will depend on the flow conditions, droplet diameter and vapor conductivity. The temperature difference $T_v - T_\ell$ may be written as $T_v - T_s$ if it is assumed that the liquid is saturated. Hence the vapor must be superheated in order for vaporization to occur. However, if Γ is zero the vapor will superheat since it receives heat from the wall without losing any of it to the liquid. Consequently, there is a direct coupling between the amount of vapor superheat and the vaporization rate.

The difficulty in determining Γ is in defining relations for A_i and H_i. As discussed by Saha [42] each of these parameters may be written as a function of the flow variables, but ultimately a correlation is required to complete the function. The interfacial area per unit volume may be written as

$$A_i = \frac{6(1-\alpha)}{\delta} \tag{4.14}$$

where δ is the droplet diameter. This diameter is strongly dependent on the flow conditions and is, therefore, usually empirically correlated. The interfacial heat transfer coefficient is correlated as a Nusselt number based on the droplet diameter:

$$H_i = \frac{k_v}{\delta}\left[2 + 0.459\left(\frac{\rho_v(V_v - V_\ell)\delta}{\mu_v}\right)^{0.55} Pr_v^{0.33}\right] \tag{4.15}$$

Again δ needs to be determined from correlation. Hence, both A_i and H_i must be correlated as functions of the flow conditions.

In view of this difficulty, Saha has combined the two parameters, A_i and H_i, into a single parameter K_1 which is then correlated as a function of the flow conditions. This approach eliminates the need to use two correlations which may be difficult to determine separately. A wide range of conditions have been used in developing this correlation as illustrated in Table 4.3. The final form of this vaporization rate correlation is given by

$$\Gamma = 6300\left[1 - \frac{P}{P_{cr}}\right]^2\left[\frac{\rho_v V_v^2 D}{\sigma}\right]^{1/2}\frac{k_v(T_v - T_s)}{D^2 i_{fg}} \tag{4.16}$$

The droplet diameter has been assumed to be proportional to the hydraulic diameter, D. The interfacial area per unit volume is seen to be inversely proportional to D with the heat transfer coefficient being proportional to k_v/D. As the vapor velocity increases, the droplets become smaller, increasing the interfacial area and increasing Γ. Hence, this model apparently contains sufficient physical characteristics to predict the vaporization of liquid droplets.

Obviously, the important quantity which this model is intended to predict is the rate of vapor generation for post-CHF conditions (or whenever vaporization of liquid droplets is significant). Unfortunately, this rate cannot be directly measured. Consequently, the assessment of the Saha model has required indirect methods. This assessment relied on

TABLE 4.3

Test Conditions used to Develop Saha Correlation For Post-CHF Γ

Pressure	1.5 MPa and 6.9 MPa
Diameter	14.9 mm and 12.6 mm
Mass Velocity	393-2600 kg/m^2s
Heat Flux	0.045 to 0.127 MW/m^2
Equilibrium Quality	0.18 to 1.50

the tight coupling between the amount of vapor superheat and the vaporization rate. For post-CHF conditions, the entire wall heat flux is received by the vapor. Part of this raises the vapor temperature with the remainder evaporating the liquid. Where the wall heat flux is known, an indirect assessment of the vaporization rate can be made if the fraction of the heat flux which raises the vapor temperature can be determined.

Hence, the assessment is done indirectly [39] in Chapter 6, where the Saha Γ model, the interfacial energy exchange model, and the interfacial momentum exchange model, as well as the solid-fluid heat transfer model, are assessed together as a group.

4.4 Interfacial Energy Exchange

A second interfacial phenomenon which must be modeled is the interfacial energy exchange rate. This energy transfer is directly related to phasic temperatures and, hence, controls the thermal non-equilibrium. Since the ability to predict thermal non-equilibrium is a key feature of THERMIT, appropriate modeling of the interfacial energy exchange is essential.

The interfacial energy exchange rate represents the rate of energy transfer from one phase to the other. This transfer can be due to either conduction, which is a function of the temperature distribution, or mass transfer. The physical picture for this transfer can be explained with the aid of Fig. 4.9. If the interface is assumed to be of a discrete, but infinitesimal, size and at saturated conditions, then the energy transfer can be modeled. For example, in Fig. 4.9a, which illustrates the thermal field for subcooled boiling conditions, the liquid adjacent to the vapor bubble interface is superheated while the vapor is saturated (or slightly subcooled). Defining the energy transfer as positive when

the vapor receives the energy, the energy transfer rate may be written as:

$$Q_i = H_{i\ell} (T_\ell - T_s) + \Gamma i_f = H_{iv} (T_s - T_v) + \Gamma i_g \qquad (4.17)$$

where $H_{i\ell}$ is the liquid-to-interface heat transfer coefficient and H_{iv} is the vapor-to-interface heat transfer coefficient. This equation shows that the rate of energy transfer from the liquid to the interface is the same as the energy transport rate from the interface into the vapor. In view of the equivalence of energy transfer rates, one may use either form.

A second example of the interfacial energy exchange is illustrated in Fig. 4.9b. In this case, which represents the liquid droplet vaporization regime (i.e., post-CHF), the vapor is superheated while the liquid is saturated. Even with this very different temperature profile, Eq. 4.17 still describes the interfacial energy exchange. Hence, Eq. 4.17 describes the general form of the interfacial energy exchange.

Notwithstanding the generality of Eq. 4.18, a practical problem remains in choosing the appropriate form of the interfacial energy exchange (i.e., either liquid-to-interface or interface-to-vapor). The choice of either form is dictated by the assumed temperature distribution for a given set of flow conditions. In THERMIT, the flow conditions have been classified as either pre-CHF or post-CHF, corresponding to the mass exchange rate models. Again the pre-CHF regime includes both subcooled and saturated boiling, while in the post-CHF regime only vaporization of entrained liquid is considered. The choice of either form is dictated by the assumed temperature distribution

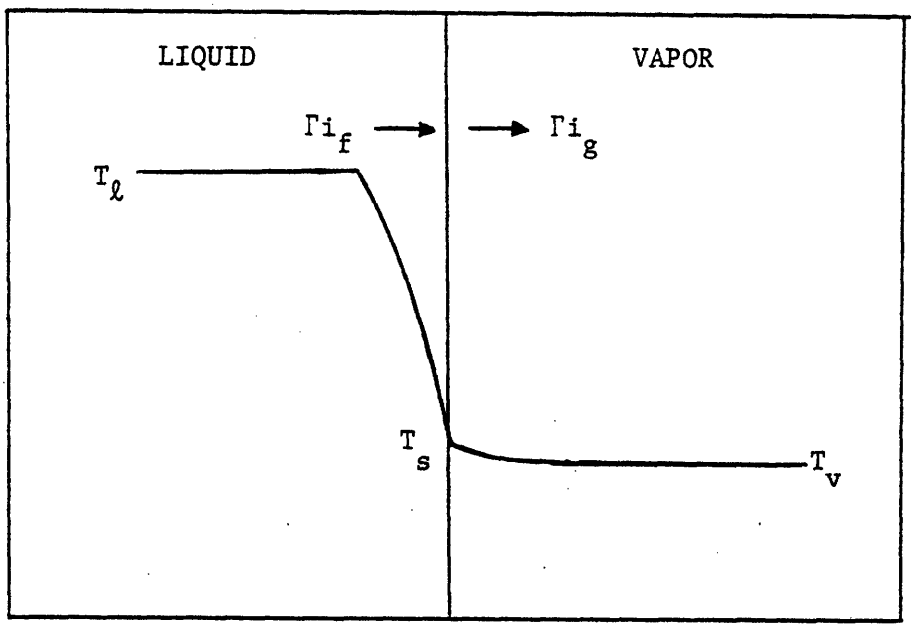

Fig. 4.9a: Temperature Distribution Near Vapor Bubble for Nucleate Boiling.

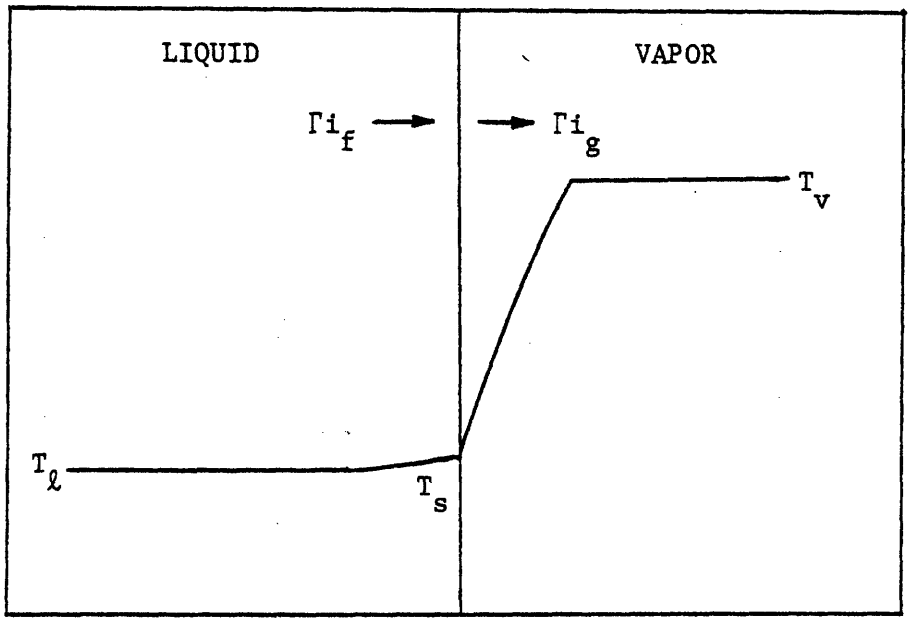

Fig. 4.9b: Temperature Distribution Near Liquid Droplet for Droplet Vaporization.

for a given set of flow conditions. In THERMIT, the flow conditions have been classified as either pre-CHF or post-CHF, corresponding to the mass exchange rate models. Again the pre-CHF regime includes both subcooled and saturated boiling, while in the post-CHF regime only vaporization of entrained liquid is considered. The choice of interfacial energy exchange model will be determined by the assumed temperature distributions for these types of boiling conditions.

In subcooled and saturated boiling conditions, a slightly superheated liquid exists at the interface and transfers energy to the vapor. However, the bulk liquid temperature is subcooled so that it would be difficult to use the liquid-to-interface energy transfer mechanism to represent the interfacial energy exchange without doing a detailed analysis of the temperature distribution in the liquid. Hence, the liquid-to-interface energy transfer will not be considered here.

On the other hand, the interface-to-vapor energy transfer can be appropriately modeled by considering the vapor to be at saturated conditions for both of these types of boiling conditions. In order to maintain the vapor at saturated conditions when the bulk liquid is subcooled, a relatively high rate of heat transfer across the interface must be assumed. This high rate can be interpreted as a large value for the vapor-to-interface heat transfer coefficient H_{iv}. Hence, if H_{iv} is chosen sufficiently large, the vapor will be maintained at saturation.

Consequently, for subcooled and saturated boiling conditions the interfacial energy exchange is modeled as an interface-to-vapor energy transfer mechanism. This exchange rate can be written as

$$Q_i = H_{iv}(T_s - T_v) + \Gamma\, i_g \tag{4.18}$$

where H_{iv} is set to a very large value (10^{11} W/m^3) in order to force the vapor to be saturated. It should be noted that since the bulk liquid temperature is not used in this equation, the liquid is unconstrained and may, therefore, be subcooled. Hence, the use of Eq. 4.18 for the interfacial energy exchange rate permits appropriate modeling of both the bulk liquid and vapor temperatures in subcooled and saturated boiling.

For post-CHF conditions, where droplet vaporization is the form of mass exchange, the superheated vapor is assumed to transfer heat by conduction to the interface while receiving energy due to the vaporization of the liquid. In this case, modeling of the vapor-to-interface energy transfer is difficult unless the detailed vapor temperature distribution is known. However, the liquid-to-interface energy exchange can be adequately modeled since the liquid is assumed to be at or near saturation. Therefore, by simply choosing a value for $H_{i\ell}$ which is sufficiently large, the liquid will be forced to saturated conditions.

Consequently, for the droplet vaporization regime, the interfacial energy exchange is modeled as a liquid-to-interface energy transfer mechanism. This exchange rate may be written as

$$Q_i = \Gamma\, i_f - H_{i\ell}\,(T_s - T_\ell) \tag{4.19}$$

where $H_{i\ell}$ is set to a large value (10^{11} W/m^3) in order to force the liquid to saturation. The bulk vapor temperature is not constrained by this

equation which allows the vapor to superheat. Hence, this model allows for the appropriate liquid and vapor temperatures to be predicted for the droplet vaporization regime.

In spite of the mechanistic nature of these two interfacial energy exchange models, assessment of these models is still required. However, validation of either model is not possible since the interfacial energy exchange cannot be directly related to a measureable quantity. Therefore, these models can only be assessed qualitatively by inference which means, when used, the models should produce the expected results. For example, in subcooled conditions the bulk liquid temperature should be subcooled while the vapor should be saturated. Alternatively, for droplet vaporization, the vapor should be superheated with the liquid saturated. If these results are predicted, then the interfacial energy exchange rate is at least qualitatively correct.

These models have been used in all of the mass exchange rate validation studies and have yielded the expected results in all cases. A typical temperature profile is illustrated in Fig. 4.10 for one of the void fraction comparison cases. It is seen that the vapor temperature follows the saturation temperature which is decreasing due to the pressure drop. The liquid temperature is initially subcooled, but eventually reaches saturation near the end of the test section. Hence, for subcooled and saturated boiling conditions the interfacial energy exchange rate given by Eq. 4.18 seems to be an appropriate choice.

For post-CHF conditions similar results are obtained. The temperature distributions for one of the Bennett cases is illustrated in Fig. 4.11. At the inlet, the liquid is subcooled but quickly becomes saturated and

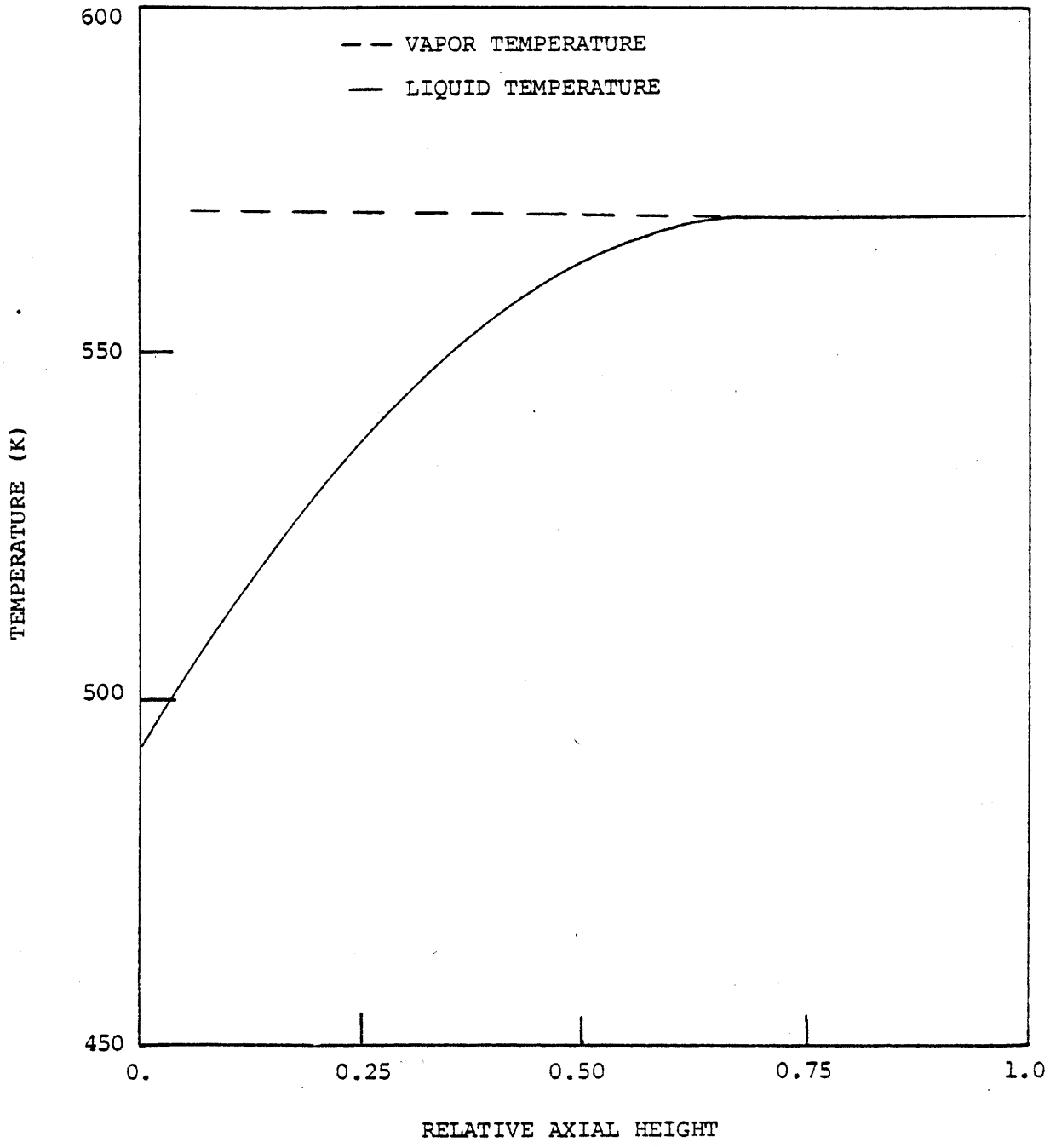

Figure 4.10: Predicted Liquid and Vapor Temperatures for Maurer Case 214-3-5

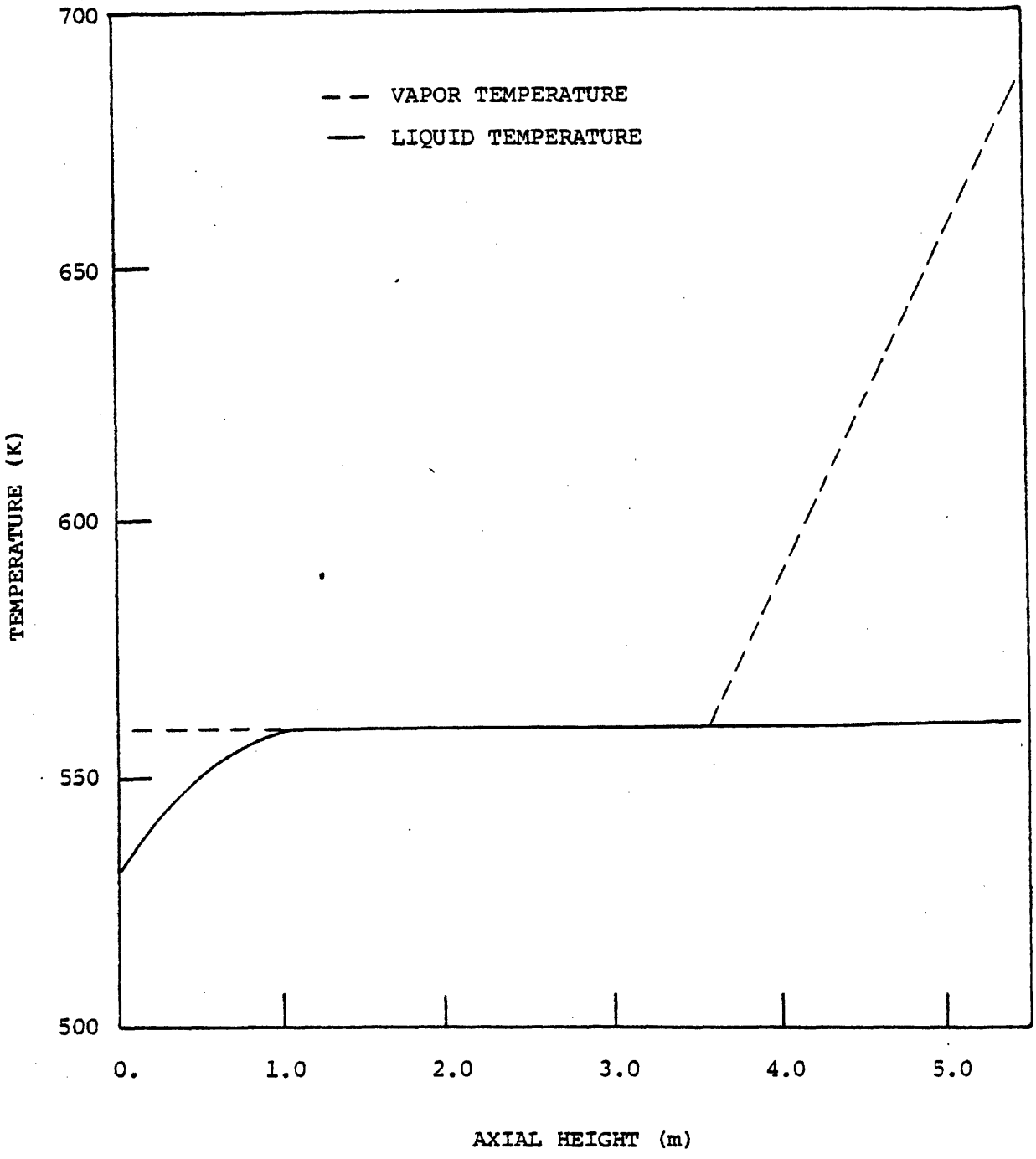

Figure 4.11: Predicted Liquid and Vapor Temperatures for Bennett Case 5336

remains so along the entire heated length. The vapor remains at saturation before CHF, but quickly superheats after CHF has been attained. These predictions are the expected result so that the interfacial energy exchange model given by Eq. 4.19 seems to be an appropriate choice for post-CHF conditions.

The above assessment has been based on the expected value for the liquid and vapor temperatures. As such, only the conduction term in the energy exchange model could be assessed. The mass exchange term (either Γi_g or Γi_ℓ) is also important, but not for steady-state conditions. That is, in steady-state the same temperature distribution is obtained whether or not the mass exchange term is included. However, for transient conditions it is essential that the mass exchange term be included. The reason for this can be understood by considering a case in which CHF occurs and the liquid is still subcooled (e.g., DNB type CHF). If the mass exchange is not included, then Q_i before CHF is

$$Q_i = H_{iv} (T_s - T_v) \tag{4.20}$$

and after CHF

$$Q_i = H_{i\ell} (T_\ell - T_s) \tag{4.21}$$

The pre-CHF expression is large and positive, i.e., $T_s > T_v$, while the post-CHF expression is large and negative. This sudden change in the value for Q_i represents a severe discontinuity and prevents convergence of the code.

If the mass exchange term is included, then Q_i will still change value but the discontinuity is not as severe. In this case, the code can converge despite the discontinuity. Hence, proper modeling of the interfacial energy exchange rate is essential for both steady-state and transient conditions.

4.5 Interfacial Momentum Exchange

The third type of interfacial exchange phenomena which must be modeled in THERMIT is the interfacial momentum exchange. This exchange represents the transfer of momentum from one phase to the other and controls the relative velocity of the two phases.

As in the case of the other interfacial exchange phenomena, the interfacial momentum exchange is strongly dependent on the flow conditions, since the structure of the two-phase flow changes with the flow conditions. As illustrated in Fig. 4.12, if the vapor concentration is low, then a bubbly flow is expected in which vapor bubbles move through a continuous liquid medium. As the vapor concentration increases the bubbles agglomorate in the center of the flow channel. At higher concentrations, an annular flow is found in which liquid coats the wall with the vapor forming a continuous central core. Of course, the possibility of liquid droplets in a continuous vapor phase also exists after CHF. In each case, as the flow pattern changes, the interfacial area changes. Since the momentum exchange is directly proportional to the interfacial area, the flow conditions are seen to have a strong influence on the interfacial momentum exchange.

In attempting to model the interfacial momentum exchange, it is necessary to consider the various forces which can act between the two

Figure 4.12: Typical Flow Patterns in Two-Phase Flow

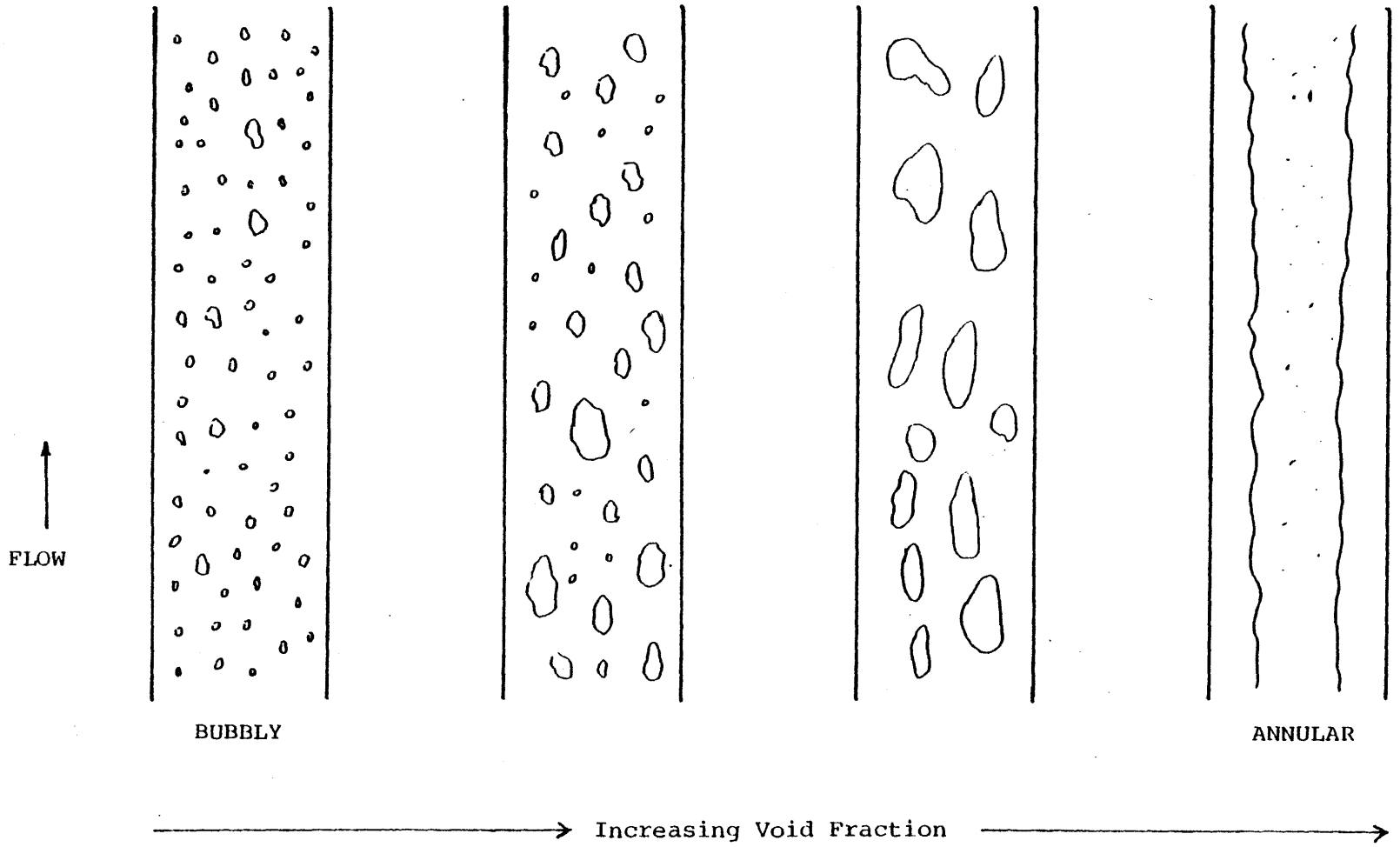

phases. At least five different forces can be postulated to exist. These may be divided into steady flow and transient flow forces. The steady flow forces include viscous, inertial and buoyancy forces while the transient flow forces include the Basset and virtual mass force [31]. Each of these forces will be significant for certain conditions and, hence, it is important to understand the characteristics of each force.

The viscous force, which arises due to the viscous shear stress and is only significant at low relative velocities, is approximately described by Stokes law. This law, originally derived for the force on a sphere moving in a viscous fluid, has since been modified to account for the motion of droplets of one fluid in a continuous second fluid. The flow of vapor bubbles in a liquid and the flow of liquid drops in a vapor are examples of such motion. The force on a single solid sphere given by Stokes law can be written as

$$F_\mu = 3\pi\mu_c D_s V_r \tag{4.22}$$

where D_s is the sphere diameter, μ_c is the viscosity of the continous phase and V_r is the relative velocity. As discussed by Soo [45], modifications of this equation are required for systems in which the droplet (or sphere) is deformable (such as vapor bubbles in liquid). An example of such a modification is given by Levich [46]:

$$F_\mu = 6\pi\mu_c D_d V_r \tag{4.23}$$

where the subscript c refers to the continuous phase and the subscript d refers to the dispersed phase. This expression is similar to other

expressions [45] and is valid for many practical droplet or bubble flow situations.

The force given by Eq. 4.23 represents the force on a single droplet. In order to convert this to a force per unit volume, Eq. 4.23 must be divided by the volume of a droplet and multiplied by the void fraction. Performing this operation yields

$$F_{\mu} = \frac{36\mu_c \alpha V_r}{D_d^2} \qquad 4 \ (4.24)$$

This expression represents the interfacial force due to viscous effects within a given control volume.

The second type of force is that due to inertial effects. This force also referred to as the drag force, represents the momentum loss due to the motion of two continuous fluid streams relative to one another. Hence, this force tends to dominate in annular flow regimes. Following Wallis [31], the shear stress between the phases may be written as

$$\tau_i = \tfrac{1}{2} C_d \rho_v V_r^2 \qquad (4.25)$$

Since the diameter of the vapor core is given by

$$D_c = D\sqrt{\alpha} \qquad (4.26)$$

the interfacial force per unit volume is

$$F_i = \frac{2C_d \rho_v v_r^2 \sqrt{\alpha}}{D} \tag{4.27}$$

where C_d is the interfacial drag coefficient. Values for C_d, appropriate for annular flow, have been formulated with Wallis recommending the following value [31],

$$C_d = .005(1 + 75(1 - \alpha)) \tag{4.28}$$

Using this coefficient the interfacial drag force can be evaluated. As indicated above, this force will be significant for annular flow and when the relative velocity is greater than zero.

The third type of force is that due to buoyancy effects. This force arises due to the difference in densities of the two phases. In a gravitational field (e.g., vertical flow), this density differences causes a force between the two phases. This force may be written as:

$$F_g = \alpha(1 - \alpha)(\rho_\ell - \rho_v)g \tag{4.29}$$

The buoyancy force will only be significant for low velocity flows or when the other forces are small relative to this force.

The fourth force is that due to virtual mass effects. This force arises from the apparent increase in mass of an accelerated particle. When a particle is accelerated relative to the surrounding fluid a potential flow field possessing kinetic energy will be established. The particle effectively accelerates this surrounding fluid, termed virtual

mass. Since the virtual mass is accelerated, it represents an additional force on the particle. Hence, as a particle is accelerated its mass appears to increase which leads to an increase in the interfacial force.

The virtual mass interfacial force has been discussed by Wallis [31] and Cheng et al. [47] and may be written as [48].

$$F_{vm} = \frac{1}{2}\alpha_d \left[\frac{1+2\alpha_d}{1-\alpha_d}\right]\rho_c \frac{d(V_d - V_c)}{dt} \tag{4.30}$$

where the subscript d refers to the dispersed phase and c refers to the continuous phase. It is seen that this force depends on the rate of change of the relative velocity and tends to decrease the lag between the phase velocities. This force will only become significant when one phase is accelerated more rapidly than the other.

The final force, potentially important in rapidly accelerating flows, is the Basset force. This force arises from the fact that as a particle is accelerated, a viscous flow field is established around the particle. This flow field introduces boundary layer development which tends to increase the drag on the particle. Unfortunately, this force is difficult to calculate, since it depends on the previous flow history. For laminar flow Basset [49] has derived the following analytical expression:

$$F_{Basset} = \frac{9\alpha_d}{D_d}\sqrt{\frac{\rho_c \mu_c}{\pi}} \int_{t_o}^{t} \frac{\partial(V_c - V_d)}{\partial\xi} \frac{d\xi}{\sqrt{t-\xi}} \tag{4.31}$$

where again the subscript d refers to the dispersed phase while the subscript c refers to the continuous phase. This force represents an instantaneous flow resistance with the previous flow history contained in the time integral. Wallis [31] shows that if laminar flow and constant acceleration are assumed, then the ratio of the Basset force to the steady drag force is given by

$$F_{Basset}/F_{Drag} = D_d/\sqrt{\frac{\pi\mu_c t}{\rho_c}} \tag{4.32}$$

At very small times, this ratio will be large and, hence, the Basset force will be significant. Consequently, for rapidly accelerating flows and short times the Basset force represents a significant interfacial force.

As indicated by the above descriptions of the important interfacial forces, each force models a specific interaction and is significant only for certain conditions. These characteristics are summarized in Table 4.4. Although not explicitly indicated, all forces except the inertial force have been formulated based on dispersed or bubble flow conditions.

It is also worth noting that, in the THERMIT interfacial momentum exchange model, only the viscous and inertial forces, which will dominate the interfacial force term for steady flow or near-steady reactor conditions have been included. For rapidly accelerating flows which are anticipated in blowdown transients both the virtual mass and Basset forces may need to be included. However, since this type of transient is not the primary application of the current research, the exclusion of these transient forces is probably justified for cases of practical interest. The buoyancy force is expected to become significant when the relative

TABLE 4.4

Summary of Liquid-Vapor Interfacial Forces

Force	Equation No.	Applicable Range	Included in THERMIT
Viscous	4.25	Low relative velocity, Bubbly or Droplet Flow	Yes
Inertial	4.28	Annular Flow	Yes
Buoyancy	4.30	Low flow conditions, Bubbly Flow	NO
Virtual Mass	4.31	Rapidly accelerating flow	NO
Basset	4.32	Rapidly accelerating flow, Short times	NO

velocity is small. Such cases exist for low flow conditions or when the wall friction is very small which are not typical of reactor conditions. Hence, for typical reactor operating conditions this force may be neglected.

In view of the simplifications to the interfacial force, it is important to remember that arbitrary application of THERMIT to different conditions is not warranted unless the appropriate interfacial forces are included. However, the forces have been clearly identified and, therefore, extention of the interfacial momentum exchange rate can be easily accomplished.

Turning now to the actual interfacial momentum exchange model in THERMIT, it is important to reiterate that only the viscous and inertial forces have been included in this model. Furthermore, in order to avoid the use of a flow regime map, this model has been formulated to be continuous for all flow regimes. Flow regime maps based on the void fraction have been used in other two-fluid model codes (for example TRAC [12]). In these maps, the void fraction determines the flow regime which then defines the appropriate interfacial momentum exchange rate to be used. However, this type of formulation is probably not warranted for the present applications. Hence, a continuous interfacial momentum exchange model has been developed. In this model, the coefficients of both the viscous and inertial forces have been approximated by simple functions of the void fraction. This approximation produces the desired numerical result while yielding appropriate values for the coefficients.

Taking both forces together, the interfacial momentum exchange model in THERMIT is

$$F_i = \left(\frac{1-\alpha}{\alpha D}\right)^2 \mu_\ell V_r + \left(\frac{1-\alpha}{\alpha D}\right) \frac{\rho_v |V_r| V_r}{2} \tag{4.33}$$

where

$$\hat{\alpha} = \max(0.1,\alpha)$$

and

$$D = \text{hydraulic diameter}$$

$$V_r = V_v - V_\ell$$

The reason for the restriction on α is to prevent a singularity when $\alpha = 0$. From the previous discussion, it should be obvious that the first term in this expression represents the viscous force while the second term represents the inertial drag force. Comparing the viscous term with Eq. 4.24, one finds that the following approximation has been made:

$$\frac{36\alpha}{D_v^2} \simeq \left(\frac{1-\alpha}{\alpha D}\right)^2 \tag{4.34}$$

where D_v is the vapor bubble diameter appropriate for bubbly flow. Since this force is only significant in bubbly flow regime, the approximation here is only appropriate for low void fractions. This fact is illustrated in Table 4.5 where the two coefficients are compared for a range of void fractions assuming representative values for the diameters. Only for void

TABLE 4.5

Comparison of Viscous Force Coefficients

α	$\frac{36\alpha}{D_v^2}$	$\left[\frac{1. - \alpha}{\alpha D}\right]^2$
0.05	4.0×10^5	8.1×10^5
0.10	5.0×10^5	8.1×10^5
0.15	5.8×10^5	3.2×10^5
0.20	6.4×10^5	1.6×10^5
0.25	6.8×10^5	9.0×10^4
0.30	7.3×10^5	5.0×10^4

Assumptions

$D = 0.01$ m

$D_v = 2(\alpha / \frac{4\pi}{3} N)^{1/3}$

with $N = 10^7$ bubbles/m^3

fractions of approximately 0.15 and less is the approximated coefficient comparable with the Levich model coefficient. However, this range corresponds to the conditions for which the viscous force is important. Furthermore, since the Levich model is only typical of the viscous force, the THERMIT viscous force term seems to be appropriate for its intended use.

The inertial force term in the interfacial momentum exchange model can be compared with Eq. 4.27. In order to equate the two expressions, the following approximation must be made:

$$2C_d \sqrt{\alpha} \approx \frac{1 - \alpha}{2\alpha} \tag{4.35}$$

These two coefficients are compared in Table 4.6 over a range of void fractions. It is seen that at low void fractions the THERMIT model predicts a higher coefficient which is necessary to have continuity between the viscous and inertial regimes. However, at higher void fractions the two are approximately the same. Since annular flow would be expected for $\alpha > 0.6$, the approximated inertial drag coefficient in THERMIT seems to be appropriate.

Hence, the formulation of the interfacial momentum exchange model seems to be satisfactory in spite of the approximations which have been made. However, as in the case of the other models, validation and assessment of the interfacial momentum exchange rate is the key to successful use of THERMIT.

The assessment of the interfacial momentum exchange model has employed the same one-dimensional void fraction measurements used to

TABLE 4.6

Comparison of Inertial Force Coefficients

α	$0.01(1 + 75(1 - \alpha))\sqrt{\alpha}$	$\frac{1 - \alpha}{2\alpha}$
0.4	0.29	0.75
0.5	0.27	0.50
0.6	0.24	0.33
0.7	0.20	0.21
0.8	0.14	0.13
0.9	0.08	0.06

assess the interfacial mass transfer rate. While the verification of the mass exchange model was concerned with the low quality void fractions, assessment of the momentum exchange rate has relied on the high quality data. The reason for this is that only for thermal equilibrium conditions (i.e., non-subcooled conditions), can the void fraction measurements be used to independently assess the momentum exchange rate. This fact can be illustrated by considering the definition of the void fraction:

$$\alpha = \frac{X}{X + (1 - X)\dfrac{\rho_v V_v}{\rho_\ell V_\ell}} \tag{4.36}$$

For a given pressure, the void fraction is seen to depend on the flow quality and the slip ratio, S ($S = V_v/V_\ell$). The flow quality has been shown to depend on the vapor generation rate by Eq. 4.12, while the slip ratio depends on the interfacial force. If the flow quality is not known, then the slip and, hence, the interfacial force cannot be determined from the void fraction alone. Fortunately, for thermal equilibrium conditions the flow quality can be calculated since the vapor generation rate simply becomes

$$\Gamma = \dot{q}_w/i_{fg} \tag{4.37}$$

with the wall heat transfer term, $\dot{q}_w$, already known. Hence, the flow quality can be determined from an energy balance so that the momentum exchange rate can be assessed with void fraction measurements.

As indicated in Section 4.3.2., a large number of void fraction comparison cases have been made. For assessing the interfacial momentum

exchange rate, only the higher quality data have been used. Generally, the THERMIT, predictions agree rather well with the measured void fraction values over the range of flow conditions considered here. Typical comparison cases, covering a wide range of pressures, are illustrated in Figures 4.13 - 4.16. It is seen that in the higher quality regimes, the measured void fraction values are satisfactorily predicted in each case. Hence, considering the range of flow conditions which have been analyzed, the interfacial momentum exchange model can be expected to be appropriate for most cases of practical interest.

The only minor deviation between the measured and predicted values occurs for some of the lower pressure cases. In these cases, THERMIT tends to underpredict the void fraction. This indicates that the slip ratio is too high or, in other words, the interfacial momentum exchange rate is too low.

In order to assess these deviations an alternative interfacial momentum exchange model has been added [4]. This model, referred to as the LASL model [50] due to its usage in many of the LASL codes, is similar to the THERMIT model in that only viscous and inertial forces are considered, but the coefficients are different. This model is given as:

$$F_i = \frac{3}{8} a \left[\frac{12\bar{\mu}}{r} + \frac{\bar{\rho} \, |V_v - V_\ell|}{2} \right] (V_v - V_\ell) \qquad (4.38)$$

where

$$\bar{\rho} = \alpha \, \rho_v + (1 - \alpha) \, \rho_\ell$$

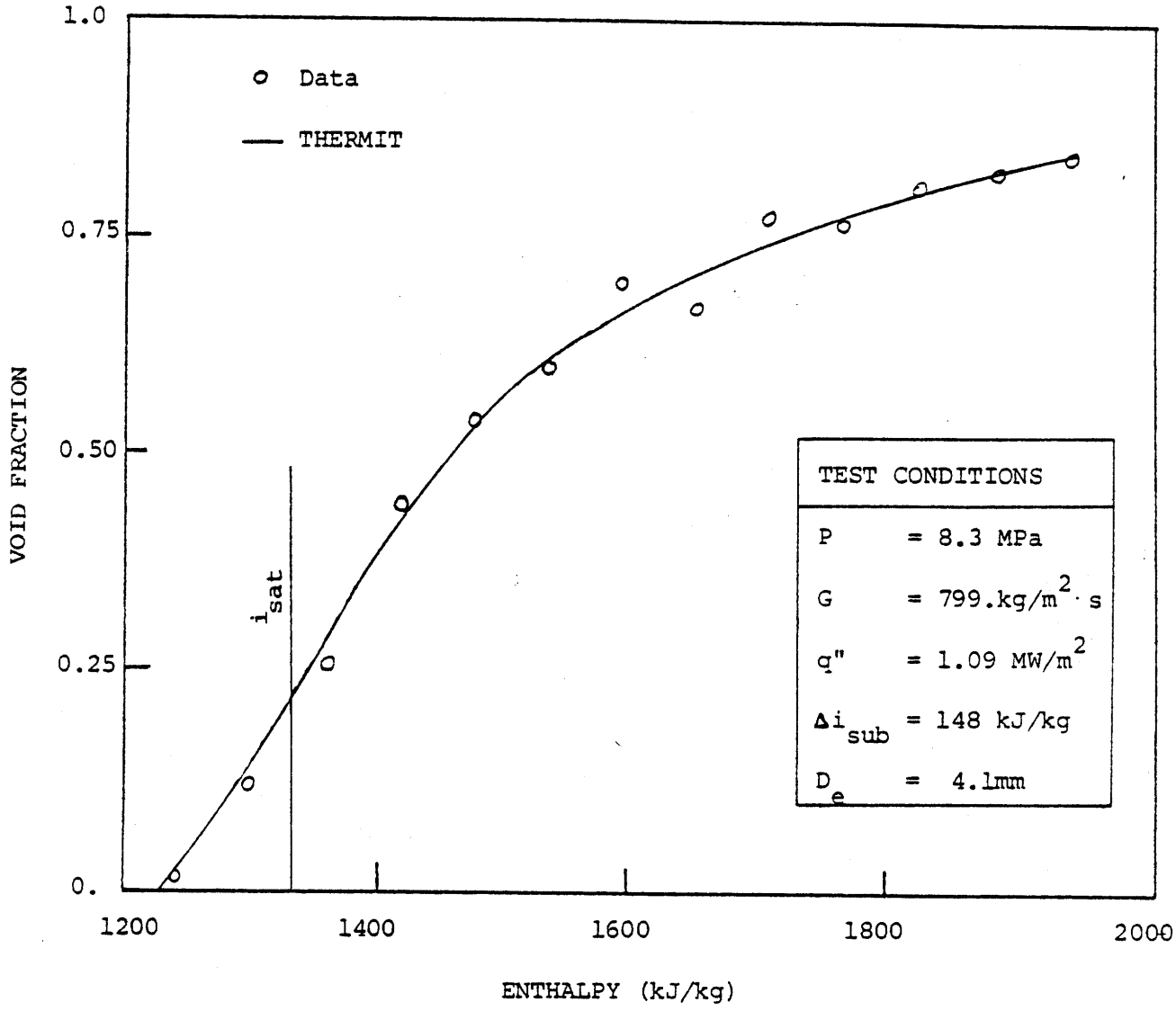

Figure 4.13: Void Fraction versus Enthalpy for Maurer Case 214-3-4

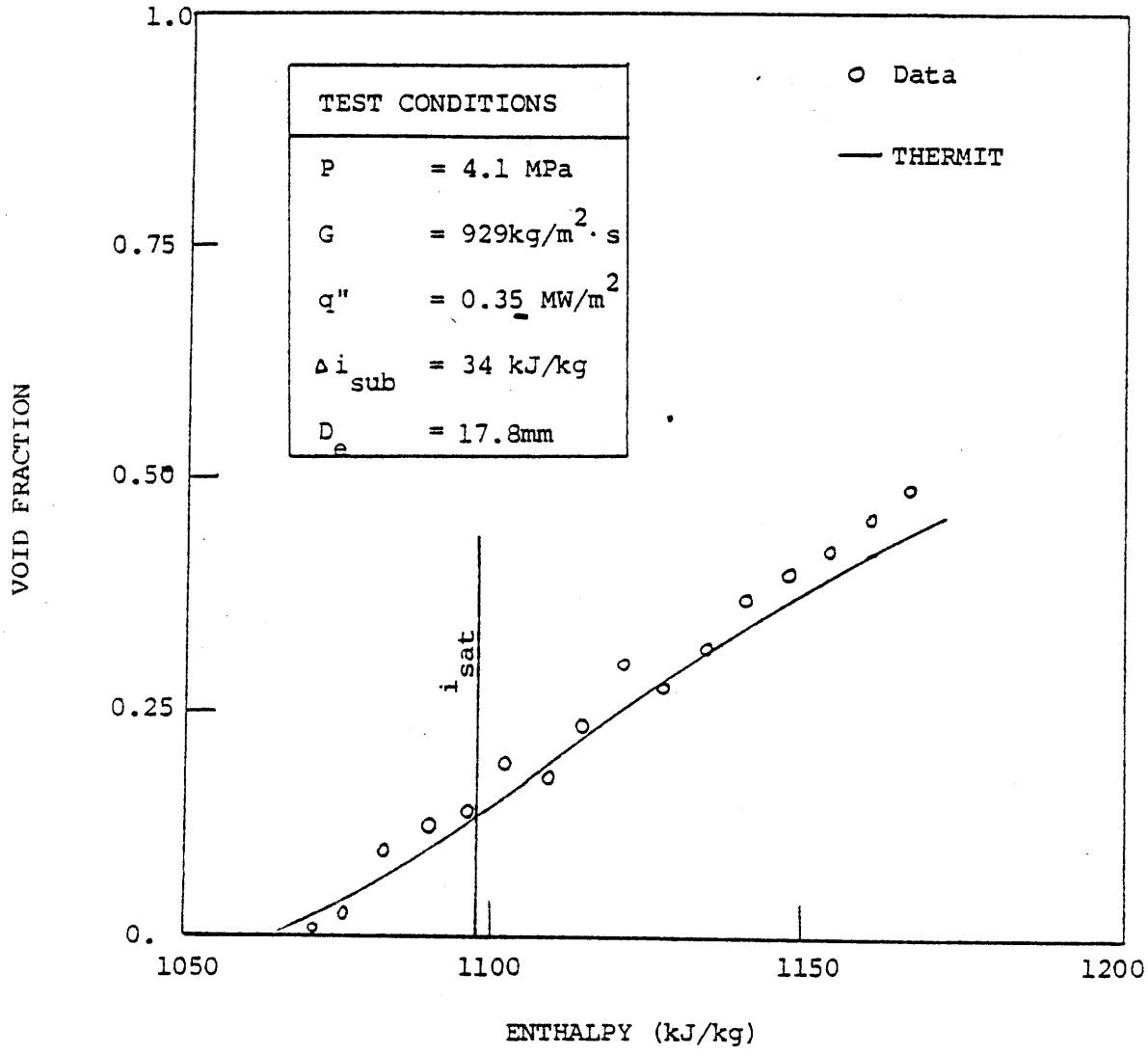

Figure 4.14: Void Fraction versus Enthalpy for Christensen Case 12

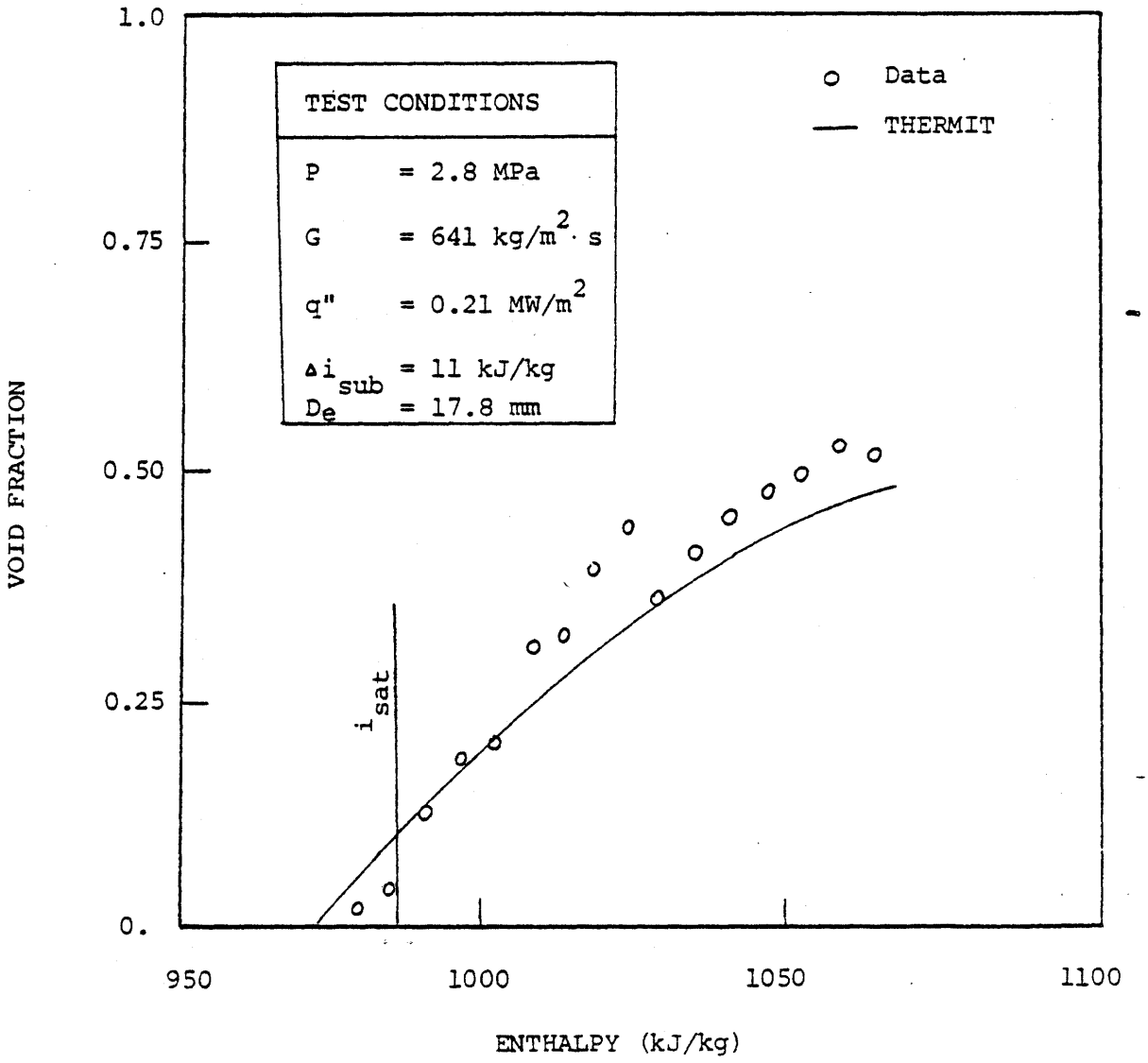

Figure 4.15: Void Fraction versus Enthalpy for Christensen Case 9

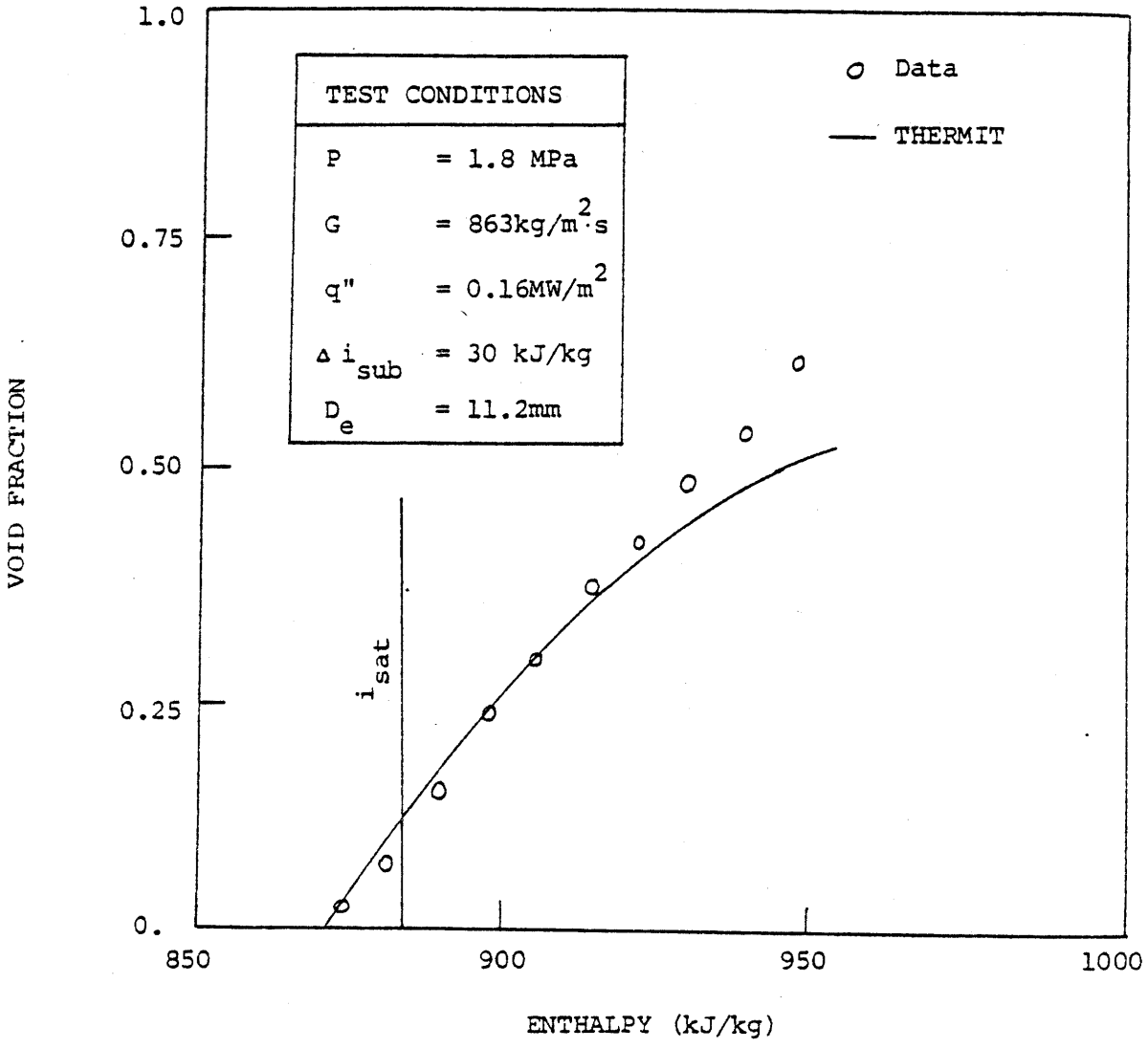

Figure 4.16: Void Fraction versus Enthalpy for Marchaterre Case 185

$$\bar{\mu} = (\alpha\, \mu_v/\rho_v + (1-\alpha)\mu_\ell/\rho_\ell)\bar{\rho}$$

$$a = a_n^{1/3}\, \tilde{\alpha}^{2/3}$$

$$r = (\tilde{\alpha}/a_n)^{1/3}$$

$$a_n = \frac{4\pi N}{3}$$

$$N \equiv 10^7/m^3$$

$$\tilde{\alpha} = \alpha \qquad \text{if } \alpha \leq 0.5$$

$$1 - \alpha \qquad \text{if } \alpha > 0.5$$

The most significant difference between these two models is the density used in the inertial force term. In THERMIT, the vapor density is used while in the LASL model the mixture density is used. The mixture density can be as much as 10 times greater than the vapor density, so that the LASL momentum exchange rate can be significantly larger.

The LASL model has been used in THERMIT and a number of the void fraction cases have been repeated. In all cases, the LASL model predicts higher void fractions than THERMIT and typically overpredicts the measured data. One such comparison case is illustrated in Fig. 4.17. The void fraction at low qualities is approximately the same for both models. However, at high qualities the LASL model predicts significantly higher void fractions.

The slip ratio predictions for this case using both of these models is illustrated in Figure 4.18. It is seen that with the LASL F_i model the slip ratio quickly attains a value of $\sim$1.24 and remains constant along the remainder of the tube. When the THERMIT F_i model is used, the slip ratio increases rapidly at first, but then levels off near the end of the channel.

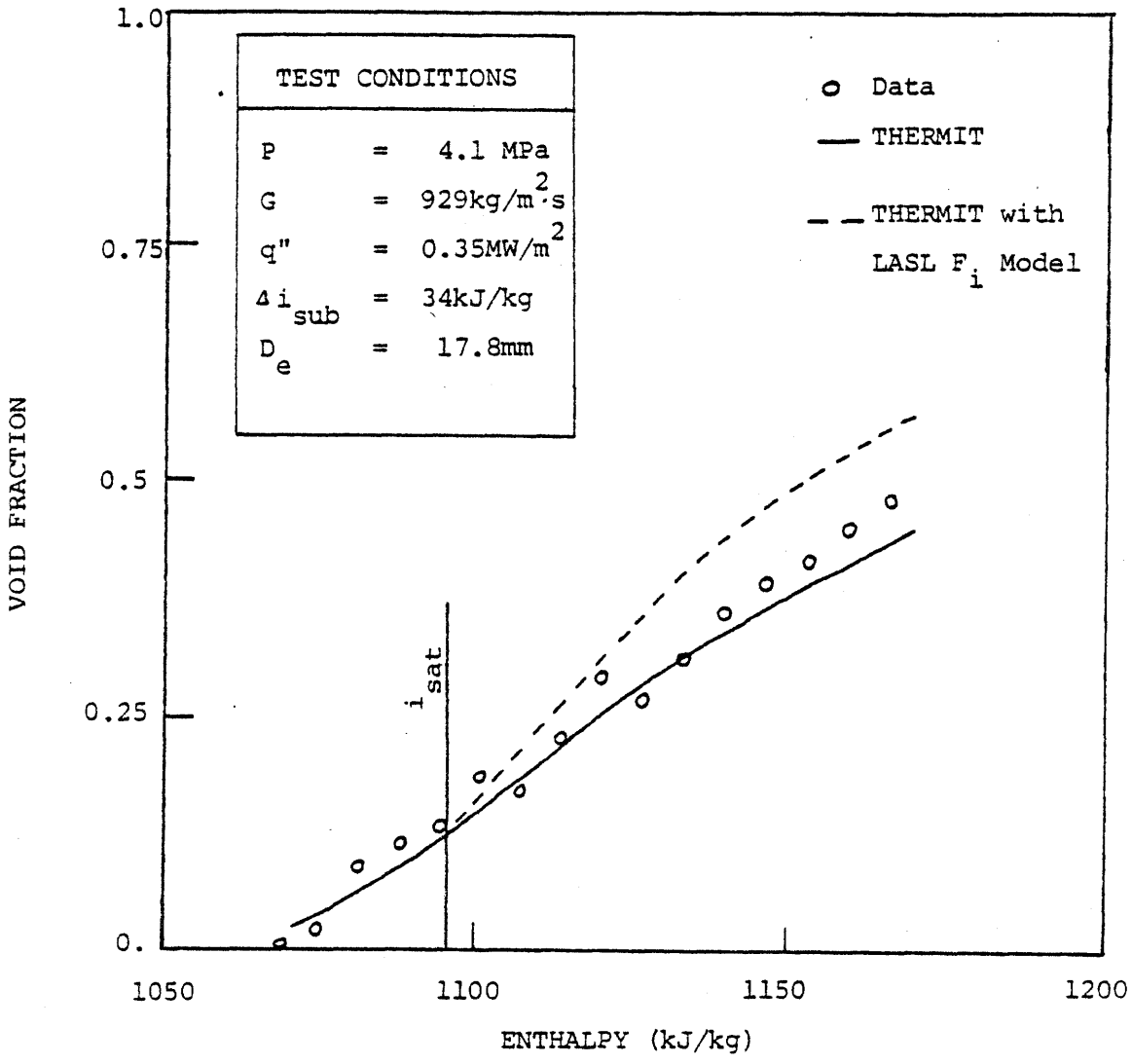

Figure 4.17: Void Fraction versus Enthalpy for Christensen Case 12

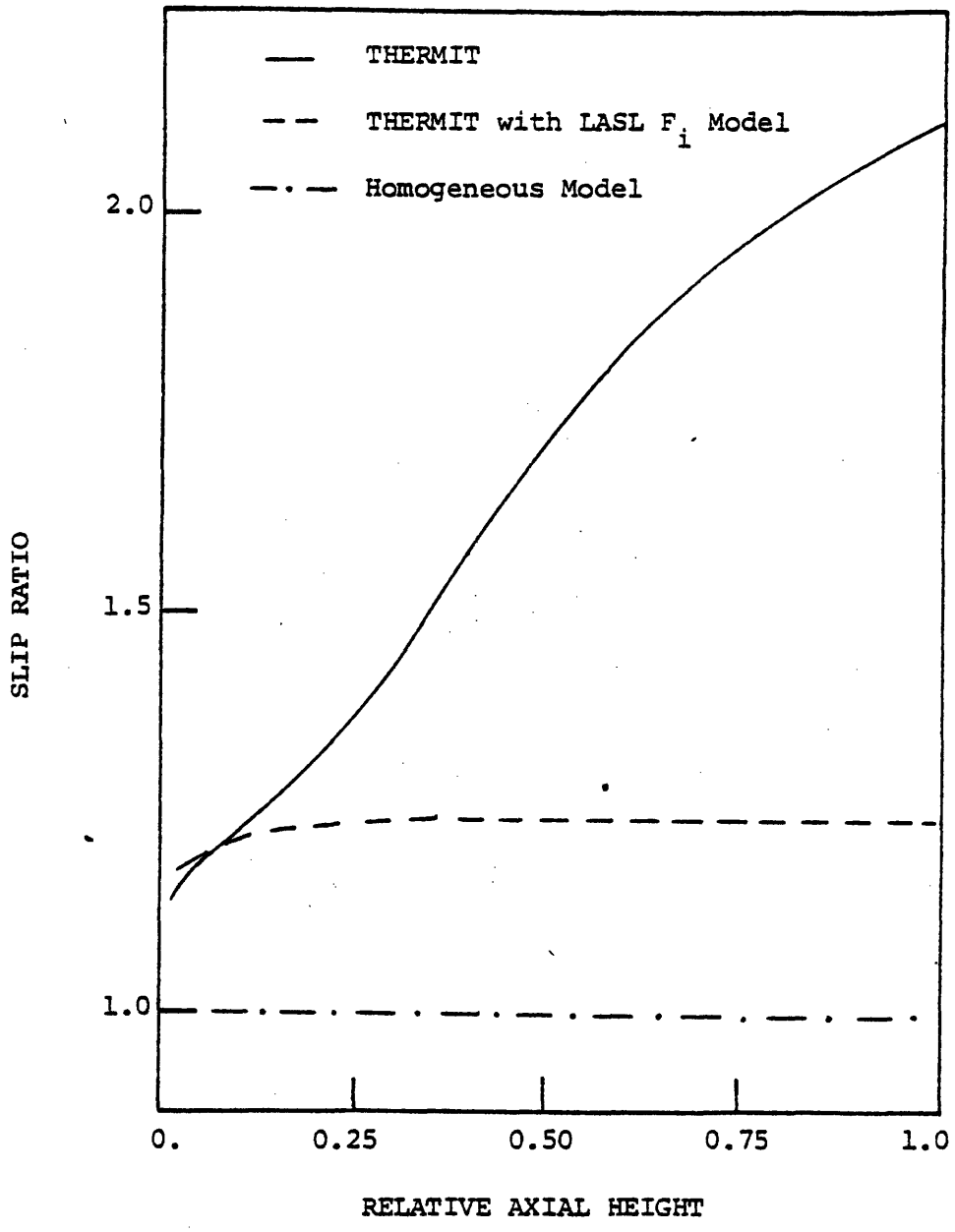

Figure 4.18: Comparison of Predicted Slip Ratios for Christensen Case 12

Of course, if a homogeneous model is used, a slip ratio of 1.0 is an imposed restriction. Since a lower slip ratio means a higher void fraction, the homogeneous model void fraction predictions will be the highest for a given quality. However, since the measurements lie between the predictions of the two models, the homogeneous model void fraction predictions will be too high. Hence, an advantage of the two-fluid model is the ability to predict the velocity profiles for each phase. These profiles are needed for accurate void fraction predictions.

In order to evaluate these two models in a more consistent manner, the measured and predicted values for Christensen's tests have been plotted on a superficial vapor velocity (J_v) versus α graph. As seen in Figure 4.19, the data tend to fall within a band between the two models. The THERMIT model forms the lower void fraction edge while the LASL model forms the upper edge. The large amount of scatter makes it difficult to definitively state which model is better. Clearly, the THERMIT model should have an increased momentum transfer rate at high J_v.

In conclusion, it can be asserted that the momentum exchange rate in THERMIT appears to be appropriate for most steady and near-steady flow reactor conditions. Rapid transients or very low flow cases may not be adequately analyzed, since the appropriate forces have been neglected. Also the use of the current model for analyzing droplet flow may not be strictly valid. Nevertheless for a large number of cases of practical interest, the current interfacial momentum exchange rate seems to be quite satisfactory.

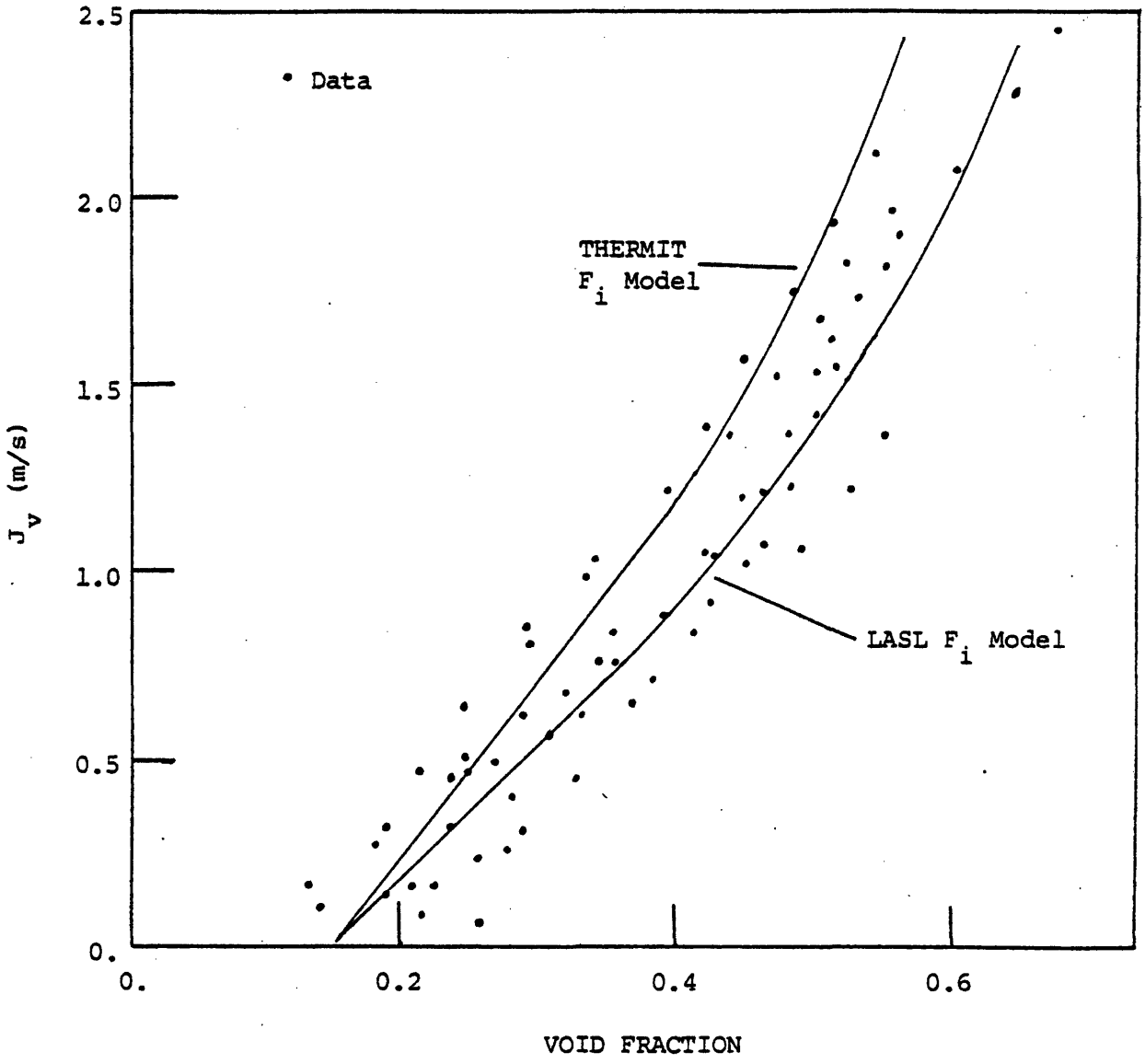

Figure 4.19: Vapor Superficial Velocity versus Void Fraction for Christensen Data

5.0 ASSESSMENT OF THE TWO-PHASE MIXING MODEL

5.1 Introduction

As discussed in Chapter 3, the original version of THERMIT has been modified so that the effects of turbulent mixing between cells are now accounted for. This modification consisted of adding a two-phase mixing model that has been formulated on physical bases using the recommendations of previous work [28, 29, 30]. Specific details of the model formulation have been presented in Section 3.3. An integral part of the model developmental effort has been the assessment of the model. This assessment has been made by comparing experimental measurements in rod-bundles for typical BWR and PWR conditions to the predictions of THERMIT. In this chapter, the results of these comparisons are presented and discussed.

As a prelude to the discussion of the results of the assessment, it is instructive to review the important phenomena being represented. The effects of turbulence, that is the transport of mass, energy and momentum due to turbulent eddy diffusion, are, on a LWR assembly scale, very localized. Even though the effect of the transport is on a scale of the order of subchannel sizes, turbulence can play a significant role for subchannel applications. To analytically describe the motion of the eddies would conceivably be the best way to model the effects of turbulence. However, this type of model is beyond the scope of the current work and a simpler, but practical engineering approach has been adapted. In this approach, the integral effect of the localized eddy transport mechanisms are embodied in the two-phase mixing model. In this context,

the integral effect means that all turbulence effects are lumped into a net mixing rate. Hence, a macroscopic modeling approach is used to represent the very complicated small-scale turbulent motion.

In the integral approach two important phenomena are represented. The first, termed turbulent mixing, results from the motion of turbulent eddies in the flow. As the turbulence level increases, so does mixing between adjacent channels, resulting in a more uniform flow. Turbulent mixing tends to eliminate flow and enthalpy gradients by promoting flow exchange between the channels. It should also be noted that turbulent mixing is important for both single-phase and two-phase flow. The second phenomenon, termed vapor diffusion, represents the observed tendency of the vapor to migrate to the unobstructed (i.e. more open) regions of the rod bundle. Since this transport mechanism occurs in the absence of pressure gradients, the vapor is said to "diffuse" to the unobstructed regions. This apparent diffusion of the vapor leads to the transport of energy and momentum in proportion to the rate of vapor transport.

Both turbulent mixing and vapor diffusion occur in the absence of pressure gradients and lead to mass, energy and momentum transport. In view of this, the analytical description of both phenomena can be included in a unified two-phase mixing model. As presented in Section 3.3, the generalized mixing terms can be written as

$$\psi = \varepsilon/\ell \left[(\rho\phi)_i - (\rho\phi)_j - ((\rho\phi)_i - (\rho\phi)_j)_{FD}\right] \tag{3.33}$$

where $\phi = 1$ in mass equations

$= e$ in energy equations

$\phi = V$ in momentum equations

$\rho = \alpha\rho_v$ in vapor equations

$= (1-\alpha)\rho_\ell$ in liquid equations

In the mass equations this term represents an additional mass exchange rate between adjacent channels. In the energy equations this term represents the apparent heat flux at channel boundaries. Finally, in the momenum equation this term is an apparent shear stress acting along the channel boundary.

The term ε/ℓ, which represents the turbulent velocity, has been assumed to be the same for both the liquid and vapor. This assumption means that the mixing rate for each phase is determined from the turbulence level of the total flow and not from the turbulence level of each phase. With this assumption, if the liquid and vapor equations are added together, then the liquid and vapor mixing terms combine to yield the mixture model formulation of Lahey [25]. This result represents the appropriate limiting value and it is important that the THERMIT two-phase mixing model reduce to this limit. It should also be noted that for single-phase conditions, the model reduces to the correct single-phase limit.

As discussed in Section 3.3, there are two parameters in this model which need to be specified to complete this model. The first is the parameter θ_M which is the value of the peak-to-single-phase mixing rate. This parameter must be specified in order to define the turbulent velocity, ε/ℓ. The second is the parameter K_M which is the proportionality constant between the fully-developed void fraction profile and the mass velocity

distribution. This parameter is important for determining the fully-developed distributions of the mass, energy and momentum. Appropriate values for these two parameters need to be specified to complete the formulation of the two-phase mixing model.

Faya [29], in an investigation of mixing parameters for a two-phase mixture model (i.e. not a two-fluid model), recommends the following values for these two parameters:

$$\theta_M = 5 \tag{5.1a}$$

$$K_M = 1.4 \tag{5.1b}$$

The selection of these values is based on numerical comparisons of the CANAL computer code [29] with experimental measurements. The magnitude of these parameters seems to be appropriate for BWR conditions [27, 32]. Since these two parameters have the same physical meaning in the THERMIT two-phase mixing model, the values given in Equation 5.1 are used for the reference case.

It should be noted that while the value of K_M may in fact be fairly constant, θ_M is expected to depend on the flow conditions. As the flow rate increases, the value for θ_M has been experimentally observed to decrease [27]. Hence, the assumption of using a constant value for θ_M may not be appropriate if the flow rate rapidly changes. However, as will be discussed in Section 5.2, the sensitivity of the predicted results to variations in θ_M is found to be small. Therefore, the assumption of constant θ_M, which simplifies the two-phase mixing model, does not appear to adversely affect the predicted results.

One of the difficulties in developing a two-phase mixing model is that the mixing terms cannot be directly compared to experimental measurements on a local basis. The problem is that these terms have not (and probably cannot) be measured. Rather, isokinetic measurements of the exit flow and enthalpy distributions in rod bundles have traditionally been used to infer the appropriateness of the above terms. These exit distributions reflect the integration of the mixing effects along the entire test section length. Appropriate modeling of the transport mechanisms due to mixing is required in order to calculate these exit distributions. Consequently, the two-phase mixing model can be assessed with measurements of this type.

The validation and assessment of the two-phase mixing model has been performed using rod-bundle measurements. In particular, three sets of experimental measurements have been examined in this study: the GE 9 rod bundle tests [36], the Ispra 16 rod BWR tests [37] and the Ispra 16 rod PWR tests [38]. In each of these tests, a large number of exit mass velocity and enthalpy distributions have been isokinetically measured. Test conditions for these tests are given in Table 5.1. The first two tests have been run at a pressure of approximately 6.9 MPa in geometries typical of a BWR, while the third test has been run at 16.0 MPa with the geometry being typical of a PWR. Hence, these tests cover the expected conditions for subchannel applications.

In the isokinetic measuring technique, flow samples are extracted from the various subchannels (defined on a coolant centered basis) at the test section exit. The sample flow rate is adjusted to match the pressure distribution that exists when the sampling device is not present. In this

TABLE 5.1

Test Conditions for Rod-Bundle Experiments

	G.E. 9-Rod	Ispra 16-Rod BWR	Ispra 16-Rod PWR
P (MPa)	6.9	7.0	16.0
G ($kg/m^2 \cdot s$)	650 to 2200	1000 to 2000	2500 to 3500
q" (MW/m^2)	0.71 to 2.1	0.12 to 0.77	0.07 to 0.11
Δi_{sub} (kJ/kg)	67 to 525	30 to 180	250 to 400
X_{out} %	3 to 22	2 to 31	-20 to 20
D_e (mm)	12.1	13.3	10.7
Length (m)	1.83	3.66	3.66
Spacer Type	Pin	Grid	Grid
Radial Power Distribution	Uniform and Non-Uniform	Uniform	Uniform

way, the sample flow rate should equal the actual flow rate for the subchannel. The enthalpy and flow rate of the sampled subchannel are then measured by calorimetry to complete the experimental procedure.

All characteristic subchannel types in the rod-bundle should theoretically be simultaneously sampled in order to insure that mass and energy are conserved. In practice, however, thorough sampling is not always done. In certain tests not all subchannel types are sampled. In other tests, all subchannel types are sampled, but not simultaneously. Consequently, significant mass and energy conservation errors are typically found in measurements of this type. These errors present a problem when comparing the measurements to the code predictions since the predictions always conserve mass. Consequently, perfect agreement between the code predictions and measurements cannot and should not be expected.

Nevertheless the assessment of the two-phase mixing model has been accomplished through comparisons of the measured and predicted exit mass velocity and quality (or enthalpy) distributions for selected cases from the above test sets. Since these comparisons have been made subsequent to the one-dimensional void fraction comparisons discussed in Chapter 4, it has been assumed that both the subcooled boiling model and the interfacial momentum exchange model are appropriate for these cases. If this assumption is made, then the bundle exit distributions can be used to assess the two-phase mixing model directly.

The general procedure for analyzing these cases can be described as follows. First the geometrical details of the test section, as provided by the experimental reports, are used to define coolant-centered subchannels in the test section. The reason for using a coolant-centered

approach is that the isokinetic measurement technique samples subchannels defined on this bais. Next, the measured inlet mass flow rate, assumed to be radially uniform at the test section inlet, and the measured inlet temperature are used to define the inlet boundary condition. The measured outlet pressure, also assumed to be radially uniform, is used as the exit boundary condition. Finally the measured power level is specified to determine the wall-to-coolant heat flux boundary condition. With these boundary conditons, the THERMIT calculations are performed until a steady-state solution is obtained. The steady-state results can then be compared with the experimental values and are discussed in this chapter.

5.2 GE 9 Rod Bundle Test

5.2.1 Test Description

The mass velocity and quality distributions at the outlet of a 9-rod electrically heated test section have been measured. Both the two-phase flow conditons and geometry of the test section are similar to those found in BWR rod bundles. The pressure for these cases is 6.9 MPa. The average exit quality ranges from 3% to 22% and mass velocities ranging from 650 to 2200 $kg/m^2 \cdot s$ have been used. These conditions are in the range of operating BWR conditions. The rod diameter and rod-to-rod pitch also closely resemble those in a BWR rod bundle. A detailed cross sectional view of the 9 rod bundle is illustrated in Figure 5.1.

While the measurements have been taken primarily for two-phase flow conditions, some measurements have been made for single-phase conditions. These single-phase cases (cases 1B to 1E in GE notation) have been run using isothermal conditions. For the two-phase cases both radially

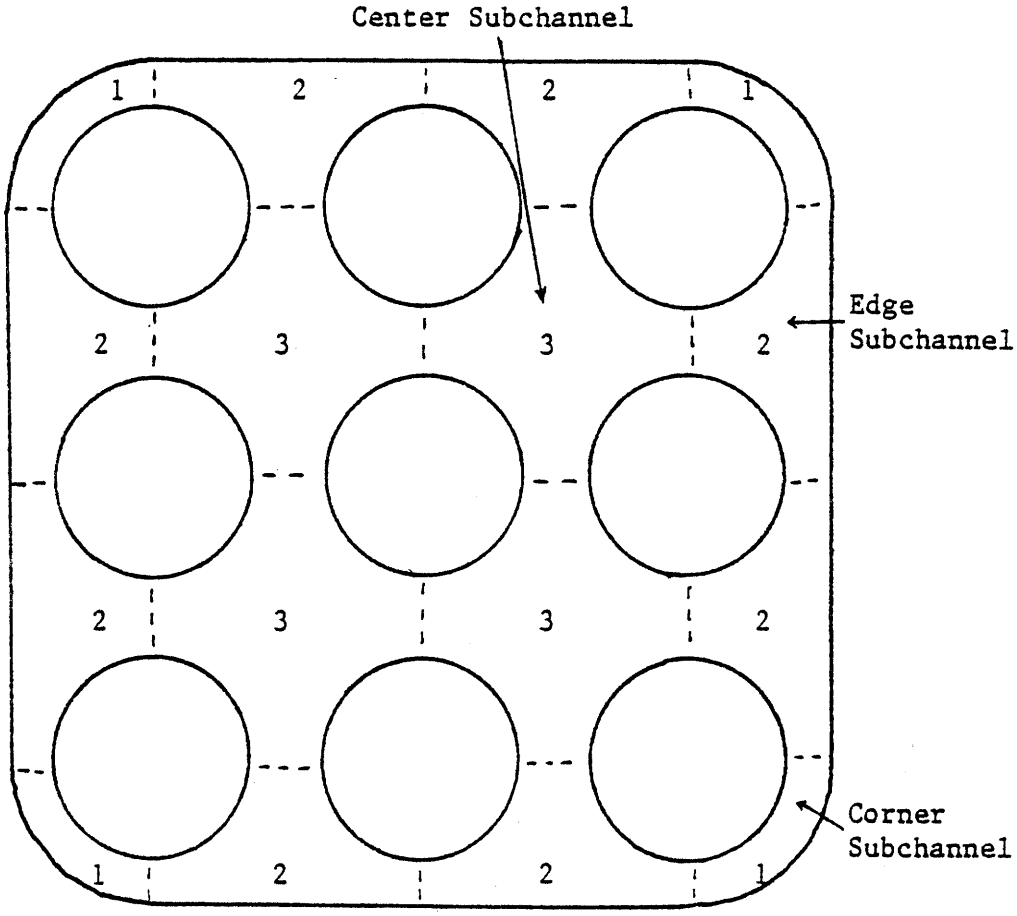

Geoemtrical Details

Rod Diameter	14.478	mm
Rod-Rod Gap	4.267	mm
Rod-Wall Gap	3.429	mm
Radius of Corner	10.2	mm
Heated Length	1829.	mm

Figure 5.1 Cross Section View of G.E. 9 Rod Bundle Used in Mass Velocity and Enthalpy Measurements

uniform (cases 2B to 2E) and radially non-uniform (cases 3B to 3E) power distributions have been utilized. For each of the two-phase cases the axial power distribution is uniform. The radial non-uniform power distribution is given in Figure 5.2.

Before discussing the comparisons, it is instructive to review the important characteristics of these measurments. As seen in Figure 5.1, there are three distinct types of subchannels; namely the corner, edge, and center subchannels. Measurements have been made in each of these subchannel types and the results will be discussed in terms of the subchannel types.

For the isothermal cases only mass velocity measurements have been made. These data are useful for assessing the single-phase characteristics of the two-phase mixing model. Since the two-phase mixing rate is a function of the single-phase value, it is important that an appropriate single-phase mixing rate be used. These measurements allow this aspect of the model to be assessed.

For the uniformly heated cases both mass velocity and quality measurements have been made. The most significant phenomenon observed in these measurments is that the quality in the corner subchannel is much lower than the bundle average. This behavior occurs in spite of the fact that the power-to-flow ratio is highest for the corner channel. This observation indicates that vapor is transported preferentially away from the corner subchannel to the more open (central) subchannels. Other than this peculiar behavior in the corner channel, the quality measurements in the other subchannels closely follow the bundle average behavior. The center subchannel always has the highest quality and is slightly above the

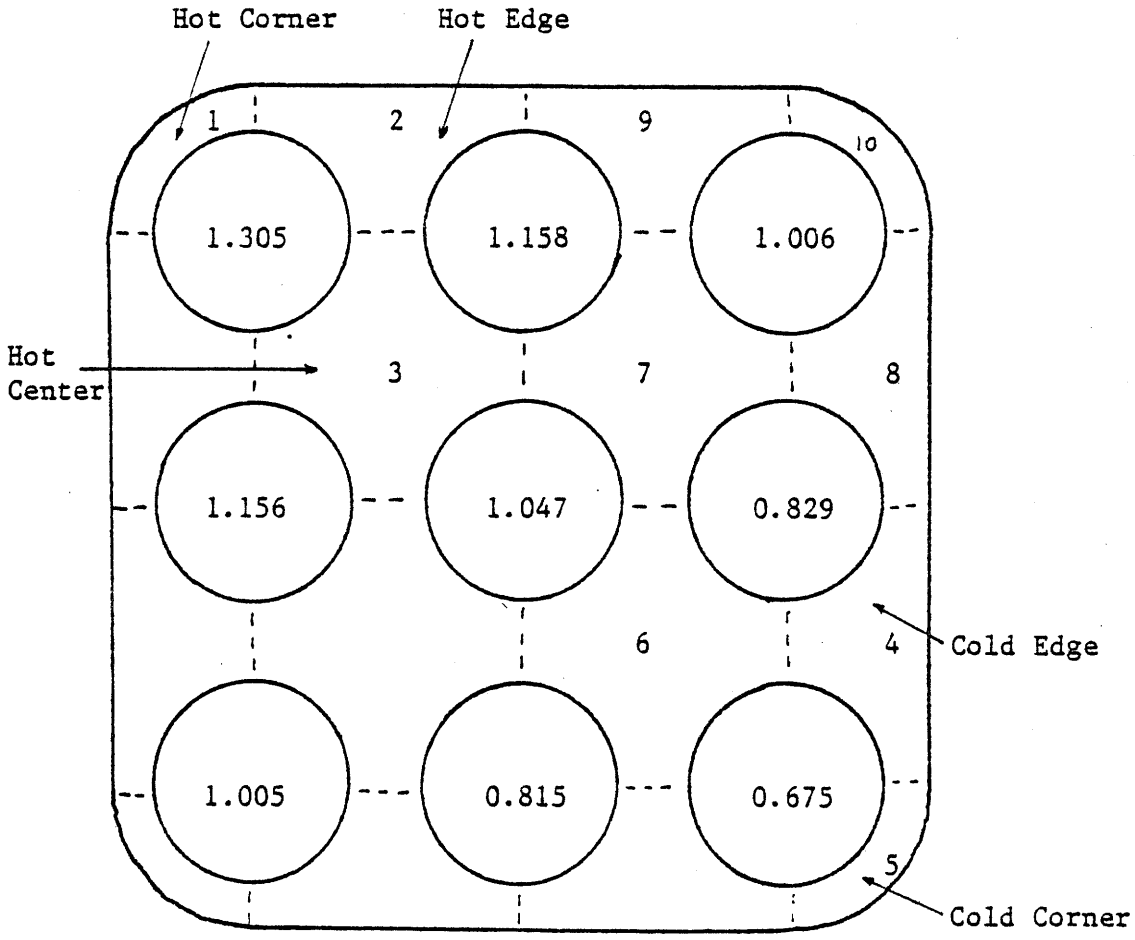

Figure 5.2 Radial Peaking Factors for Non-Uniformly Heated Case

bundle average. The edge subchannel is usually at or slightly below the average quality.

In the non-uniformly heated cases, mass velocity and quality measurements have been made in five different subchannels (see Figure 5.2). Actually, for a non-uniform power distribution, there are ten distinct subchannel types. Sampling has been done in only five of these ten subchannel types because of experimental difficulties [51]. Consequently mass and energy balances could not be evaluated. The highest quality is found in the hot center subchannel while the cold side subchannel shows the lowest quality. It is interesting to note that, although the hot corner subchannel has a higher than average quality, its quality is less than that in the hot center subchannel.

The rod-bundle used in this experiment did not contain grid spacers. Rather, spacer pins were used to prevent rod motion. Frictional losses due to these pins have been reported [36]. These losses are important in determining the flow distribution and have been included in the THERMIT hydraulic modeling.

A thorough error analysis has not been performed for these measurements. Consequently it is difficult to judge the quality of the data. However, there are a few relevent points that should be considered. The first is that sampling of the subchannels was not done simultaneously. Consequently, accurate mass balances were not always obtained. In fact, continuity errors as large as 5% have been reported. A second point is that the repeatability of the measurements was not reported. Consequently, it is difficult to quantify the error of a single measurement. Finally, for the non-uniform cases, only five subchannels were sampled of the ten

characteristic types. Hence, mass and energy errors could not even be evaluated for these cases. Furthermore, only a limited number of non-uniform power cases (4 to be exact) were made making it difficult to identify any trends in the data.

Estimates of errors in individual measurements have been made. Errors in individual mass velocity measurements are estimated to be 3%, while errors in the quality measurements are estimated to be 0.02 in quality [36]. It should be noted, however, that, due to the difference in flow areas of the various subchannels, a 3% error in the center subchannel velocity has a much larger effect on the total continuity error than a 3% error in the corner subchannel. Hence, the continuity error is very sensitive to errors in the center subchannel mass velocity measurement. This point must be considered when evaluating the results of the experimental comparisons.

5.2.2 Single-Phase Comparisons

The comparisons of the single-phase mass velocity measurements with the predictions of THERMIT have been found to be in overall good agreement. Tabulated mass velocity comparisons are presented in Appendix B with Figure 5.3 graphically illustrating the good agreement between data and predictions. It is seen that the mass velocity in the center and edge subchannels is well-predicted by THERMIT over the entire range of average mass velocities. The mass velocity in the corner subchannel is satisfactorily predicted although some minor deviations are observed at low and higher average mass velocities. These deviations are not too significant considering the estimated error in the measurements. Hence, the two-phase mixing model reduces to the single-phase limit as expected.

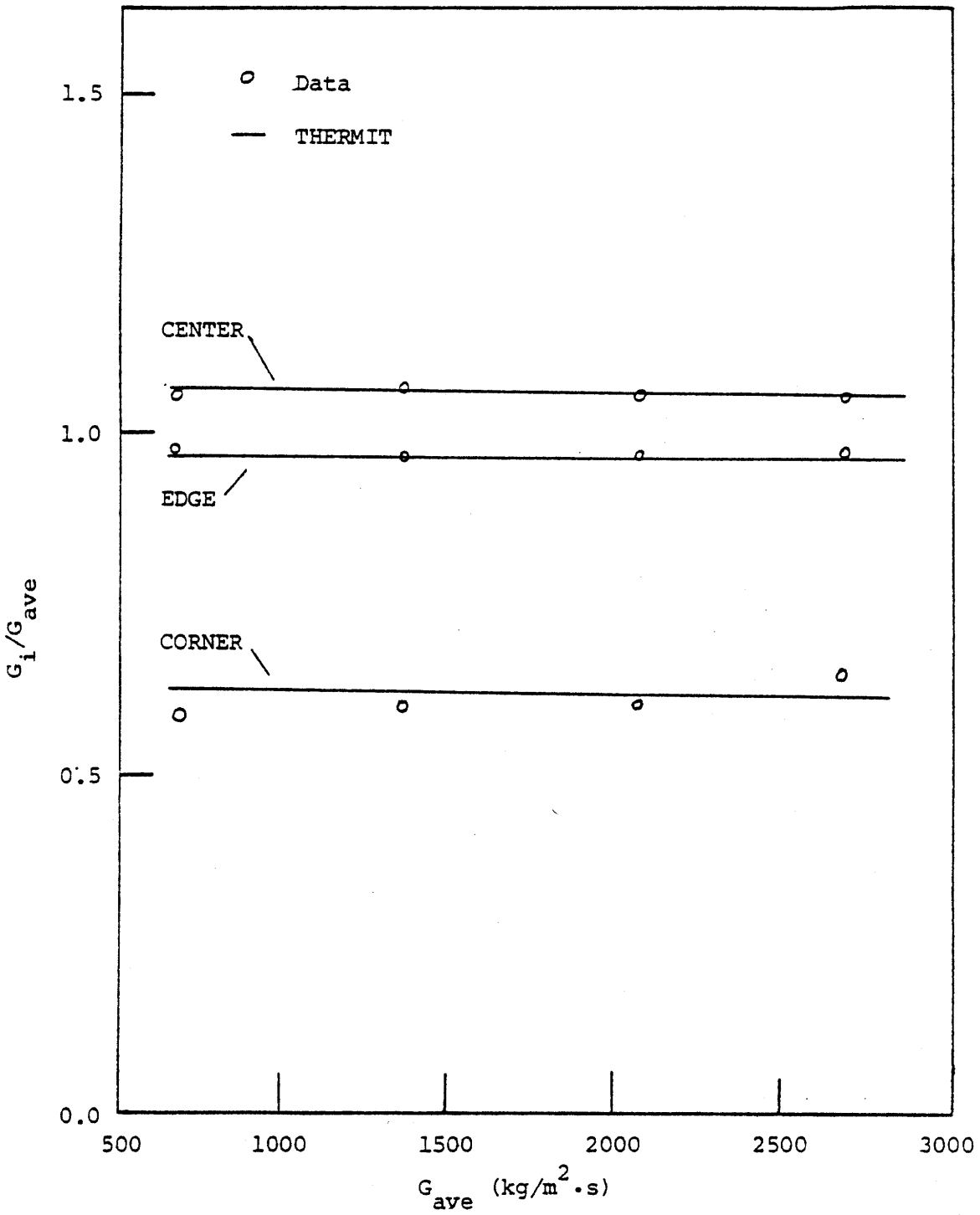

Figure 5.3: Comparison of Measured and Predicted Mass Velocities for G.E. Isothermal Tests

Furthermore, the single-phase mixing rate seems to be appropriate for these cases.

5.2.3 Uniformly-Heated Cases

For the uniformly heated cases, comparisons have been made for a wide spectrum of mass velocities and qualities. Test conditions along with the measured and predicted exit mass velocity and quality distributions are tabulated in Appendix B. It should also be noted that for a few cases THERMIT predictions have been made without using the two-phase mixing model. These predictions demonstrate the importance of the two-phase mixing.

On the whole, the agreement between the measured and predicted values is rather good. The quality distributions as a function of the bundle average quality are illustrated in Figure 5.4 to 5.6. For the corner subchannel it is seen that the quality is significantly less than the bundle average over the entire quality range. The predicted values follow the trend in the data very well, although a slight underprediction of the data is seen at the highest quality. Without the two-phase mixing model, the quality is greatly overpredicted and these results are in very poor agreement with the data.

For the edge subchannel the quality is also satisfactorily predicted by THERMIT. The majority of the data are slightly below the bundle average and this trend is predicted by THERMIT. However, in the highest quality case the predictions tend to be less than the measured value.

For the center subchannel, it is seen that the measured quality is consistently greater than the average. THERMIT successfully predicts this trend and the results are in very good agreement with the measured values.

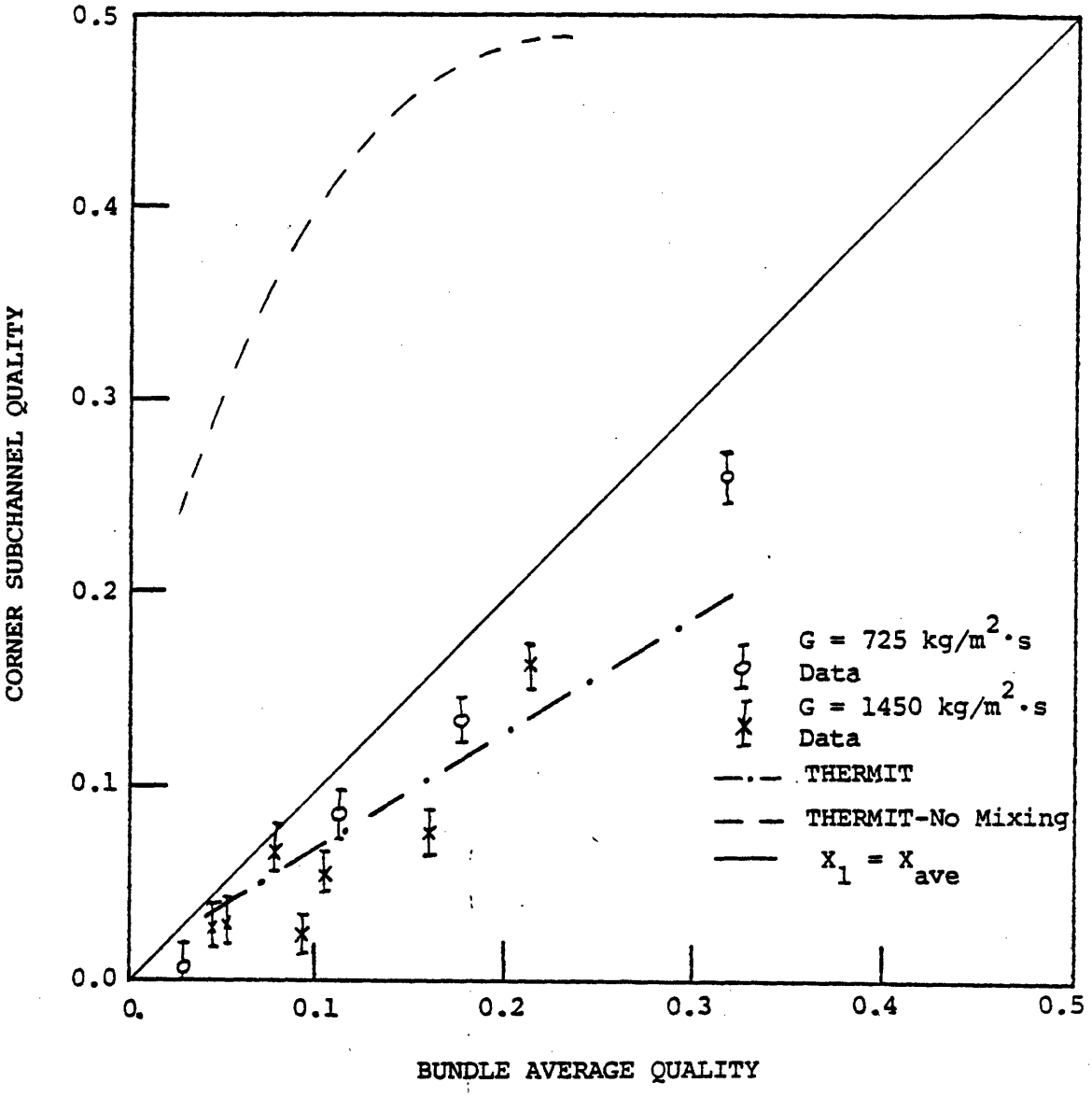

Figure 5.4: Comparison of Measured and Predicted Exit Quality in Corner Subchannel for G.E. Uniformly Heated Cases

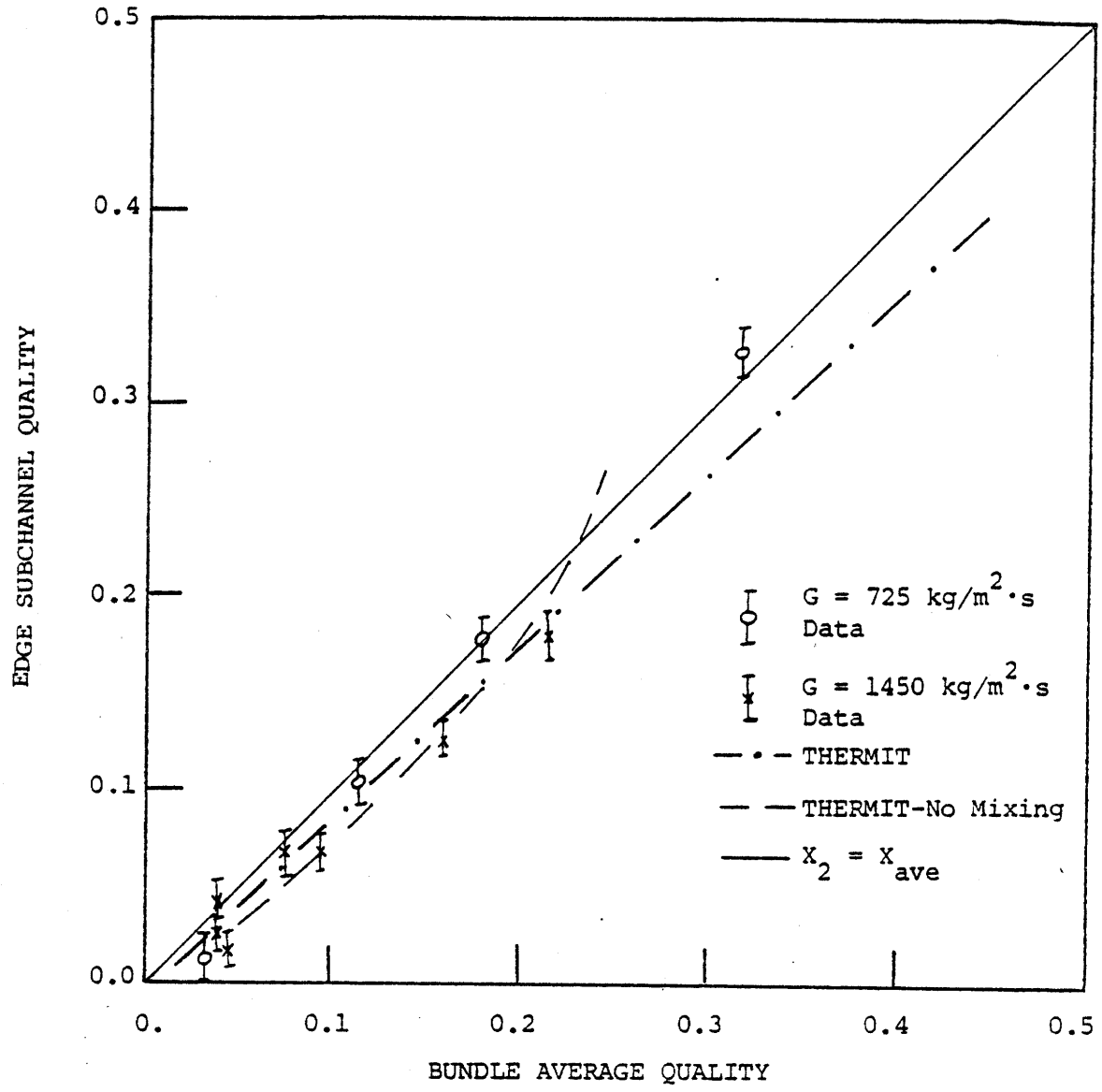

Figure 5.5: Comparison of Measured and Predicted Exit Quality in Edge Subchannel for G.E. Uniformly Heated Cases

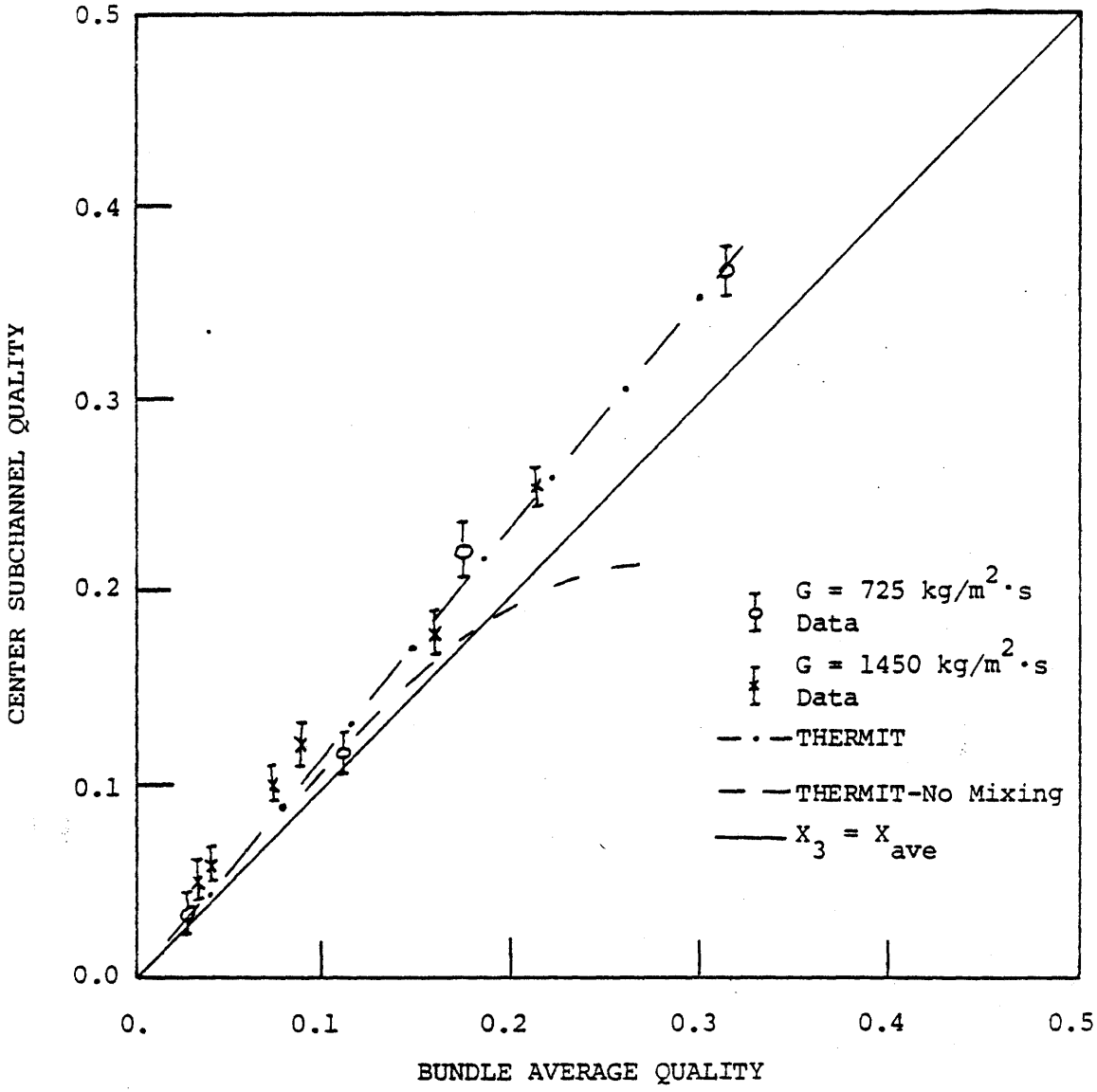

Figure 5.6: Comparison of Measured and Predicted Exit Quality in Center Subchannel for G.E. Uniformly Heated Cases

Without the two-phase mixing model, the predictions at high qualities (> 15%) tend to deviate significantly from the data. Overall, it is seen that the quality distribution is well-predicted by THERMIT.

The mass velocity comparisons are illustrated in Figure 5.7. The predicted mass velocity values for the center and edge subchannels are seen to be in fairly good agreement with the data. The predicted corner mass velocity values are found to be in satisfactory agreement although a few points are underpredicted by as much as 10%. However, as seen in Figure 5.7 if the two-phase mixing effects are not included, then substantial underprediction of the data is found. Compared with these predictions, the results for the corner subchannel are seen to be quite good. Furthermore, in view of the uncertainties in the measurements, the predicted results seem to be satisfactory. Hence, due to the good agreement in both the quality and mass velocity distributions, the current formulation of the two-phase mixing model seems to be appropriate.

5.2.4 Evaluation of Mixing Parameters

As discussed in Section 5.1, the two mixing parameters, θ_M and K_M, have been set to the recommended values of 5.0 and 1.4, respectively. The choice of these values has been based on the work of Faya [29]. While these values are probably also appropriate for THERMIT, different values may, in fact, be more optimal. Therefore, the sensitivity of the predictions to variations in θ_M and K_M for the 2E series cases have been studied. Values of θ_M ranging from 1 to 10 along with variations of K_M from 1 to 2 have been used in this study. These variations cover the range of possible values for these parameters and illustrate the sensitivity of the code predictions.

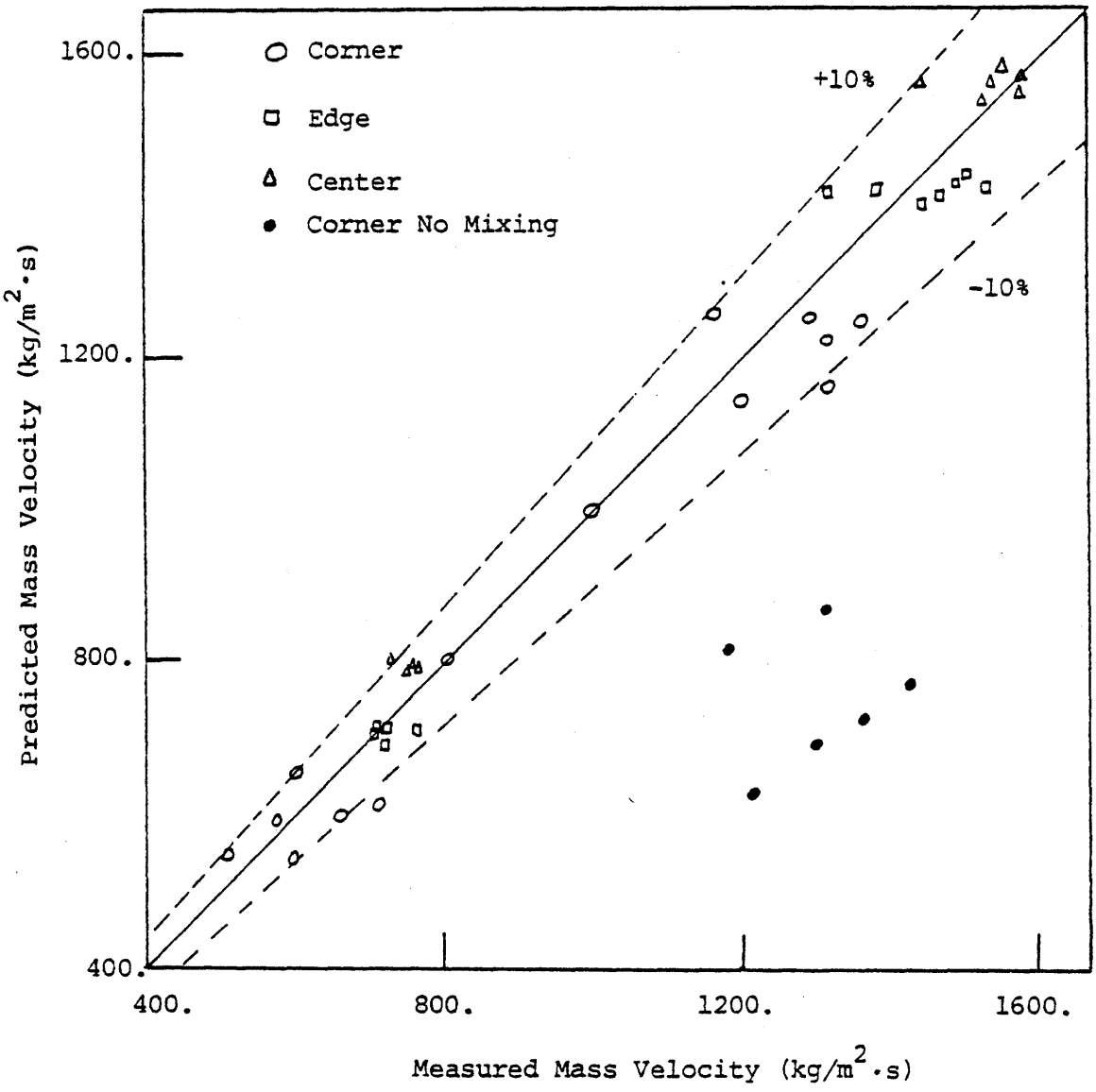

Figure 5.7: Comparison of Measured and Predicted Mass Velocities for G.E. Uniformly Heated Tests

Physically, θ_M controls the level of mixing for two-phase conditions. As θ_M is increased, the mixing rate increases leading to a more uniform flow and quality distribution. The effect of varying θ_M for the 2E cases, which represent typical cases, is illustrated in Figure 5.8 ($K_M = 1.4$). While the variation of θ_M affects all subchannels, the corner subchannel results are seen to be the most sensitive to the value of θ_M. As θ_M is increased from 1 to 10, the enthalpy (quality) in the corner channel decreases while the mass velocity increases. The changes in the enthalpy are relatively small. However, the mass velocity is seen to show large variations. The large variations in the corner subchannel mass do not significantly affect the mass continuity so that the mass velocities in the edge and center subchannels do not change by a large amount. The difference between $\theta_M = 5$ and $\theta_M = 10$ cases is seen to be relatively small. For these particular cases it may appear that a large value of θ_M may be warranted. However, for the majority of cases (both here and in the following sections) a value of $\theta_M = 5$ seems to be satisfactory.

The parameter K_M has also been varied from 1.0 to 2.0 (with $\theta_M = 5$). Physically, as K_M increases the fully-developed void fraction profile becomes steeper and the amount of vapor diffusion will be greater. Consequently, more vapor will be transported from the corner to the center subchannel. This effect is illustrated in Figure 5.9 for a typical case (2E2). The results show that as K_M is increased the quality in the corner subchannel decreases and the mass velocity increases. The center subchannel shows the opposite trend while the quality in the edge subchannel is virtually unchanged. For this case, a high value of K_M would tend to bring the corner subchannel results into better agreement, but will make

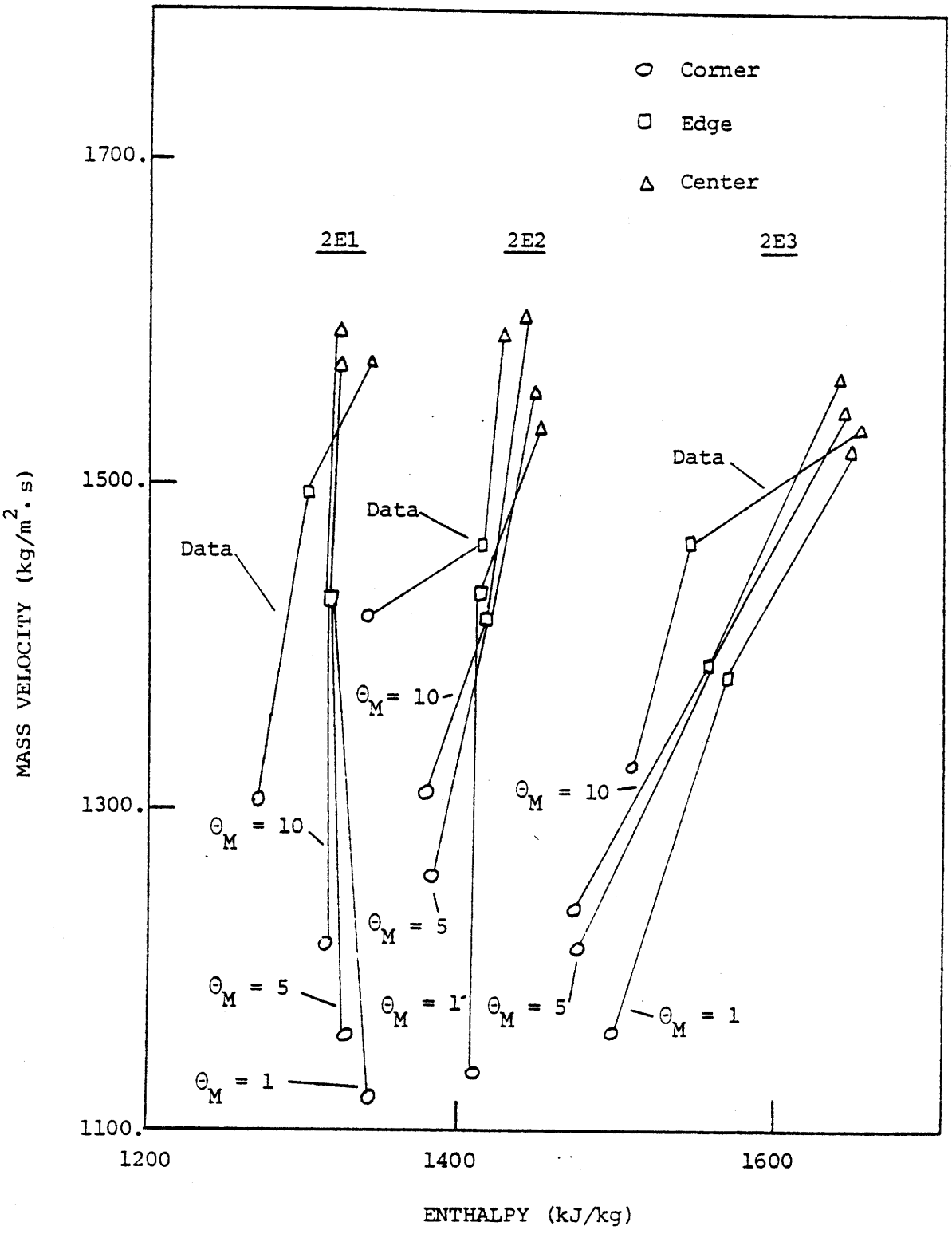

Figure 5.8: Comparison of G.E. 2E Cases with Θ_M Varied from 1 to 10

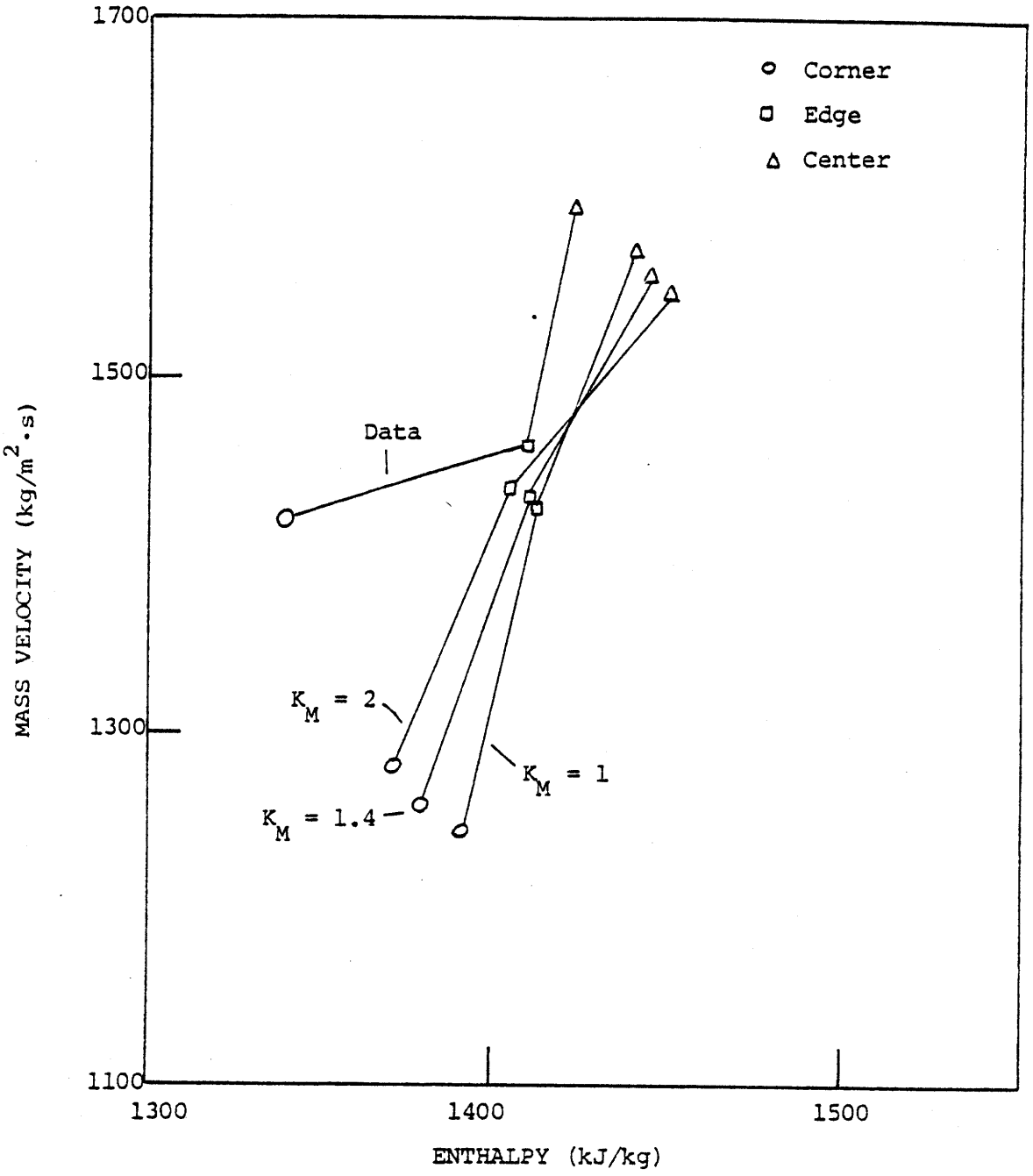

Figure 5.9: Comparison of THERMIT Predictions for Case 2E2 with Variations in K_M

the center subchannel results worse. Hence, it is not possible to improve the agreement by varying K_M alone.

It should also be noted that the changes in the mass velocity distributions are greater for θ_M variations than for K_M variations. Of course, θ_M is varied over a larger range. The changes in the quality distributions are found to be nearly the same for either θ_M or K_M variations.

The results of this sensitivity study indicate the importance of θ_M and K_M on the mass velocity and quality distributions. The mass velocity distribution is most affected by θ_M. However, the $\theta_M = 5$ and $\theta_M = 10$ cases give similar results which supports the use of the $\theta_M = 5$ assumption. The quality distribution is virtually unaffected by variations in either θ_M or K_M. Since neither the quality or mass velocity is overly sensitive to variations in K_M, the use of the $K_M = 1.4$ assumption is appropriate.

5.2.5 Non-Uniformly Heated Cases

Four tests using the non-uniform radial power distribution (illustated in Figure 5.2) have been made. In these tests exit mass velocity and quality measurements have been taken in five of the ten characteristic subchannel types. Due to the limited amount of data and because mass and energy balances could not be evaluated, it is difficult to assess the two-phase mixing model with this data. In spite of the shortcoming of the measurements, comparisons between the measured and predicted distributions have been made.

The results of the comparisons are listed in Appendix B. Figure 5.10 shows that the quality distribution can be satisfactorily predicted in each case. Nearly all of the predictions lie within 0.025 (in quality) of the measured value. Only in case 3E1 is the hot center subchannel

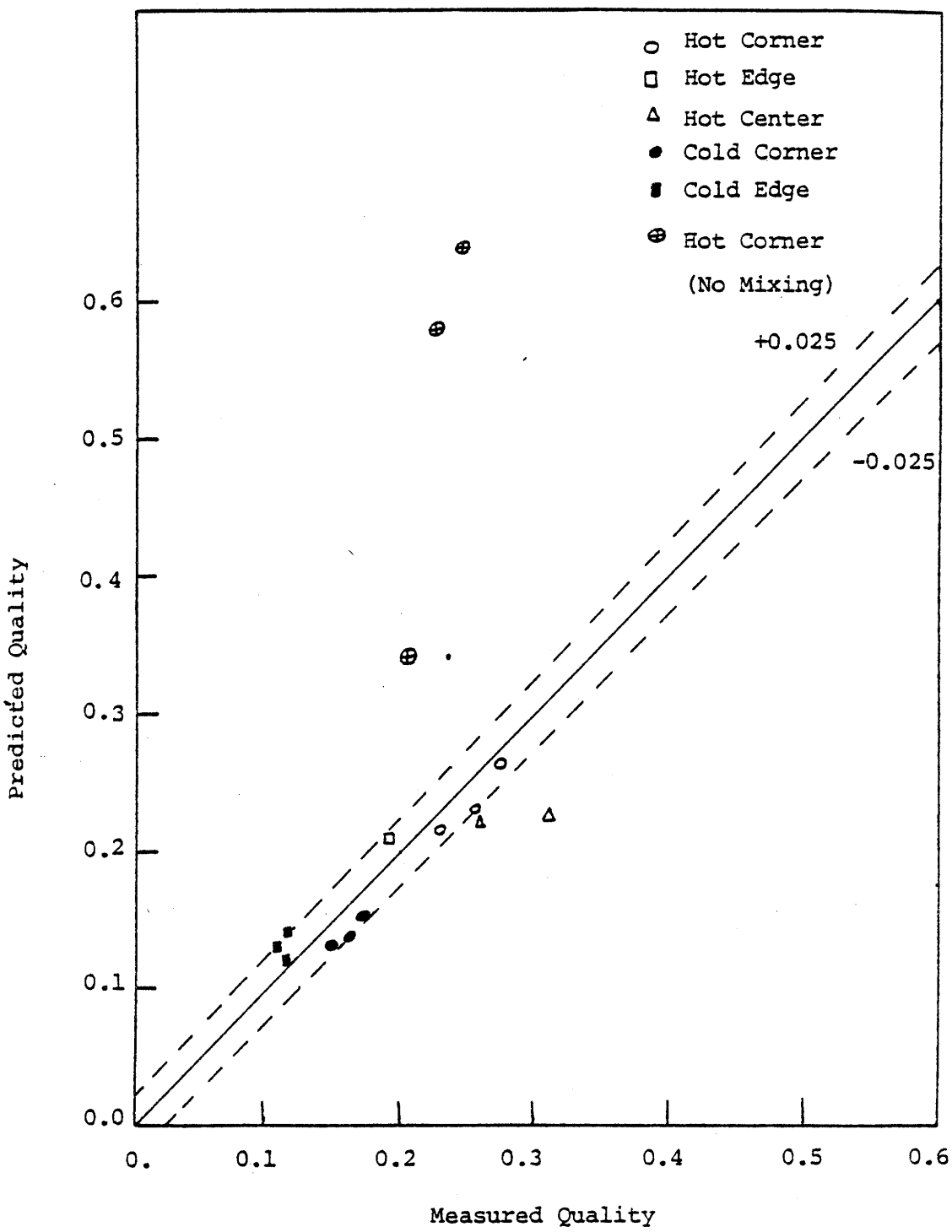

Figure 5.10: Comparison of Measured and Predicted Quality for G.E. Non-Uniformly Heated Tests

underpredicted by more than 0.05. On the whole, and in view of the limitations of these measurements, the predicted quality distributions are found to be in good agreement with the data.

Comparisons between the measured and predicted mass velocities are illustrated in Figure 5.11. It is seen that a majority of the data is predicted within 10%. In particular, the hot corner, hot edge and cold edge velocities are well-predicted. However, the agreement for the hot center and cold corner is only fair. As discussed above, the mass flow error for these cases could not be evaluated so that is is difficult to assess the accuracy of the measurements. Hence, although the agreement in the mass velocities is not as good as expected, the comparisons indicate that, overall, THERMIT is satisfactorily predicting the exit mass velocity and quality distributions for the non-uniformly heated cases.

5.3 Ispra BWR tests

5.3.1 Test Description

Mass velocity and quality distribution have been measured in a 16-rod electrically heated test section at Ispra [37]. As in the case of the G.E. tests, both the two-phase flow conditions as well as the geometrical characteristics of the test section closely matched those found in a BWR. The nominal pressure was 6.9 MPa, exit qualities ranged from 2% to 31% and mass velocities of 1000, 1500, and 2000 $kg/m^2 \cdot sec$ have been used. The geometrical details of the test section are illustrated in Figure 5.12 and it is seen that the rod diameter and rod-to-rod pitch are similar to those found in a BWR bundle.

Approximately 225 test cases have been reported in reference 37. For

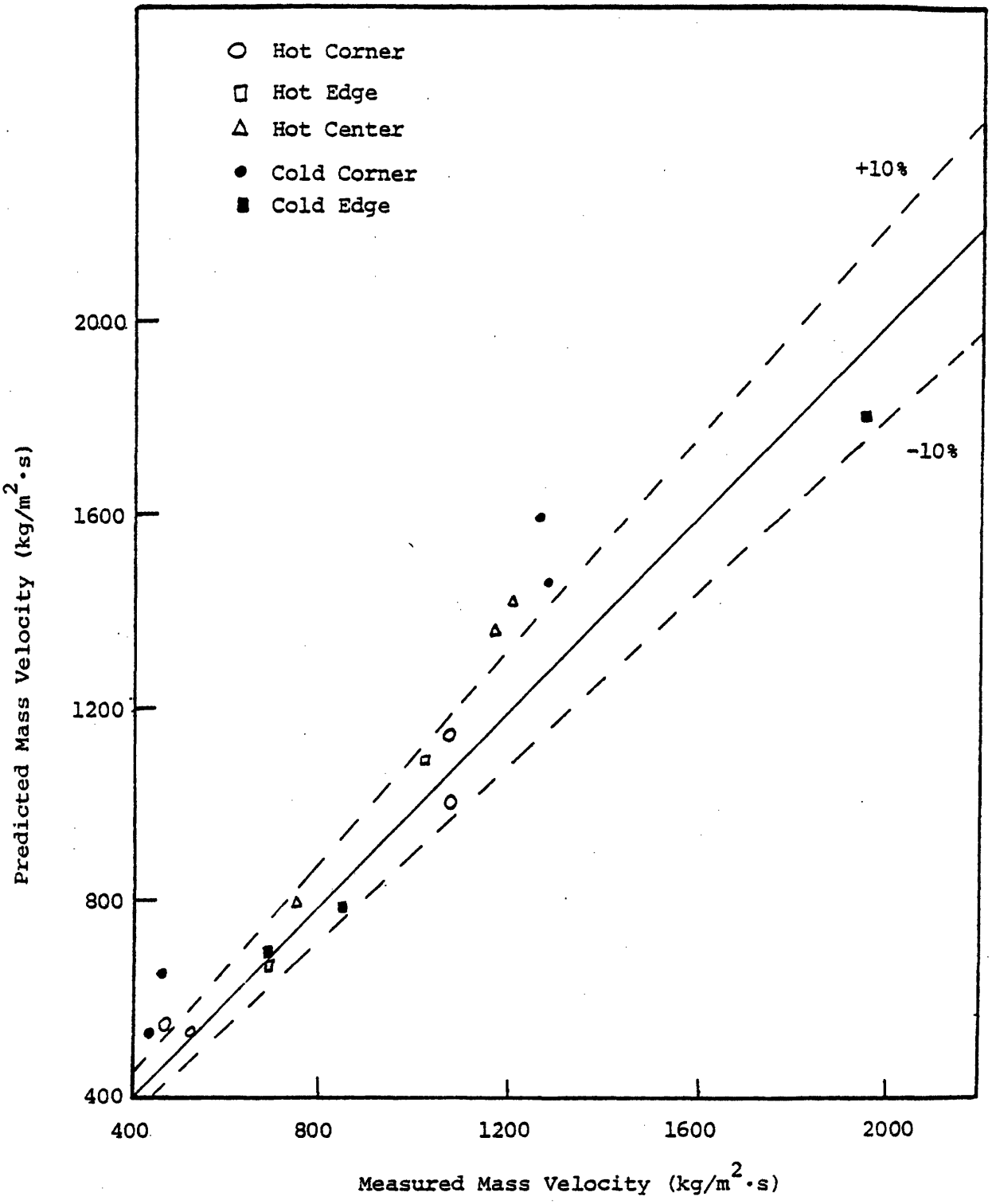

Figure 5.11: Comparison of Measured and Predicted Mass Velocities for G.E. Non-Uniformly Heated Tests

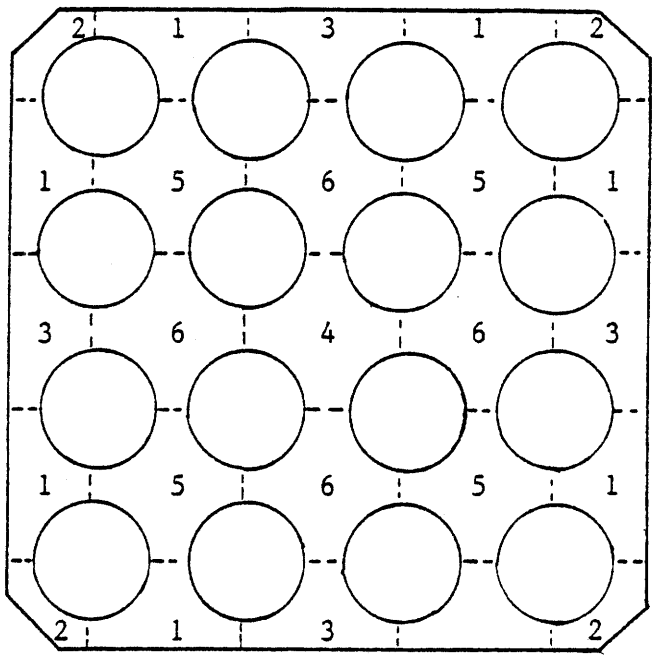

Geometrical Details

Rod Diameter	15	mm
Rod-Rod Clearance	4.5	mm
Rod-Wall Clearance	3.37	mm
Corner Radius	104.1	mm
Heated Length	3660	mm

Figure 5.12 Cross Sectional View of Ispra BWR Test Section

each case, simultaneous isokinetic sampling at the test section exit in four of the six distinct subchannel types have been performed. The sampled subchannels along with the numbering scheme are indicated in Figure 5.12. A uniform power distribution has been used in all cases.

Three important differences between the Ispra test section and G.E. test section can be identified. First, the Ispra test section was 3.66m long, which is the nominal BWR bundle length, while the G.E. bundle was only 1.83m long. Since the two test sections were operated at approximately the same mass velocity, inlet temperatures and outlet qualities, the heat flux in the Ispra bundle is much less than that used in the G.E. bundle. The second difference is the number of rods in each bundle. The Ispra bundle has 16 rods while the G E. bundle has 9 rods. With 16 rods there are six distinct subchannel types rather than three types in a 9 rod bundle. The third difference is that the Ispra bundle used grid spacers while the G.E. bundles used spacer pins. The loss coefficients associated with the grids are much larger than those for the pins and are very important for proper modeling of the hydraulic characteristics of the bundle. Unfortunately, these loss coefficients were not measured and only estimated values have been reported. Since additional information is not available for the grid loss coefficients, the estimated values have been used in the subsequent analyses.

The general trends in the quality measurements show many of the same characteristics found in the G.E. tests. For example, the quality in the corner subchannel is below the average even though the mass velocity in this subchannel is the lowest. The quality in the other subchannels closely follows the bundle average behavior, again as seen in the G.E.

tests.

In the mass velocity measurements one main difference between the G.E. and Ispra tests can be seen. The difference is that, while in both tests the corner mass velocity is below the average, in the Ispra tests it is much lower than average. This result is attributed to the use of grid spacers which have a higher loss coefficient in the corner subchannel. Besides this difference, the mass velocities in the other subchannels show the same qualitative behavior in both test sections.

The estimated errors in the individual mass velocity and quality measurements are on the order to 3% [37]. However, since only four of the six characteristic subchannels were sampled, a mass balance could not be calculated. Attempts to estimate the continuity error indicate that errors as high as 8% may be possible [37]. This error is rather large, but is compensated by the fact that numerous measurements were made for the same conditions. Consequently, the data show significant spread, but this would be expected for measurements of this type. With these measurements, evaluation of the two-phase mixing model is easier since the trends in the data are much clearer.

5.3.2 Results

For the Ispra BWR tests a total of eleven representative cases have been simulated with THERMIT. These cases cover a range of qualities at each of the three mass velocity values (i.e. 1000, 1500, and 2000 $kg/m^2 \cdot sec$). It should be noted that for all of these cases, θ_M is set to 5.0 while K_M is set to 1.4. Also as in the case of the G.E. tests, uniform inlet velocity and uniform outlet pressure boundary conditions have been used.

Comparisons between the measured and predicted quality and mass velocity distributions have been made. In Appendix B, the test conditions, measured and predicted values as well as the predictions using the original version of THERMIT (i.e. no mixing) are listed. Through these comparisons, the two-phase mixing has been assessed.

On the whole, the quality distribution is well-predicted for each subchannel. Figures 5.13 to 5.16 show the comparisons between the measured and predicted quality values for the various subchannels. In each figure, the shaded areas represents the spread in the actual measured values. For the corner subchannel, the predicted values are in very good agreement with the measured values (see Figure 5.13). If the mixing model is not included, then the quality is significantly overpredicted. Hence, as in the G.E. cases, the inclusion of the effects of mixing are essential for accurate predictions of the corner subchannel quality. It should also be noted that COBRA IIIC cannot predict the correct quality behavior of the corner subchannel [53].

In the edge subchannel, good agreement between the measured and predicted qualities is also found (see Figure 5.14). For both of the center subchannels, THERMIT tends to predict qualitites which are on the high side of the data at high bundle average quality (see Figure 5.15 and 5.16). However, on the whole, the quality distribution is very well predicted by THERMIT for these cases.

The mass velocity comparisons are illustrated in Figure 5.17 and 5.18. Figure 5.17 shows the comparisons for the edge and corner subchannel results. It is seen that the THERMIT predictions for the corner subchannel are consistently high. This result may be due to one of two reasons.

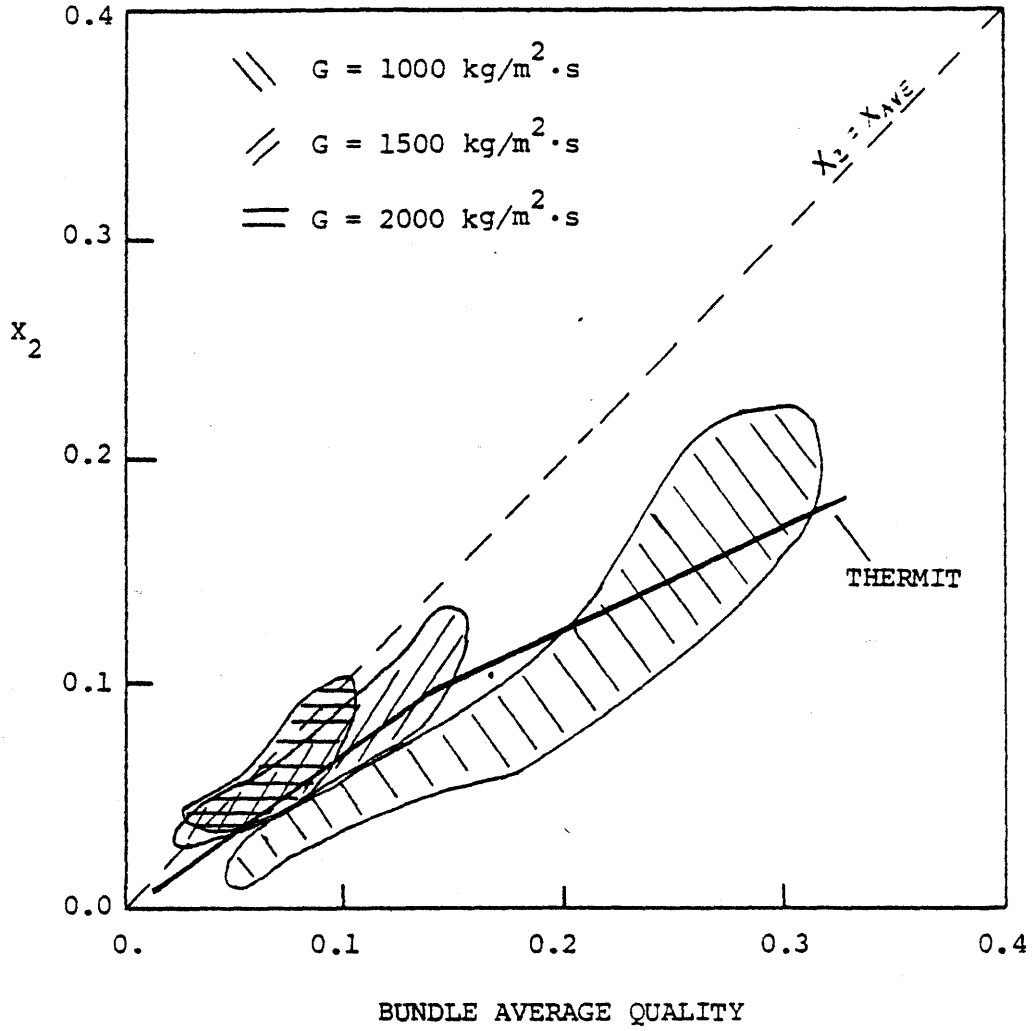

Figure 5.13: Comparison of Measured and Predicted Exit Quality of Subchannel 2 — Ispra BWR Tests

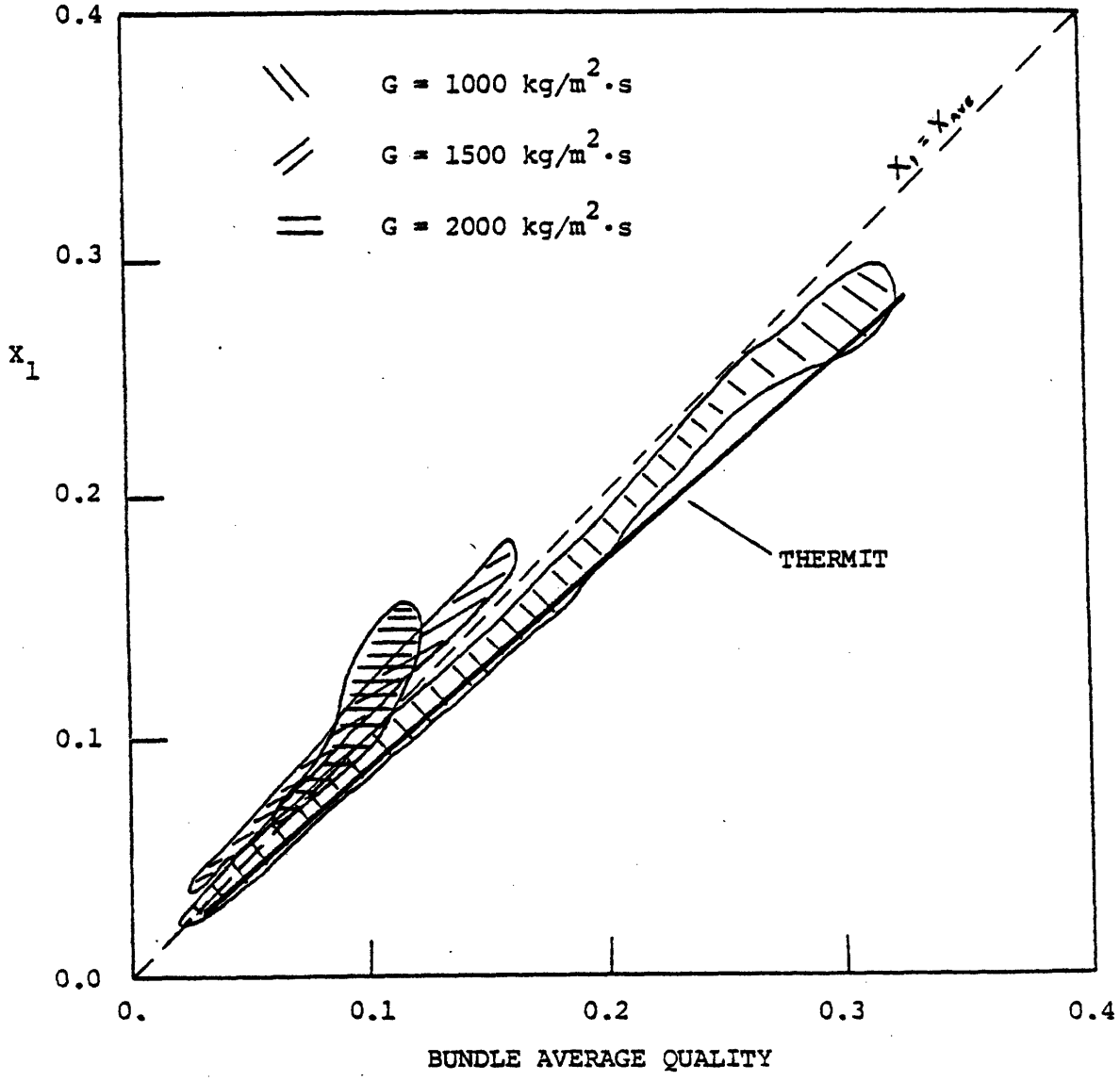

Figure 5.14: Comparison of Measured and Predicted Quality for Subchannel 1 versus Bundle Average Quality — Ispra BWR Tests

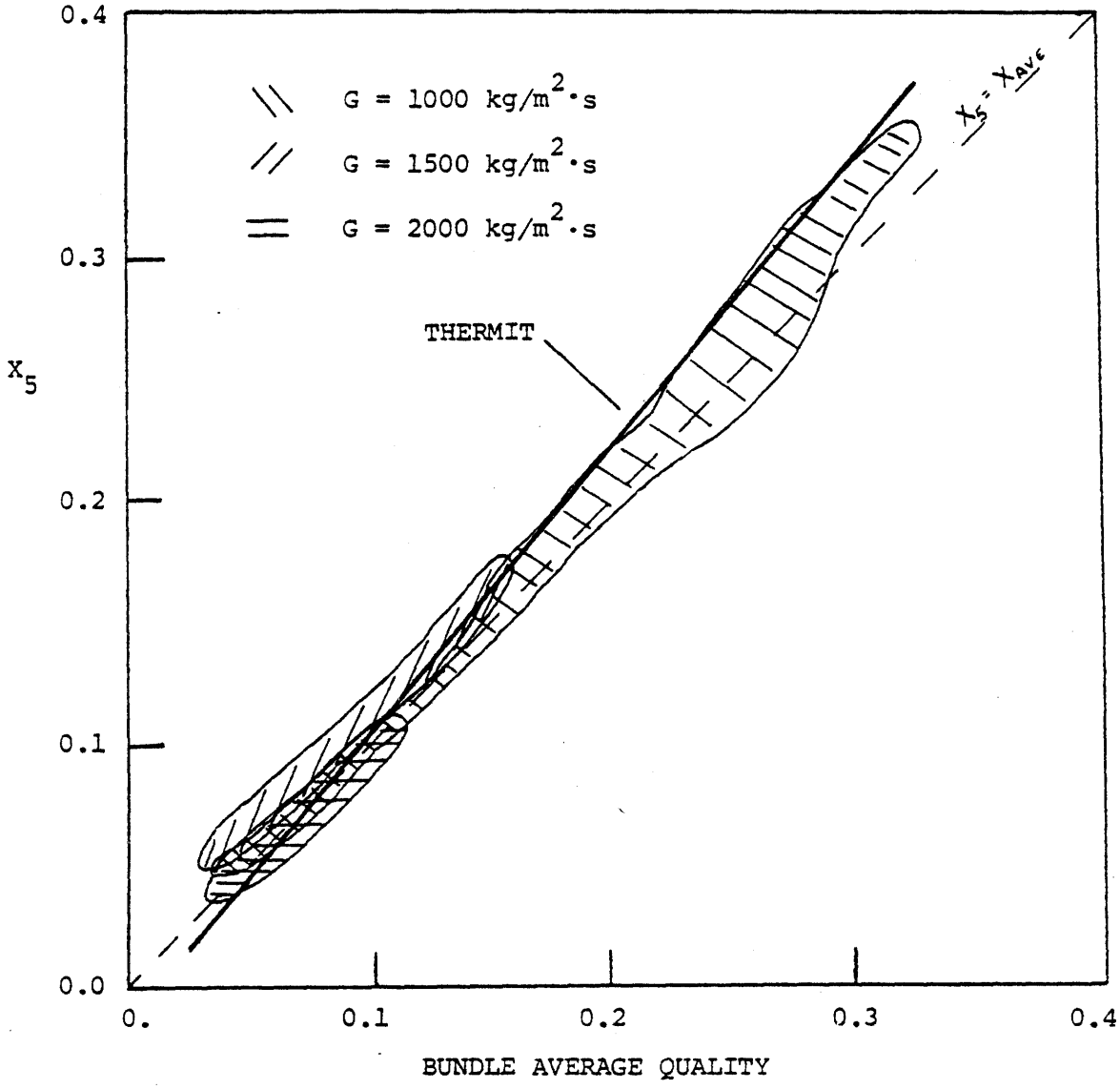

Figure 5.15: Compaison of Measured and Predicted Quality for Subchannel 5 versus Bundle Average Quality — Ispra BWR Tests

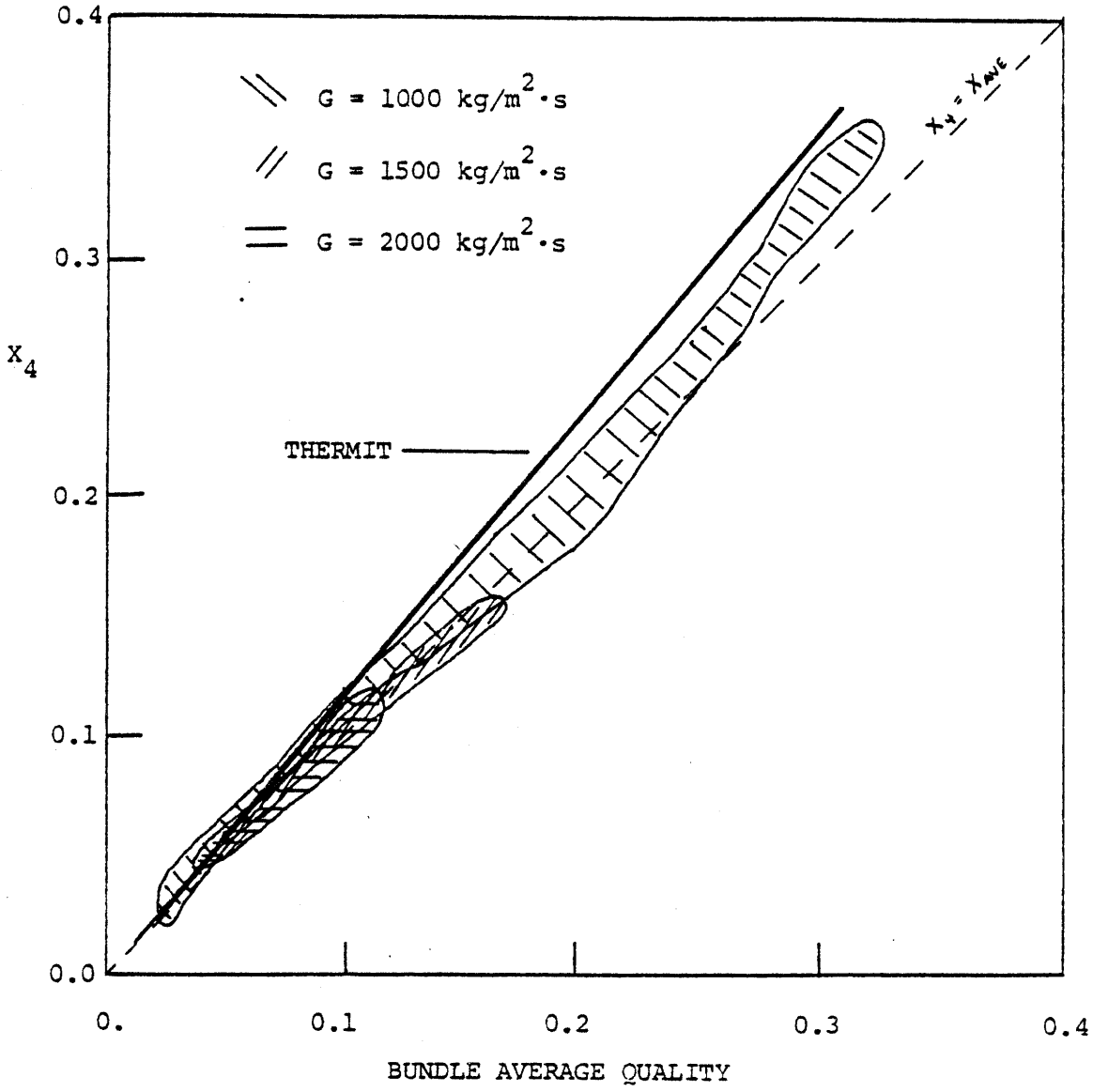

Figure 5.16: Comparison of Measured and Predicted Quality for Subchannel 4 versus Bundle Average Quality — Ispra BWR Tests

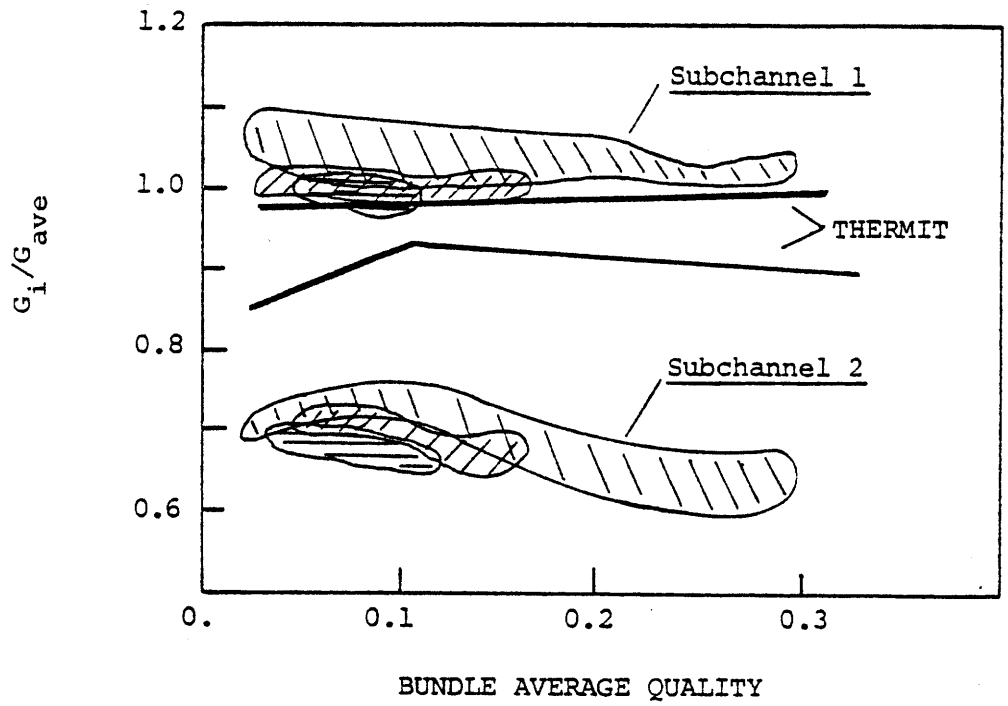

Figure 5.17: Comparison of Measured and Predicted Mass Velocities for Subchannels 1 and 2 — Ispra BWR Tests

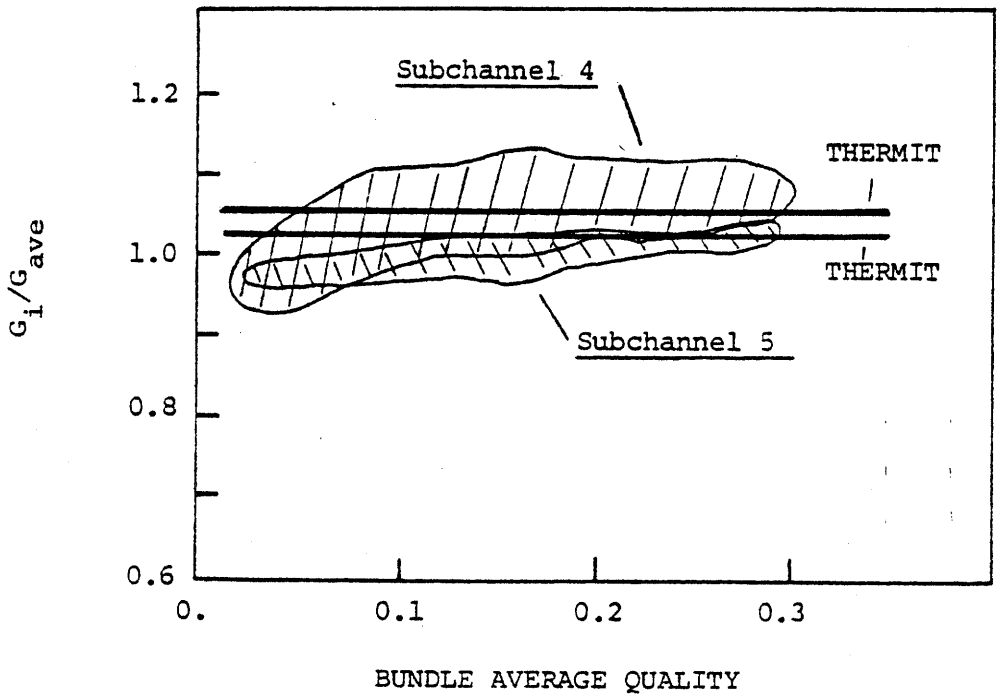

Figure 5.18: Comparison of Measured and Predicted Mass Velocities for Subchannels 4 and 5 — Ispra BWR Tests

First, the mixing rate may be too high which, as seen in Section 5.2.4, leads to higher mass velocity values. However, these cases have also been run without including the effects of mixing and the mass velocity is still overpredicted. The second reason may be that the grid coefficients are not correct. As discussed by Lahey [25], proper modeling of the grids is essential for predicting the correct flow distribution. In fact experimental measurements have shown that the trends in flow distribution can be significantly different in a rod-bundle with grids compared to one without [52]. Since THERMIT models the grids as simple pressure losses, it may be anticipated that the deviations in the corner subchannel mass velocity are due to improper grid modeling.

The mass velocity in the edge subchannel is seen to be slightly underpredicted. However, the agreement is satisfactory. The deviations in the predictions may again be due to the grid modeling.

The mass velocity comparisons for the two center subchannels are illustrated in Figure 5.18. It is seen that the predictions in both subchannels are nearly the same. The agreement for subchannel 5 is very good in all cases. The predictions for subchannel 4 are also found to be quite satisfactory.

In summary, it has been shown that the predicted quality distribution is in overall good agreement with the data for these cases. Furthermore, the lower than average behavior of the corner subchannel is well predicted by THERMIT. This trend cannot be predicted by COBRA IIIC [53]. The mass velocity distribution is found to be satisfactorily predicted in view of the uncertainties in the grid spacer modeling. The corner subchannel shows the largest deviations, but this subchannel will also be the most sensitive

to the grid coefficient.

5.4 Ispra 16 Rod PWR Cases

5.4.1 Test Description

Until recently, there have been no consistent experiments to determine the steady-state mass velocity and quality distributions in typical PWR geometry and for typical PWR operating conditions. The usual problem with most previous work is that only a few of the characteristic subchannels were sampled [54]. However, recent experiments performed at Ispra [38] represent the first consistent effort to determine the mass velocity and quality distributions for PWR conditions.

These experiments have been conducted in a 16 rod electrically heated test section. Rod diameters and rod-to-rod spacing closely resemble those found in a PWR rod-bundle. Details of this test section are given in Fig. 5.19. The operating conditions for these tests also simulated PWR conditions. The nominal pressure was 16.0 MPa, the mass velocity ranged from 2500 to 3000 $kg/m^2 \cdot sec$, and the exit quality ranged from -20% to +20%. The high end of the quality range served to simulate two-phase flow conditions which might occur in transients.

As in the case of the Ispra BWR tests, grid spacers have been used to maintain the rod spacing. Unfortunately, details of the spacer design are not available. Consequently, the grid loss coefficient could only be estimated. However, as indicated in the last section, the mass velocity distribution is strongly dependent on the grid modeling. Therefore, some error in the predictions will most likely result from the lack of detailed

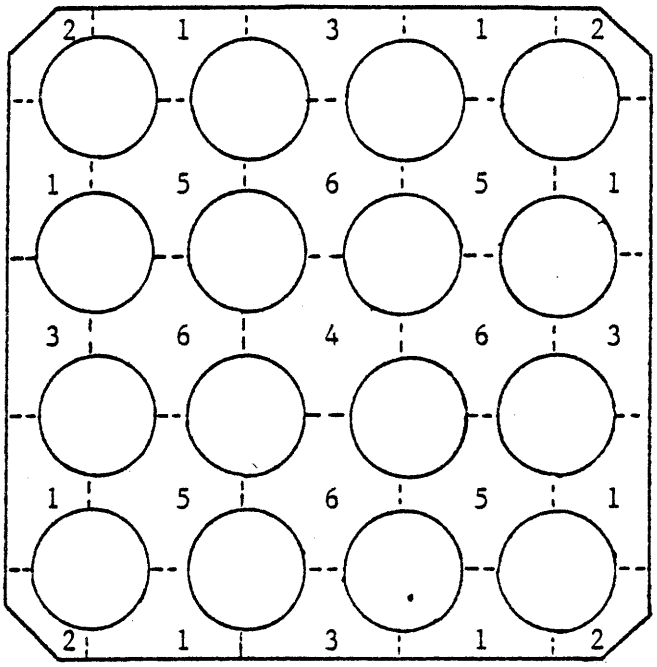

Geometrical Details

Rod Diameter	10.75	mm
Rod-Rod Clearance	3.55	mm
Rod-Wall Clearance	2.93	mm
Corner Secant	8.3	mm
Heated Length	3660	mm

Figure 5.19 Cross Sectional View of Ispra PWR Test Section

grid modeling.

The experimental measurements indicate that the subchannel exit mass velocity and quality distributions closely follow the bundle average values. Unlike the BWR cases, the quality in the corner subchannel is not significantly below the average. This result shows that the pressure plays an important role in determining the flow and enthalpy distributions. The higher mixing rate in the BWR bundle seems to be a direct result of the larger specific volume of the vapor (for BWR $\rho_v = 36.1$ kg/m^3; for PWR $\rho_v = 85.4$ kg/m^3).

The most likely reason the typical BWR corner subchannel behavior is not found in the PWR cases is that the increased pressure alters the flow regime. The slug-annular transition quality varies from approximately 0.1 at 7.0 MPa to 0.21 at 16.0 MPa. Physically, this result indicates that a bubbly flow can be maintained up to higher qualities at the higher pressure. In terms of the vapor diffusion rate, if annular flow does not occur then it is more difficult to transport the vapor from the corner subchannel to the center subchannel. Hence, the vapor diffusion rate is lower at the high pressure.

Error estimates for these measurements are comparable to those found for the Ispra BWR tests. That is, individual flow and enthalpy errors are on the order to 3% [38]. However, in the PWR tests five of the six characteristic subchannels have been sampled, which allows for more accurate assessment of the continuity and energy errors.

5.4.2 Results

Comparisons between the measured and predicted mass velocities and qualities have been made for the PWR cases. As in the BWR cases, the

values for the mixing parameters θ_M and K_M are 5.0 and 1.4 respectively. Using these values, a few representative cases have been analyzed. However, due to the proprietary nature of these measurements, only graphical illustrations of the comparisons will be given.

Overall, the quality predictions of THERMIT agree quite well with the measurements. Figures 5.20 to 5.24 illustrate these comparisons. As discussed above, it is seen that the quality in each subchannel is very near the bundle average value, even for the corner subchannel. THERMIT is able to predict this trend rather well. Good agreement between the measured and predicted values is also found for each of the subchannels. COBRA IIIC/MIT also predicts the correct trend in the data. This indicates that the effects of mixing are not as important for these cases.

The mass velocity measurements are found to be satisfactorily predicted by THERMIT. Figures 5.25 and 5.26 show the comparison between the measured and predicted values. Except for the corner subchannel, the predicted mass velocities are always within 10% of the data. The corner subchannel shows a significant underprediction for subcooled conditions. However, since the qualities are in such good agreement, these deviations are probably due to the grid modeling. On the whole, and in view of the approximate grid modeling, the mass velocity distribution is satisfactorily predicted by THERMIT.

The good overall agreement shows that the mechanistic formulation of the two-phase mixing model is also appropriate for PWR conditions. This is an important result since it verifies the assumption that mechanistic models can be extended beyond their data base range.

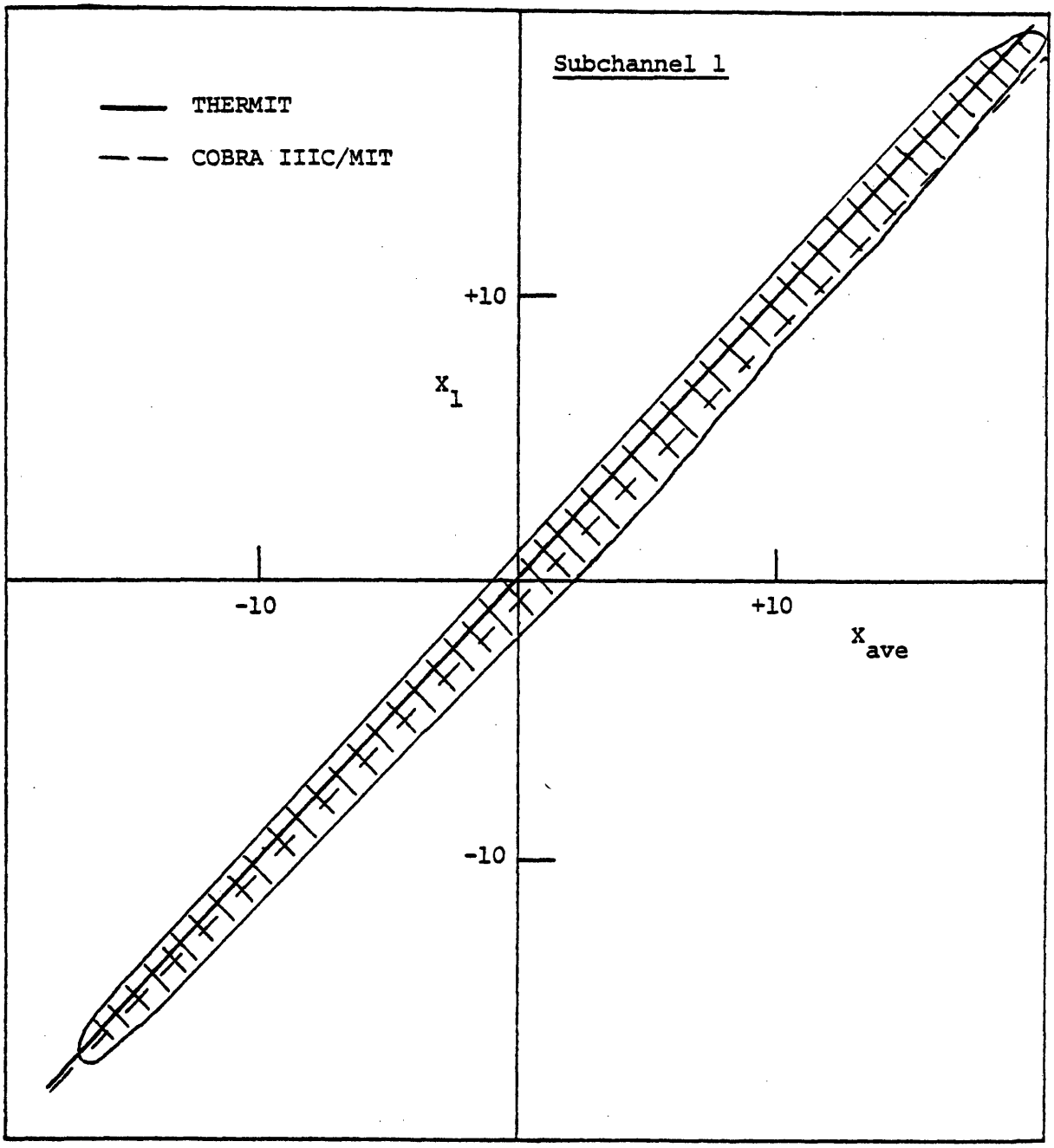

Figure 5.20: Comparison of Measured and Predicted Exit Quality for Subchannel 1 versus Bundle Average Quality - Ispra PWR Tests (COBRA IIIC/MIT Results form Reference 38)

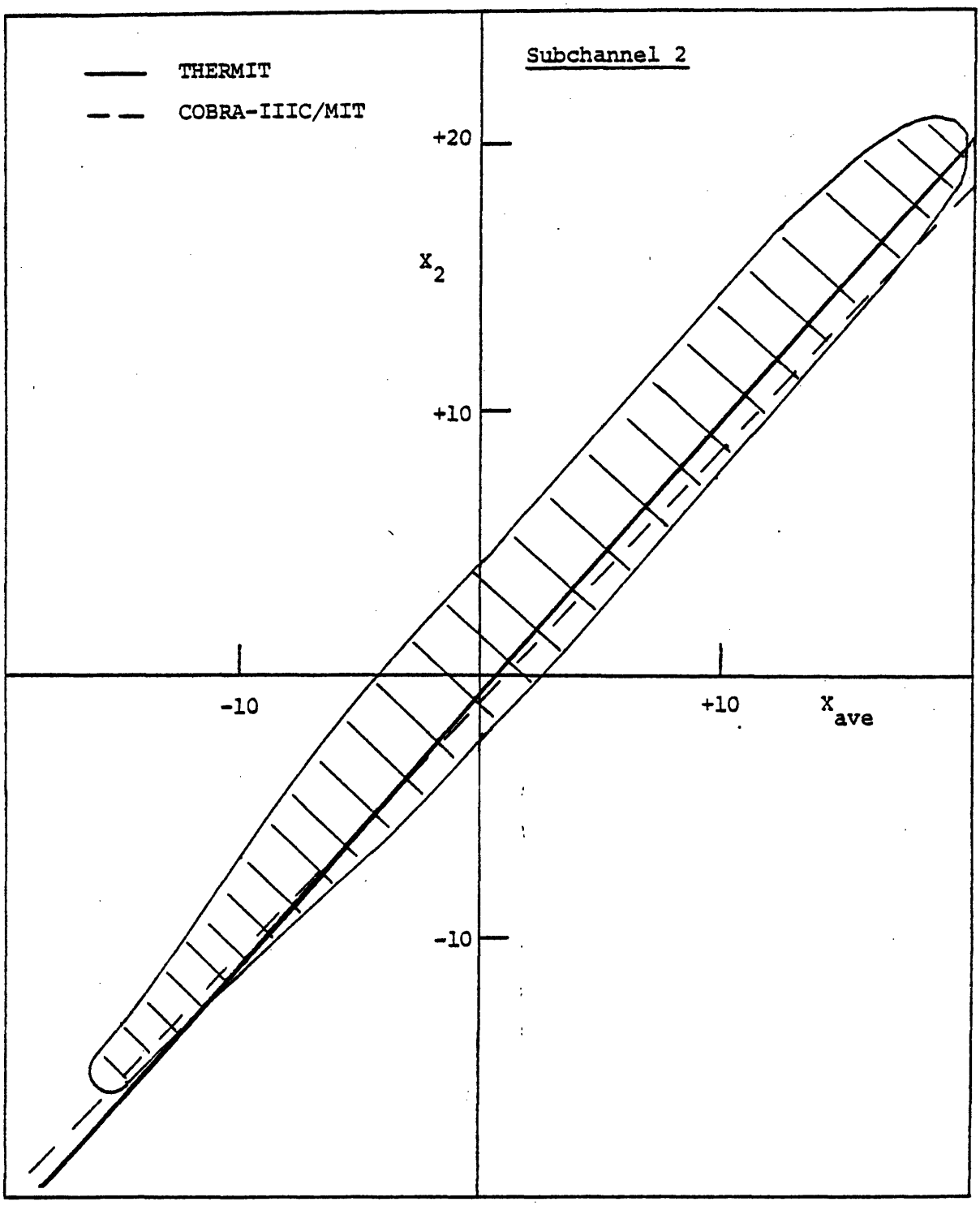

Figure 5.21: Comparison of Measured and Predicted Exit Quality for Subchannel 2 versus Bundle Average Quality - Ispra PWR Tests (COBRA IIIC/MIT Results from Reference 38)

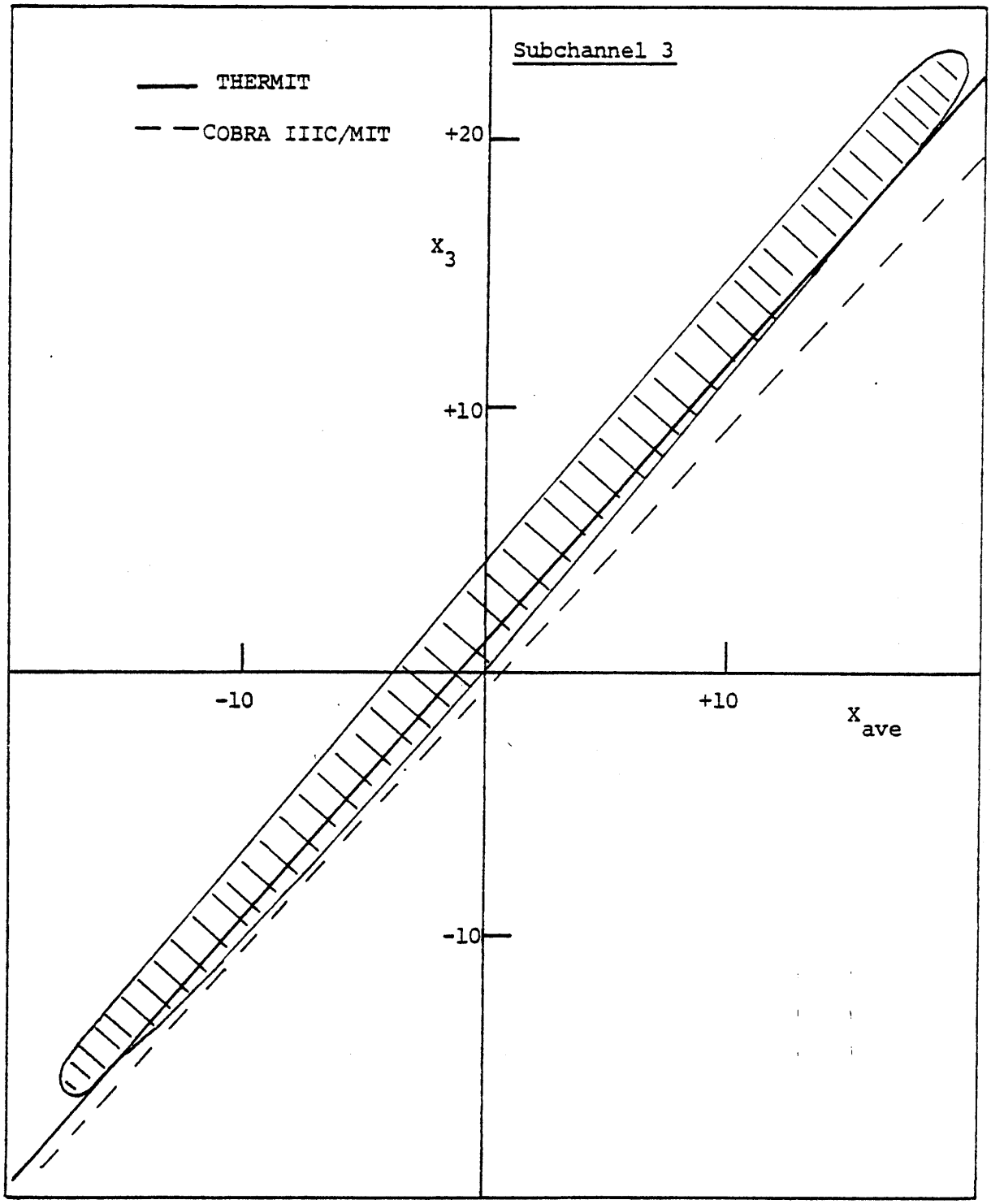

Figure 5.22: Comparison of Measured and Predicted Exit Quality for Subchannel 3 versus Bundle Average Quality - Ispra PWR Tests (COBRA IIIC/MIT Results from Reference 38)

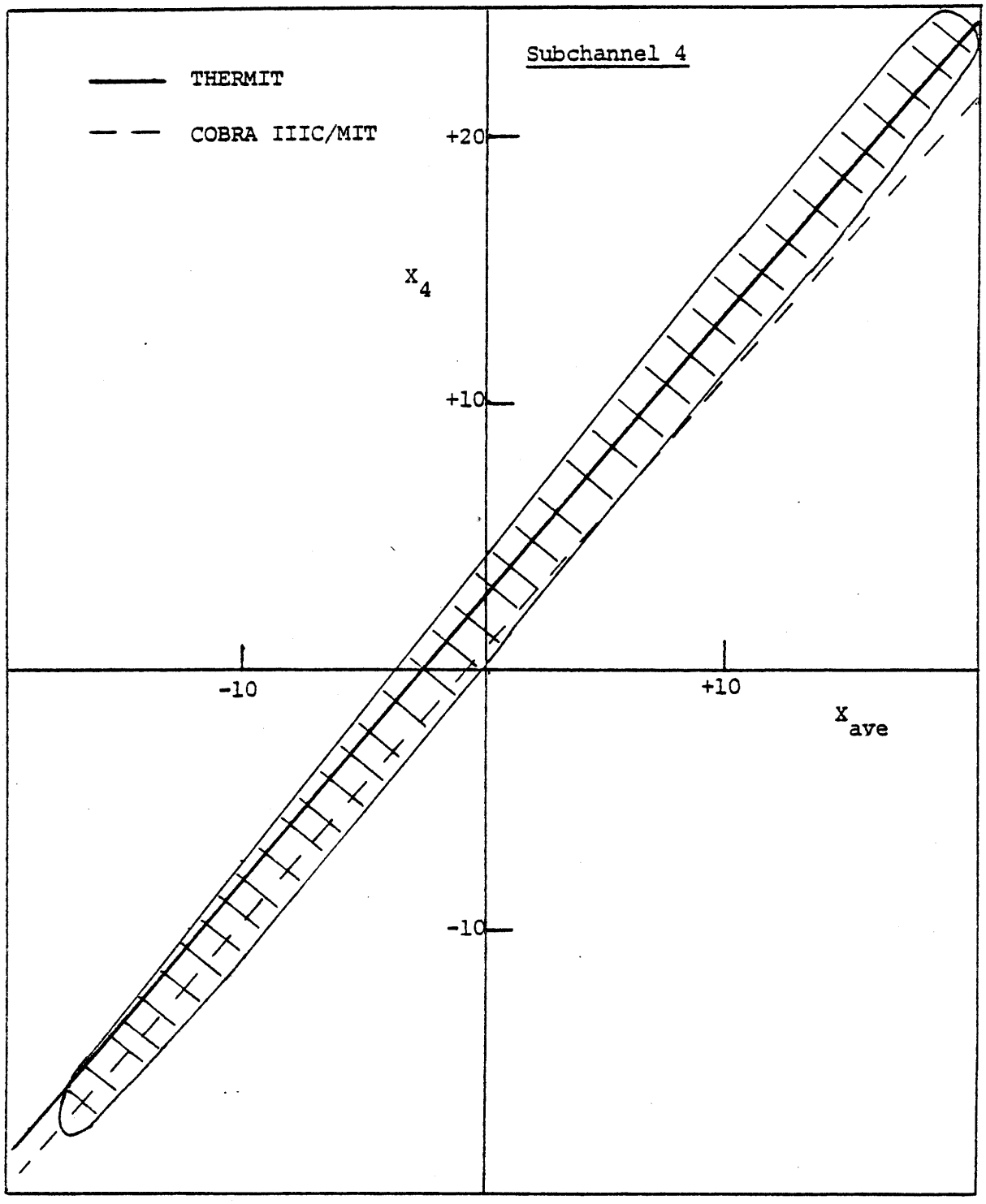

Figure 5.23: Comparison of Measured and Predicted Exit Quality for Subchannel 4 versus Bundle Average Quality - Ispra PWR Tests (COBRA IIIC/MIT Results form Reference 38)

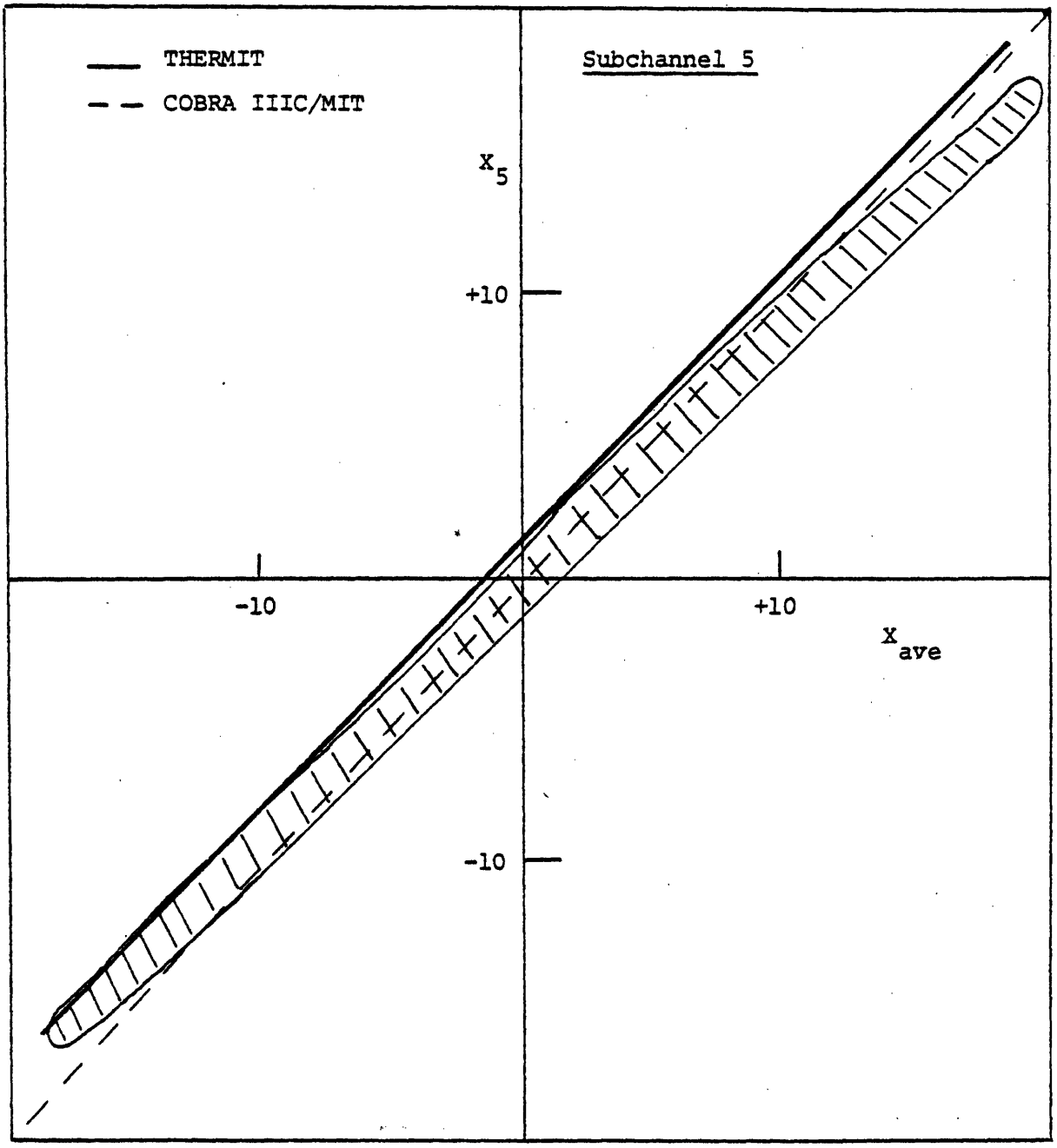

Figure 5.24: Comparison of Measured and Predicted Exit Quality for Subchannel 5 versus Bundle Average Quality - Ispra PWR Tests (COBRA IIIC/MIT Results from Reference 38)

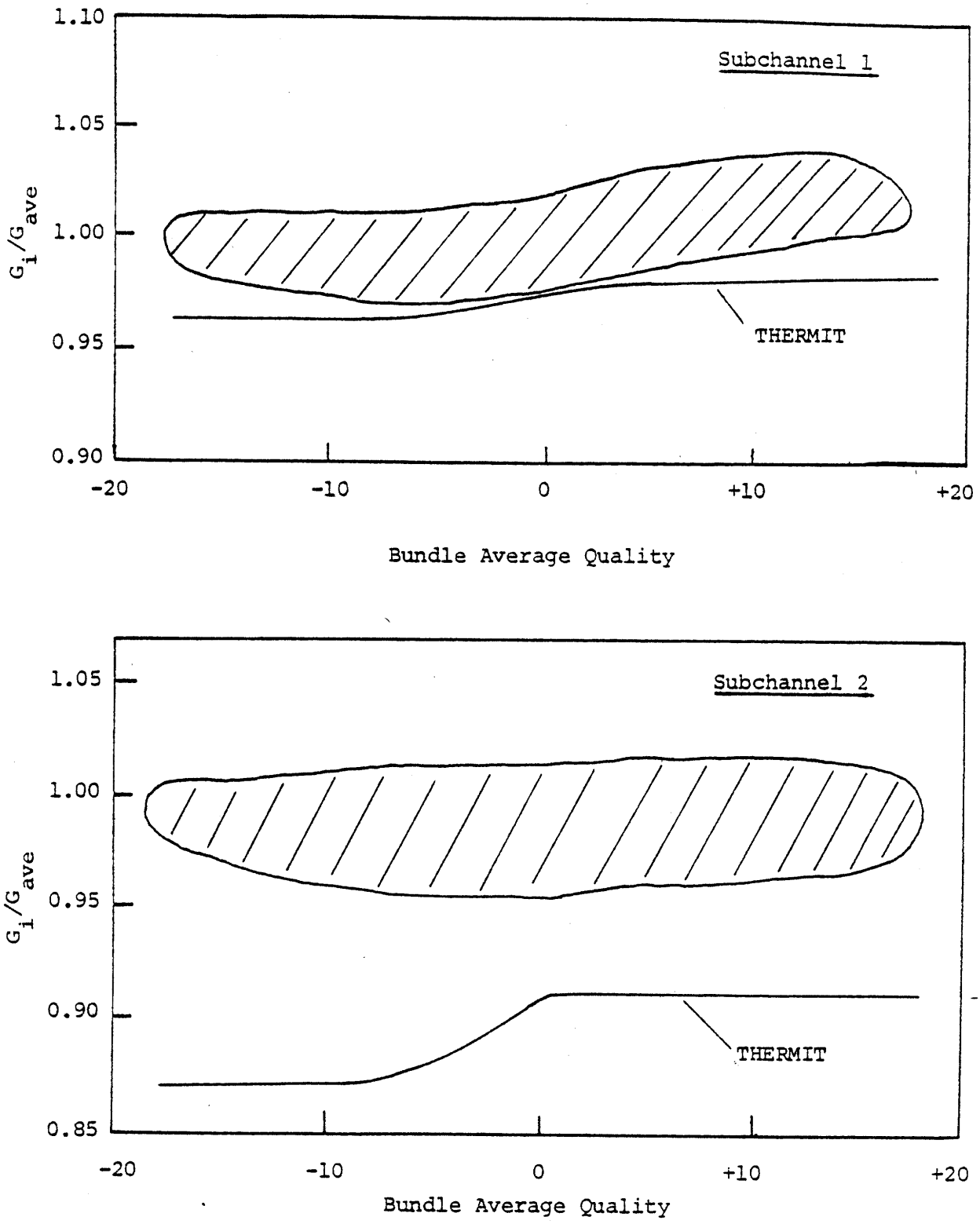

Figure 5.25: Comparison of Measured and Predicted Mass Velocities for Ispra PWR Tests

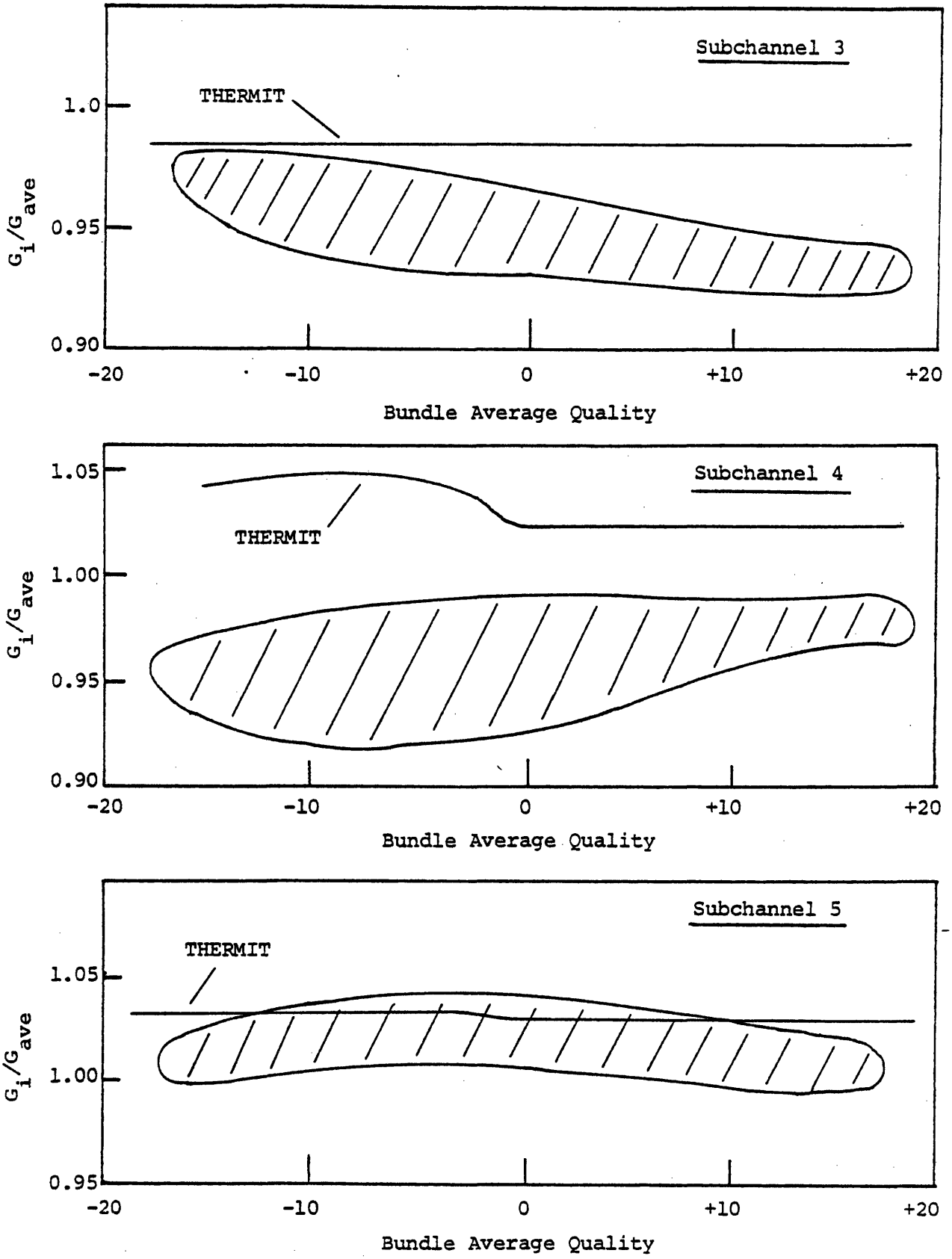

Figure 5.26: Comparison of Measured and Predicted Mass Velocities for Ispra PWR Tests

Consequently, in addition to assessing the two-phase mixing model for PWR conditions, this study has shown that the two-phase mixing model may be used for a wide range of conditions.

5.5 Conclusions

The above discussion of the two-phase mixing model assessment has shown that the current formulation of this model is appropriate for a wide range of conditions. Both BWR and PWR subchannel quality distributions have been successfully predicted. This good agreement includes predicting the lower than average quality in the corner subchannel for BWR conditions as well as predicting the more or less uniform behavior for PWR conditions. It should be emphasized that the same mixing parameters have been used for both types of conditions. Thus, the formulation of the two-phase mixing model seems to be well-founded.

A review of the predicted mass velocity distributions indicates that although, on the whole, the predictions are good, the mass velocity in the corner subchannel for the Ispra tests is usually not well predicted. In the BWR tests the corner mass velocity is overpredicted, while in the PWR tests, it is underpredicted. These deviations cannot be explained in terms of the mixing model so it has been assumed that improper grid modeling may be the cause of the errors. However, it should be reiterated that all mass velocities are usually predicted to within 10% of the measurements which seems to be satisfactory considering the inherent experimental errors.

The variations in the mixing parameters θ_M and K_M have illustrated the dependence of the flow and enthalpy distributions to these parameters. Increases in either θ_M or K_M tend to increase the quality and decrease the

mass velocity in the center subchannels, while decreasing the quality and increasing the mass velocity in the corner subchannels. The predicted distributions are not overly sensitive to these parameters. Therefore, in view of the good agreement over the wide range of conditions studied here, it may be concluded that the two-phase mixing model is appropriate for both BWR and PWR conditions.

6.0 THE HEAT TRANSFER MODEL

6.1 Introduction

Heat transfer from the fuel rod to the coolant not only represents the energy input to the coolant, but also serves as a boundary condition for the fuel rod temperature calculations. In the energy conservation equation, the source term, Q_w, is that due to the rod heat transfer. On the other hand, the solution of the time-dependent heat conduction equation within the fuel rod involves the rod heat transfer as a boundary condition for the temperature profile in the fuel rod.

A fundamental difficulty arises when seeking to model heat transfer phenomena over a wide range of conditions. Typically, heat transfer modeling involves application of empirical correlations to determine the heat transfer coefficient, H, which relates the heat flux q" to the temperature difference between the wall and fluid:

$$q'' = H(T_w - T_f) \tag{6.1}$$

A typical boiling curve, seen in Fig. 6.1, illustrates that the relationship between the heat flux and the temperature difference is very complicated so that the heat transfer coefficient is not a simple function. Nevertheless, for a limited range of application, heat tranfser coefficients can be found and correlated as functions of the flow conditions. Within the limits for which a correlation has been developed, the accuracy of the correlation is generally found to be satisfactory. Therefore, for a given set of flow conditions accurate heat transfer analysis can be performed provided an appropriate heat transfer coefficient is chosen.

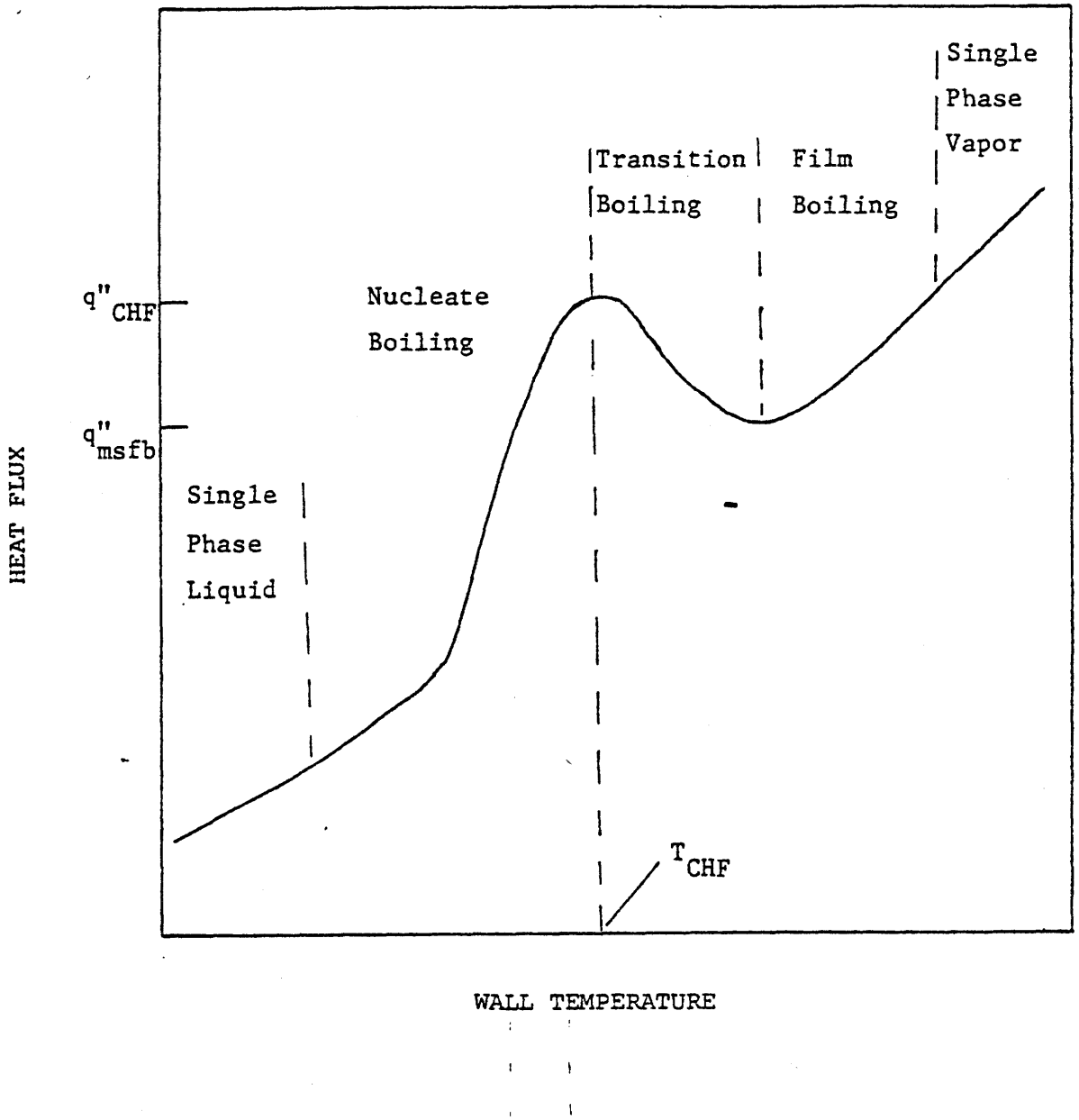

Figure 6.1: Typical Boiling Curve

However, for the wide range of flow conditions which may be anticipated for LWR transients, no one correlation could possibly be accurate over the entire range of conditions. Consequently, this requirement means that the heat transfer model will actually contain a number of correlations which collectively should cover the range of anticipated conditions. However, since these correlations will be used in a computer code, it is necessary that a logical scheme be developed to select the appropriate coefficient for a given set of conditions. Hence, the heat transfer model, also referred to as the heat transfer package, consists of a number of heat transfer correlations and a logic system which dictates the choice for the application.

A heat transfer model, proposed by Bjornard [20], had been originally incorporated into THERMIT. This model, referred to as the BEEST (best estimate) heat transfer package had been developed for PWR blowdown heat transfer analysis. As such, correlations covering high and low pressures, pre-CHF and post-CHF conditions as well as a wide range of anticipated mass velocities have been included. The basic idea behind this model is that a complete boiling curve can be constructed for any location of interest. Then, based on the local flow conditions an appropriate heat transfer coefficient can be selected.

In order to have this ability to construct a complete boiling curve, correlations for all of the anticipated heat transfer regimes must be included. The BEEST model considers five major heat transfer regimes which include forced convection to liquid, nucleate boiling, transition boiling, film boiling and forced convection to the vapor. Within each of these regimes, except transition boiling, further division can be made depending on the flow conditions so that a total of ten regimes are

actually modeled (see Table 6.1 for summary of heat transfer correlations).

The other important feature of the BEEST model is its heat transfer regime selection system. This system uses local instantaneous values for the flow as input to the selection scheme. As illustrated in Fig. 6.2, there are four main checks used in the selection system. First, if the quality is greater than 0.99, then single-phase vapor heat transfer is assumed. Second, if the wall temperature is less than the saturation temperature, no boiling can occur so that single-phase liquid heat transfer is assumed. For conditions between the first two checks, that is two-phase flow conditions, the two remaining checks compare the wall temperature to the minimum stable film boiling temperature, T_{msfb}, and the critical heat flux temperature, T_{CHF}. If the wall temperature is greater than T_{msfb}, then film boiling is assumed. If the wall temperature is less than T_{CHF}, then nucleate boiling is assumed. For wall temperatures between T_{msfb} and T_{CHF} transition boiling is assumed. Thus, the selection system is simple and computationally efficient.

However, as stated before, the BEEST package had originally been developed for PWR blowdown heat transfer analysis. As such the assumptions and simplifications that were made in developing the model may not be appropriate for non-blowdown transients which are the primary focus of the present work. Hence, the heat transfer model has been assessed for conditions of interest, primarily by comparisons with experimental data. This assessment has led to modifications in both the correlations and the heat transfer regime selection system. These modifications are discussed in the next section. Following this, the results of the steady-state and transient comparisons with experimental measurements are presented in Section 6.3.

TABLE 6.1

Summary of Heat Transfer Correlations

Regime	Correlation
1. Forced convection to single-phase liquid	Sieder-Tate
2. Natural convection to single-phase liquid	McAdams
3. Subcooled boiling	Chen
4. Nucleate boiling	Chen
5. Transition boiling	Interpolation between q_{CHF} and q_{msfb}
6. High P, high G film boiling	Groeneveld 5.7*
7. Low P, high G film boiling	Modified Dittus-Boelter*
8. Low x film boiling	Modified Bromley
9. Forced convection to single-phase vapor	Sieder-Tate
10. Natural convection to single phase vapor	McAdams
Regime Checkpoints	**Correlation**
1. Critical Heat Flux	Biasi, W-3**, CISE-4** Bowring**, Barnett**, Hench-Levy**
2. Minimum Stable Film Boiling Temperature	Henry
3. Slug-Annular Transition	Wallis**

* Correlation deleted in this research
** Correlation added in this research

Figure 6.2 BEEST Heat Transfer Logic

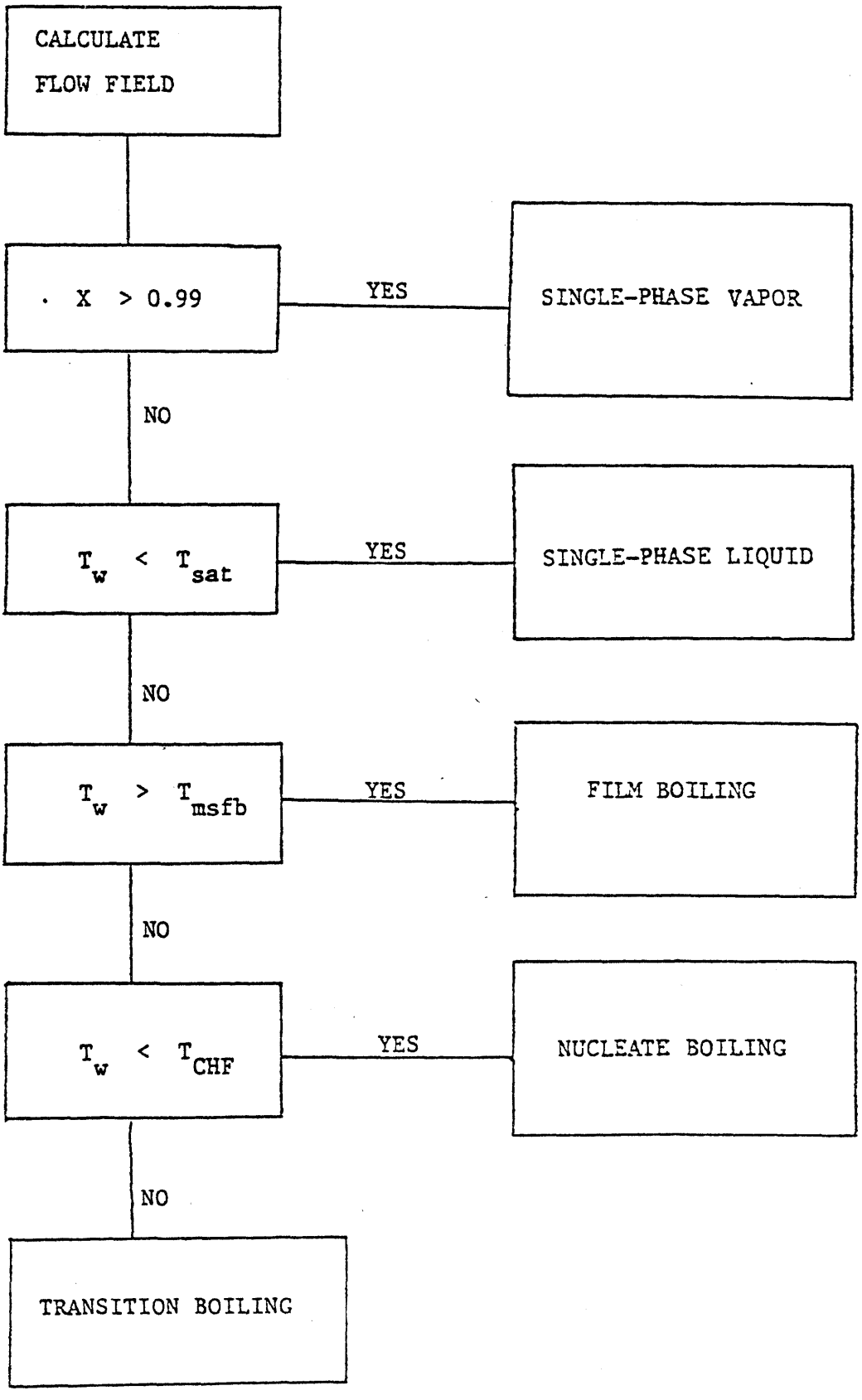

6.2 Modifications

6.2.1 Critical Heat Flux Conditions

In reviewing the BEEST heat transfer model, two major simplifications were found not to be strictly valid for steady-state and non-blowdown transient conditions. The first simplification concerns the treatment of the CHF calculation. In the BEEST model only the Biasi [55] correlation had been included for CHF predictions. The selection of the Biasi correlation for blowdown applications was based on the fact that this correlation has a data base which covers a wide range of pressures and includes both upflow and downflow conditions. This correlation is a "dry-out" CHF correlation which is consistent with the expected CHF mechanism during a blowdown. Hence, the Biasi correlation seemed well-suited for blowdown conditions.

In steady state as well as for transients at high pressure, it is more appropriate to consider a heat transfer regime map constructed on a heat flux-versus-quality plane. Figure 6.3 illustrates the different heat transfer regimes encountered in forced convective boiling as functions of heat flux and quality. As shown, heat transfer in forced convective boiling can be divided into two regions, one in which liquid wets the heated wall and the second in which the liquid is prevented from continuous contact with the heated wall by vapor. The transition from the first to the second region is characterized by the critical heat flux (CHF) line. There are two possible mechanisms leading to the occurrence of critical heat flux. At low quality, CHF is due to the departure from nucleate boiling (DNB). At high quality, CHF is due to cessation of annular flow when the liquid film on the wall disappears due to evaporation and entrainment; it is referred to as dryout. In Figure 6.3, Line A-B-C

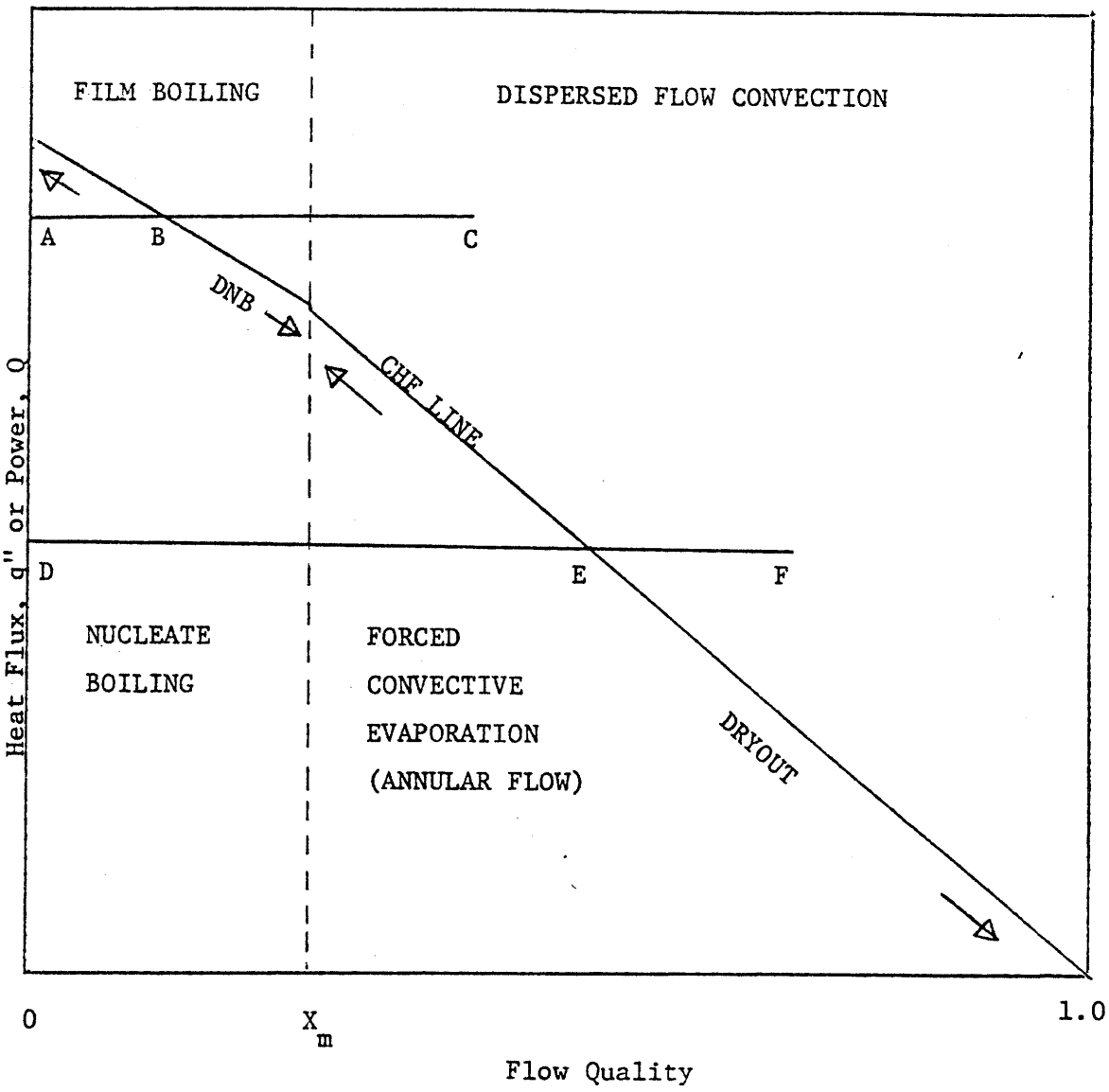

Figure 6.3 Two-Phase Heat Transfer Map in Forced Convective Boiling

corresponds to the DNB-type CHF (Point B), and Line D-E-F corresponds to the dryout-type CHF (Point E). Consequently the Biasi correlation alone would not be sufficient to analyze all the anticipated flow conditions considered in this work. The CHF predictive capability has been improved by adding new correlations to the heat transfer package, as will be discussed in Section 6.2.4 and Chapter 7.

6.2.2 Pre-CHF Boiling Heat Transfer

The possible heat transfer mechanism in the pre-CHF boiling flow are subcooled and saturated nucleate boiling, and annular forced convective boiling (or evaporation). As discussed by Lahey and Moody [25], the form of the nucleate boiling correlation may be given as

$$q'' = K(T_w - T_s)^m \tag{6.2}$$

where K is usually a pressure dependent constant. For the three correlations here, the values for m are

$m = 4$ Jens-Lottes

$m = 2$ Thom

$m = 0.99$ Chen

However, only the Chen correlation covers both saturated and subcooled boiling as well as annular convective boiling; moreover, it is applicable for a wide range of flow rates; therefore, the Chen correlation is used for pre-CHF boiling heat transfer in the present model.

6.2.3 Post-CHF Heat Transfer

The second major simplification in the BEEST model concerns the dispersed flow convection. The BEEST heat transfer package uses heat transfer correlations based on liquid vapor thermal-equilibrium conditions. As discussed previously, thermal non-equilibrium in the dispersed flow regime may be significant. Modifications have been made to the heat transfer selection scheme so that in the dispersed flow regime wall transfers heat only to the vapor phase.

All light water reactors are designed such that critical heat flux will not be encountered during normal operating conditions. But, in the lifetime of a nuclear power plant it may be hypothesized that an accident may occur such that critical heat flux will be exceeded in the reactor core, and may have the potential of causing damage to the fuel elements. In an event of LOCA or anticipated transient in which CHF has been exceeded, the accurate prediction of fuel-center-line-melt depends on the accuracy of the predicted post-CHF heat transfer coefficient which is required in the calculation as a boundary condition. Furthermore, in PWR once through steam generators, post-CHF heat transfer is an important heat transfer mechanism. Therefore, an accurate prediction of post-CHF heat transfer is of great interest for both the reactor safety application and the design of steam generators.

As illustrated in Figure 6.3, the post-CHF heat transfer may be categorized into film boiling and dispersed flow convection. At high qualities, post-CHF heat transfer is that of dispersed flow. At low qualities or subcooled conditions, film boiling occurs just downstream of DNB. As quality increases, film boiling gradually transforms into dispersed flow. Although transition boiling may occur under certain conditions,

generally more conservative estimates are obtained if one chooses to neglect transition boiling, which occurs over a short axial length.

6.2.3.a Dispersed Flow Heat Transfer

In dispersed flow, the wall is cooled primarily by vapor. The contribution from the entrained droplets is negligible, as reported by Iloeje et al., [65]. Thus, most of the heat from the wall is consumed in superheating the vapor next to the wall, and only part of that heat is transferred from the vapor to evaporating the liquid droplets. The degree of thermal non-equilibrium (vapor superheat) depends on the flow rate--the higher the flow rate, the more effective is the heat transfer between the liquid droplets and the vapor continuum. Conversely, if the flow rate is low, the interfacial heat transfer is less efficient; hence, thermal non-equilibrium is more pronounced.

Historically, three types of dispersed flow heat transfer models can be found in the literature: i) thermal equilibrium model, ii) frozen quality model and iii) thermal non-equilibrium model.

i) Thermal equilibrium model

This type of correlation is purely empirical based on the single phase heat transfer correlation of Dittus-Boelter as applied to vapor, but contains corrections for the presence of liquid in the flow. The assumption of thermal equilibrium of vapor and liquid does not agree with experimental findings [66]; except at high flow where the liquid-vapor heat exchange is efficient, and near the dryout location where the vapor does not have sufficient time to become superheated. Heat transfer correlations of this model are Groeneveld 5.7 [67] and Bishop [68] correlations.

ii) Frozen quality model

In the frozen quality assumption it is assumed that no evaporation takes place, and that heat is absorbed by vapor only. The no evaporation assumption leads to overprediction of the degree of vapor superheat in the post-dryout regime except at very low flows where liquid droplet-vapor heat exchange is very inefficient. This assumption was first investigated by Bennett [39].

iii) Thermal non-equilibrium models

The models assuming thermal non-equilibrium lie in between the above two extremes of very efficient and very inefficient vapor-liquid heat transfer. The models were initially developed by Laverty and Rohsenow [69] at MIT. Later, similar models varying in degree of theoretical treatment have been suggested by Forslund and Rohsenow [88], (1966), Bennett et al. [39], (1967), Hynek et al. [71], (1969), Plummer et al. [65], (1974), Groeneveld and Delmorme [70], (1976), Jones and Zuber [72], (1977), Saha et al. [73], (1977) and Yoder [74], (1980). The Γ correlation of Saha et al. has been adopted by the two-fluid code THERMIT. In the thermal non-equilibrium model, it is assumed that the heat flux from the wall is absorbed by the vapor. A semi-empirical correlation is used to describe the heat transfer rate between the vapor and the liquid. The key parameter for successful prediction of thermal non-equilibrium in dispersed flow is the determination of actual vapor flow quality, which, with the appropriate interfacial energy and momentum equations and a suitable single-phase vapor heat transfer correlation, for a given wall heat flux, determines the temperature drop between the wall and the vapor, $T_w - T_v$. The Sieder-Tate single-phase vapor forced convection correlation [75] has been applied in THERMIT-2.

6.2.3.b Film Boiling Heat Transfer

Film boiling in forced convective boiling occurs in subcooled or low quality conditions. Visual observations have shown that during film boiling a thin vapor film is formed between the heated wall and the liquid. Bubbles released from the vapor film are carried away by the liquid; thus, the vapor-liquid interface appears to be irregular. At low flow or pool boiling, it is assumed that vapor film flow is laminar, that negligible interfacial shear stresses occur, and that the intervals at which bubble columns are released from the film, depending on the orientation, obeys Taylor or Helmholtz instability. These assumptions are the bases for the well-known pool film boiling correlations of Bromley [76] and Berenson [77]. However, at higher low, the film flow becomes turbulent. As the quality increases, the liquid becomes hydrodynamically unstable, and the regime is transformed into dispersed flow.

In the present heat transfer model the following approach, which combines the Bromley [76] film boiling and the Sieder-Tate [75] vapor forced convection, is used to describe low quality film boiling:

$$h_{FB} = (1 - \alpha)h_{Bromley} + \alpha h_{S-T} \qquad (6.3)$$

This correlation is used as long as the quality $x < x_m$ (See Fig. 6.4). Otherwise, the dispersed flow heat transfer is assumed.

6.2.4 Transition Boiling Heat Transfer

At the onset of flow film boiling, an unstable mix of nucleate and film boiling is sometimes observed. In THERMIT-2, it is assumed (as in BEEST) that transition boiling is composed of both nucleate and film boiling. As shown in Fig. 6.1, transition boiling heat transfer is bounded between CHF and MSFB, hence; it is assumed to be the sum of the weighted contribution

from q''_{CHF} and q''_{MSFB}:

$$q''_{TB} = \varepsilon q''_{CHF} + (1-\varepsilon)\ q''_{MSFB} \tag{6.4}$$

where $$\varepsilon = ((T_w - T_{MSFB})/(T_{CHF} - T_{MSFB}))^2$$

However, the transition from nucleate boiling to stable film boiling usually occurs in a very short period of time. Therefore, in steady-state conditions, transition boiling can be ignored in light-water-reactor applications.

6.2.5 Heat Transfer Regime Selection Logic

In light of the above discussion, a new heat transfer regime selection logic has been developed for application in the two fluid code THERMIT-2. The logic is applicable for steady-state and non-blowdown transient analyses in light water reactors. The major modifications are: 1) replacement of post-CHF two-phase mixture heat transfer correlations with single-phase vapor correlations, 2) elimination of transition boiling heat transfer in steady state applications, and 3) addition of CHF correlations for BWR and PWR conditions. The new heat transfer regime selection logic and the interfacial mass and energy constitutive relations of the two fluid model, together allow for thermal non-equilibrium in the post-CHF regimes. The new heat transfer model also extends CHF predictability to rod bundles in PWR and BWR conditions.

In the present two-fluid heat transfer model, it is suggested that the transition boiling heat transfer can be neglected in steady state. As such, it is not necessary to calculate T_{CHF} and T_{MSFB} at each location and instance in time. However, more CHF correlations are needed for the prediction of departure from nucleate boiling (DNB) as well as CHF in

rod bundles. Since Biasi is only applicable for predictions of dryout in tubes, W-3 [78], CISE-4 [57], Barnett [79], Hench-Levy [80], and Bowring [81] CHF correlations have been included. W-3 is a DNB-type CHF correlation intended for low quality and subcooled conditions. CISE-4, Barnett, Hench-Levy, and Bowring are high quality dryout type CHF correlations. Among these CHF correlations, W-3, Barnett, and Hench-Levy have been developed for use in rod bundles. Assessment of these CHF correlations with the two fluid code THERMIT-2 is discussed in Chapter 7.

The selection logic of the present heat transfer model is illustrated in Figure 6.4. The model uses the Wallis slug-annular transition criteria to determine the boundary between the DNB-type and dryout-type CHF. The Wallis criteria can be solved for the flow quality x_m to give

$$X_m = \frac{0.4(\rho_\ell D_e \Delta\rho)^{\frac{1}{2}} + 0.6\ G}{G((\rho_\ell/\rho_g)^{\frac{1}{2}} + 0.6)} \tag{6.5}$$

This implies that it is assumed that DNB occurs only in nucleate boiling regimes and dryout occurs only in annular flow regime. If the flow quality, x, is below the transition quality, x_m, the DNB-type CHF correlation of W-3 is automatically used to check whether DNB has been exceeded or not. However, this is done only for pressures greater than or equal to 6.9 MPa, due to the limitation of the W-3 correlation. Otherwise, CHF is checked by any of the six CHF correlations available to the user. Once CHF has been exceeded, the dispersed-flow or film boiling heat transfer regime is assumed. The Chen correlation is used for both saturated and subcooled pre-CHF boiling.

In transient conditions, the selection logic follows that of BEEST (Fig. 6.5); except that the Wallis criteria is used as a check to

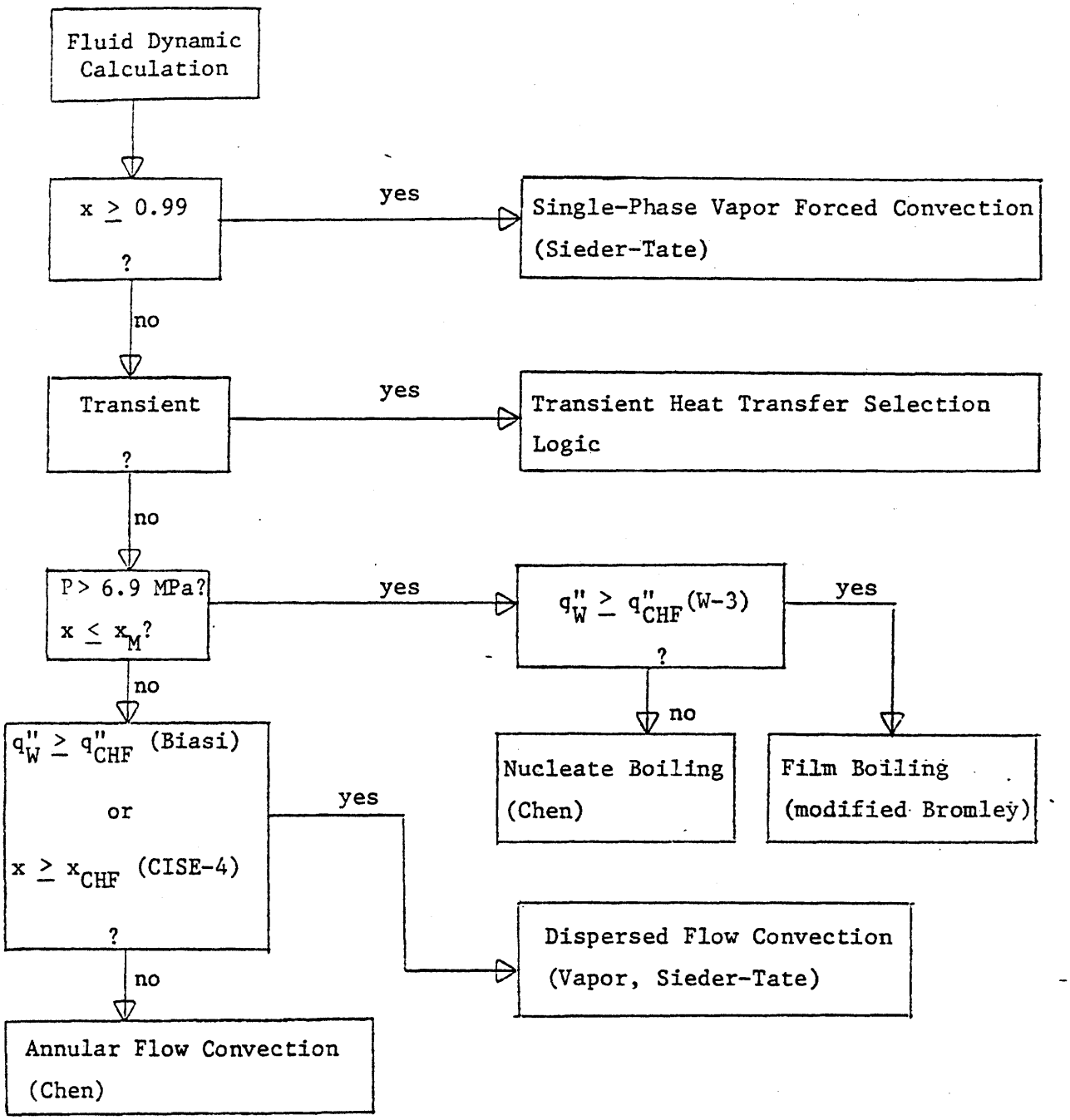

Figure 6.4 Steady State Heat Transfer Regime Selection Logic

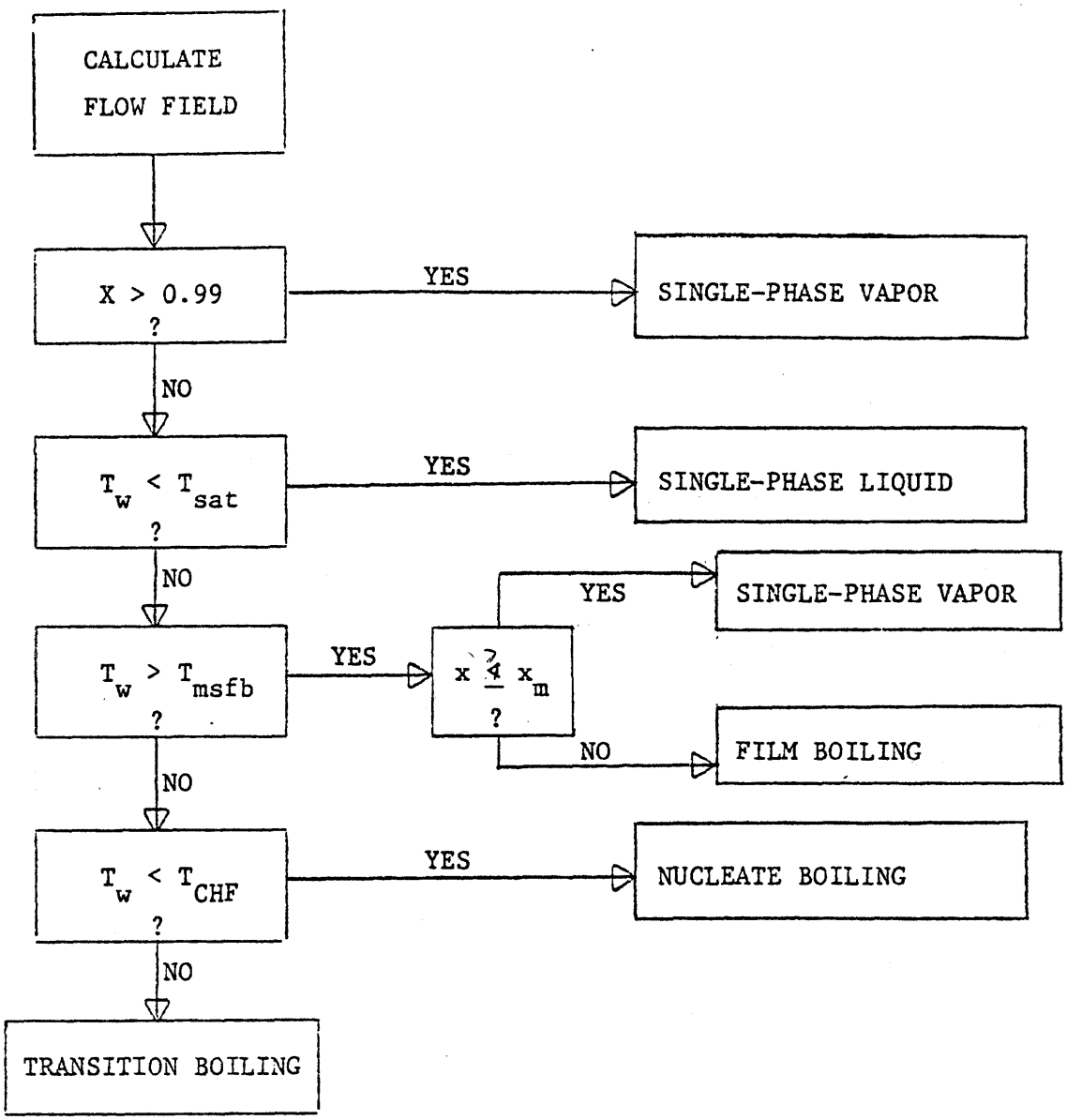

Figure 6.5 Transient Heat Transfer Regime Selection Logic

distinguish film boiling from dispersed flow convection. As previously stated, transition boiling is bypassed for LWR steady state LWR condition.

6.3 Assessment

The overall model as described above has been assessed by making comparisons with both steady-state and transient measurements. The purpose of this effort has been to identify the reliability of the predictions of this model.

Two different sets of experimental measurements have been used in this study. The first set is the Bennett [39] test measurements while the second is the G.E. transient CHF measurements in a 9-rod bundle [39]. The Bennett tests, already discussed in connection with the verification of the droplet vaporization model, are steady-state measurements in which CHF occurs at locations upstream of the exit. Since wall temperature measurements were made along the entire heated length, both pre-CHF and post-CHF measurements are available. Consequently, this data is well-suited for evaluating the entire heat transfer model for steady-state conditions.

The second set of measurements used in this study are the G.E. transient CHF test data. In these tests, simulated BWR fuel rods are subjected to a variety of flow transients with the time and location of the critical heat flux being measured. This data allows for the CHF predictive capability to be evaluated for transient conditions.

Together, these two sets of experimental measurements permit the assessment of the main features of the heat transfer model. The steady-state results are discussed in this Section while the transient results are discussed in Chapter 7.

The Bennett tests have been used to assess the THERMIT heat transfer model for steady-state conditions. In these tests, wall temperature measurements have been made along vertically heated tubes having lengths of either 3.6m or 5.5m. A wide range of conditions have been covered in these tests as summarized in Table 6.2.

Both pre-CHF and post-CHF temperatures have been measured with typical data illustrated in Fig. 6.6. There are two distinguishing regimes in this figure which can be identified. The first is the pre-CHF regime which extends from the inlet to the CHF location. In this regime, the heat transfer mechanism is predominantly the nucleate boiling type so that measurements in this regime can be used to assess the nucleate boiling heat transfer correlation in THERMIT. The second regime is the post-CHF regime. As discussed in Section 4.3.3, the wall temperatures in this regime are utilized to assess the droplet vaporization model which, strictly speaking, prevents independent validation of the heat transfer correlations. However, the appropriateness of the correlations in this regime can still be assessed. Between the two regimes lies the CHF location. Due to the obvious location of this point, it is rather easy to assess the CHF correlations using this data.

In view of the nature of the data, the assessment effort has been divided into two categories:

(1) pre-CHF regime assessment

(2) post-CHF regime assessment.

6.3.1 Pre-CHF Heat Transfer Assessment

For the pre-CHF regime, the comparisons have indicated that THERMIT consistently overpredicts the wall temperatures when using the Chen correlation [59]. This behavior is illustrated in Figures 6.7 to 6.11.

TABLE 6.2

Bennett Test Conditions for CHF in Tubes

Outlet Pressure	6.9 MPa
Diameter	12.6 mm
Mass Velocity	664 to 5180 $kg/m^2 \cdot s$
Heat Flux	0.56 to 1.77 MW/m^2
Inlet Subcooling	72 to 146 kJ/kg
Tube Length	3.66 and 5.56 m

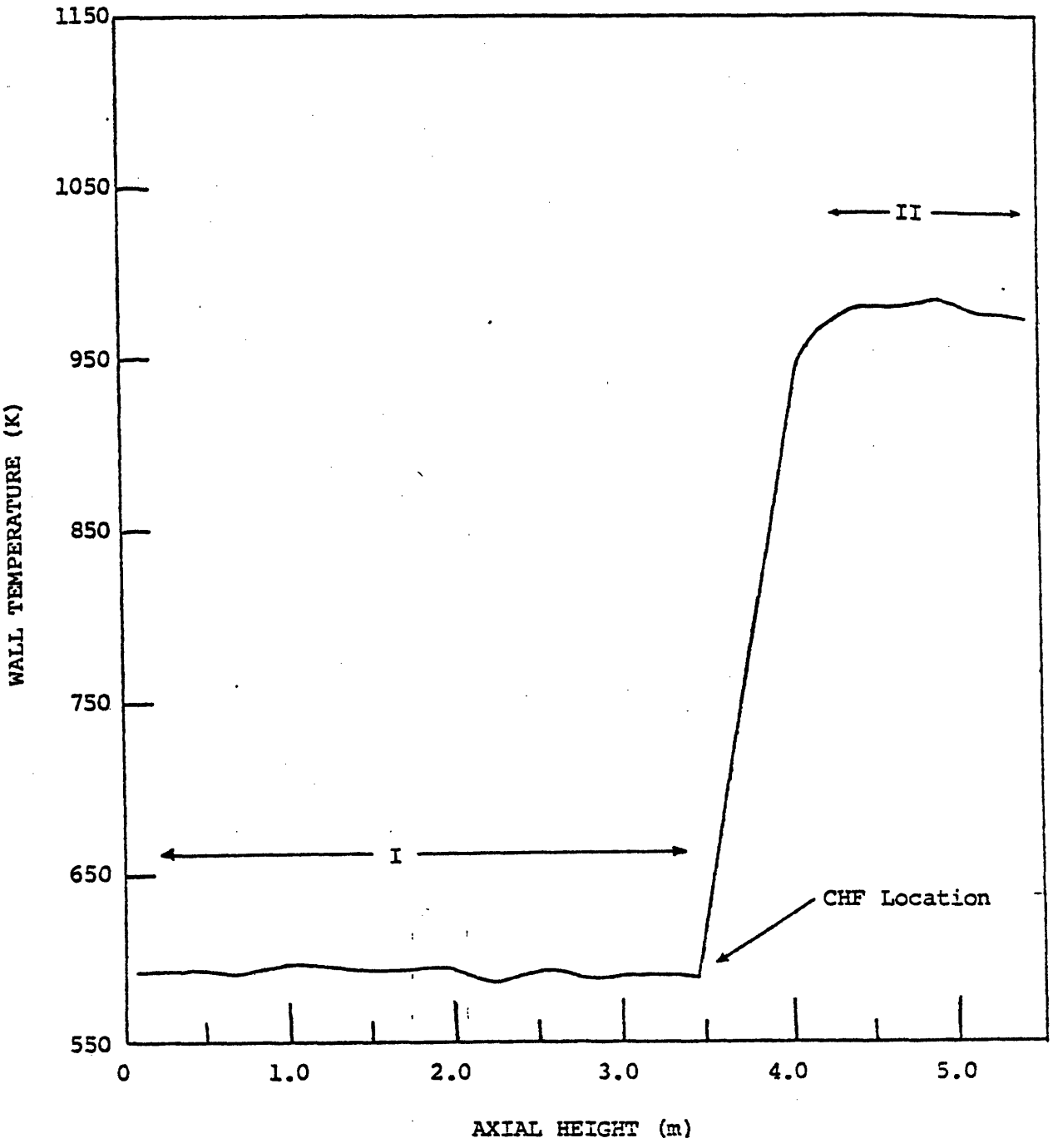

Figure 6.6: Typical Wall Temperature Distribution for Bennett Case 5273

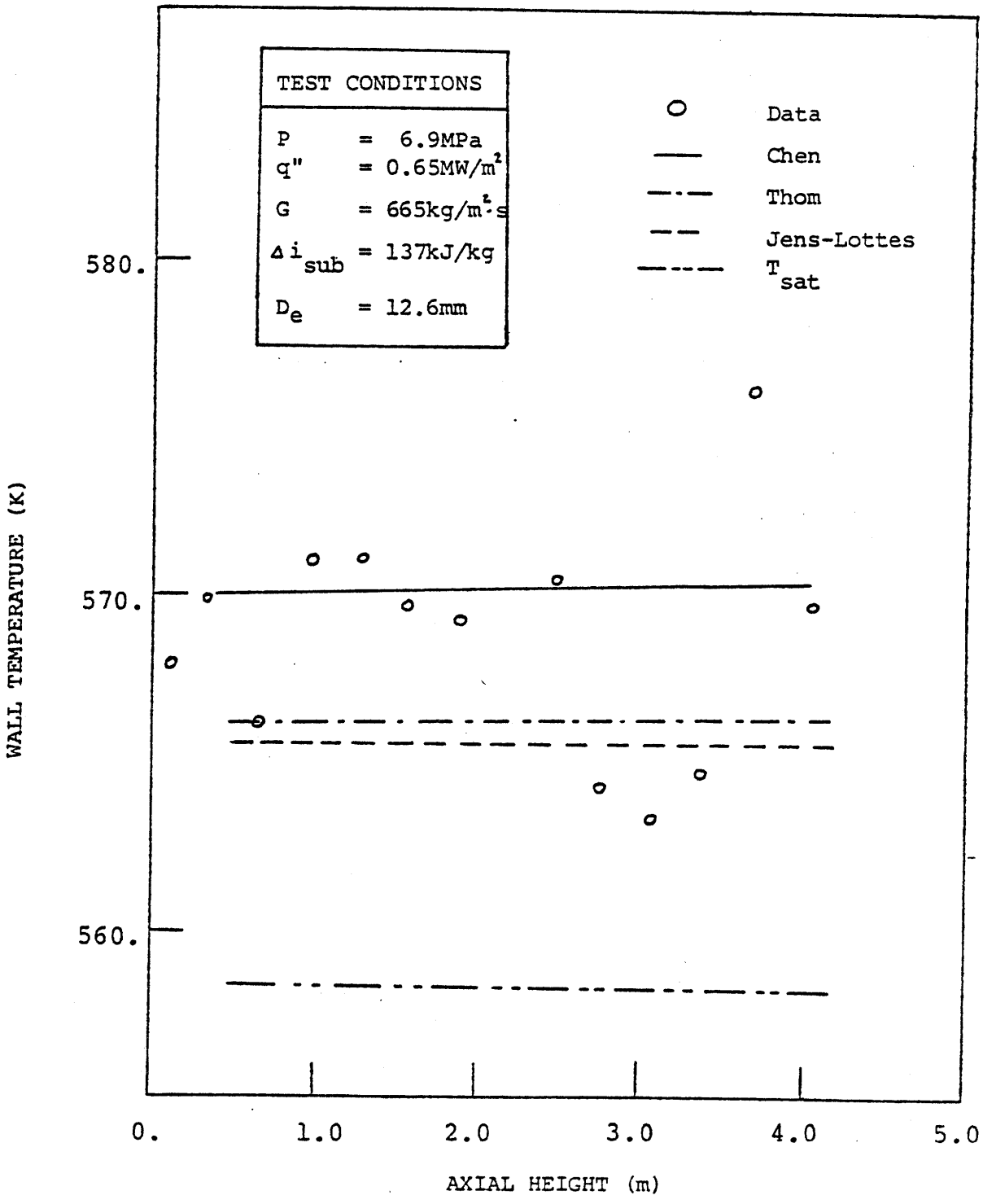

Figure 6.7: Comparison of Measured and Predicted Pre-CHF Wall Temperatures for Bennett Case 5332

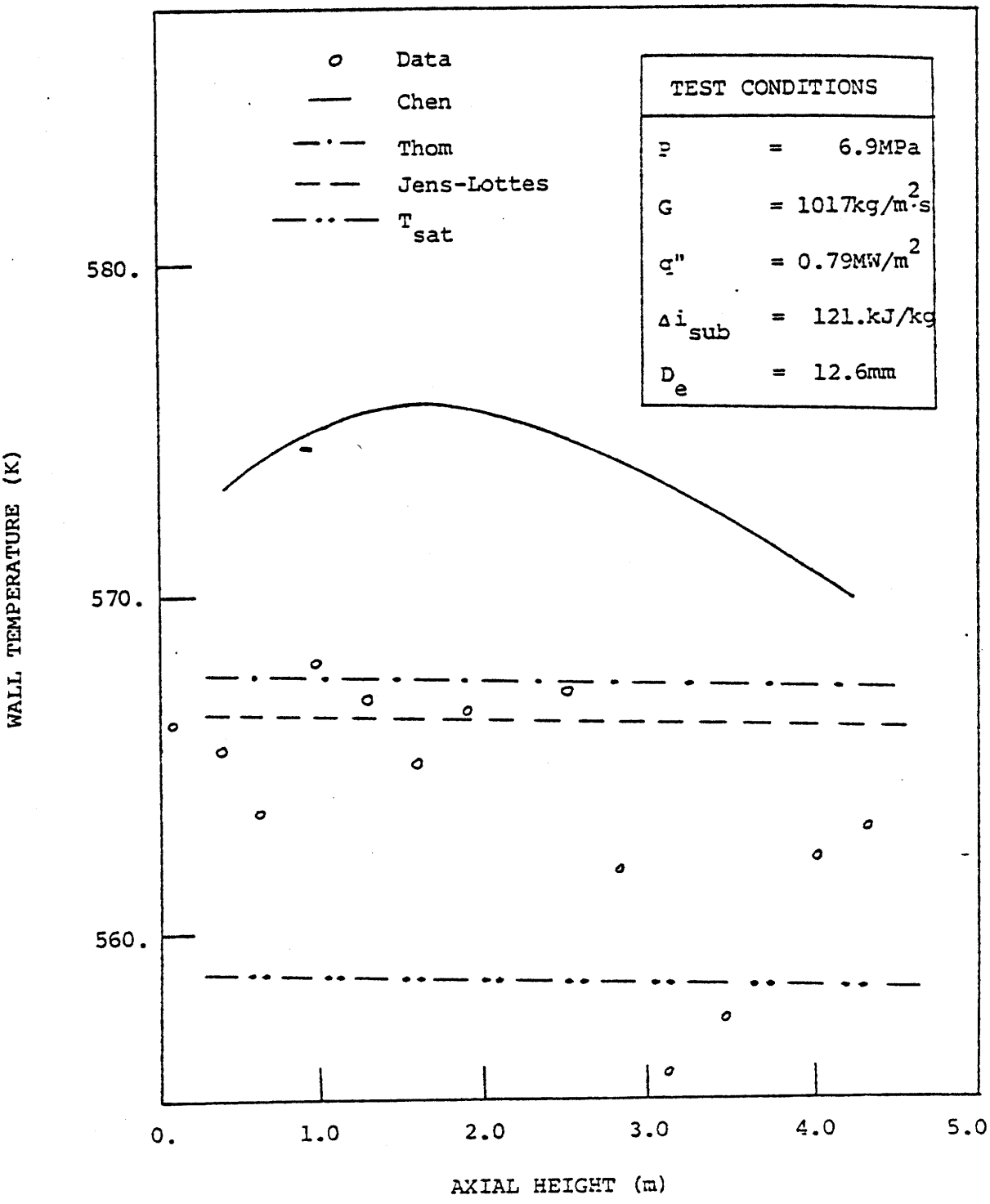

Figure 6.8: Comparison of Measured and Predicted Pre-CHF Wall Temperatures for Bennett Case 5276

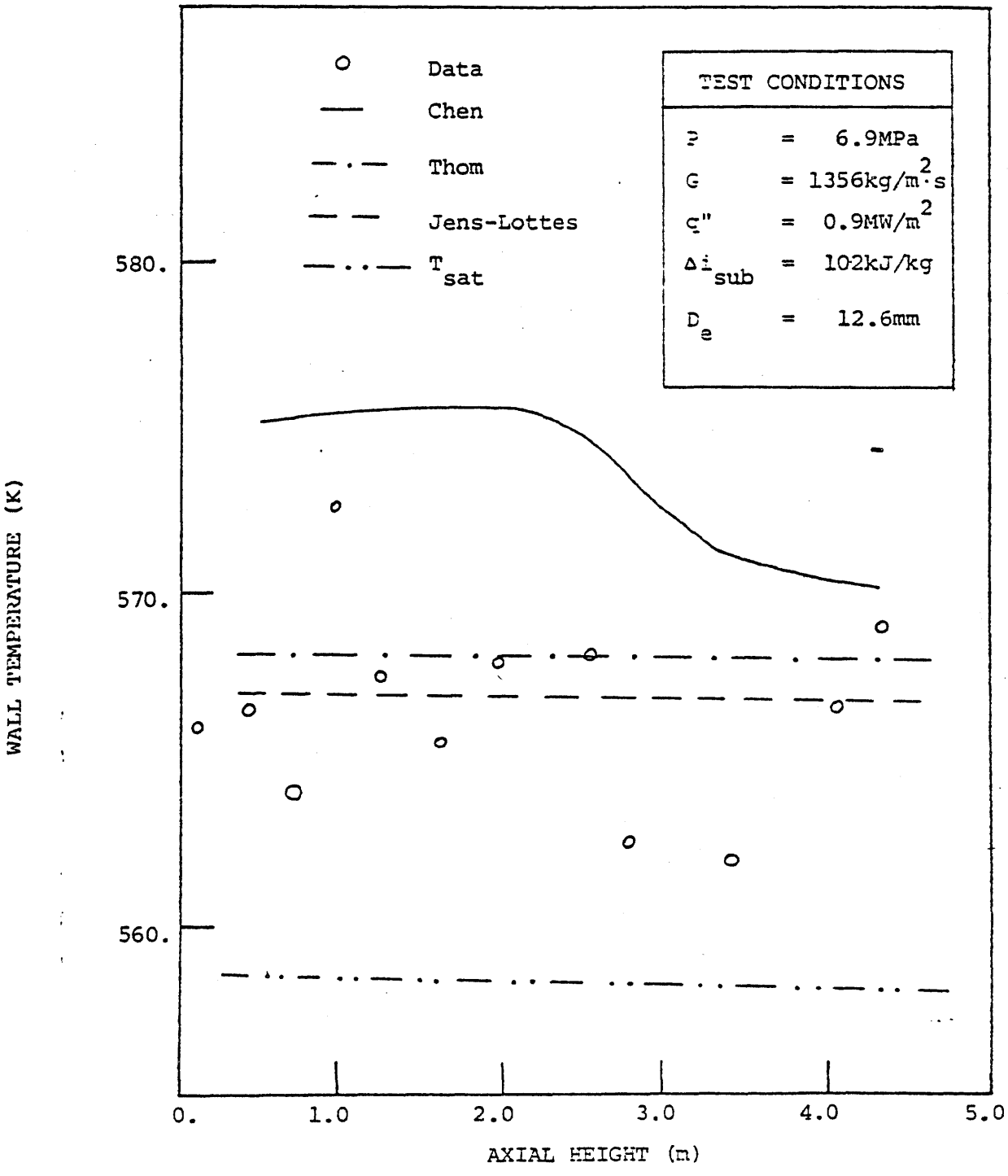

Figure 6.9: Comparison of Measured and Predicted Pre-CHF Wall Temperatures for Bennett Case 5253

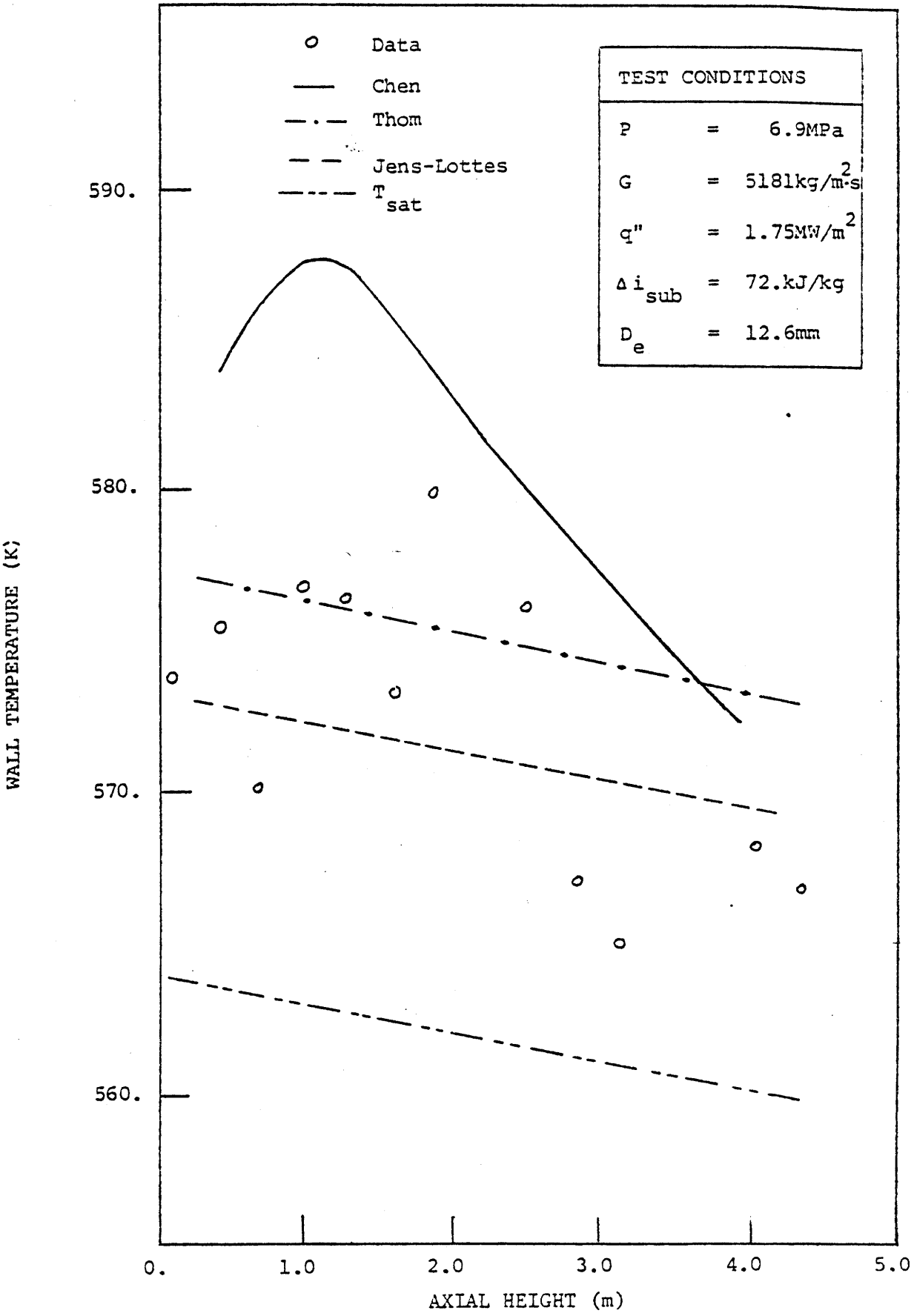

Figure 6.10: Comparison of Measured and Predicted Pre-CHF Wall Temperatures for Bennett Case 5394

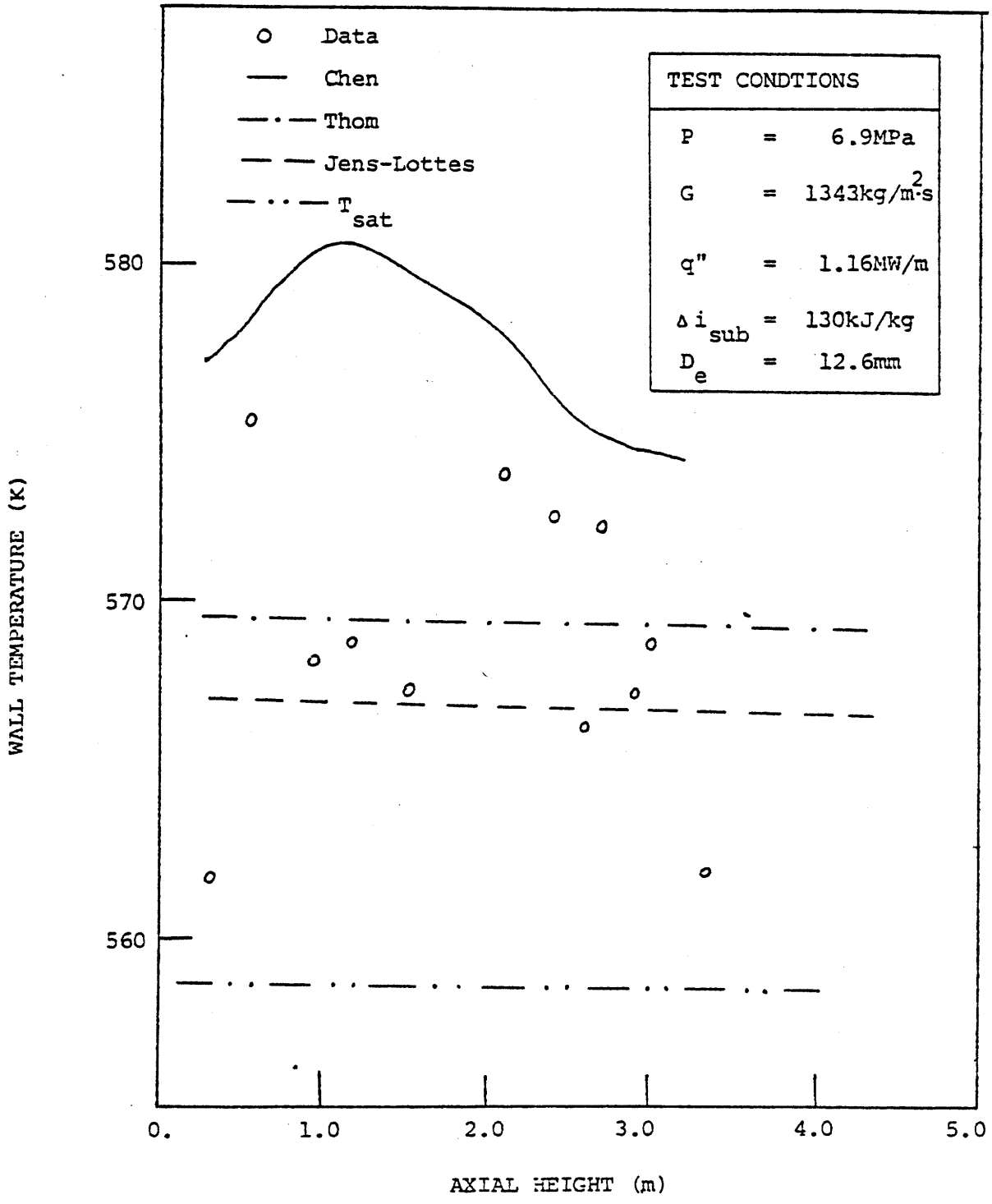

Figure 6.11: Comparison of Measured and Predicted Pre-CHF Wall Temperatures for Bennett Case 5451 (Length = 3.66m)

It is seen that, except for the lower heat flux case, the wall temperatures are typically overpredicted by 10K. This overprediction indicates that the Chen heat transfer coefficient is too low for these cases.

However, it should be noted that there is considerable scatter in the data and no error analysis is reported for these measurements. Some data points are obviously in error (for example those below the saturation temperature) and the fluctuations from one point to the next are physically too large. Two features of this experiment may account for these observations. First, the primary intent of these experiments was to measure post-CHF temperatures, so that there was little emphasis on accurately measuring the pre-CHF temperatures. Second, the thermocouples were placed on the outside of the tube. Consequently, the inside wall temperatures were not directly measured, but were calculated. These two features of the experiment may account for the relatively poor data for the pre-CHF conditions.

The above cases have also been reanalyzed using two other heat transfer correlations. For this study the Thom correlation [60] and the Jens-Lottes correlation [61] have been used. Both of these correlations are nucleate boiling correlations, while the Chen correlation is a combination of a forced convection vaporization and nucleate boiling correlation.

One final observation can be made for these comparisons. While the Thom and Jens-Lottes correlations show linear temperature profiles, the Chen correlation temperature distribution shows an initial increase to a maximum followed by a decrease. This behavior illustrates the influence of the forced convection vaporization. As the quality is increased, the

liquid film on the wall decreases and the more efficient forced convection vaporization heat transfer mechanism begins to dominate. The heat transfer coefficient for this regime is higher than the nucleate boiling coefficient so that the wall temperatures decrease. The predicted trend is seen very clearly in Fig. 6.10. Only the Chen correlation is able to predict this trend.

6.3.2 Post-CHF Heat Transfer Assessment

The post-CHF experimental data of Bennett are used for post-CHF heat transfer assessment also. In the two-fluid formulation, dispersed-flow convective heat transfer depends on the interfacial energy, mass, and momentum exchange models as well as the wall-vapor film heat transfer correlation. No single model can be assessed independently. In order to predict the wall temperature, the heat transfer coefficient and the vapor film temperature must be determined. Although, the heat transfer coefficient can be given by a correlation, the determination of the vapor temperature depends on the interfacial energy, mass and momentum exchange models. In THERMIT-2, the mass exchange model is based on the Saha correlation, and the interfacial energy and momentum exchange models are introduced in Chapter 4. The wall to vapor heat transfer is given by the Sieder-Tate correlation.

The cases studied are shown in Figures 6.12 to 6.14. As seen, the predictions are in very reasonable agreement with the experiments. Since the dryout position is somewhat underpredicted (by the CPR correlation CISE-4), the position of dryout is corrected to match the experimentally observed position. It should also be pointed out that the present model does not account for heat transfer due to radiation and droplet

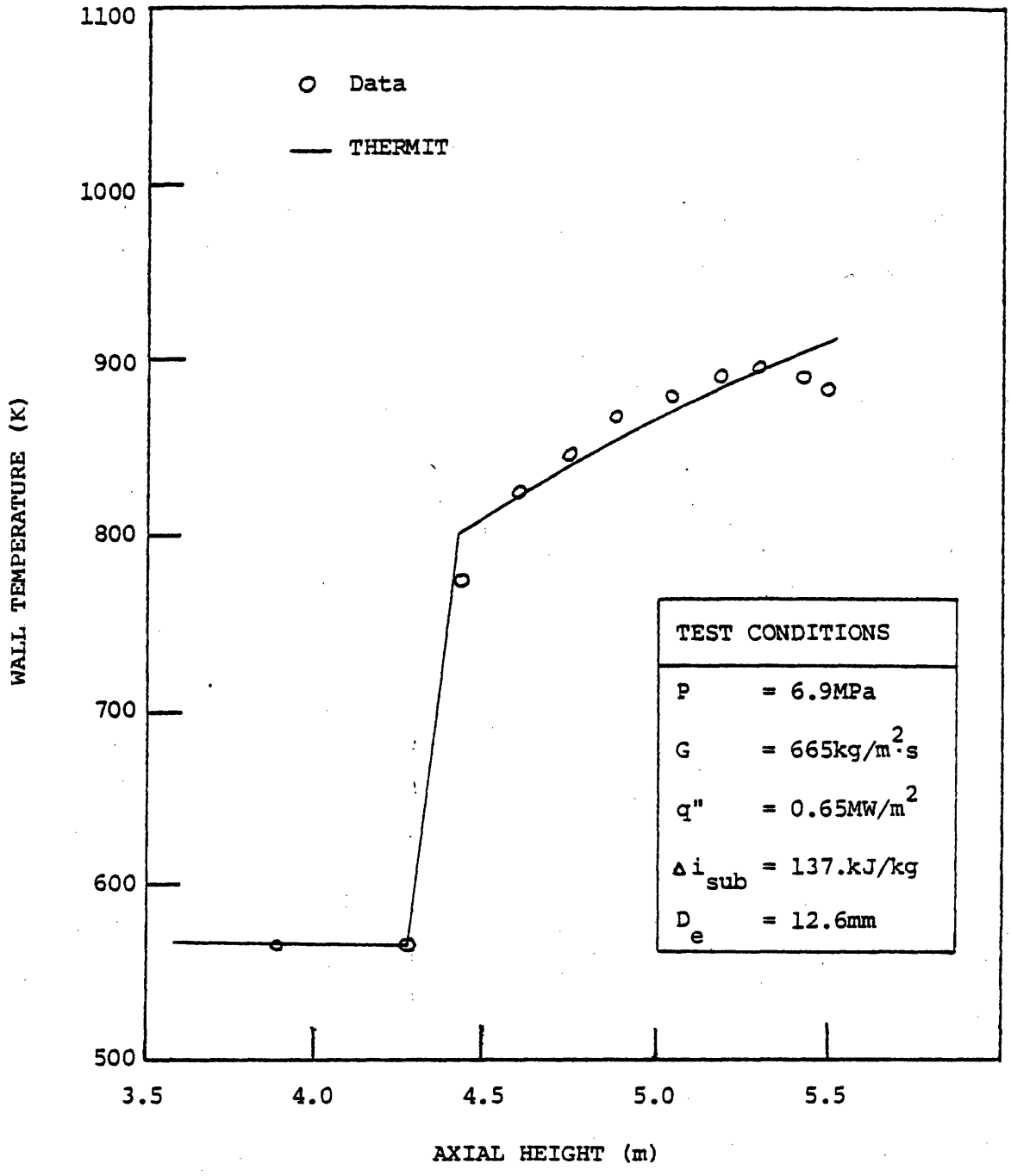

Figure 6.12: Wall Temperature Comparisons for Bennett Case 5332 (Length = 5.56m) with Adjusted CHF Position.

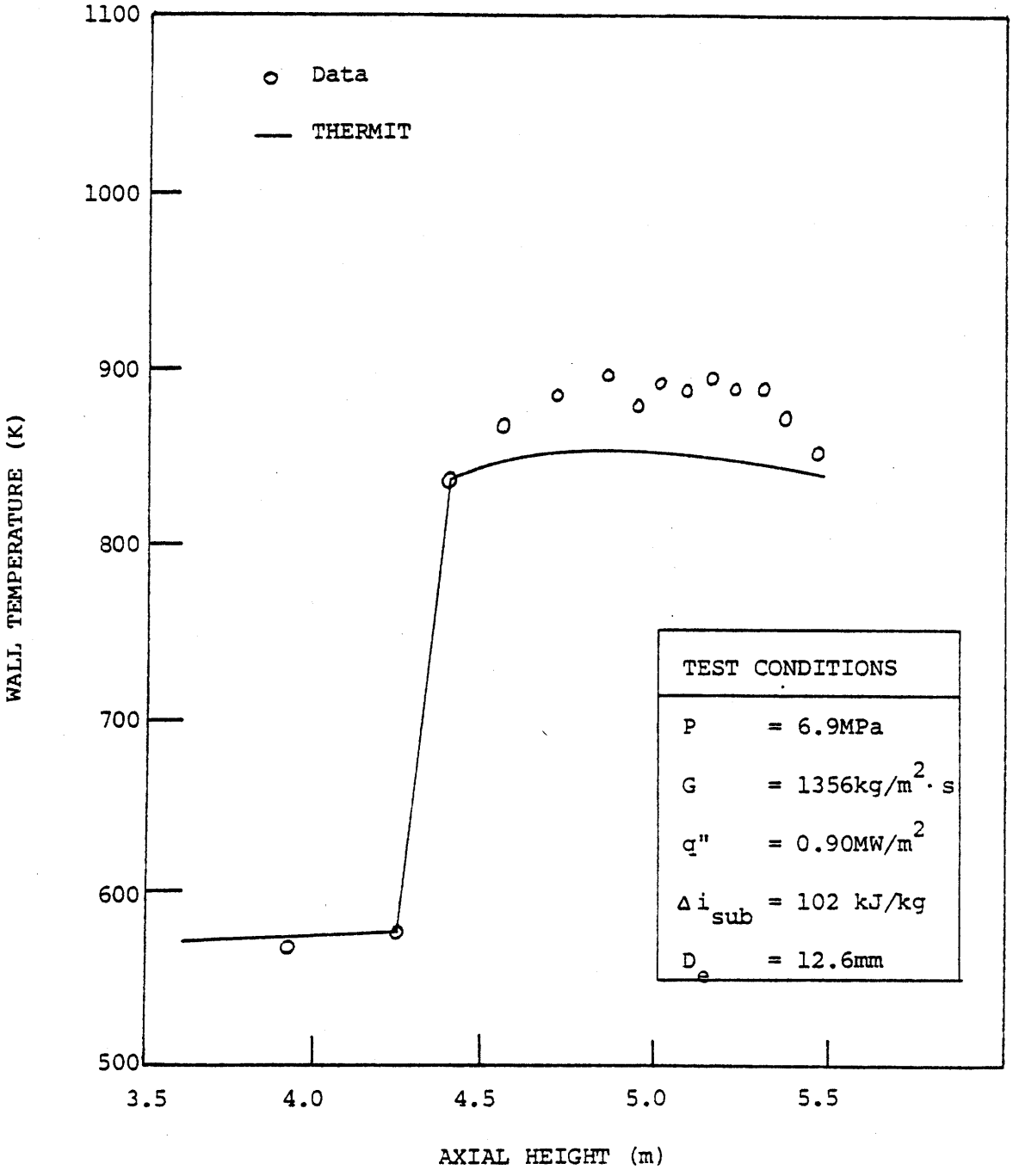

Figure 6.13: Wall Temperature Comparisons for Bennett Case 5253 (Length = 5.56m) with Adjusted CHF Position.

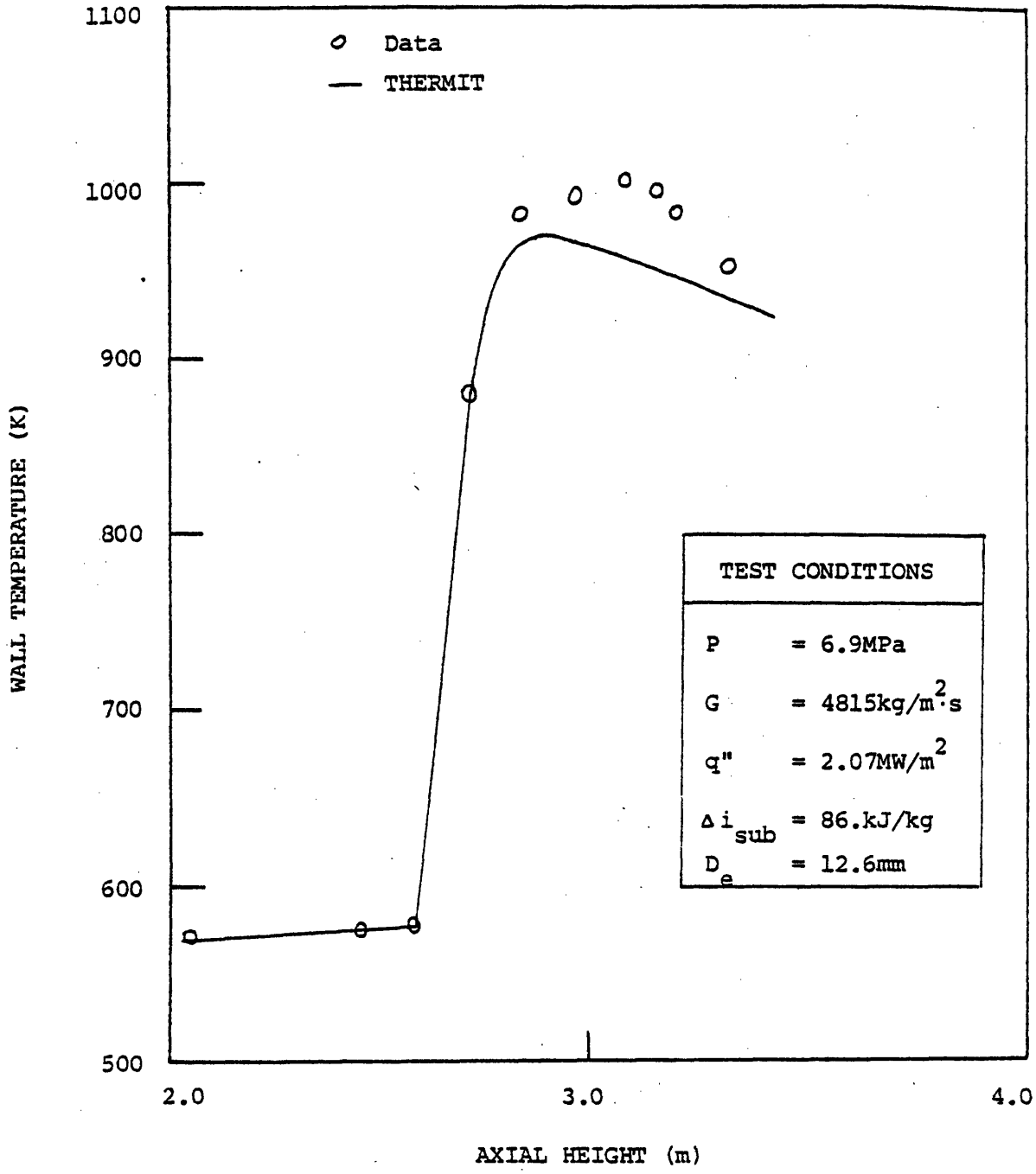

Figure 6.14: Wall Temperature Comparisons for Bennett Case 5442 (Length = 3.66m) with Adjusted CHF Position

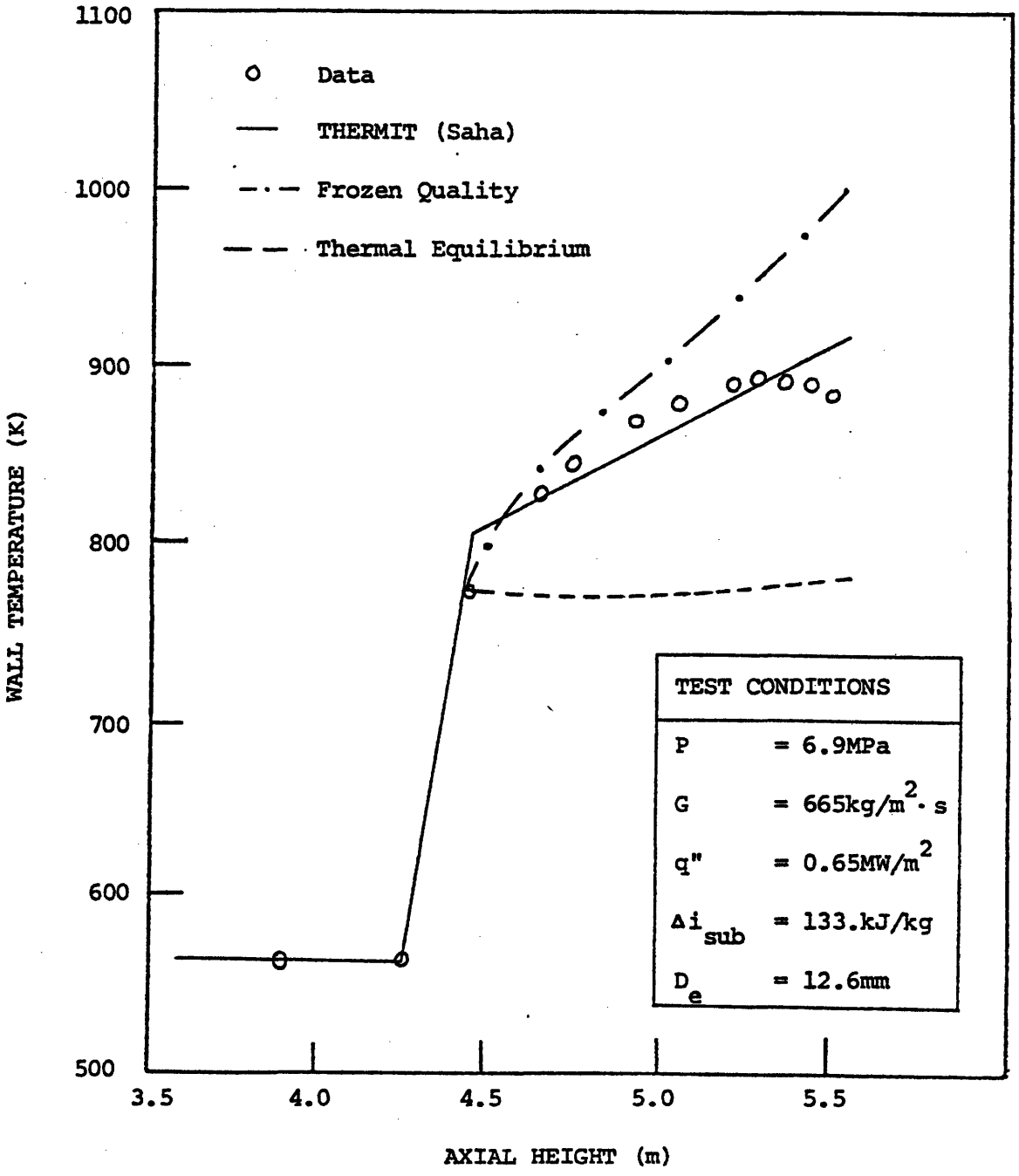

Figure 6.15: Comparison of Wall Temperature Predictions Using Various Γ Models for Bennett Case 5332

impingement. However, these mechanisms account for only a few percent of the total heat transfer [74]. In general, the predictions of the wall temperature profile agree very well with the trends indicated by the data, except at the exit, which may be due to axial conduction heat transfer out of the test section.

The THERMIT-2 predictions of post-CHF test data of Bennett [39] using the equilibrium and frozen quality models are compared with the non-equilibrium model in Figure 6.15. For the thermal equilibrium model, the Groeneveld 5.7 correlation and the saturated vapor generation model of Nigmatulin were used. For the frozen quality model, after CHF had been exceeded, vapor generation was suppressed, and no heat exchange between the phases was allowed. The CISE-4 CPR correlation was used to predict the onset of CHF.

As shown, the thermal equilibrium model wall temperature predictions fall below the data. On the other hand, the frozen quality model over predicts the wall temperature. The thermal non-equilibrium predictions lie in between the two extremes.

7.0 CHF PREDICTION ASSESSMENT

7.1 Introduction

As discussed in Chapter 6, CHF plays an important role in the heat transfer package. Therefore, one of the tasks in this project has been the assessment of CHF predictability of THERMIT-2. Originally, Biasi [55] was the only CHF correlation available. Due to its limited applications, W-3 [78], CISE-4 [57], Bowring [81], Barnett [79], and Hench-Levy [80] correlations have been included. These correlations are summarized in Appendix B. Both Bowring and Biasi were correlated from uniformly-heated, round tube dryout data. The CISE-4 correlation was also correlated from dryout data obtained in uniformly heated round tubes. However, it is based on the critical quality-boiling length approach. Furthermore, the application of CISE-4 in rod bundles is possible by introducing the ratio between the heated and wetted perimeter into the correlation [82]. Barnett was correlated from dryout data in uniformly heated annuli. Barnett has been shown to predict rod bundle data with remarkable accuracy [83]. Hench-Levy was correlated from rod-bundle dryout data using the limit-line approach. Finally, W-3 is a DNB-type, rod bundle correlation.

The assessment of the applicability of these correlations, except Hench-Levy, in round tubes and rod bundles under steady state and transient conditions has been undertaken with THERMIT-2. The summary of the assessment program is given in Table 7.1.

7.2 Steady State CHF Predictions in Rod Bundles

Predictions of the critical heat flux in rod bundles using local subchannel flow conditions and the bundle-average flow conditions have been studied with THERMIT-2. For the BWR core conditions, the two-phase

TABLE 7.1

Summary of CHF Correlation Assessment

Correlations Available in THERMIT-2	Condition for which the correlation has been checked			
	Steady-State		Transient	
	Tube	Bundle	Tube	Bundle
Biasi	X	X	X	X
CISE-4	X	X	X	X
Bowring		X	X	
W-3		X		
Barnett		X		X
Hench-Levy				

turbulent mixing phenomenon leads to substantial alterations in the quality distribution in the rod bundle. Therefore, one would expect that CHF would be more accurately predicted with the subchannel method rather than with bundle-average (lumped single-channel) method. Since rod bundle CHF correlations are usually correlated with bundle averaged parameters and fluid variables, their application in the subchannel method is questionable. If one considers each subchannel in the rod bundle as a round tube, and replaces the tube diameter by the equivalent diameter, the round tube CHF correlations can be applied in the subchannel analysis, as well as in the bundle-average analysis.

The two-fluid model of two-phase flow in THERMIT-2 has the capability of subchannel analysis. The field equations for the conservation of mass, momentum, and energy include a term that accounts for the effects of turbulent mixing and vapor diffusion between subchannels. The mathematical formulation has been discussed in Chapter 2. In the model for the mixing, it is observed that the sum of the liquid and vapor mixing equations leads to the model applied in the mixture approach [25,28].

7.2.a CHF under BWR Conditions

The CHF data of G.E. 9-rod bundle experiment [52] are used in this investigation. The cross sectional view of the test section is shown in Figure 7.1. As seen, there are three types of subchannels; namely the center, corner and side subchannels. In the experiment, although all rods were heated uniformly, CHF was observed first in the corner rods. Table 7.2 shows the predicted Minimum Critical Power Ratios (MCPR) and the Minimum Critical Heat Flux Ratios (MCHRF) by CISE-4* [57],

* The equivalent hydraulic diameter is used in place of the tube diameter in CISE-4. Although, the use of equivalent heated diameter has been suggested [66], equivalent hydraulic diameter gives better predictions. See Appendix C.

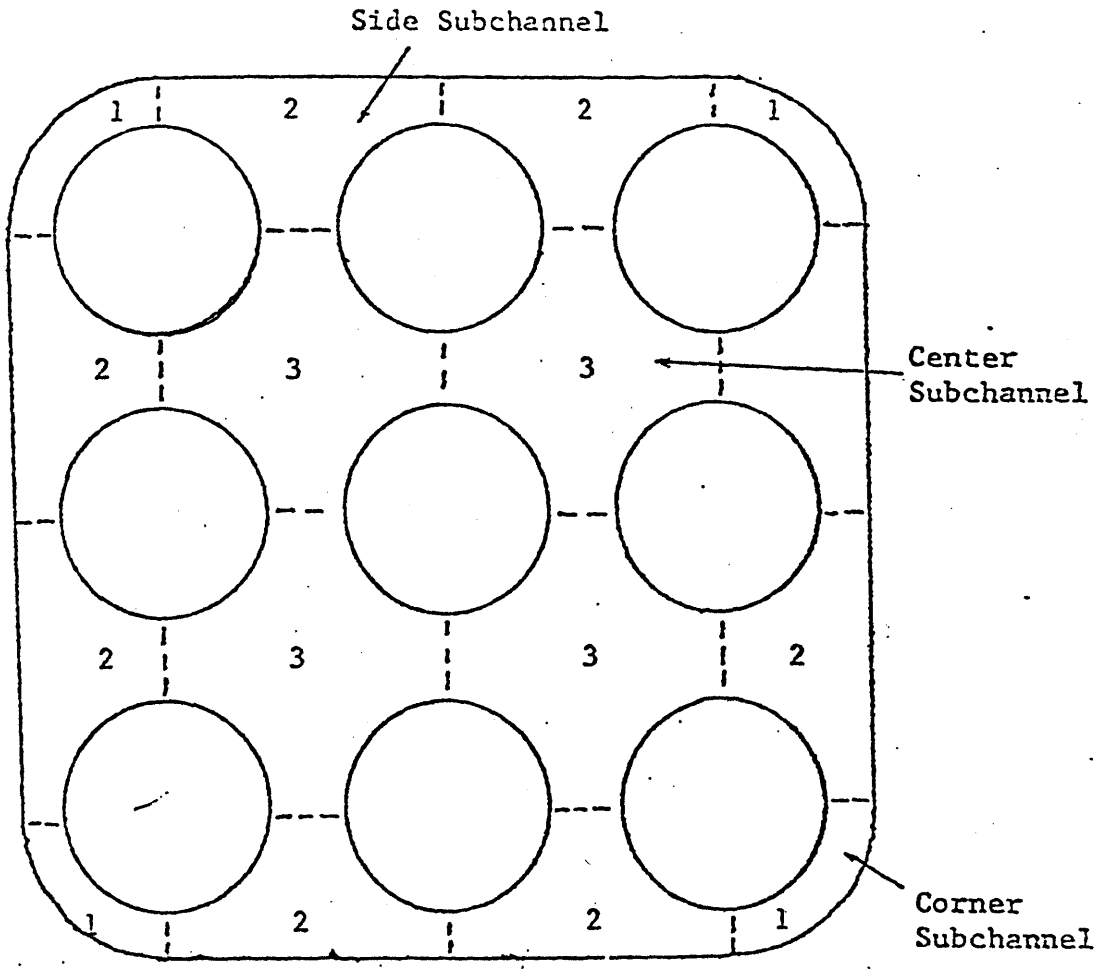

Geometrical Details

Rod Diameter	14.3	mm
Rod-Rod Gap	4.42	mm
Rod-Wall Gap	3.51	mm
Radius of Corner	10.2	mm
Heated Length	1829	mm

Figure 7.1: Cross Sectional View of G.E. 9-Rod Bundle Used in CHF Study.

TABLE 7.2

Comparison of GE 9-Rod Bundle CHF Experiment

(Pressure: 6.9 MPa)

Run #	G_2 (kg/m^2-s)	x_{CHF}	CISE-4 (MCPR)		Biasi (MCHFR)		Bowring (MCHFR)		Barnett (MCHFR)	
			Sub	Bundle	Sub	Bundle	Sub	Bundle	Sub	Bundle
278	681	.4885	0.854	0.867	1.192	1.548	1.634	2.109	0.708	0.794
279	678	.4640	0.883	0.903	1.222	1.511	1.676	2.061	0.713	0.808
280	678	.4242	0.932	0.957	1.272	1.490	1.735	2.024	0.770	0.864
271	1024	.3749	0.893	0.929	1.174	1.357	1.351	1.633	0.760	0.828
272	1024	.3518	0.929	0.963	1.148	1.377	1.356	1.587	0.763	0.835
273	1020	.3328	0.948	0.985	1.156	1.376	1.393	1.577	0.775	0.850
266	1367	.2957	0.935	0.970	1.194	1.428	1.206	1.425	0.754	0.855
267	1358	.2582	1.019	1.060	1.300	1.450	1.307	1.456	0.807	0.893
268	1362	.2349	1.030	1.061	1.282	1.368	1.304	1.404	0.841	0.901
297	1690	.2038	1.056	1.090	1.327	1.418	1.231	1.216	0.856	0.914
298	1691	.1783	1.025	1.108	1.225	1.280	1.157	1.217	0.807	0.890
299	1687	.1510	1.043	1.132	1.228	1.258	1.183	1.215	0.584	0.901

Sub = subchannel method
Bundle = bundle-average method

Biasi [55] and Bowring [81] correlations using both subchannel and bundle-average methods. It is seen that in every case the subchannel method is more conservative than the bundle-average method. CISE-4 is shown to have the best predictions. Furthermore, CISE-4 consistently predicts MCPR in the side subchannel which is faced by both corner and side rods, which is at good agreement with the experimental finding. Biasi and Bowring, on the other hand, are always non-conservative and predict MCHFR to be in the center subchannel. It is worth noting that only CISE-4 includes a factor accounting for the difference between the heated and wetted parameters in the corner and side subchannels, which may be the reason that CISE-4 is able to predict the CHF location correctly, as well as predict CPR reasonably well on a bundle average basis.

The same cases have been studied with the annulus correlation of Barnett. The predictions are shown in Table 7.2. The similar trend is observed, that is, the subchannel method is more conservative than the bundle-average method. Furthermore, the MCHF location was consistently predicted by Barnett to be in the corner subchannel.

7.2.b CHF under PWR Condition

The W-3 correlation has been assessed with the 20-rod PWR bundle data of Bettis Lab [84]. The cross-sectional view and the geometry of the test section are given in Fig. 7.2. The data studied were taken from uniformly heated rod bundle where CHF occurred at the exit. Since W-3 was correlated based on bundle averaged parameters, the bundle-average method was used in this analysis. Table 7.3 summarizes the test conditions and the predictions. As shown, W-3 is generally non-conservative for mass fluxes lower than 1600 Kg/m^2-s. It should be noted that these tests were performed in a tight lattice, atypical of commercial PWR designs.

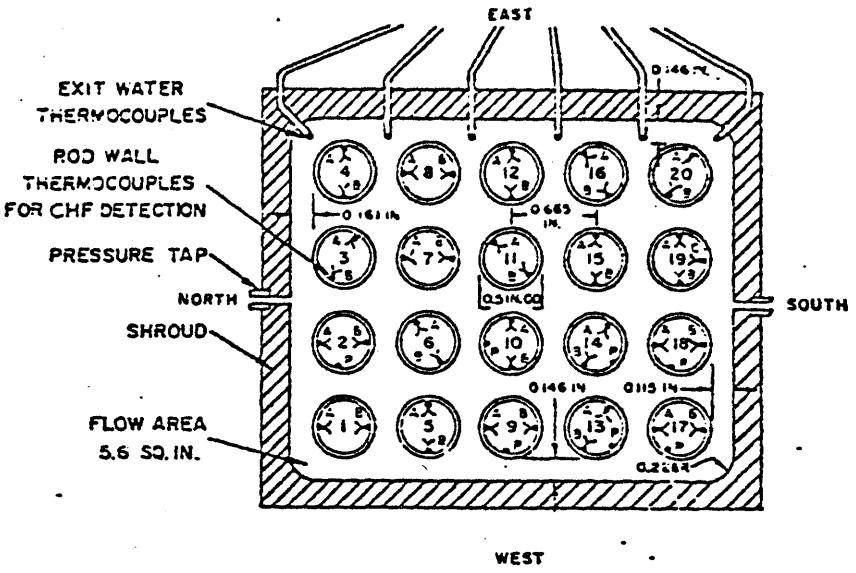

Rod Diameter = 1.27 cm

Flow Area = 3.614×10^{-4} m^2

Heated Length = 2.438 m

Wetted Perimeter = 1.115 m

Hydraulic Diameter = 1.31 cm

Figure 7.2: Cross Section of Uniformly Heated Bettis Rod Bundle Test Section Neat Exit End (Ref. 84).

TABLE 7.3

Bettis 20-Rod PWR Bundle CHF Experiment (P = 13.8 MPa)
and W-3 Correlation Prediction MCHFR

No.	Q(MW)	G(Kg/m^2-s)	H_{in}(KJ/Kg)	x_{CHF}	MCHFR
14-1	2.738	802	605	12.7	1.268
10-2	2.181	1188	1137	15.1	1.222
9-5	2.879	1204	872	7.1	1.128
4-5	2.175	1579	1268	13.6	1.163
3-5	2.677	1594	1137	10.6	1.517
6-5	2.242	2376	1428	15.5	1.019
4-8	2.916	2376	1277	9.9	0.899
26-4	2.806	3084	1410	12.7	0.848
5-3	3.167	3110	1340	9.3	0.804

Also, the W-3 correlation is recommended for mass flux range $1356 < G < 6780$ Kg/m^2-s.

7.3 Transient CHF Predictions

CHF may also occur under transient accidnet conditions in nuclear reactors. Since all the CHF correlations used in the present analysis are based on data obtained under quasi steady-state fluid conditions, the transient CHF predictive capability of THERMIT-2 is assessed with the assumption that the steady-state CHF correlations may be applied in transient conditions. The technique employed here involves using the thermal-hydraulic code to provide the instantaneous local fluid conditions as the input for the steady-state CHF correlations. It should be noted that for typical LWR flow transients, the CHF conditions appear to have been well predicted by steady state correlations [64]. However, for power transients the steady state correlations appear to be too conservative [87].

7.3.1 Transient CHF in Tubes

The transient CHF data of AEEW [85] are used for the assessment of transient CHF in round tubes. In the experiment, power-jump and flow-decay transients were investigated. The power transients were obtained by short circuiting a high speed breaker causing an immediate jump in power in the test section, and the flow transients were initiated by switching off the circulation pump with decay coastdown while holding power constant. The heat flux was kept uniform in all cases. The inlet mass velocity histories for the power-jump and flow-decay transients are illustrated in Figures 7.3 and 7.4. These velocities were used as inlet boundary conditions in THERMIT.

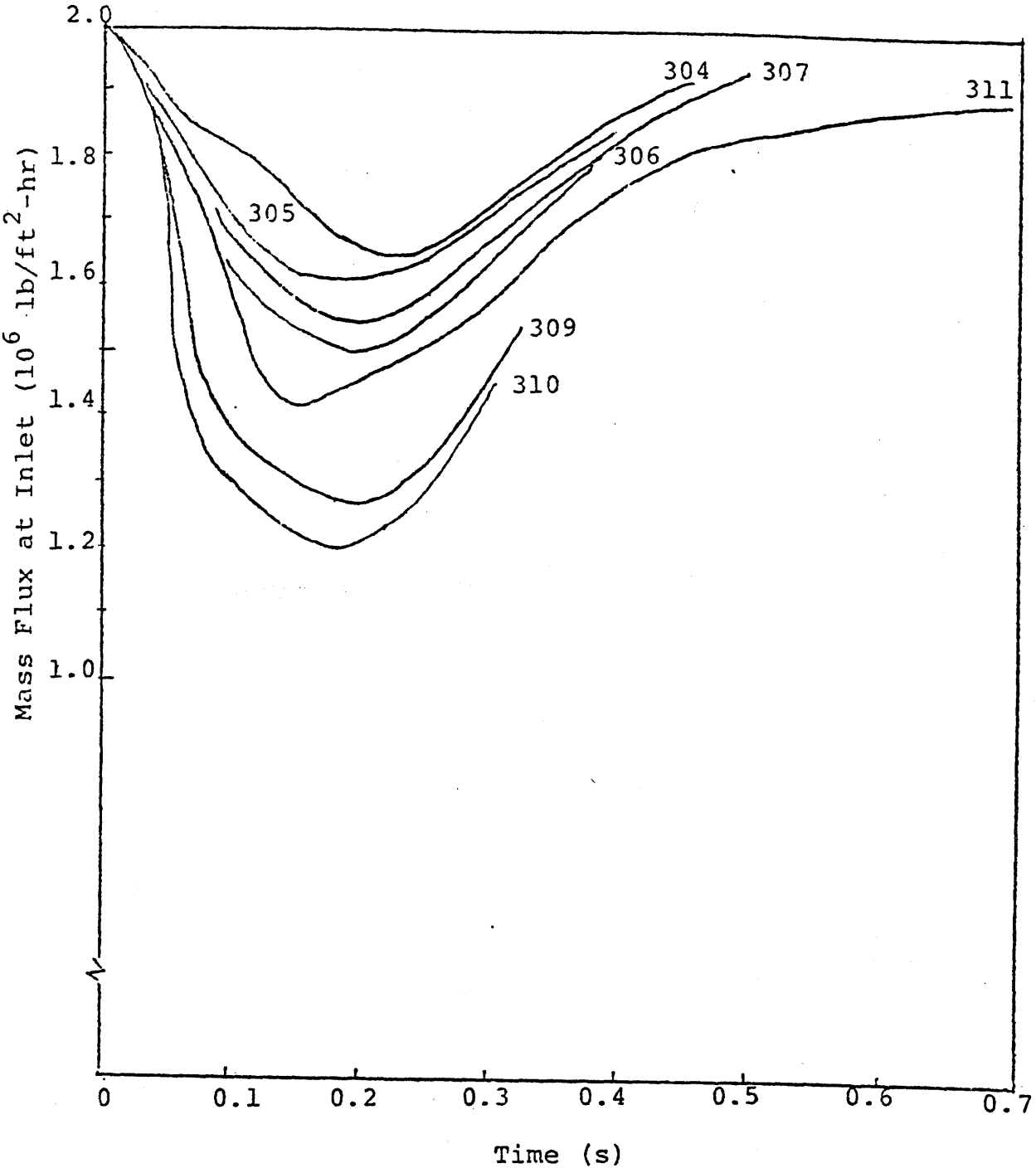

Figure 7.3: Response of Inlet Mass Velocity to Power Jumps on the Uniformly Heated 12 Ft. Tube in AEEW Experiments (Ref. 85).

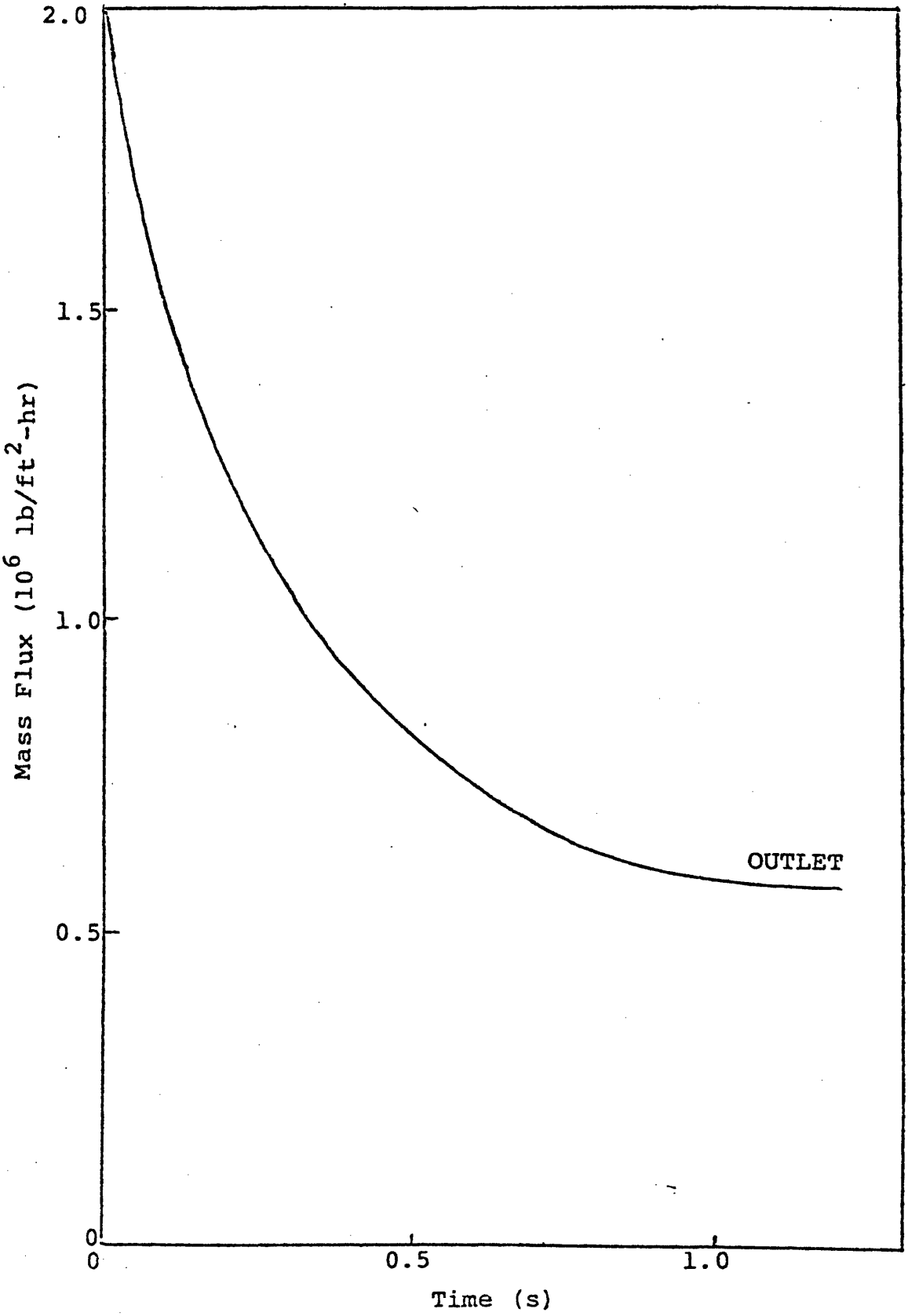

Figure 7.4: A Typical Flow Rundown in the Uniformly Heated 12 ft. Tube in AEEW Experiments (Ref. 85).

The comparisons of the predicted time-to-CHF using the CISE-4, Biasi, and Bowring correlations with the measured values are tabulated in Tables 7.4 and 7.5. It is seen that CISE-4 consistently predicts CHF earlier than the measurements for both types of transients. In the power-jump transients, Biasi predicts no CHF except for the two cases with large power changes; and it consistently overpredicts the time to CHF in the flow-decay transients. Bowring, on the other hand, predicts CHF prematurely in the power transients. In flow transients, it agrees well with the data for some cases, and underpredicts the reported time-to-CHF for others. Note, the CHF mechanisms in these tests were identified to be that of dryout.

7.3.2 Transient CHF in Rod Bundles

The flow transient CHF measurements taken in G.E. 9-rod bundles have been compared with THERMIT predictions. In the experiment, the rod bundles were initially brought to a steady flow condition, and the transient was then initiated by instantaneously decreasing the inlet flow rate by half using a fast closing valve. The flow rate was maintained at this lower value until CHF occurred. The test section of the 9-rod bundle is the same as the ones used in steady-state CHF experiment (See Fig. 7.1). In all cases, the axial and radial power distributions were held uniform.

The descriptions of the test cases studied are given in Table 7.6. The instrument traces for each case are given in Figures 7.5 to 7.7. Figures 7.8 through 7.10 show the results of the THERMIT-2 simulation of the test cases 175, 179, and 181. The figures show the minimum critical power ratio (MCPF) or the minimum critical heat flux ratio (MCHFR) histories predicted by CISE-4, Biasi, and Barnett using both the subchannel and bundle-average methods. Again, the subchannel method is more conservative:

TABLE 7.4

Moxon-Edwards Power Jump Transients

(AEEW)

Run	$Q_{initial}$ (KW)	ΔQ (KW)	t_{CHF}(sec) measured	$t_{CHF,predicted}$ (sec)		
				Biasi	CISE-4	Bowring
311	90.4	51.5	0.7	$\left(\frac{MCHFR}{1.28}\right)$	0.45	0.43
307	111.6	37.6	0.51	$\left(\frac{MCHFR}{1.17}\right)$	0.355	0.25
309	112.4	61.7	0.33	0.284	0.205	0.075
304	120.7	32.2	0.47	$\left(\frac{MCHFR}{1.13}\right)$	0.308	0.155
306	119.0	40.8	0.4	$\left(\frac{MCHFR}{1.03}\right)$	0.235	0.095
310	118.3	66.1	0.31	0.209	0.105	0.05
305	1232	32.3	0.4	$\left(\frac{MCHFR}{1.09}\right)$	0.267	0.11

G_i = 2713 kg/m^2-sec

ΔH_{inlet} = 5.12 x 10^4 J/kg (inlet subcooling)

P = 6.9 MPa

L = 3.66 m

I.D. = 1.08 cm

TABLE 7.5

Moxon-Edwards Flow Decay Transients (AEEW)

Run	Q (KW)	t_{CHF} measured (sec)	$t_{CHF,predicted}$ (sec)		
			Biasi	CISE-4	Bowring
276	118.8	0.95	1.085	0.665	1.04
279	133.4	0.52	0.83	0.415	0.55
280	136.4	0.55	0.785	0.36	0.43
281	139.9	0.51	0.725	0.29	0.225
282	142.5	0.44	0.695	0.245	0.185

P = 6.9 MPa

G_i = 2713 Kg/m^2-sec

G_f = 1000 Kg/m^3-sec

ΔH_i = 51.2 KJ/Kg (inlet subcooling)

L = 3.66 m

I.D. = 1.08 cm

TABLE 7.6

Test Conditions for G.E. 9-Rod Bundle Flow Transient Cases 175, 179 and 181

	Case No.		
Item	175	179	181
Q(MW)	812	841	856
G_i(kg/m^2-s)	844	1383	1375
G_i/G_f	0.47	0.30	0.29
Time-to-CHF (sec)	1.51	2.13	1.2

System Pressure = 6.9 MPa

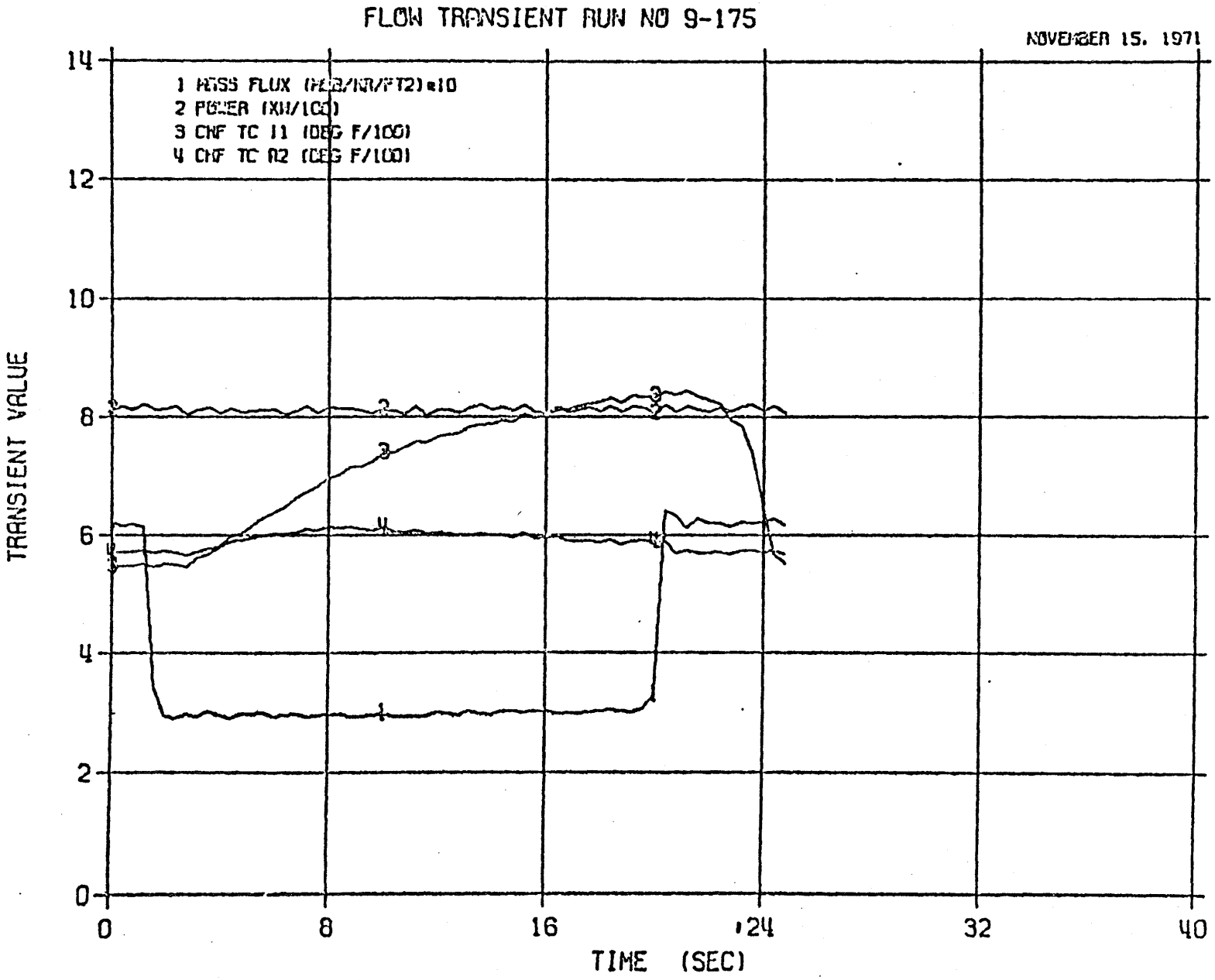

Fig. 7.5: Instrumentation Traces for Case 9-175

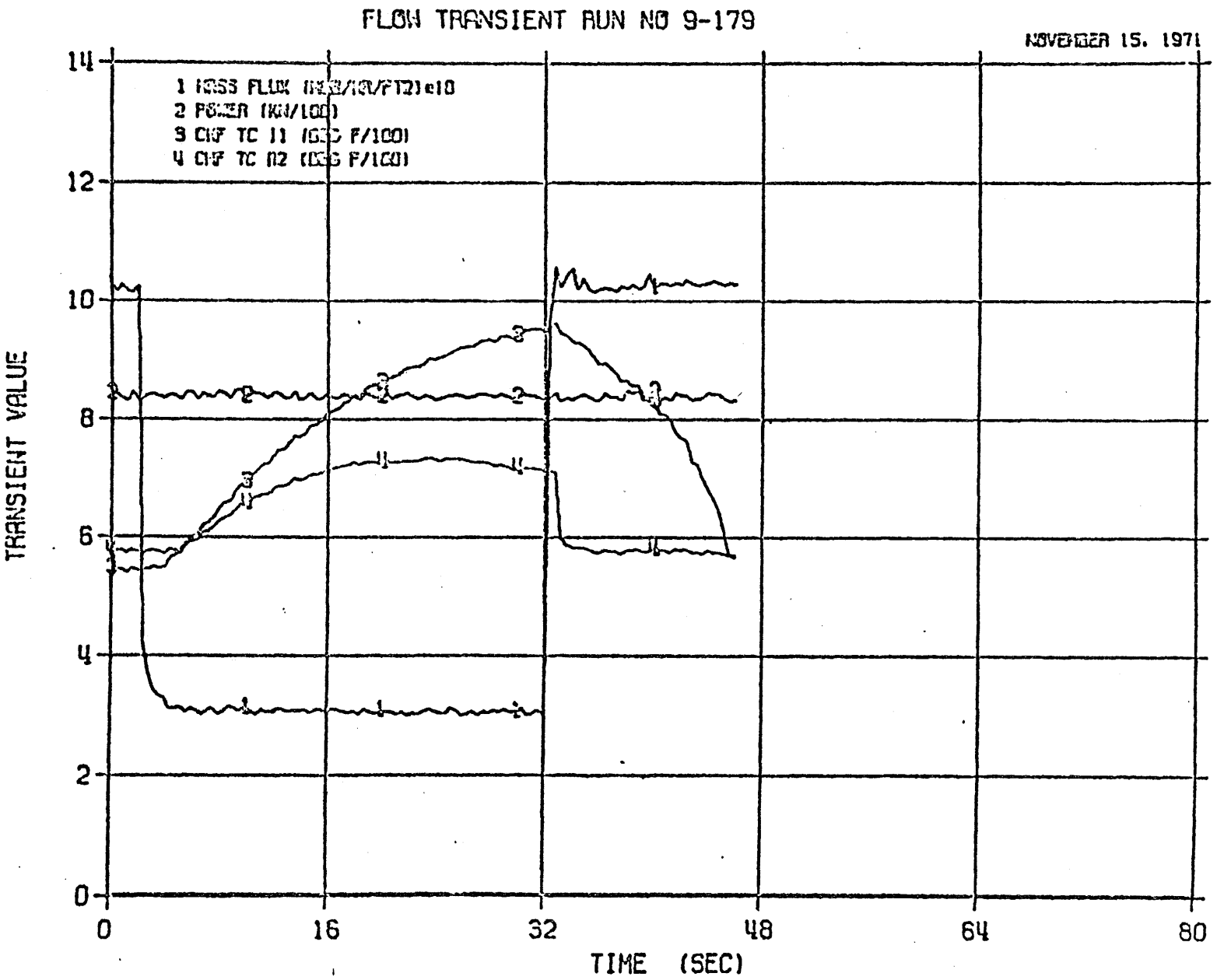

Fig. 7.6: Instrumentation Traces for Case 9-179

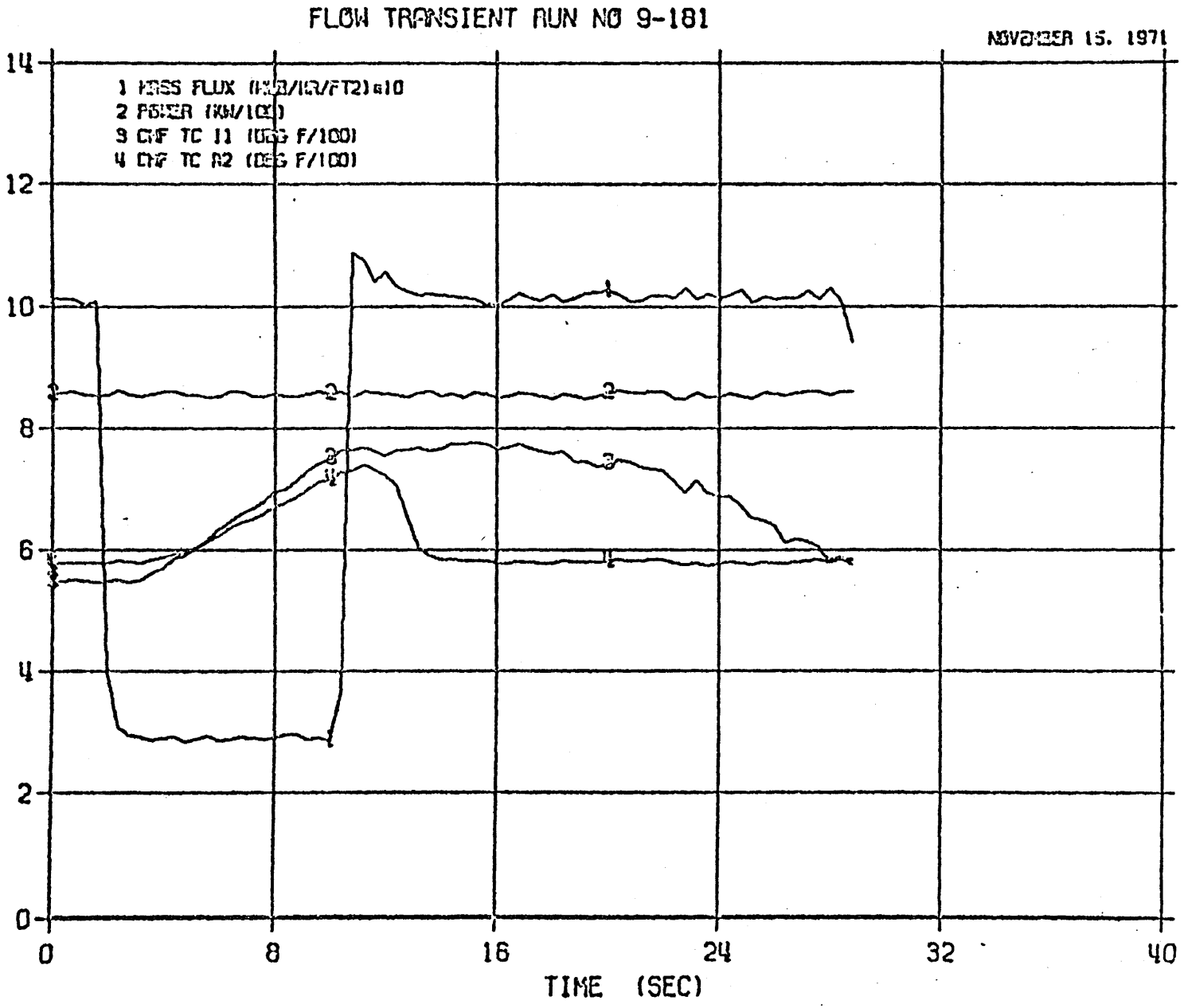

Fig. 7.7: Instrumentation Traces for Case 9-181

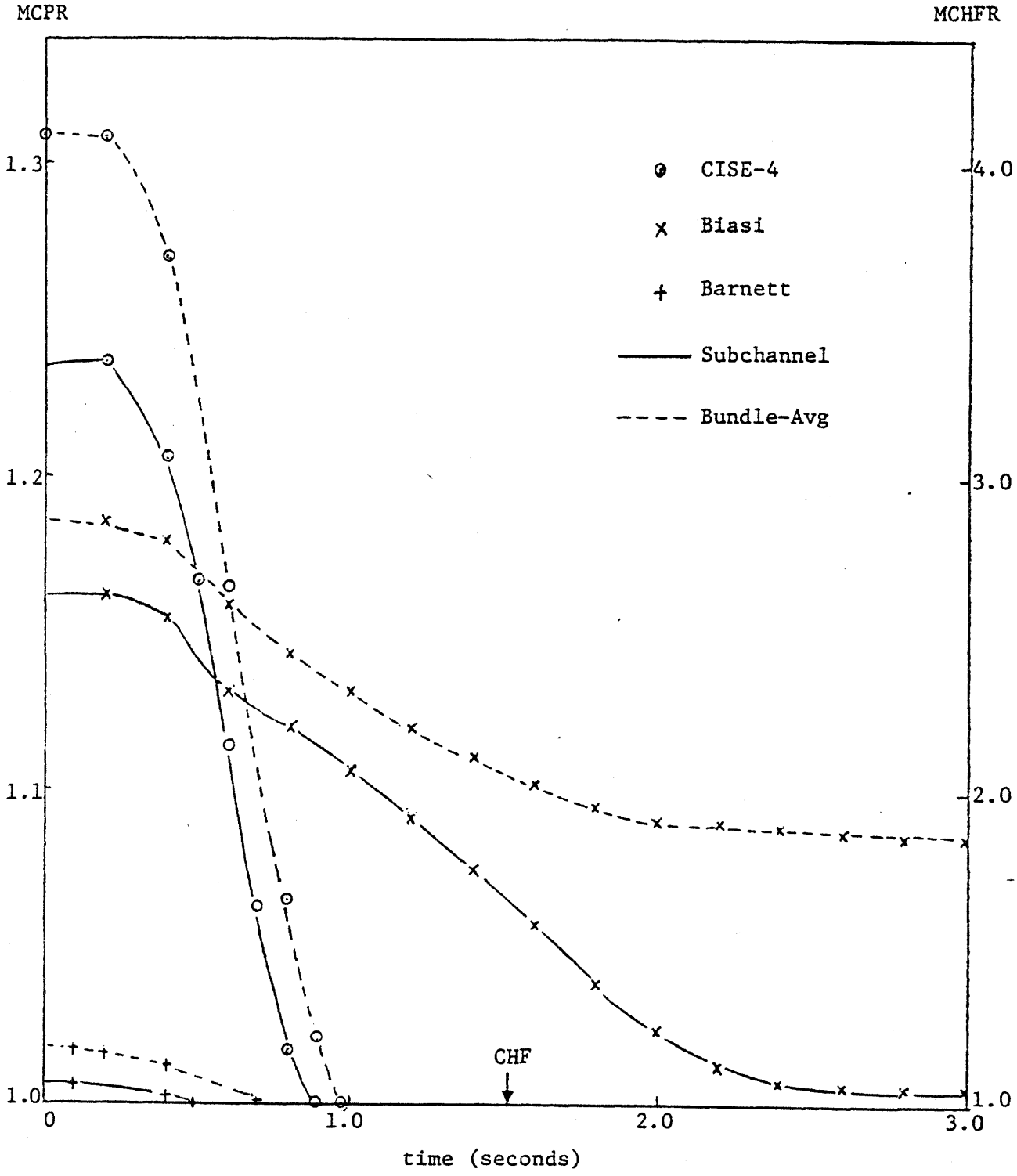

Fig. 7.8: Comparison of Measured and Predicted Time-to-CHF for Case 9-175.

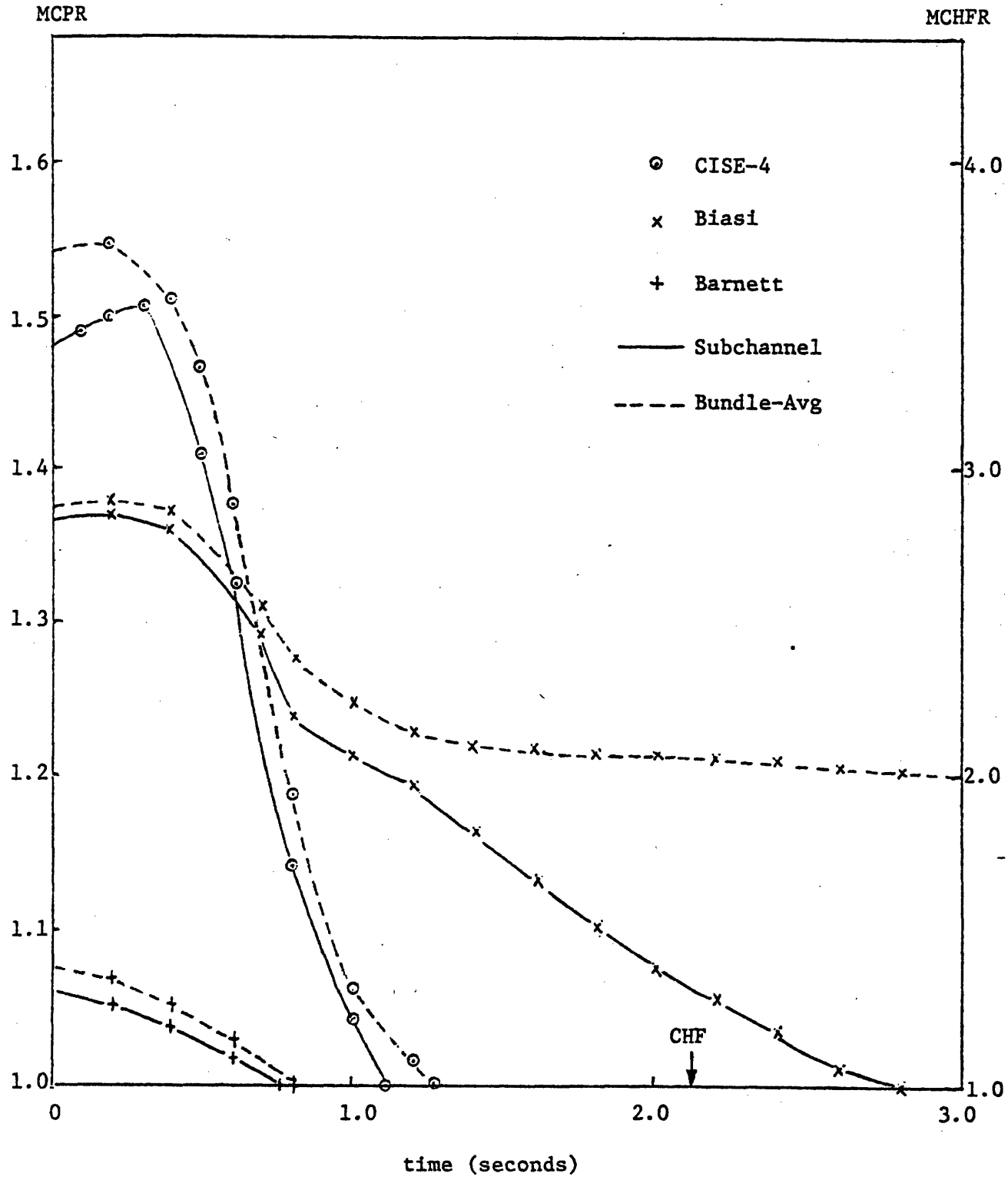

Fig. 7.9: Comparison of Measured and Predicted Time-to-CHF for Case 9-179.

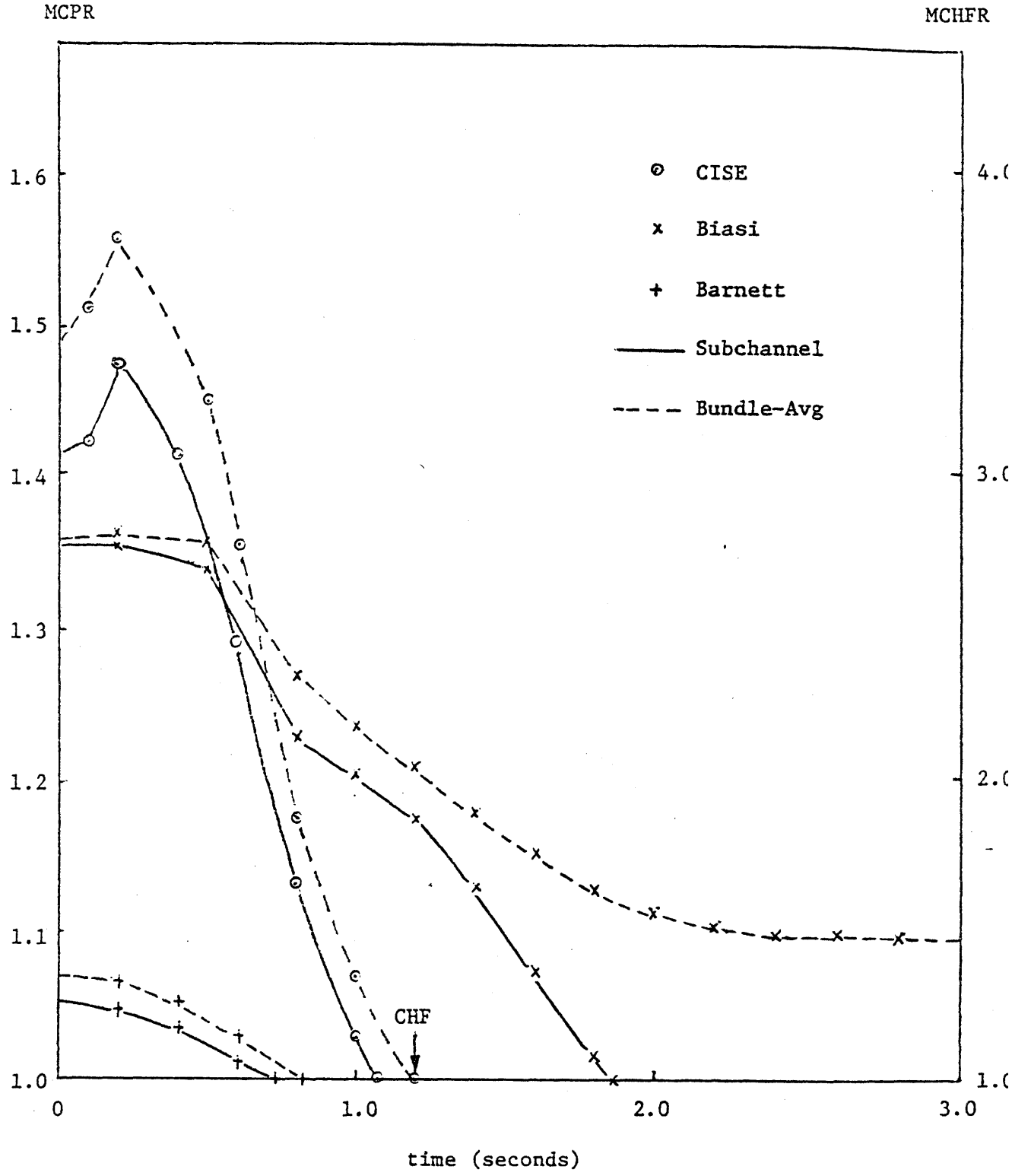

Fig. 7.10: Comparison of Measured and Predicted Time-to-CHF for Case 9-181.

that is, the method predicts CHF earlier than the bundle-average method. As seen, the Barnett correlation leads to substantial underprediction of the times-to-CHF in each case, while Biasi indicates no CHF (Case 175) or overprediction of the time-to-CHF (cases 179 and 181), whereas CISE-4 gives the best time-to-CHF predictions in all cases, with some conservatism.

7.4 Comparison with other Works

Steady state CHF tests of G.E. 9-rod bundle have been investigated by Loomis [86] using COBRA-3C/MIT. Predictions using the single-channel (bundle-average) and subchannel methods for test cases 266 and 268 are given in Table 7.7. It is seen that the subchannel method is more conservative, in agreement with the results obtained by THERMIT-2.

Van Haltern [63] has investigated time-to-CHF under flow decay and power transients in the G.E. 16-rod bundles. In his work, the predictions of a number of CHF correlations using MEKIN code were compared with the data. In every case, substantial underprediction of time-to-CHF has been found, as illustrated in Fig. 7.11. This is similar to the trend observed in the THERMIT-2 predictions.

7.5 Summary and Conclusions

The predictability of five CHF correlations have been analyzed by comparing the experimental data with THERMIT-2 predictions. The results are summarized in Table 7.8. It is seen that CISE-4 and Barnett are the best for BWR applications in terms of conservatism. Whereas, Biasi is the most non-conservative. Bowring is shown to be non-conservative in steady-state rod bundle tests, and is generally conservative in single-tube transient tests. Both Barnett and CISE-4 have been shown to be

Table 7.7

Comparison of MCPR and MCHFR Predictions
Using Single Channel and Subchannel Analysis
(Ref. 86)

Test Case No.	Analysis Method	CISE-4 MCPR	Hench-Levy MCHFR
266	Single channel	0.9320	0.6017
	Subchannel	0.7657	0.5955
268	Single channel	0.0950	0.6665
	Subchannel	0.9126	0.6241

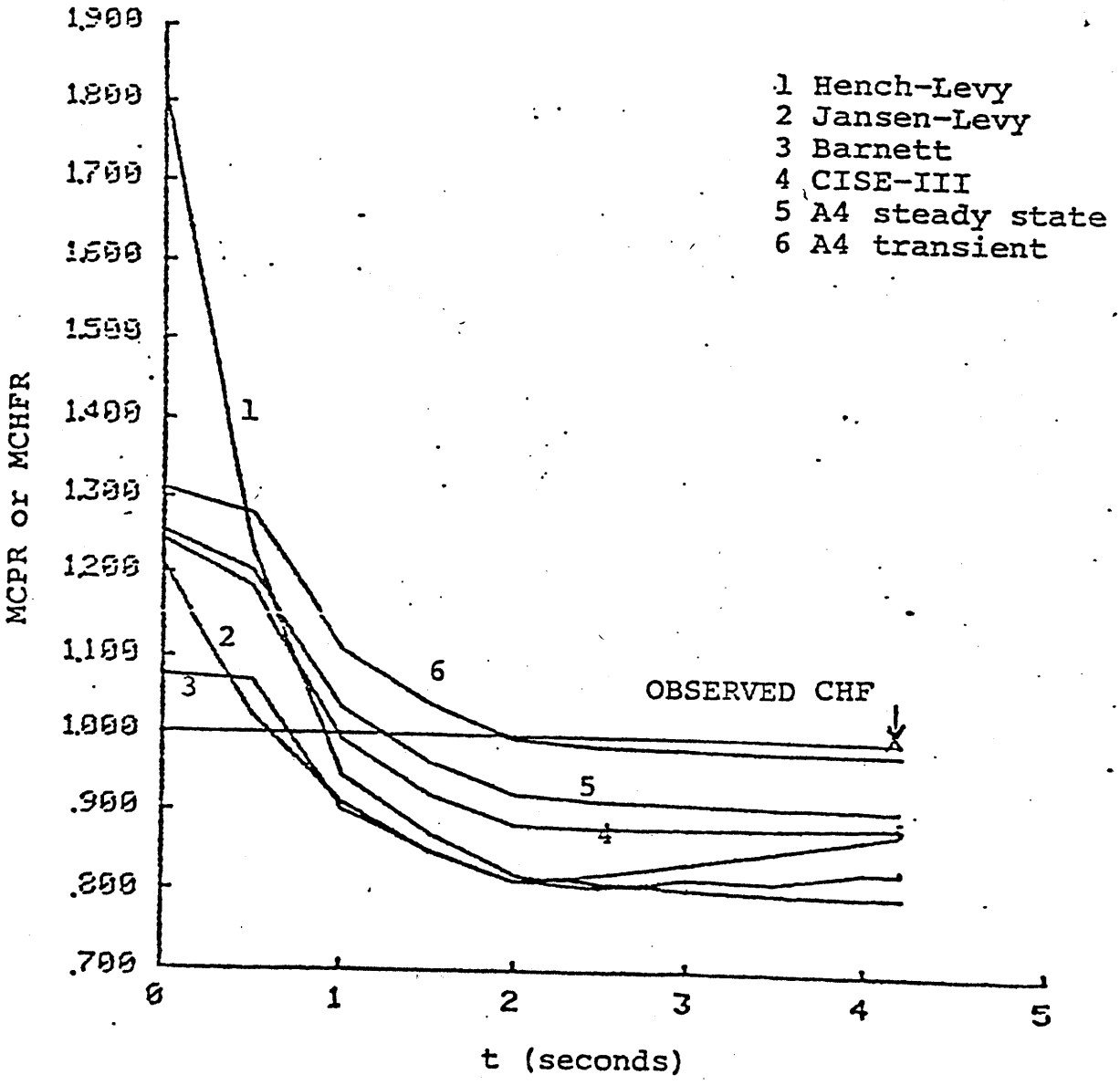

Fig. 7.11

MCPR and MCHFR predictions for test 101
(Ref. 63)

TABLE 7.0

Summary of CHF Assessment Results

		Barnett	Biasi	Bowring	CISE-4	W-3
Bennett Single Tube			◑		◑	
G.E. 9-Rod Steady State	Subchannel	○	●	●	◑	
	Bundle	○	●	●	◑	
Bettis (PWR) 20 Rod Steady State	Bundle					◐
Moxon-Edwards Single Tube Transient	Power-Jump		◐	○	○	
	Flow Decay		●	◑	○	
G.E. 9-Rod Transient	Subchannel	○	●		○	
	Bundle	○	●		○	

○ Conservative

● Non-Conservative

◑ Mostly Conservative

◐ Mostly Non-Conservative

successful in predicting CHF in rod bundles. However, one must bear in mind that all except W-3 are correlated from either single-tube or annular CHF data. The results also show that the subchannel analyses always yield more conservative CHF predictions than the bundle-average analyses. However, CISE-4 appears to be applicable for both sub-channel and rod-bundle analyses.

The results indicate that the CHF correlations can be used to predict anticipated transients with their expected conservatism or non-conservatism as in steady-state, with a thermal-hydraulic code providing the instantaneous fluid information. However, caution must be exercised when the transient goes beyond the pressure or mass flux range of the data base of the correlation (see Fig. 7.12).

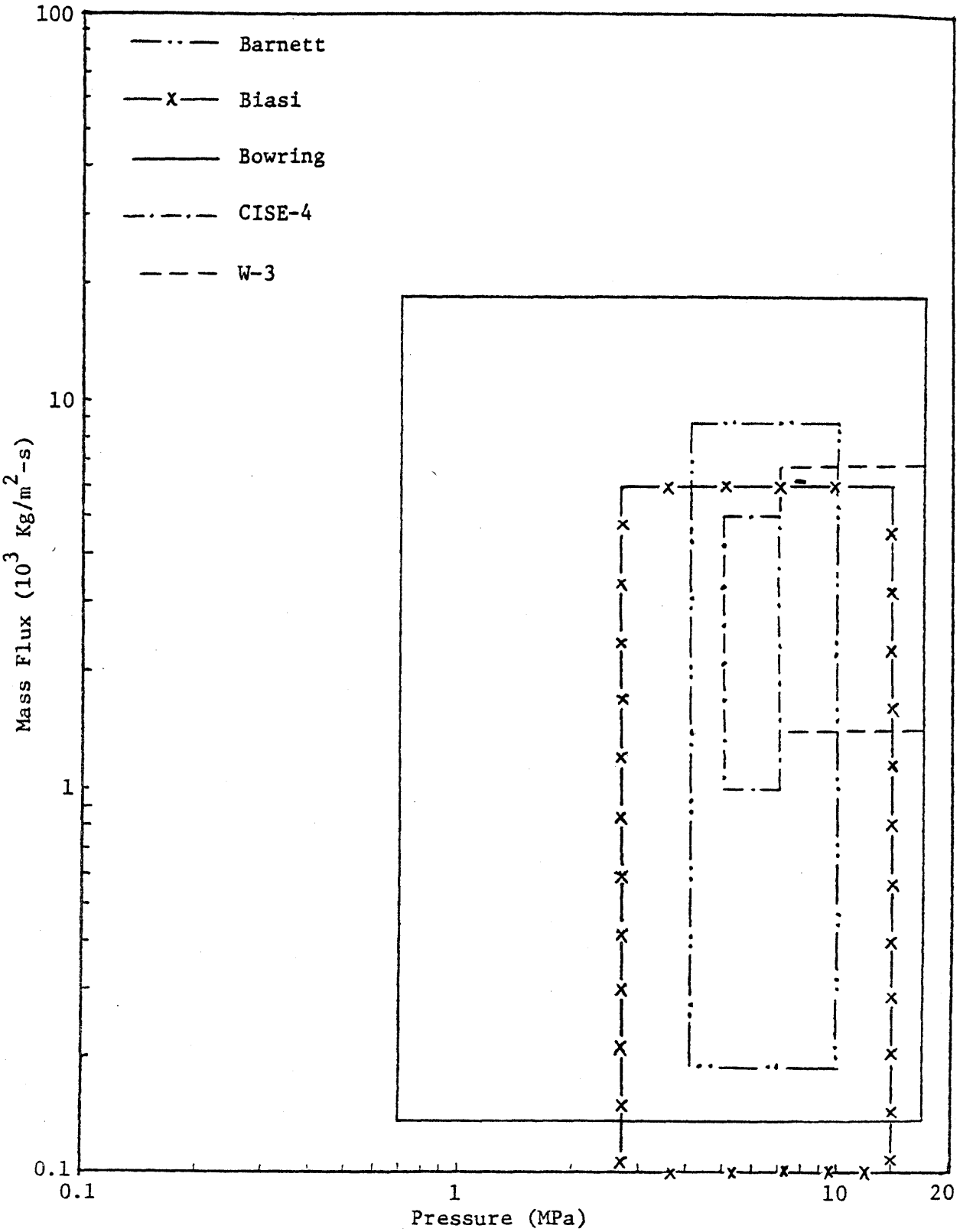

Fig. 7.12: Comparison of CHF Correlation Data Bases

REFERENCES

1. C. L. Wheeler et al., "COBRA-IV-I: An Interim Version of COBRA for Thermal-Hydraulic Analysis of Rod Bundle Nuclear Fuel Elements and Cores," BNWL-1962, (1976).

2. D. S. Rowe, "COBRA IIIC: A Digital Computer Program for Steady-State and Transient Thermal Hydraulic Analysis of Rod Bundle Nuclear Fuel Elements," BNWL-1695, (1973).

3. W. H. Reed and H. B. Stewart, "THERMIT; A Computer Program for Three-Dimensional Thermal-Hydraulic Analysis of Light Water Reactor Cores," M.I.T. Report prepared for EPRI, (1978).

4. J. E. Kelly and M. S. Kazimi, "Development and Testing of the Three-Dimensional, Two-Fluid Code THERMIT for LWR Core and Subchannel Applications, "M.I.T. Energy Laboratory, Report No. MIT-EL 79-046, (1979).

5. D. R. Liles and W. H. Reed, "A Semi-Implicit Method for Two-Phase Fluid Dynamics," Journal of Computational Physics, 26, p. 390, (1978).

6. F. H. Harlow and A. A. Amsdem, "A Numerical Fluid Dynamics Calculation Method for All Flow Speeds, " Journal of Computational Physics, 8, p. 197, (1971).

7. V. L. Shah, et al., "Some Numerical Results with the COMMIX-2 Computer Code," NUREG-CR-0741, (1979).

8. M. J. Thurgood and J. M. Kelly, "COBRA TF: Model Description," NRC Advanced Code Review Group Meeting, Silver Spring, Maryland, (1980).

9. J. E. Kelly and M. S. Kazimi, "THERMIT-2: A Two-Fluid Model Computer Code for LWR Rod Bundle Analysis," M.I.T. Energy Laboratory Report, (to be published).

10. L. Wolf, et al., "WOSUB, A Subchannel Code for Steady-State and Transient Thermal-Hydraulic Analysis of BWR Fuel Pin Bundles," MIT-EL-78-025, (1977).

11. W. T. Sha, et al., "COMMIX-1, A Three-Dimensional Transient Single Phase Component Computer Program for Thermal-Hydraulic Analysis," NUREG-0415, (1978).

12. J. F. Jackson, et al., "TRAC-PIA: An Advanced Best-Estimate Computer Computer Program for PWR LOCA Analysis," NUREG/CR-0665, (1979).

13. M. Massoud, "A Condensed Review of Nuclear Reactor Thermal-Hydraulic Computer Codes for Two-Phase Flow Analysis," M.I.T. Energy Laboratory, Report No. MIT-EL 79-018, (1980).

14. W. T. Sha, "A Summary of Methods Used in Rod-Bundle Thermal-Hydraulic Computer Codes for Two-Phase Flow Analysis," Turbulent Forced Convection in Channels and Rod Bundles Conference, Instanbul, (1978).

15. J. A. Boure, "Mathematical Modeling and the Two-Phase Constitutive Equations," European Two-Phase Flow Group Meeting, Haifa, Israel, (1975).

16. J. Weisman and R. W. Bowring, "Methods of Detailed Thermal and Hydraulic Analysis of Water-Cooled Reactors," Nuclear Science and Engineering, 57, p. 255, (1975).

17. J. J. Ginoux, Two-Phase Flows and Heat Transfer with Application to Nuclear Reactor Design Problems, McGraw-Hill, New York, (1978).

18. G. P. Gaspari, A. Hassid and G. Vanoli, "Some Considerations on Critical Heat Flux in Rod Clusters in Annular Dispersed Vertical Upward Two-Phase Flow," Energia Nucleare, 17, p. 643, (1970).

19. C. W. Stewart, et al, "COBRA IV: The Model and the Method," BNWL-2214, (1977).

20. T. A. Bjornard, "Blowdown Heat Transfer in a Pressurized Water Reactor," Ph.D. Thesis, Department of Nuclear Engineering, M.I.T., (1977).

21. H. B. Stewart, "Stability of Two-Phase Flow Calculations Using Two-Fluid Models," Journal of Computational Physics, 33, No. 2, p. 259, (1979).

22. J. G. Delhaye and J. L. Achard, "On the Averaging Operators Introduced in Two-Phase Flow Modeling," Specialists' Meeting on Transient Two-Phase Flow, Toronto, (1976).

23. J. F. McFadden, et al, "An Evaluation of State-of-the-Art Two-Velocity Two-Phase Flow Models and Their Applicability to Nuclear Reactor Transient Analysis," EPRI NP-143, (1976).

24. J. T. Rogers, and N. E. Todreas, "Coolant Interchannel Mixing in Reactor Fuel Rod Bundles Single-Phase Coolants," in Heat Transfer in Rod Bundles, ASME, (1968).

25. R. T. Lahey and F. J. Moody, The Thermal Hydraulics of a BWR, ANS Monograph, (1975).

26. J. M. Gonzalez-Santalo and P. Griffith, "Two-Phase Flow Mixing in Rod Bundle Subchannels," ASME, 72-WA/NE-19, (1972).

27. D. S. Rowe and C. W. Angle, "Crossflow Mixing Between Parallel Flow Channels During Boiling," BNWL-371, (1967).

28. S. G. Beus, "Two-Phase Turbulent Mixing Model for Flow in Rod Bundles," WAPD-T-2438, (1970).

29. A. J. Faya, "Development of a Method for BWR Subchannel Analysis," Ph.D. Thesis, M.I.T. Department of Nuclear Engineering, (1979).

30. J. T. Rogers and R. G. Rosehart, "Mixing by Turbulent Interchange in Fuel Bundles, Correlations and Inferences," ASME, 72-HT-53, (1972).

31. G. B. Wallis, One Dimensional Two-Phase Flow, McGraw-Hill Book Company, New York, (1969).

32. Drew and R. T. Lahey Jr., "An Analytic Derivation of a Subchannel Void-Drift Model," Transactions of the ANS, 33, (1979).

33. G. W. Maurer, "A Method of Predicting Steady-State Boiling Vapor Fraction in Reactor Coolant Channels," WAPD-BT-19, (1960).

34. H. Christensen, "Power-to-Void Transfer Functions," ANL-6385, (1961).

35. J. F. Marchaterre, et al, "Natural and Forced-Circulation Boiling Studies," ANL-5735, (1960).

36. R. T. Lahey Jr., et al, "Two-Phase Flow and Heat Transfer in Multirod Geometries: Subchannel and Pressure Drop Measurements in a Nine-Rod Bundle for Diabatic and Adiabatic Conditions," GEAP-13049, (1970).

37. H. Herkenrath and W. Hufschmidt, "Experimental Investigation of the Enthalpy and Mass Flow Distribution Between Subchannels in a BWR Cluster Geometry (PELCO-S)," EUR-6585-EN, (1979).

38. H. Herkenrath, W. Hufschmidt and L. Wolf, "Experimental Investigation of the Enthalpy and Mass Flow Distributions in Subchannels of a 16-Rod PWR Bundle (EUROP)," European Two-Phase Flow Group Meeting, Glasgow, (1980).

39. A. W. Bennett, et al, "Heat Transfer to Steam-Water Mixtures Flowing in Uniformly Heated Tubes in Which the Critical Heat Flux Has Been Exceeded," AERE-R-5373, (1967).

40. B. S. Shiralkar, et al, "Transient Critical Heat Flux - Experimental Results," GEAP-13295, (1972).

41. S. Nijhawan, et al, "Measurement of Vapor Superheat in Post-Critical Heat Flux Boiling," 18th National Heat Transfer Conference, San Diego, (1979).

42. P. Saha, "A Non-Equilibrium Heat Transfer Model for Dispersed Droplet Post-Dryout Regime," International Journal of Heat and Mass Transfer, 23, p. 481, (1980).

43. S. Y. Ahmad, "Axial Distribution of Bulk Temperature and Void Fraction in a Heated Channel with Inlet Subcooling," Journal of Heat Transfer, 92, p. 595, (1970).

44. P. Saha and N. Zuber, "Point of Net Vapor Generation and Vapor Void Fraction in Subcooled Boiling," Proceeding of the 5th International Heat Transfer Conference, (1974).

45. S. L. Soo, Fluid Dynamics of Multiphase Systems, Blaisdell Publishing Co., Waltham, MA, (1967).

46. V. G. Levich, Physicochemical Hydrodynamics, Prentice-Hall, Inc., Englewood Cliffs, NJ, (1962).

47. L. Y. Cheng, D. A. Drew, and R. T. Lahey, Jr., "Virtual Mass Effects in Two-Phase Flow," NUREG/CR-0020, (1978).

48. M. Ishii and N. Zuber, "Drag Coefficient and Relative Velocity in Bubbly, Droplet or Particulate Flows," AIChE Journal, 25, No. 5, p. 843, (1979).

49. A. B. Basset, Hydrodynamics, Dover Publications Inc., New York, (1961).

50. W. C. Rivard and M. D. Torrey, "Numerical Calculation of Flashing from Long Pipes Using a Two-Fluid Model," LA-6104-MS, (1975).

51. R. T. Lahey, Jr., "Out-of-Pile Subchannel Measurements in a Nine-Rod Bundle for Water at 1000 PSIA," Progress in Heat and Mass Transfer, 6, p. 345, (1972).

52. R. T. Lahey, Jr., et al, "Deficient Cooling, 7th Quarterly Progress Report," GEAP-10221-7, (1971).

53. H. Herkenrath, W. Hufschmidt, and F. Lucchini, "Experimental Subchannel Investigation in a 16 Rod Test Section by Means of the Isokinetic Sampling Technique," 2nd Multi-Phase Flow and Heat Transfer Symposium-Workshop, Miami Beach, (1979).

54. F. S. Castellana and J. E. Casterline, "Subchannel Flow and Enthalpy Distributions at the Exit of a Typical Nuclear Fuel Core Geometry," Nuclear Science and Engineering, 22, p. 3, (1972).

55. L. Biasi, et al, "Studies on Burnout, Part 3," Energia Nucleare, 14, No. 9, p. 530, (1967).

56. L. S. Tong, Boiling Crisis and Critical Heat Flux, TID-25887, AEC Critical Review Series, (1972).

57. G. P. Gaspari, A. Hassid and F. Lucchini, "A Rod-Centered Subchannel Analysis with Turbulent (Enthalpy) Mixing For Critical Heat Flux Prediction in Rod Clusters Cooled by Boiling Water," 5th International Heat Transfer Conference, Tokyo, (1974).

58. T. A. Bjornard and P. Griffith, "PWR Blowdown Heat Transfer," Thermal and Hydraulic Aspects of Nuclear Reactor Safety - Vol. 1, Light Water Reactors ASME Symposium, (1977).

59. J. C. Chen, "A Correlation for Boiling Heat Transfer to Saturated Fluids in Convective Flow," ASME, 63-HT-34, (1963).

60. J. R. S. Thom et al., Boiling in Sub-cooled Water During Flow Up Heated Tubes and Annuli," Proceedings of the Institution of Mechanical Engineers, 180, part 3C, p. 226, (1965).

61. W. H. Jens and P. A. Lottes, "Analysis of Heat Transfer, Burnout, Pressure Drop and Density Data for High Pressure Water," ANL-4627, (1951).

62. J. G. Collier, Convective Boiling and Condensation, McGraw-Hill Book Co., New York, (1972).

63. M. L. Van Haltern, "A Sensitivity Study of Thermal-Hydraulic Correlations in the Computer Code MEKIN," S.M. Thesis, Department of Nuclear Engineering, M.I.T., (1980).

64. J. C. Leung, "Transient Critical Heat Flux and Blowdown Heat Transfer Studies," Ph.D. Thesis, Department of Chemical Engineering, Northwestern University, (1980).

65. D. N. Plummer, D. C. Iloeje, W. M. Rohsenow, P. Griffith, E. Ganic, "Post Critical Heat Transfer to Flowing Liquid in a Vertical Tube," MIT Heat Transfer Lab Report No. 72718-91, 1974.

66. A. Era, G. P. Gaspari, A Hassid, A. Milani, and R. Zavattarelli, "Heat Transfer in the Liquid Deficient Region for Steam-Water Mixture at 70 Kg/cm^2 Flowing in Tubular and Annular Conduits," CISE-R 184 (1966).

67. D. C. Groeneveld, "Post-Dryout Heat Transfer at Reactor Operating Conditions," AECL-4513, 1973.

68. A. A. Bishop, R. O. Sandberg, and L. S. Tong, "Forced Convective Heat Transfer at High Pressure after the Critical Heat Flux," ASME 65-HT-31, 1965.

69. W. F. Laverty and W. M. Rohsenow, "Film Boiling of Saturated Liquid Nitrogen Flowing in a Vertical Tube," J. of Heat Transfer, 89, pp. 90-98 (1967).

70. D. C. Groeneveld and G. G. J. Delarme, "Prediction of Thermal Non-Equilibrium in the Post-Dryout Regime," Nuclear Engineering and Design, 36 (1976) 17-26.

71. S. J. Hynek, W. M. Rohsenow, A. E. Bergles, "Forced-Convection Dispersed-Flow Film Boiling," MIT Heat Transfer Lab Report No. DSR 70586-63, 1969.

72. D. C. Jones and N. Zuber, "Post-CHF Heat Transfer: A Non-Equilibrium, Relaxation Model," ASME, 77-HT-79.

73. P. Saha, B. S. Shiralkar, and G. E. Dix, "A Post-Dryout Heat Transfer Model Based on Actual Vapor Generation Rate in Dispersed Droplet Regime," ASME, 77-HT-80.

74. G. L. Yoder, Jr., "Dispersed Flow Film Boiling," Dept. of M. E., Ph.D. Thesis, March 1980.

75. E. N. Sieder and G. E. Tate, "Heat Transfer and Pressure Drop of Liquids in Tubes," Ind. Eng. Chem., 28(12) 1429-1435 (1936).

76. L. A. Bromley, "Heat Transfer in Stable Film Boiling," Chem. Eng. Prog., Vol. 46, No. 5, 1950, pp. 221-226.

77. P. J. Berenson, "Film Boiling Heat Transfer from a Horizontal Surface," ASME, 60-WA-147, 1960.

78. L. S. Tong, "Prediction of Departure from Nucleate Boiling for an Axially Non-Uniform Heat Flux Distribution," J. Nuclear Energy, G, 21 (1967).

79. P. G. Barnett, "A Correlation of Burnout Data for Uniformly Heated Annuli and Its Use for Predicting Burnout in Uniformly Heated Rod Bundles," AAEW-R-463 (1966).

80. J. E. Hench and S. Levy, Nucleonics, 24(11): 41 (1966).

81. R. W. Bowring, "Simple but Accurate Round Tube, Uniform Heat Flux, Dryout Correlation over the Pressure Range 0.7 to 17 MN/m^2 (100 to 2500 psia)," AEEW-R-789.

82. S. Bertoletti et al., "Heat Tranfser Crisis with Steam-Water Mixtures," Energia Nucleare, Vol. 12, No. 3, pp. 121-171 (1965).

83. P. G. Barnett, "A Comparison of the Accuracy of Some Correlations for Burnout in Annuli and Rod Bundles," AEEW-R-558 (1968).

84. B. W. Le Tourneau and S. J. Green, "Critical Heat Flux and Pressure Drop Tests with Parallel Upflow of High Pressure Water in Bundles of Twenty 1/2-in. Rods," Nuclear Science and Engineering, 43, 1971.

85. D. Moxon and P. A. Edwards, "Dryout During Flow and Power Transients," AEEW-R-553 (1967).

86. J. N. Loomis and W. D. Hinkle, "Reactor Core Thermal-Hydraulic Analysis - Improvement and Application of the Code COBRA-IIIC/MIT," Energy Lab Report No. MIT-EL 80-027, September 1980.

87. F. Mayinger, "Steady State Critical Heat Flux in Water-Cooled Reactor Fuel Elements," in Two-Phase Flows and Heat Transfer , Jean J. Ginoux, ed., Hemisphere, 1978.

88. R. P. Forslund and M. W. Rohsenow, "Thermal Non-Equilibrium in Dispersed Flow Film Boiling in a Vertical Tube," MIT Heat Transfer Lab Report No. 75312-44, 1966.

Appendix A: Derivation of the THERMIT Conservation Equations

A.1 Introduction

The procedure for deriving the governing equations in THERMIT from the local, instantaneous balance equations is presented in this section. This derivation consists of a straightforward application of time and space averaging operators along with clear identification of the resulting terms. Examples of the derivation approach for a two-fluid model may be found in references 22 and 23.

Besides identifying the assumptions used in the THERMIT conservation equations, two important terms have now been retained in the equations which were not included in the original THERMIT equations. The first is the term describing the effects of turbulent mixing. This term originates from the averaging procedure and must be included for subchannel or plena applications. The second term is that describing the liquid-to-vapor transport of either energy or momentum due to mass exchange across liquid-vapor interfaces. This term arises from the application of the volume averaging operator and is important for transient applications. The inclusion of these terms enhances the physical modeling capability of THERMIT.

Before presenting the actual derivation, the necessary mathematical theories and notation will be discussed. Since both time and volume averaging are required in this derivation, it is convenient to introduce notation to represent these terms. The time average of an arbitrary variable B is defined by

$$\overline{B}_k \equiv \frac{1}{T}\int_T B_k \, dt \qquad (A.1)$$

where T is a characteristic time interval for time averaging. In a similar way, the volume average of the variable B is defined by

$$\langle \overline{B_k} \rangle = \frac{1}{W_k} \int_w \overline{B_k}\, dw \tag{A.2}$$

where W_k is the volume of the kth phase within an arbitrary volume W. Since the volume, W, may contain both fluid and structure, it is useful to define the porosity, γ, and void fraction, α. These two terms are given by

$$\gamma = \frac{\text{Fluid Volume}}{\text{Total Volume}} = \frac{W_f}{W} \tag{A.3}$$

$$\alpha_k = \frac{\text{Volume of kth phase}}{\text{Fluid Volume}} = \frac{W_k}{W_f} \tag{A.4}$$

where $\Sigma W_k = W$ and $W_\ell + W_v = W_f$.

The two theorems which are essential for this derivation are the Reynolds transport theorem and the Gauss theorem. The Reynolds transport theorem allows the time derivative of a volume integral to be transformed into the sum of a volume integral and a surface integral. This theorem is given as

$$\frac{\partial}{\partial t} \int_w B\, dw = \int_w \frac{\partial B}{\partial t}\, dw + \int_A B\vec{V}_i \cdot \vec{n}\, dA \tag{A.5}$$

where $\vec{V}_i$ is the velocity of the surface and $\vec{n}$ is the unit vector normal to the surface A.

The Gauss theorem transforms the volume integral of the divergence of a field into the sum of the divergence of a volume integral plus a surface integral. This theorem is given by

$$\int_w \nabla\cdot\vec{B}\, dw = \nabla\cdot\int_w \vec{B}\, dw + \int_A \vec{n}\cdot\vec{B}\, dA \qquad (A.6)$$

where again $\vec{n}$ is the normal to surface A.

A.2 Time Averaging

With these preliminary steps it is now possible to begin the derivation. The local, instantaneous form of the mass, energy, and momentum conservations equations for the kth phase may be written in the concise form:

$$\frac{\partial}{\partial t}(\rho_k \Psi_k) + \nabla\cdot(\rho_k \Psi_k \vec{V}_k) + \nabla\cdot\vec{J}_k - \rho_k \phi_k = 0 \qquad (A.7)$$

where k= ℓ or v and Ψ, J and ϕ are defined in Table A.1. The time and volume averaging will be performed on this equation. Once this has been done, the appropriate volues for Ψ, J and ϕ will be substituted to obtain the mass, energy and momentum equations.

In this derivation, the time-averaging will be performed first. As discussed by Delhaye and Achard [22], the order in which the time and volume averaging operators are applied does not matter. By integrating equation A.7 over a time interval and applying equation A.1 one finds

$$\overline{\frac{\partial \rho_k \Psi_k}{\partial t}} + \overline{\nabla\cdot(\rho_k \Psi_k \vec{V}_k)} + \overline{\nabla\cdot\vec{J}} - \overline{\rho_k \phi_k} = 0 \qquad (A.8)$$

Each variable in this equation is replaced by the sum of its time average component plus a fluctuating component. For example, the density term may be written as

TABLE A.1

Summary of Terms Used in Conservation Equations

Equation	Ψ_k	$\vec{J}_k$	Φ_k
Mass	1	0	0
Energy	e_k	$q_k + P_k \vec{V}_k - \bar{\bar{\tau}}_k \vec{V}_k$	0
Momentum	$\vec{V}$	$P_k \bar{\bar{I}} - \bar{\bar{\tau}}_k$	$\vec{g}$

$$\rho_k = \overline{\rho}_k + \rho_k' \tag{A.9}$$

By definition, the time integral of each of the fluctuating components is zero (eg. $\overline{\rho}_k'=0$). Substituting the expanded variables into Eq. (A.8) and simplifying yields the following expression:

$$\frac{\partial \overline{\rho}_k \overline{\Psi}_k}{\partial t} + \nabla\cdot\overline{\rho}_k \overline{\Psi}_k \overline{V}_k + \nabla\cdot\vec{J}_k - \overline{\rho}_k \overline{\phi}_k + \frac{\partial \overline{\rho_k' \Psi_k'}}{\partial t} + \nabla\cdot[\overline{\rho_k' \Psi_k' V_k'}$$

$$+ \overline{\rho_k \overline{\Psi}_k V_k'} + \overline{\overline{\rho}_k \Psi_k' \vec{V}_k'} + \overline{\rho_k \Psi_k V_k}] - \overline{\rho_k' \phi_k'} = 0 \tag{A.10}$$

where it has been assumed that

$$\overline{\frac{\partial B}{\partial t}} = \frac{\partial}{\partial t}\overline{B} \tag{A.11}$$

and

$$\overline{\nabla\cdot\vec{B}} = \nabla\cdot\overline{\vec{B}} \tag{A.12}$$

The terms containing fluctuating quantities in Eq. (A.10) are lumped together into the term R'_k so that the final version of the time-averaged conservation equation is

$$\frac{\partial \overline{\rho}_k \overline{\Psi}_k}{\partial t} + \nabla\cdot(\overline{\rho}_k \overline{\Psi}_k \overline{\vec{V}}_h) + \nabla\cdot\overline{\vec{J}}_k - \overline{\rho}_k \overline{\phi}_k + R_k' = 0 \tag{A.13}$$

A.3 Volume Averaging

The second step in the derivation involves the volume averaging of Eq. (A.11). This equation is integrated over an arbitrary volume, W, which may contain liquid, vapor or structure (see Fig. A.1). By

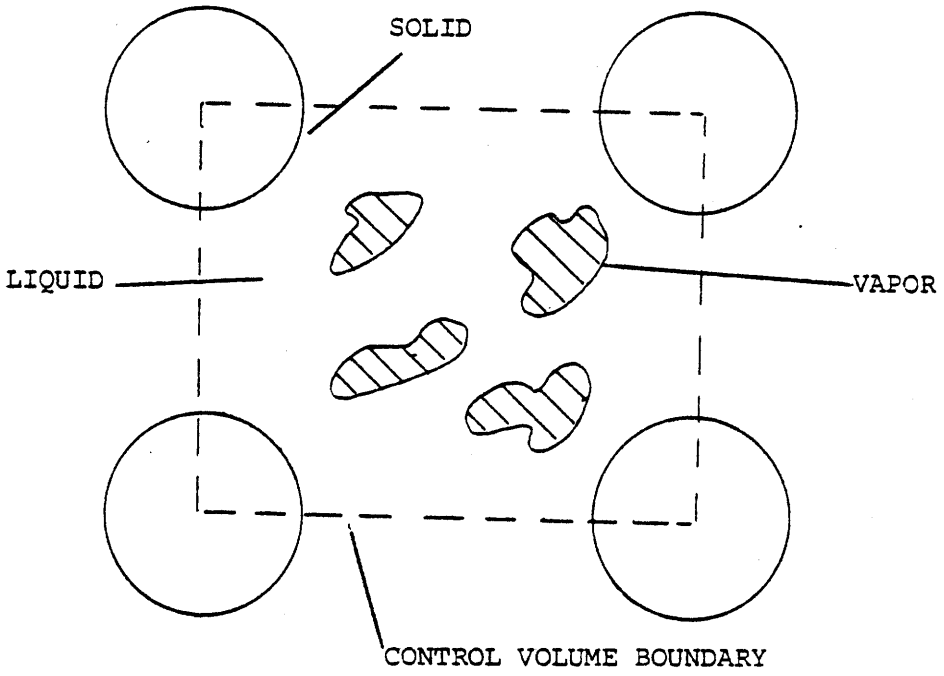

Figure A.1: Illustration of Control Volume Containing Liquid, Vapor, and Solid

performing this integration, Eq. (A.13) becomes

$$\frac{1}{W}\int \frac{\partial}{\partial t}(\overline{\rho}_k \overline{\Psi}_k) + \nabla\cdot(\rho_k \Psi_k \overline{\vec{V}}_k + \overline{\vec{J}}_k) - \overline{\rho}_k \overline{\phi}_k + R_k \; dW = 0 \qquad (A.14)$$

The Reynolds transport theorem, Eq. (A.5), is applied to the first term of this equation. By using this theorem and using the relation

$$\frac{1}{W}\int \overline{B}_k \; dW = \alpha_k \gamma < \overline{B_k} > \qquad (A.15)$$

the first term can be written as

$$\frac{1}{W}\int \frac{\partial}{\partial t}(\overline{\rho}_k \overline{\Psi}_k)dW = \frac{\partial}{\partial t}\alpha_k \gamma < \overline{\rho}_k \overline{\Psi}_k > - \frac{1}{W}\int_A \overline{\rho_k} \overline{\Psi_k} \vec{V}_i\cdot\vec{n} \; dA \qquad (A.16)$$

The Gauss theorem Eq. (A.6) is now applied to the second term of Eq. (A.14) to obtain

$$\frac{1}{W}\int \nabla\cdot(\overline{\rho}_k \overline{\Psi}_k \overline{\vec{V}}_k + \overline{\vec{J}}_k) = \nabla\cdot(\alpha_k \gamma(<\overline{\rho}_k \overline{\Psi}_k \overline{\vec{V}}_k \overline{\vec{J}}_k>) + \frac{1}{W}\int_A (\overline{\rho}_k \overline{\Psi}_k \overline{\vec{V}}_k + \overline{\vec{J}}_k)\cdot\vec{n} \; dA \qquad (A.17)$$

The area over which the surface integrals are applied includes all internal surfaces within volume W. Hence, these integrals can be divided into two components; one for the surfaces between phases and one for the fluid-solid surfaces. The general surface integral can be written as

$$\int_A B\, dA = \int_{A_i} B\, dA + \int_{A_s} B\, dA \tag{A.18}$$

where A_i is the area between phases and A_s is the fluid-solid surface area. This property of the surface integrals will be used to simplify the conservation of energy and momentum equations.

Combining Eqs. (A.14, A.16 & A.17) and using Eq. (A.15) one obtains

$$\begin{aligned} &\frac{\partial}{\partial t}\left(\alpha_k \gamma \langle \overline{\rho_k}\ \overline{\Psi_k} \rangle\right) + \nabla\cdot\left(\alpha_k \gamma \left(\langle \overline{\rho_k}\ \overline{\Psi_k}\ \overline{\vec{V}_k} \rangle + \langle \vec{J}_k \rangle\right)\right) \\ &\quad - \alpha_k \gamma \langle \overline{\rho_k}\ \overline{\phi_k} \rangle = - \alpha_k \gamma \langle R_k' \rangle + \frac{1}{W} \int_A \left(\overline{\rho_k}\ \overline{\Psi_k} (\vec{V}_i - \overline{\vec{V}_k}) - \overline{\vec{J}_k}\right)\cdot \vec{n}\, dA \end{aligned} \tag{A.19}$$

This equation can be simplified further by dividing each time-averaged variable into its spatially averaged component plus a fluctuating component. For example, the density term may be written as

$$\overline{\rho_k} = \langle \overline{\rho_k} \rangle + \overline{\rho_k}' \tag{A.20}$$

It should be noted that the volume integral of each of the fluctuating components is zero (e.g., $\langle \overline{\rho_k}' \rangle = 0$).

Substituting these expressions into Eq. (A.17) and simplifying yields the following expression

$$\frac{\partial}{\partial t}\left(\alpha_k\gamma\overline{\langle\rho_k\rangle}\overline{\langle\Psi_k\rangle}\right) + \nabla\cdot\left(\alpha_k\gamma\,\langle\rho_k\rangle\overline{\langle\Psi_k\rangle}\overline{\langle\vec{V}_k\rangle} + \overline{\langle\vec{J}_k\rangle}\right)\Big) - \alpha_k\gamma\overline{\langle\rho_k\rangle}\overline{\langle\phi_k\rangle}$$

$$- \frac{1}{W}\int_A \left(\overline{\langle\rho_k\rangle}\overline{\langle\Psi_k\rangle}(\vec{V}_i - \overline{\vec{V}}_k) - \overline{\langle\vec{J}_k\rangle}\right)\Big)\cdot\vec{n}\,dA$$

$$= \frac{1}{W}\int_A \Big(\left(\overline{\rho}_k'\,\overline{\Psi}_k' + \overline{\langle\rho_k\rangle}\,\overline{\Psi}_k' + \overline{\rho}_k'\overline{\langle\Psi_k\rangle}\right)(\vec{V}_i - \overline{\vec{V}}_k)\cdot\vec{n} - \overline{\vec{J}}_k\cdot\vec{n}\Big)\,dA \qquad (A.21)$$

$$- \frac{\partial}{\partial t}\left(\alpha_k\gamma\,\overline{\rho}_k'\,\overline{\Psi}_k'\right) - \nabla\cdot\Big(\alpha_k\gamma\big(\overline{\langle\rho_k\rangle}\,\overline{\Psi}_k'\,\overline{\vec{V}}_k' + \overline{\rho}_k'\overline{\langle\Psi_k\rangle}\,\overline{\vec{J}}_k'$$

$$+ \overline{\rho}_k'\,\overline{\Psi}_k'\overline{\langle\vec{V}_k\rangle} + \overline{\rho}_k'\,\overline{\Psi}_k'\,\overline{V}_k'\big)\Big) - \alpha_k\gamma\,\overline{\rho}_k'\,\overline{\phi}_k' - \alpha_k\gamma\overline{\langle R_k'\rangle}$$

This expression may be simplified as follows. Since THERMIT implicitly accounts for volume porosity in the formulation of its finite difference equations, the porosity factor , γ, can be set equal to unity. Further simplifications can be made by assuming that the fluctuating density terms are zero:

$$\overline{\rho}_k' = 0 \qquad (A.22)$$

Physically this assumption means that the phase density is uniform in the control volume and is valid provided the volume is not too large. By applying this assumption and lumping together all non-integral fluctuating terms into M'_k Eq. (A.21) may be written as

$$\frac{\partial}{\partial t}(\alpha_k \langle\overline{\rho_k}\rangle\langle\overline{\Psi_k}\rangle) + \nabla\cdot(\alpha_k(\langle\overline{\rho_k}\rangle\langle\overline{\Psi_k}\rangle\langle\overline{\vec{V}_k}\rangle + \langle\overline{\vec{J}_k}\rangle) - \alpha_k\langle\overline{\rho_k}\rangle\langle\overline{\phi_k}\rangle$$

$$= \frac{1}{W}\int_A (\langle\overline{\rho_k}\rangle\langle\overline{\Psi_k}\rangle(V_i - \overline{\vec{V}_k}) - \langle\overline{\vec{J}_k}\rangle)\cdot\vec{n})\,dA + \frac{1}{W}\int_A \langle\overline{\rho_k}\rangle\,\overline{\Psi_k}'(\vec{V}_i - \overline{\vec{V}_k}) \tag{A.23}$$

$$- \overline{\vec{J}_k}')\cdot\vec{n}dA - M'_k$$

This equation is the general form of the time and volume averaged conservation equation. The mass, momentum and energy equations will now be obtained by substituting the appropriate values for Ψ_k, J_k and ϕ_k into Eq. (A.23).

A.4 Conservation of Mass

The conservation of mass equation is obtained by substituting $\Psi = 1$, $\phi_k = 0$, $J_k = 0$ into Eq. (A.23). Performing this substitution, one obtains

$$\frac{\partial}{\partial t}(\alpha_k\langle\overline{\rho_k}\rangle) + \nabla\cdot(\alpha_k\langle\overline{\rho_k}\rangle\langle\overline{\vec{V}_k}\rangle) = \frac{1}{W}\int_A \langle\overline{\rho_k}\rangle(\vec{V}_i - \overline{\vec{V}_k})\cdot\vec{n}dA - M'_k \tag{A.24}$$

where M'_k represents the mass exchange due to turbulent fluctuations. The surface integral can be identified as the interfacial mass exchange rate, Γ_k. Therefore, Eq. (A.24) can be written as

$$\frac{\partial}{\partial t}(\alpha_k\langle\overline{\rho_k}\rangle) + \nabla\cdot(\alpha_k\langle\overline{\rho_k}\rangle\langle\overline{\vec{V}_k}\rangle = \Gamma_k - M'_k \tag{A.25}$$

This equation is the same as that used in THERMIT with the time and space average notation dropped and using

$$\alpha_v = \alpha$$

$$\alpha_\ell = 1 - \alpha$$

$$\Gamma_v = \Gamma$$

$$\Gamma_\ell = -\Gamma \qquad \text{(A.26)}$$

$$M'_v = W_{tv}$$

$$M'_\ell = W_{t\ell}$$

With these expressions the vapor and liquid mass conservation equations are given by:

Vapor Mass Equation

$$\frac{\partial}{\partial t}(\alpha\rho_v) + \nabla\cdot(\alpha\rho_v \vec{V}_v) = \Gamma - W_{tv} \qquad \text{(A.27)}$$

Liquid Mass Equation

$$\frac{\partial}{\partial t}((1-\alpha)\rho_\ell) + \nabla\cdot((1-\alpha)\rho_\ell \vec{V}_\ell) = -\Gamma - W_{t\ell} \qquad \text{(A.28)}$$

A.5 Conservation of Momentum

The conservation of momentum equation, which is actually a vector equation, is found by using $\Psi_k = \vec{V}_k$, $\phi_k = \vec{g}$ and $\vec{J}_k = P_k \overline{\overline{I}} - \overline{\overline{\tau}}_k$ in Eq. (A.23). Since viscous stress terms are assumed to be small and are not included in the present THERMIT formulation the viscous stress term $\overline{\overline{\tau}}_k$ is set to zero.

$$\frac{\partial}{\partial t}\left(\alpha_k \langle\overline{\rho_k}\rangle\langle\overline{\vec{V}_k}\rangle\right) + \nabla\cdot\left(\alpha_k\langle\overline{\rho_k}\rangle\langle\overline{\vec{V}_k}\rangle\langle\overline{\vec{V}_k}\rangle\right) + \nabla\alpha_k\langle\overline{P_k}\rangle - \alpha_k\langle\overline{\rho_k}\rangle\vec{g}$$

$$= \frac{1}{W}\int_A \left[\left(\langle\overline{\rho_k}\rangle\langle\vec{V}_k\rangle(\vec{V}_i - \overline{\vec{V}}_k)\cdot\vec{n} - \langle\overline{P_k}\rangle\vec{n}\right]dA \qquad (A.29)$$

$$+ \frac{1}{W}\int_A \left[\langle\overline{\rho_k}\rangle\vec{V}_k'(\vec{V}_i - \overline{\vec{V}}_k)\cdot\vec{n} - \overline{P}_k'\vec{n}\right]dA - \vec{M}'_k$$

The area integrals can be simplified by dividing the integrations into the liquid-vapor interfacial and fluid-structure conponents. On fluid-structure surfaces, the velocities are assumed to be zero. Also, on the liquid-vapor interfaces, the fluctuating velocity $\overline{V}_k'$ is assumed to be zero. Using these assumptions the area integrals can be rearranged as follows

$$\frac{1}{W}\int_A \left(\langle\overline{\rho_k}\rangle\langle\overline{\vec{V}}_k\rangle(\vec{V}_i - \overline{\vec{V}}_k)\cdot\vec{n} - \langle\overline{P_k}\rangle\vec{n}\right]dA$$

$$+ \frac{1}{W}\int_A \left(\langle\overline{\rho_k}\rangle\overline{V}_k'(\vec{V}_i - \overline{\vec{V}}_k)\cdot\vec{n} - \overline{P}_k'\vec{n}\right]dA \qquad (A.30)$$

$$= \frac{1}{W}\int_{A_i}\left[\langle\overline{\rho_k}\rangle\langle\overline{\vec{V}}_k\rangle(\vec{V}_i - \overline{\vec{V}}_k)\cdot\vec{n}dA - \frac{1}{W}\int_{A_i}\overline{P}_k'\vec{n}\,dA\right.$$

$$\left. - \frac{1}{W}\int_A \langle\overline{P_k}\rangle\vec{n}\,dA\right.$$

The first and second integrals of the right hand side represent the momentum exchange across the liquid-vapor interface and are replaced with the term $\vec{F}_{ik}$. The third integral represents the fluid-structure interactions, or wall friction, and is replaced by $\vec{F}_{wk}$. By applying Eq. (A.6) with B = 1, the fourth term can be written as

$$\frac{1}{W}\int_A \langle\overline{P_k}\rangle \vec{n}dA = \langle\overline{P_k}\rangle \int_A \frac{\vec{n}}{W} dA = - \langle\overline{P_k}\rangle \nabla\alpha_k \tag{A.31}$$

Combining these expressions, the momentum equations are given by

$$\frac{\partial}{\partial t}(\alpha_k\langle\overline{\rho_k}\rangle\langle\overline{\vec{V}_k}\rangle) + \nabla\cdot(\alpha_k\langle\overline{\rho_k}\rangle\langle\overline{\vec{V}_k}\rangle\langle\overline{\vec{V}_k}\rangle) + \alpha_k \nabla\langle\overline{P_k}\rangle$$

$$= -\vec{F}_{wk} - \vec{F}_{ik} + \alpha_k \langle\overline{\rho_k}\rangle \vec{g} - \vec{M}_k' \tag{A.32}$$

Again by dropping the time and space average notation identifying $\vec{M}_k'$ as the momentum exchange due to turbulence, $\vec{F}_{tk}$, the momentum equation may be written in THERMIT notation as

$$\frac{\partial}{\partial t}(\alpha\rho_k \vec{V}_k) + \nabla(\alpha_k \rho_k \vec{V}_k \vec{V}_k) + \alpha_k \nabla P_k$$

$$= -\vec{F}_{wk} - \vec{F}_{\ell k} + \alpha_k \rho_k \vec{g} - \vec{F}_{tk} \tag{A.33}$$

As discussed in Reference 3, Eq. (A.33) represents the conservative form of the momentum equation, while the non-conservative form is used in THERMIT. To obtain the non-conservative form, the first two terms of Eq. (A.33) are differentiated by parts and then simplified using the mass Eq. (A.25). Performing this operation one obtains

$$\alpha_k\rho_k \frac{\partial\vec{V}_k}{\partial t} + \alpha_k\rho_k \vec{V}_k\cdot\nabla \vec{V}_k + \alpha_k \nabla P_k = -\vec{F}_{wk} - \vec{F}_{ik} + \alpha_k\rho_k \vec{g}$$

$$- \vec{F}_{tk} - (\Gamma_k - W_{tw})\vec{V}_k \tag{A.34}$$

It is now assumed that the momentum exchange due to mass exchange can be included in the interfacial momentum exchange term, $\vec{F}_{ik}$, and that the pressure, P_k, is the same for each phase (i.e., $P_v = P_\ell = P$). Then, the vapor and liquid momentum equations may be written as

Vapor Momentum Equation

$$\alpha\rho_v \frac{\partial \vec{V}_v}{\partial t} + \alpha_v\rho_v \vec{V}_v\cdot\nabla\vec{V}_v + \alpha\nabla P = - \vec{F}_{wv} - \vec{F}_{iv} + \alpha\rho_v \vec{g} - \vec{F}_{tv} \tag{A.35}$$

Liquid Momentum Equation

$$\begin{aligned}(1-\alpha)\rho_\ell \frac{\partial \vec{V}_\ell}{\partial t} + (1-\alpha)\rho_\ell \vec{V}_\ell \cdot \nabla\vec{V}_\ell + (1-\alpha)\nabla P \\ = -\vec{F}_{w\ell} - \vec{F}_i + (1-\alpha)\rho_\ell\vec{g} - \vec{F}_{i\ell}\end{aligned} \tag{A.36}$$

A.6 Conservation of Energy

The conservation of energy equation is obtained by using $\Psi_k = e_k$, $\phi_k = 0$ and $\vec{J}_k = \vec{q}_k + P_k\vec{V}_k - \bar{\bar{\tau}}_k\cdot\vec{V}_k$. Once again the viscous terms are neglected so that $\bar{\bar{\tau}} = 0$. Substituting these terms into Eq. (A.23) yields

$$\begin{aligned}&\frac{\partial}{\partial t}\left(\alpha_k\langle\overline{\rho_k}\rangle\langle\overline{e_k}\rangle\right) + \nabla\cdot\left(\alpha_k\left(\langle\overline{\rho_k}\rangle\langle\overline{e_k}\rangle\langle\overline{\vec{V}_k}\rangle + \langle\overline{\vec{q}_k}\rangle + \langle\overline{P_k}\rangle\langle\overline{\vec{V}_k}\rangle\right)\right) \\ &= \frac{1}{\forall}\int_A \left(\langle\overline{\rho_k}\rangle\langle\overline{e_k}\rangle(\vec{V}_i - \overline{\vec{V}}_k) - \langle\overline{\vec{q}_k}\rangle - \langle\overline{P_k}\rangle\overline{\vec{V}}_k\right)\cdot\vec{n}dA \\ &+ \frac{1}{\forall}\int_A \left(\langle\overline{\rho_k}\rangle\overline{e}_k'(\vec{V}_i - \overline{\vec{V}}_k) - \overline{\vec{q}}' - \overline{P}_k'\overline{\vec{V}}_k\right)\vec{n}dA - M_k'\end{aligned} \tag{A.37}$$

In order to reduce this equation to the form used in THERMIT it is necessary to use the following assumptions. First, the conduction term $\vec{q}_k$ is neglected everywhere except in the area integrals. This assumption is appropriate if the energy transfer due to convection is much larger than that due to conduction. For water systems, this assumption is valid at all but very low flow rates.

Second, it is assumed that the work dissipation term, $\alpha_k \langle \vec{V}_k \rangle \nabla \langle \overline{P}_k \rangle$, can be neglected due to its small value compared to the other terms.

Next the area integrals are divided into liquid-vapor and fluid-solid components. As in the case of the momentum equations, it is assumed that the velocity on fluid-solid interfaces is zero. The integrals can then be rearranged and identified as follows:

$$\frac{1}{W}\int_{A_i} (\langle \overline{\rho_k} \rangle \langle \overline{e_k} \rangle (\vec{V}_i - \vec{\overline{V}}_k) - \vec{\overline{q}}_k - \overline{P}_k \vec{\overline{V}}_k) \cdot \vec{n} dA = Q_{ik} \tag{A.38}$$

$$\frac{1}{W}\int_A \langle \overline{P_k} \rangle \vec{\overline{V}}_k \cdot \vec{n}\, dA = \frac{1}{W} \langle \overline{P_k} \rangle \int \vec{\overline{V}}_k \cdot \vec{n}\, dA = \langle \overline{P_k} \rangle \frac{\partial \alpha}{\partial t} \tag{A.39}$$

$$\frac{1}{W}\int - \vec{\overline{q}}_k \cdot \vec{n}\, dA = Q_{wk} \tag{A.40}$$

Combining these expressions the energy conservation equation may be written as

$$\frac{\partial}{\partial t}\left(\alpha_k \langle\overline{\rho_k}\rangle\langle\overline{e_k}\rangle\right) + \nabla\cdot\left(\alpha_k \langle\overline{\rho_k}\rangle\langle\overline{e_k}\rangle\langle\overline{\vec{V}_k}\rangle + \langle\overline{P_k}\rangle \nabla\cdot \alpha_k \langle\overline{\vec{V}_k}\rangle\right)$$

$$+ \langle\overline{P_k}\rangle \frac{\partial \alpha_k}{\partial t} = Q_{wk} + Q_{ik} - M_k' \qquad \text{(A.41)}$$

Dropping the time and volume averaging notation and identifying M_k' as the energy exchange due to turbulence, Q_{tk}, the vapor and liquid energy conservation equations may be written as:

Vapor Energy Equation

$$\frac{\partial}{\partial t}\left(\alpha\rho_v e_v\right) + \nabla\cdot\left(\alpha\rho_v e_v \vec{V}_v\right) + P\nabla\cdot\left(\alpha\vec{V}_v\right) + P\frac{\partial \alpha}{\partial t} = Q_{wv} + Q_{iv} - Q_{tv} \qquad \text{(A.42)}$$

Liquid Energy Equation

$$\frac{\partial}{\partial t}\left((1-\alpha)\rho_\ell e_\ell\right) + \nabla\cdot\left((1-\alpha)\rho_\ell e_\ell \vec{V}_\ell\right) + P\nabla\cdot(1-\alpha)\vec{V}_\ell)$$

$$- P\frac{\partial \alpha}{\partial t} = Q_{w\ell} + Q_{i\ell} - Q_{t\ell} \qquad \text{(A.43)}$$

A.7 Discussion of Assumption

To complete the discussion on the derivation of the THERMIT conservation equations, the important assumptions that have been made will be repeated. Beginning with the mass equation, it is recalled that two main assumptions have been used to obtain the THERMIT form of this equation. The first is that the interfacial area integral can be equated with the inter-fluid mass exchange rate;

$$\Gamma = \frac{1}{W} \int_{A_i} \overline{\langle \rho_k \rangle} (\vec{V} - \bar{\vec{V}}_k) \cdot \vec{n} \, dA \tag{A.44}$$

This integral represents the transfer of mass across liquid-vapor interfaces and, hence, it is appropriate to associate the mass exchange rate with this integral. The second assumption, is that the turbulent mass exchange term can be equated to the terms which contain fluctuating quantities;

$$W_{tk} = M_k' \tag{A.45}$$

The expression for W_{tk} can be written out in full as

$$W_{tk} = \nabla \cdot (\alpha_k \overline{\langle \rho_k \rangle} \, \bar{V}_k') + \alpha_k \nabla \cdot (\langle \bar{\rho}_k \, \bar{\vec{V}}_k' \rangle) \tag{A.46}$$

This term represents the mass exchange due to both temporal and spatial fluctuations and, hence, it is appropriate to associate this term with the turbulent mass exchange rate. In THERMIT this term is approximated as

$$W_{tk} = \nabla \cdot (\frac{\varepsilon}{\ell} ((\alpha_k \rho_k)_i - (\alpha_k \rho_k)_j)) \tag{A.47}$$

where ε/ℓ is the turbulent velocity (see Section 3.3 for more details).

In the momentum equation, the first assumption is that the viscous shear forces can be neglected. This assumption is valid for reactor conditions because the viscous force is small compared to the other forces. The second assumption is that the pressure is the same for each phase

(i.e., $P = P_\ell = P_v$). This assumption is appropriate provided the control volumes are not too large.

Assumptions concerning the integrals and fluctuating terms have also been made. The wall friction term and interfacial friction term are:

$$\vec{F}_{wk} = \frac{1}{W} \int_{A_s} \bar{P}'_k \, \vec{n} \, dA \tag{A.48}$$

$$\vec{F}_{ik} = \frac{1}{W} \int_{A_i} [\langle\overline{\rho_k}\rangle\langle\overline{\vec{V}_k}\rangle(\vec{V}_i - \bar{\vec{V}}_k)\cdot\vec{n} - \overline{P_k}'\,\vec{n}]\,dA + (\Gamma - W_{tk})\langle\bar{\vec{V}}_k\rangle \tag{A.49}$$

The final term which is identified is the $\vec{F}_{tv}$. In THERMIT, only the Z-direction component is included. As in the case of the mass equation, the temporal and spatial fluctuating terms give rise to the turbulence effects. This term can be written as

$$F^z_{tk} = \alpha_k \nabla\cdot(\langle\overline{\rho_k}\rangle\langle\overline{V^z_k}\rangle\,\bar{\vec{V}}_k') + \alpha_k \nabla\cdot(\langle\bar{\rho}_k\,\bar{V}^z_k\,\overline{V_k}'\rangle) \tag{A.50}$$

In THERMIT, this term is approximated by

$$F^z_{tk} = \nabla\cdot(\frac{\varepsilon}{\ell}((\alpha_k\rho_k\,V^z_k)_i - (\alpha_k\rho_k\,V^z_k)_j)) \tag{A.51}$$

In the energy equation it is again assumed that viscous effects can be neglected and that the pressure is the same for each phase with a control volume. It is also assumed that heat conduction between channels and the work dissipation term can be neglected due to their relatively small values.

Assumptions concerning the various integrals and fluctuating terms have also been made. The wall heat transfer term has been associated with the fluid-solid area integral of the heat conduction term;

$$Q_{wk} = -\frac{1}{W}\int_{A_i} \vec{\bar{q}}_k' \cdot \vec{n}\, dA \tag{A.52}$$

The energy exchange between phases due to mass transfer and conduction is associated with the interfacial energy exchange rate;

$$Q_i = \frac{1}{W}\int_{A_i} (\langle\overline{\rho_k}\rangle\langle\bar{e}_k\rangle(\vec{\bar{V}}_i - \vec{\bar{V}}_k) - \vec{\bar{q}}_k - \bar{P}_k' \vec{\bar{V}}_k)\cdot\vec{n}\, dA \tag{A.53}$$

The final term to be identified is the energy exchange due to turbulence. This term is associated with the fluctuating terms and may be written as

$$Q_{tk} = \nabla\cdot(\alpha_k\langle\overline{\rho_k}\rangle\langle\overline{e_k}\rangle \vec{\bar{V}}_k') + \alpha_k \nabla\cdot(\langle\bar{\rho}_k \bar{e}_k \vec{\bar{V}}_k'\rangle) \tag{A.54}$$

where fluctuations in both the density and internal energy have been neglected. In THERMIT this term is approximated as

$$Q_{tk} = \nabla\cdot(\frac{\varepsilon}{\ell}((\alpha_k \rho_k e_k)_i - (\alpha_k \rho_k e_k)_j)) \tag{A.55}$$

By using all of the above assumptions, the THERMIT conservation equations have been obtained from the local, instantaneous balance equations. This discussion has attempted to identify the major simplifying assumptions to obtain these equations. The form of the

equations used in THERMIT can now be understood in terms of their origin and restrictions caused by neglecting certain phenomena.

Appendix B Two-Phase Mixing Model Assessment Results

The tabulated results of the two-phase mixing model assessment effort are presented in this Appendix. The test conditions for the various experiments used in this effort are listed in Table B.1. The G.E. isothermal test comparisons are presented in Table B.2. For the heated G.E. tests, Table B.3 contains uniformly heated test comparisons while the non-uniformly heated test comparisons are given in Table B.4. Finally, the Ispra BWR test comparisons are presented in Table B.5.

For each of these tables the measured and predicted exit mass velocity and quality (except for the isothermal tests) distributions are given. The bundle average mass velocity and exit quality are also listed. For certain cases, the code predictions without the two-phase mixing model are given as a means of comparison. Further details of these comparisons have been given in Chapter 5.

TABLE B.1

Test Conditions for Rod-Bundle Experiments

	G.E. 9-Rod	Ispra 16-Rod BWR	Ispra 16-Rod PWR
P (MPa)	6.9	7.0	16.0
G ($kg/m^2 \cdot s$)	650 to 2200	1000 to 2000	2500 to 3500
q" (MW/m^2)	0.71 to 2.1	0.12 to 0.77	0.07 to 0.11
Δi_{sub} (kJ/kg)	67 to 525	30 to 180	250 to 400
X_{out} %	3 to 22	2 to 31	-20 to 20
D_e (mm)	12.1	13.3	10.7
Length (m)	1.83	3.66	3.66
Spacer Type	Pin	Grid	Grid
Radial Power Distribution	Uniform and Non-Uniform	Uniform	Uniform

TABLE B.2

Comparison of Measured and Predicted Exit Mass Velocities

For Isothermal Tests in 9 Rod G.E. Tests

Case Number	$\overline{G}$ ($kg/m^2 \cdot s$)	Mass Flow Error (%)	G_{1_2} ($kg/m^2 \cdot s$)	G_{2_2} ($kg/m^2 \cdot s$)	G_{3_2} ($kg/m^2 \cdot s$)
1B					
Data	650	-1.6	422	627	713
THERMIT			454	605	755
THERMIT (No Mixing)			440	584	736
1C					
Data	1343	+0.7	951	1274	1560
THERMIT			1003	1261	1525
THERMIT (No Mixing)			926	1259	1607
1D					
Data	2048	+0.46	1485	1954	2292
THERMIT			1535	1923	2323
THERMIT (No Mixing)			1399	1906	2435
1E					
Data	2672	+1.06	2197	2591	2970
THERMIT			2010	2518	3035
THERMIT (No Mixing)			1829	2491	3182

TABLE B.3

Comparison of Measured and Predicted Exit Quality and Mass Velocity Distributions for Uniformly Heated 9-Rod G.E. Cases

Case Number	$\overline{G}$ ($kg/m^2 \cdot s$)	$\overline{X}_{out}$	Mass Error (%)	Quality Error	X_1	X_2	X_3	G_1 ($kg/m^2 \cdot s$)	G_2 ($kg/m^2 \cdot s$)	G_3 ($kg/m^2 \cdot s$)
2B2										
Data	719	0.029	-1.5	-0.01	0.003	0.014	0.03	505	707	732
THERMIT				,	0.037	0.025	0.028	550	690	809
2B4										
Data	726	0.176	-0.0	+0.015	0.133	0.18	0.22	711	701	760
THERMIT					0.109	0.156	0.21	617	701	800
2C1										
Data	1438	0.042	-0.05	-0.006	0.029	0.018	0.059	1309	1446	1461
THERMIT					0.037	0.039	0.046	1161	1391	1571

TABLE B.3 (continued)

Case Number	$\overline{G}$ ($kg/m^2 \cdot s$)	$\overline{X}_{out}$	Mass Error (%)	Quality Error	X_1	X_2	X_3	G_{1_2} ($kg/m^2 \cdot s$)	G_{2_2} ($kg/m^2 \cdot s$)	G_{3_2} ($kg/m^2 \cdot s$)
2C2										
Data	1449	0.075	+0.05	+0.009	0.063	0.075	0.10	1313	1394	1552
THERMIT					0.056	0.069	0.084	1221	1411	1572
2D1										
Data	732	0.110	+0.74	-0.002	0.083	0.105	0.117	576	760	754
THERMIT					0.091	0.101	0.121	602	713	798
2D3										
Data	732	0.318	0.03	+0.019	0.26	0.33	0.36	665	722	764
THERMIT					0.19	0.28	0.38	603	713	802
2E1										
Data	1465	0.035	2.8	0.0	0.004	0.025	0.05	1288	1495	1576
THERMIT					0.039	0.03	0.039	1250	1417	1567
THERMIT (No Mixing)					0.20	0.02	0.032	695	1485	1655

TABLE B.3 (continued)

Case Number	$\overline{G}$ (kg/m^2·s)	$\overline{X}_{out}$	Mass Error (%)	Quality Error	X_1	X_2	X_3	G_{1_2} (kg/m^2·s)	G_{2_2} (kg/m^2·s)	G_{3_2} (kg/m^2·s)
2E2										
Data	1465	0.106	3.24	-0.007	0.049	0.097	0.105	1418	1462	1600
THERMIT					0.076	0.096	0.11	1259	1431	1559
THERMIT (No Mixing)					0.30	0.081	0.106	783	1477	1646
2E3										
Data	1438	0.215	2.6	-0.007	0.16	0.18	0.25	1309	1466	1527
THERMIT					0.138	0.19	0.25	1219	1392	1554
THERMIT (No Mixing)					0.48	0.20	0.19	855	1370	1687
2G1										
Data	1451	0.038	-4.9	0.003	0.031	0.044	0.042	1196	1313	1549
THERMIT					0.049	0.033	0.041	1142	1408	1570
THERMIT (No Mixing)					0.29	0.017	0.032	640	1493	1632

TABLE B.3 (continued)

Case Number	$\bar{G}$ (kg/m^2·s)	$\bar{X}_{out}$	Mass Error (%)	Quality Error	X_1	X_2	X_3	G_{1_2} (kg/m^2·s)	G_{2_2} (kg/m^2·s)	G_{3_2} (kg/m^2·s)
2G2										
Data	1465	0.09	2.5	-0.008	0.02	0.068	0.110	1356	1507	1533
THERMIT					0.075	0.084	0.10	1241	1432	1563
THERMIT (No Mixing)					0.37	0.06	0.089	721	1515	1620
2G3										
Data	1451	0.16	4.1	-0.009	0.074	0.127	0.176	1173	1535	1573
THERMIT					0.11	0.146	0.185	1273	1411	1549
THERMIT (No Mixing)					0.46	0.12	0.165	799	1482	1604

TABLE B.4

Comparison of Measured and Predicted Quality and Mass Velocity Distributions for G.E. Non-Uniformly Heated Cases

Case Number	$\overline{G}$ $\left(\frac{kg}{m^2 \cdot s}\right)$	$\overline{X}_0$	X_1	X_2	X_3	X_4	X_5	G_1 $\left(\frac{kg}{m^2 \cdot s}\right)$	G_2 $\left(\frac{kg}{m^2 \cdot s}\right)$	G_3 $\left(\frac{kg}{m^2 \cdot s}\right)$	G_4 $\left(\frac{kg}{m^2 \cdot s}\right)$	G_5 $\left(\frac{kg}{m^2 \cdot s}\right)$
3B2												
Data	726	0.032	0.08	0.042	0.108	-.043	.009	543	688	753	685	434
THERMIT			0.064	0.057	0.058	-.015	-.017	538	673	802	696	564
THERMIT (No Mixing)			0.192	0.059	0.06	-.03	-.02	409	802	840	653	518
3D1												
Data	739	0.084	0.123	--	--	-.037	.024	437	--	--	852	454
THERMIT			0.113	0.124	0.135	+.009	-.005	547	654	756	791	682
THERMIT (No Mixing)			0.49	0.132	0.127	-.009	.012	384	638	786	797	615

TABLE B.4 (continued)

Case Number	$\bar{G}$ $\frac{kg}{m^2 \cdot s}$	$\bar{X}_0$	X_1	X_2	X_3	X_4	X_5	G_1 $\frac{kg}{m^2 \cdot s}$	G_2 $\frac{kg}{m^2 \cdot s}$	G_3 $\frac{kg}{m^2 \cdot s}$	G_4 $\frac{kg}{m^2 \cdot s}$	G_5 $\frac{kg}{m^2 \cdot s}$
3E1												
Data	1465	0.035	0.106	--	0.163	-.036	.002	1077	--	1156	1255	1940
THERMIT			0.077	0.078	0.076	-.017	-.02	986	1177	1381	1625	1815
THERMIT (No Mixing)			0.44	0.095	0.08	-.016	-.038	555	1091	1363	1467	1960
3E2												
Data	1438	0.10	0.16	0.167	0.227	.034	.075	1085	1024	1207	2000	1275
THERMIT			0.099	0.122	0.143	.05	.029	1137	1293	1441	1584	1469
THERMIT (No Mixing)			0.55	0.183	0.16	.01	.036	648	1102	1368	2015	1307

TABLE B.5

Comparison of Measured and Predicted Quality and Mass Velocity Distributions

for Ispra 16-Rod BWR Cases

Case Number	$\bar{G}$ ($kg/m^2 \cdot s$)	$\bar{X}_0$	X_1	X_2	X_4	X_5	G_{1_2} ($kg/m^2 \cdot s$)	G_{2_2} ($kg/m^2 \cdot s$)	G_{4_2} ($kg/m^2 \cdot s$)	G_{5_2} ($kg/m^2 \cdot s$)
130.3										
Data	998	.085	.077	.04	.08	.086	995	724	1007	978
THERMIT			.073	.054	.094	.092	962	882	1038	1026
THERMIT (No Mixing)			.075	.11	.086	.085	911	663	1110	1111
131.2										
Data	1000	.148	.128	.066	.144	.164	979	667	979	983
THERMIT			.13	.099	.178	.168	944	888	1023	1008
THERMIT (No Mixing)			.13	.22	.146	.144	899	573	1095	1095

TABLE B.5 (continued)

Case Number	$\overline{G}$ (kg/m^2·s)	$\overline{X}_0$	X_1	X_2	X_4	X_5	G_{1_2} (kg/m^2·s)	G_{2_2} (kg/m^2·s)	G_{4_2} (kg/m^2·s)	G_{5_2} (kg/m^2·s)
107.3										
Data	1017	.155	.142	.067	.172	.152	987	686	1047	1012
THERMIT			.134	.103	.18	.173	972	917	1055	1041
THERMIT (No Mixing)			.139	.23	.152	.152	936	595	1135	1134
99.3										
Data	1000	.219	.176	.083	.189	.22	1027	648	1037	973
THERMIT			.171	.127	.24	.23	960	891	1055	1043
THERMIT (No Mixing			.21	.51	.18	.19	886	537	1152	1136
109.6										
Data	999	.284	.26	.177	.30	.30	947	629	1012	978
THERMIT			.23	.158	.33	.32	971	883	1057	1048
THERMIT (No Mixing)			.27	.59	.27	.27	910	575	1126	1118

TABLE B.5 (continued)

Case Number	$\overline{G}$ (kg/m^2·s)	$\overline{X}_0$	X_1	X_2	X_4	X_5	G_{1_2} (kg/m^2·s)	G_{2_2} (kg/m^2·s)	G_{4_2} (kg/m^2·s)	G_{5_2} (kg/m^2·s)
125.4										
Data	1524	.04	.045	.021	.037	.05	1448	1048	1592	1489
THERMIT			.037	.029	.045	.044	1464	1324	1604	1583
THERMIT (No Mixing)			.033	.096	.043	.041	1424	841	1672	1690
124.4										
Data	1520	.084	.086	.051	.08	.092	1408	1029	1710	1621
THERMIT			.075	.058	.094	.092	1472	1365	1575	1559
THERMIT (No Mixing)			.074	.199	.084	.086	1411	803	1686	1675
141.8										
Data	1528	.144	.162	.117	.133	.166	1416	934	1572	1430
THERMIT			.127	.101	.16	.158	1484	1405	1596	1575
THERMIT (No Mixing)			.13	.45	.142	.144	1421	762	1693	1692

TABLE B.5 (continued)

Case Number	$\overline{G}$ (kg/m^2·s)	$\overline{X}_0$	X_1	X_2	X_4	X_5	G_{1_2} (kg/m^2·s)	G_{2_2} (kg/m^2·s)	G_{4_2} (kg/m^2·s)	G_{5_2} (kg/m^2·s)
118.2										
Data	1984	.029	.028	.015	.039	.037	1901	1334	1975	1970
THERMIT			.027	.021	.031	.031	1894	1707	2086	2057
THERMIT (No Mixing)			.027	.031	.03	.032	1832	1331	2195	2187
113.4										
Data	1994	.083	.074	.038	.084	.074	1869	1296	2064	2000
THERMIT			.074	.058	.092	.089	1939	1804	2069	2049
THERMIT (No Mixing)			.072	.22	.083	.084	1851	1015	2196	2187
115.4										
Data	1976	.122	.139	.075	.106	.106	1845	1239	2152	2039
THERMIT			.101	.078	.124	.121	1938	1821	2051	2033
THERMIT (No Mixing)			.096	.29	.113	.118	1869	1016	2195	2162

Appendix C

Heat Transfer Correlations

For the logic of selecting these correlations, refer to Figures 6.4 and 6.5, and Table 6.1 in Chapter 6. All units are SI.

Sieder-Tate (vapor or liquid) [75]

$$h_{ST} = 0.023 \frac{k}{D} Re^{0.8} Pr^{0.33} (\mu/\mu_w)^{0.14}$$

(Fluid properties at bulk fluid temperature, except μ_w at T_w)

McAdams (vapor or liquid) [89]

$$h_{MA} = 0.13\ k\ [\rho^2 g\ \beta(T_w - T)\ Pr/\mu^2\ ]^{0.33}$$

(Fluid properties should be at a fluid film temperature; T is either T_v or T_ℓ)

Chen [59]

$$q_{Chen} = h_{fc}(T_w - T_\ell) + h_{nb}(T_w - T_{sat})$$

$$h_{fc} = 0.023 \frac{k_\ell}{D} Re_\ell^{0.8} Pr_\ell^{0.4} F$$

$$h_{nb} = 0.00122\ S\left[\frac{k_\ell c_{P\ell}}{\sigma}\right]^{0.5} Pr_\ell^{-0.29}\ \rho_\ell^{0.25} (P_w - P)^{0.75} \left[\frac{c_{P\ell}(T_w - T_{sat})\rho_\ell}{h_{v\ell}\ \rho_v}\right]^{0.24}$$

$$F = \begin{cases} 1 & X_{tt}^{-1} \leq 0.1 \\ 2.35\ (X_{tt}^{-1} + 0.213)^{0.736} & X_{tt}^{-1} > 0.1 \end{cases}$$

$$X_{tt}^{-1} = [x/(1-x)]^{0.9} \; (\rho_\ell/\rho_v)^{0.5} \; (\mu_v/\mu_\ell)^{0.1}$$

$$S = \begin{cases} [1 + 0.12\ Re_{TP}^{1.14}]^{-1} & Re_{TP} < 32.5 \\ [1 + 0.42\ Re_{TP}^{0.78}]^{-1} & 32.5 \leq Re_{TP} \leq 70 \\ 0.1 & Re_{TP} > 70 \end{cases}$$

$$Re_{TP} = 10^{-4}\ F^{1.25}\ (1-\alpha)\ \rho_\ell v_\ell D/\mu_\ell$$

Modified Bromley [20]

$$h_{mB} = 0.62 \left[\frac{g(\rho_\ell-\rho_v)\ \rho_v\ k_v^3\ h'_{v\ell}}{\lambda_c\ \mu_v\ (T_w - T_{sat})}\right]^{0.25}$$

$$h'_{v\ell} = h_{v\ell} + \frac{1}{2}\ c_{Pv}\ (T_w - T_{sat})$$

$$\lambda_c = 2\pi[\sigma/g(\rho_v-\rho_\ell)]^{0.5}$$

Low Quality Film Boiling

$$h_{FB} = \alpha\ h_{sT} + (1-\alpha)\ h_{mB}$$

Minimum Stable Film Boiling Temperature [20]

$$T_{MSFB} = T_{HN} + (T_{HN} - T_\ell)\ [(\rho k c_p)_\ell\ /(\rho k c_p)_w]^{0.5} - \Psi(P)$$

$$T_{HN} = \begin{cases} 581.5 + 0.01876\ (P - 1.034 \cdot 10^5)^{0.5}, & P \leq P_o \\ 630.39 + 0.004321\ (P - P_o)^{0.5} & P > P_o \end{cases}$$

$$P_o = 68.95 \cdot 10^5\ Pa$$

Minimum Stable Film Boiling Temperature (continued)

$$\Psi(P) = \begin{cases} 0 & P \geq 4.826 \cdot 10^5 \text{ Pa} \\ 127.3 - 26.37 \cdot 10^{-5} P & P < 4.826 \cdot 10^5 \text{ Pa} \end{cases}$$

Note: $(\rho k c_p)_w$ above refers to properties of the wall itself, i.e., clad surface material properties.

Appendix D

CHF Correlations

Biasi [55]

Use the second expression below for G 300 kg/m^2-sec; for higher G, use the larger of the two values:

$$q''_{Biasi} = 2.764 \cdot 10^7 \, (100\ D)^{-n} \, G^{-1/6} \, [1.468\ F(P_{bar})\ G^{-1/6} - x] W/m^2$$

$$q''_{Biasi} = 15.048 \cdot 10^7 \, (100\ D)^{-n} \, G^{-0.6} \, H(P_{bar}) \, [1-x]\ W/m^2$$

$$F(P_{bar}) = 0.7249 + 0.099\ P_{bar} \exp(-0.032\ P_{bar})$$

$$H(P_{bar}) = -1.159 + 0.149 P_{bar} \exp(-0.019\ P_{bar}) + 9P_{bar}\ (10 + P^2_{bar})^{-1}$$

Note: $P_{bar} = 10^{-5} P$

$$n = \begin{cases} .4 & D > 0.01 \text{ m} \\ .6 & D \leq 0.01 \text{ m} \end{cases}$$

Data Base:

Diameter:	0.3 to 3.75 cm
Length:	20 to 600 cm
Pressure:	2.7 to 140 bar
Mass flux:	10 to 600 g/cm^2-s
Quality:	$1/(1+\rho_l/\rho_g)$ to 1

CHF-Void [20]

$$q''_{CHF} = 0.1178\ (1-\alpha)\ h_{v\ell}[\sigma g\ (\rho_\ell\ \rho)\rho_v^2]^{0.25}\ W/m^2$$

Data Base:

(See Ref. 90)

CISE-4 [57]

$$\langle x \rangle_c = \frac{D_h}{D_e}\left[a\ \frac{L_{Bc}}{L_{Bc} + b}\right]$$

where

$$a = \frac{1}{1 + 1.481 \cdot 10^{-4}(1 - P/P_{CR})^{-3}G} \qquad \text{if } G \leq G^*$$

and

$$a = \frac{1 - P/P_{CR}}{(G/1000)^{1/3}} \qquad \text{if } G > G^*$$

where $G^* = 3375\ (1 - P/P_c)^3$

and

$$b = 0.199\ (P_c/P-1)^{0.4}\ G\ D_e^{1.4}$$

Data Base:

P = 4.96 to 6.89 MPa
G = 1085 to 4069 kg/m^2-s
L = 0.76 to 3.66 m
D = 1.02 to 1.98 cm

Bowring [81] (in SI units)

$$q''_{CHF} = \frac{A - BH_{fg}\, x}{C} \quad W/m^2$$

where

$$A = \frac{2.317\ (H_{fg}\ DG/4)\ F_1}{1 + .0143\ F_2 D^{1/2}\ G}$$

$$B = \frac{DG}{4}$$

$$C_1 = \frac{0.077\ F_3\ DG}{1 + 0.347\ F_4 (\frac{G}{1356})^n}$$

$$P_R = 0.145\ P$$

$$n = 2.0 - 0.5\ P_R$$

for $P_R < 1$

$$F_1 = (P_R^{18.942}\ e^{20.89(1-P_R)} + 0.917)/1.917$$

$$F_2 = F_1/[(P_R^{1.316}\ e^{2.444(1-P_R)} + 0.309)/1.309]$$

$$F_3 = (P_R^{17.023}\ e^{16.658(1-P_R)} + 0.667)/1.667$$

$$F_4 = F_3 P_R^{1.649}$$

for $P_R > 1$

$$F_1 = P_R^{-0.368}\ e^{0.648(1-P_R)}$$

$$F_2 = F_1/P_R^{0.448}\ e^{0.245(1-P_R)}$$

$$F_3 = P_R^{0.219}$$

$$F_4 = F_3 P_R^{1.649}$$

Data Base:

P: 0.2-19 MN/m^2

D: 2-45 mm

L: 0.15 - 3.7 m

G: 136 - 18,600 $Kg/s\text{-}m^2$

W-3 [78]

$$\frac{q''_{CHF}}{10^6} = \{(2.022 - 0.0004302\ P) + (0.1722 - 0.0000984\ P)$$
$$\times \exp[(18.177 - 0.004129\ P)\ X]\}$$
$$\times [(0.1484 - 1.596\ X + 0.1729X\ |X|)(G/10^6) + 1.037]$$
$$\times (1.157 - 0.869\ X)$$
$$\times [0.2664 + 0.8357 \exp(-3.151\ D_E)]$$
$$\times [0.8258 + 0.000794\ (h_f - h_{IN})]\ Btu/hr\ ft^2$$

For a non-uniform heat flux the critical heat flux is given as

$$q''_{CHF,NU} = q''_{CHF,U}/F$$

where

$$F = \frac{C}{q''_{local}\,[1-\exp(-C\ell_{DNB,EU})]} \int_0^{\ell_{DNB}} q''(z) \exp[-C(\ell_{DNB,N} - z)]dz$$

$$C = 0.44\ \frac{(1 - \chi_{DNB})^{7,9}}{(G/10^6)^{1.72}}\ in.^{-1}$$

ℓ_{DNB} = axial location at which DNB occurs, in.

Data Base:

$P = 1000$ to 2300, psia

$G = 1.0 \cdot 10^6$ to $5.0 \cdot 10^6$, lb/(h ft^2)

$D_e = 0.2$ to 0.7, in.

$\chi_{loc} \leq 0.15$

$H_{in} \geq 400$ Btu/lb

$L = 10$ to 144, in.

$\frac{\text{heated perimeter}}{\text{wetted perimeter}} = 0.88$ to 1.00

heat flux is in Btu/(h ft^2).

Barnett [79]:

$$q''_{CHF} = 10^6 \frac{A(h_{fg}/649) + B(h_{ls}-h_i)}{C - Z} \quad \text{Btu/hr-ft}^2$$

where

$$A = 67.45 D_h^{0.08} (G \cdot 10^{-6})^{0.192} \{1-0.744\exp[-0.512 D_e (G \cdot 10^{-6})]\}$$

$$B = 1.85 \cdot D_h^{1.261} (G \cdot 10^{-6})^{-0.0817}$$

$$C = 185 \cdot D_e^{1.415} (G \cdot 10^{-6})^{0.212}$$

For Annuli the heated and wetted equivalent diameters,

D_h and D_e, are given by

$$D_e = (D_s - D_I)$$

and

$$D_h = (D_s^2 - D_I^2)/D_I$$

where D_s is the diameter of the shroud and D_I is the diameter of the inner rod.

Data Base:

Vertical upflow of water in annuli geometry

Diameter of inner rod: 0.375 to 3.789 in.

Diameter of shroud: 0.551 to 4.006 in.

Heated length: 24.0 to 108.0 in.

Mass flux ($9 \cdot 10^{-6}$): 0.140 to 6.20 lbm/hr-ft^2

Inlet subcooling: 0 to 412 Btu/lbm

Uniform axial heat flux.

Hench-Levy [80]

$$(q''_c/10^6) = F_p \frac{BTU}{hr\text{-}ft^2}$$

for $(<x_e>) \leq 0.273 - 0.212\ TANH^2(3G/10^6)$

$$(q''_c/10^6 = F_p[1.9 - 3.3 <x_e> - 0.7\ TANH^2 \cdot (3G/10^6)]\ Btu/hr\text{-}ft^2$$

for $0.273 - 0.212\ TANH^2\ (3G/10^6) \leq (<x_e>)$

$$\leq 0.5 - 0.269\ TANH^2\ (3G/10^6) + 0.0346 \cdot TANH^2\ (\frac{2G}{10^6})$$

$$(q''_c/10^6) = F_p[0.6 - 0.7 <x_e> - 0.09\ \ TANH^2\ (2G/10^6)]\ Btu/hr\text{-}ft^2$$

for $(<x_e>) \geq 0.5 - 0.269\ TANH^2\ (3G/10^6) + 0.0346\ TANH^2\ (\frac{2G}{10^6})$

where

$$F_p = \left[1.1 - 0.1\left(\frac{p - 600}{400}\right)^{1.25}\right]$$

Data Base:

P = 600 to 1450 psia

G = $0.2 \cdot 10^6$ to $1.6 \cdot 10^6$ lb/h-ft^2

D_e = 0.324 to 0.485 in.

rod to rod and

rod to wall spacings greater than 0.060 in.

Appendix D1

On the Use of CISE-4 Correlation

When CISE-4 is applied in rod bundles, question arises regarding whether the equivalent hydraulic diameter, D_e, or the equivalent heated diameter, D_h, should be used in place of the tube diameter, D. D_e and D_h are defined respectively as:

$$D_e = \frac{4(\text{flow area})}{\text{wetted perimeter}}$$

and

$$D_h = \frac{4(\text{flow area})}{\text{heated perimeter}}$$

Table E.1 gives the CHF predictions using both D_e and D_h in G.E. 9-rod bundles. As seen, the equivalent hydraulic diameter gives slightly better predictions. Therefore, it is recommended to use D_e in place of D in CISE-4.

TABLE D.1

Comparison of CHF Predictions Using Equivalent Hydraulic Diameter and Equivalent Heated Diameter in CISE-4 in G.E. 9-Rod Bundles

Run #	Subchannel Method		Bundle-Average Method	
	D_e	D_h	D_e	D_h
278	0.854	0.724	0.867	0.772
279	0.883	0.762	0.903	0.807
280	0.932	0.816	0.957	0.858
271	0.893	0.709	0.929	0.789
272	0.929	0.749	0.963	0.820
273	0.948	0.775	0.985	0.839
266	0.935	0.699	0.970	0.790
267	1.019	0.735	1.060	0.875
268	1.030	0.811	1.061	0.872
297	1.056	0.794	1.090	0.868
298	1.025	0.790	1.108	0.893
299	1.043	0.816	1.132	0.914

D_e = equivalent hydraulic diameter

D_h = equivalent heated diameter

Appendix E

Steam Water Transport Properties

All units are SI.

Liquid Thermal Conductivity

$$k_\ell \ (W/m\text{-}°K) = 0.686 - 5.87 \cdot 10^{-6} \ (T_\ell - 415)^2 + 7.3 \cdot 10^{-10} P$$

range: $273°K \leq T_\ell \leq 573°K$

error: <5%

Vapor Thermal Conductivity

$$K_V(W/m\text{-}K) = -0.0123 + 7.8 \cdot 10^{-9} P + 2.44 \cdot 10^{-16} P^2 + 1.25 \cdot 10^{-11} T_v(80 \cdot 10^5 - P)$$

range: $373 \ K \leq T_v \leq 623 \ K, \ 10^5 Pa \leq P \leq P_{sat}$

error: <10%

Liquid Viscosity

$$\mu_\ell \ (kg/m\text{-}sec) = \frac{25.3}{T_\ell^2 + 91 \ T \ - 8.58 \cdot 10^4}$$

range: $273°K \leq T_\ell < 623°K$

error: 6%

nearest singularity: $T_\ell = 251°K$

Vapor Viscosity

$$\mu_v \text{ (kg/m-sec)} = \frac{11.4}{T_v^2 - 884T_v + 1.36 \cdot 10^6}$$

range: $373°K \leq T_v \leq 623°K$

error: 3%

nearest singularity: $T_v = 822°K$

Surface Tension

$$\sigma\, g^{-1} \text{(kg/m)} = \frac{80.72 - 0.126T_\ell}{5140 + T_\ell}$$

range: $373°K \leq T_\ell \leq 623°K$

error: 2%

Appendix F

Fuel Rod Material Properties

The following are the fits developed for use in THERMIT-2 to represent the material properties of fuel and zircaloy cladding.

The Table at the end of this Appendix shows the default values used when constant properties are requested, together with the conditions to which these values correspond.

All units are SI.

Fuel Heat Capacity

$$\rho c_p \ (J/m^3 - °K) = \theta_d \ [a_o + a_1 T + a_2 T^2 + a_3 T^3] \cdot (1 + 0.045 \ \theta_{Pu})$$

Coefficients for UO_2:	for mixed oxide:
$a_o = 1.78 \cdot 10^6$	$a_o = 1.81 \cdot 10^6$
$a_1 = 3.62 \cdot 10^3$	$a_1 = 3.72 \cdot 10^3$
$a_2 = -2.61$	$a_2 = -2.57$
$a_3 = 6.59 \cdot 10^{-4}$	$a_3 = 6.13 \cdot 10^{-4}$

range: $300°K \leq T \leq 3000°K$

error: 2%

Note: θ_d is fraction of theoretical density; θ_{Pu} is fraction of PuO_2 in mixed oxide fuel.

Fuel Thermal Conductivity

$$k(W/m-°K) = [1-\beta(1-\theta_d)] \cdot [b_o + b_1 T + b_2 T^2]$$

$$\beta = 2.74 - 5.8 \cdot 10^{-4} T$$

Coefficients for UO_2: for mixed oxide:

$b_o = 10.8$ $b_o = 9.88$

$b_1 = -8.84 \cdot 10^{-3}$ $b_1 = -8.44 \cdot 10^{-3}$

$b_2 = 2.25 \cdot 10^{-6}$ $b_2 = 2.25 \cdot 10^{-6}$

range: $400°K \leq T \leq 2500°K$

error: 10%

Note: The porosity factor term $[1 - \beta(1-0.95)]^{-1}$ has been incorporated in the polynomial fit.

Clad Heat Capacity

$$\rho c_p \ (J/m^3-°K) = \begin{cases} 1.673 \cdot 10^6 + 721.6\ T, & T < 1090°K \\ 5.346 \cdot 10^6 + 3.608 \cdot 10^4 |T-1170|, & 1090°K \leq T \leq 1254°K \\ 2.316 \cdot 10^6, & T > 1254°K \end{cases}$$

range: $300°K \leq T$

error: 5% for $T \leq 1090°K$

Clad Thermal Conductivity

$$k(W/m-°K) = c_o + c_1 T + c_2 T^2 + c_3 T^3$$

$c_o = 7.51$ $c_2 = -1.45 \cdot 10^{-5}$

$c_1 = 2.09 \cdot 10^{-2}$ $c_3 = 7.67 \cdot 10^{-9}$

range: $300°K \leq T \leq 1800°K$

error: ~20%

TABLE F.1

Constant Rod Property Values

Material:	Property:	Value:	Condition:
fuel	ρc_p	$3.3835 \cdot 10^6$	T=1500°K
fuel	k	2.36	θ_d=0.95, θ_{Pu}=0
clad	ρc_p	$2.106 \cdot 10^6$	T = 600°K
clad	k	16.5	

Appendix G

Interfacial Exchange Models

G.1 Interfacial Mass Exchange Models (Γ)

pre-Chf:

A. Nigmatulin: [12]

$$\Gamma = \Gamma_{evap.} + \Gamma_{cond}$$

$$\Gamma_{evap.} = K\,\rho_\ell\,\alpha(1-\alpha)(R_g T_{sat})^{\frac{1}{2}}\,(T_\ell - T_{sat})/T_{sat}$$

$$\Gamma_{cond} = K\,\rho_v(1-\alpha)^2(R_g T_{sat})^{\frac{1}{2}}\,(T_v - T_{sat})/T_{sat}$$

where $K = 1.3333 \cdot 10^{14})^{1/3}\ (\alpha)^{2/3}$

and R_g = gas constant for water vapor

$= 21.4942$

B. Ahmad (Subcooled vapor generation model) [43]

$$\Gamma = \begin{cases} 0 & , \text{ if } T_\ell \leq T_d \\ \dfrac{T_\ell - T_d}{T_{sat} - T_d}\ \Gamma_e + \Gamma_c, & \text{if } T_d < T_\ell < T_{sat} \\ \Gamma_e & , \text{ if } T_\ell \geq T_{sat} \end{cases}$$

where

$$\Gamma_e = q_w/h_{fg}$$

$$\Gamma_c = A_i H_i (T_\ell - T_v)/h_{fg}$$

and $T_d = T_{sat} - q''_w/H_A$

where q_w is the power transferred to the coolant

T_d is the bubble departure temperature

$$H_A = \frac{k_\ell}{D} \; 2.44 \; Re^{1/2} \; Pr^{1/3} \left(\frac{h_{in}}{h_f}\right)^{1/3} \left(\frac{h_{fg}}{h_f}\right)^{1/3}$$

$$A_i = 3 \; \alpha / R_b$$

where

$$R_b = \begin{cases} R_{bo} & ; \; \alpha < 0.1 \\ R_{bo} \; \left(\frac{9\alpha}{1-\alpha}\right)^{1/3} & ; \; \alpha \geq 0.1 \end{cases}$$

and

$$R_{bo} = 0.45 \; \left(\frac{\sigma}{\Delta\rho}\right)^{1/2} \{1 + 1.34 \; [(1-\alpha) \; v_\ell]^{1/3}\}^{-1}$$

and

$$H_i = \begin{cases} k_\ell / 0.15 \; R_{bo} & \text{if } T_v \leq T \\ k_\ell k_v / (0.01 \; R_{bo} \; k_\ell + 0.015 \; R_{bo} \; k_v), & \text{if } T_v > T_\ell \end{cases}$$

post CHF:

A. Saha (dispersed flow) [73]

$$\Gamma = \frac{Kl \; k_v (T_v - T_{sat})(1 - \alpha)}{D^2 h_{fg}}$$

where

$$Kl = 6300 \; (1 - P/P_{cr})^2 (P_v V^2 D/\sigma)^{1/2}$$

G.2 Interfacial Energy Exchange Models (Q_i)

pre-CHF:

$$Q_i = H_i (T_{sat} - T_v) + \Gamma h_g$$

post-CHF:

$$Q_i = H_i (T_{sat} - T_\ell) - \Gamma h_f$$

where $H_i = 10^{11}$ W/m^3-°K

G.3 Interfacial Momentum Exchange Models (F_i)

pre-CHF:

A. M.I.T. Model

$$F_i = \left(\frac{1-\hat{\alpha}}{\hat{\alpha} D}\right)^2 \mu_\ell v_r + \left(\frac{1-\hat{\alpha}}{\hat{\alpha} D}\right) \frac{\rho_v v_r v_r}{2}$$

where $\hat{\alpha} = \max(0.1, \alpha)$

B. LASL Model

$$F_i = \frac{3}{8} a \left\{ \frac{12\bar{\mu}}{r} + \frac{\bar{\rho}|v_r|}{2} \right\} v_r$$

where

$$\bar{\rho} = \alpha\rho_v + (1-\alpha)\rho_\ell$$

$$\mu = \left(\frac{\alpha\mu_v}{\rho_v} + \frac{(1-\alpha)\mu_\ell}{\rho_\ell}\right) \bar{\rho}$$

$$a = a_n^{1/3} \hat{\alpha}^{2/3}$$

$$r = (\hat{\alpha}/a_n)^{1/3}$$

where

$$a_n = 4\pi N/3$$

$$N = 10^7 \text{ m}^{-3}$$

$$\hat{\alpha} = \begin{cases} \alpha & , \text{ if } \alpha \leq 0.5 \\ 1-\alpha & , \text{if } \alpha \geq 0.5 \end{cases}$$

Appendix H

Assessment of Two-Phases Pressure Drop Predictions

At a given pressure and power, the determination of the mass flux depends on the overall pressure-drop prediction in a flow channel. In two-phase flow, the pressure drop prediction is very sensitive to the two-phase friction correlation used. In THERMIT, two phase friction-factor multipliers of Martinelli-Nelson [H-1], Martinelli-Nelson-Jones [H-2], and Levy [H-3] are available to the user. The assessment of these multipliers have been investigated by comparing the predicted two-phase pressure drop with measured values. Diabetic, two-phase pressure drop measurements in tubes and annuli obtained at CISE [H-4] are used for this purpose. The test conditions are given in Table H.1. All tests were made with subcooled inlet condition. The predicted and measured values are compared in Tables H.2 and H.3. The error analysis is summarized in Table H.4. It is seen that the Martinnelli-Nelson-Jones two-phase friction-factor multiplier has slightly better predictions than the rest. While the pressure drop does not appear to be predictable better than ± 50%, the pressure drop itself in these tests is a very small fraction of the system pressure. This raises the possibility of relatively large experiment errors as well.

TABLE H.1

CISE Diabatic Two-Phase Pressure Drop Data

Round Tube:

I.D:	0.6 cm
Length:	4.0 m
Mass Flux:	1124 - 2980 Kg/m^2-s
Pressure:	69 bars
Inlet Qual:	-0.015 to -0.240

Annulus:

I.D.:	1.7 cm
O.D:	1.5 cm
Length:	3.28 m
Mass Flux:	790 - 3830 Kg/m^2-s
Pressure:	70 bars
Inlet Qual:	-0.014 to -0.186

TABLE H.2

Two-Phase Pressure Drop Prediction in Round Tube

Test #	G (Kg/m^2-s)	x_{in}	x_e	$\Delta P_{meas.}$ (MPa)	ΔP(MPa)		
					Mart	M-J	Levy
19	1124	-0.051	.724	0.164	0.191	0.111	0.044
20	1124	-0.178	.701	0.143	0.169	0.100	0.044
24	1124	-0.243	.707	0.108	0.162	0.097	0.045
35	2198.8	-0.045	.484	0.246	0.544	0.331	0.120
36	2198.8	-0.131	.470	0.227	0.473	0.293	0.114
37	2198.8	-0.23	.443	0.247	0.410	0.259	0.109
10	2979	-0.015	.427	0.349	0.918	0.569	0.202
11	2975	-0.087	.417	0.371	0.800	0.503	0.190
12	2979	-0.190	.388	0.349	0.646	0.417	0.173

Round tube D = 0.006 m

L = 4.0 m

P = 70 bars

TABLE H.3

Two-Phase Pressure Drop Prediction in Annulus

Test #	G (Kg/m^2-s)	x_{in}	x_e	ΔP_{meas} (MPa)	ΔP(MPa)	
					Mart	M-J
100	787	-0.014	0.761	0.329	0.293	0.166
101	790	-0.186	0.692	0.296	0.248	0.145
80	1105	-0.065	0.601	0.325	0.490	0.265
81	1105	-0.135	0.580	0.301	0.446	0.244
76	2193	-0.072	0.344	0.512	1.147	0.705
77	2189	-0.152	0.328	0.492	0.967	0.597
54	3040	-0.069	0.250	0.820	1.510	1.008
107	3052	-0.156	0.248	0.770	1.290	0.868
104	3819	-0.049	0.228	1.011	2.017	1.412
105	3830	-0.141	0.214	0.935	1.641	1.152

Annulus: D_o = 0.017 m L = 3.28 m

D_i = 0.015 m P = 70 bars

D_e = 0.002 m

TABLE H.4

Two-Phase Pressure Drop Assessment

Data

CISE Diabatic Round Tube and Annulus

Correlations	N	Δp Error (%)
Martinelli-Nelson-Jones	19	-51 to +63
Martinelli-Nelson	19	-11 to +121
Levy	9	-42 to -73
Rough Tube	9	+23 to +170

References for Appendix H

H-1. R. C. Martinelli and D. B. Nelson, "Prediction of Pressure Drop during Forced Circulation Boiling of Water," Trans. ASME, 70, 695 (1948).

H-2. A. B. Jones, "Hydrodynamic Stability of a Boiling Channel," KAPL-2170, Knolls Atomic Power Laboratory (1961).

H-3. S. Levy, "Steam Slip - Theoretical Prediction from Momentum Model," J. Heat Mass Transfer, 82 (1960).

H-4. G. P. Gaspari et al., "Pressure Drops in Steam-Water Mixture," CISE-4-83 (1964).

NOMENCLATURE

A	Area
C_d	Drag Coefficient
C_p	Specific Heat
D	Diameter
e	Internal Energy
F_g	Gravitational Force
F_i	Vapor-Liquid Interfacial Momentum Exchange Rate
F_t	Turbulent Momentum Exchange Rate
F_w	Wall Frictional Force
g	Gravitational Constant
G	Mass Flux
H	Heat Transfer Coefficient
i	Enthalpy
J_v	Superficial Vapor Velocity
k	Thermal Conductivity
K_M	Mixing Model Parameter
L	Length
P	Pressure
Pr	Prandtl Number
Q_i	Interfacial Heat Transfer Rate
Q_t	Turbulent Heat Transfer Rate
Q_W	Wall Heat Transfer Rate
$\dot{q}$	Power
q''	Heat Flux
R_b	Bubble Radius

Nomenclature (continued)

Re	Reynolds Number
S	Slip Ratio (V_v/V_ℓ)
S_{ij}	Gap Spacing Between Coolant Channels
t	Time
T	Temperature
T_d	Bubble Departure Temperature
V	Velocity
V_R	Relative Velocity ($V_v - V_\ell$)
W	Volume
W'	Turbulent Mixing Rate
W''_t	Turbulent Mass Flux
W_t	Mass Exchange Due to Turbulence
X	Quality
α	Void Fraction
σ	Surface Tension
ϕ	Parameter Defined in Eq. (3.33)
Γ	Vapor Generation Rate
ρ	Density
μ	Viscosity
θ	Mixing Model Parameter
ϵ/ℓ	Turbulent Velocity
ψ	Generalized Mixing Rate Term
τ	Turbulent Shear Force
$\hat{o}$	Droplet Diameter

Nomenclature (continued)

Subscripts

i,j,k	Nodal Locations
f	Saturated Liquid
g	Saturated Vapor
ℓ	Liquid
s	Saturation
v	Vapor
w	Wall

Superscripts

x,y,z	Spatial Directions

Acronyms

ATWS	Anticipated Transient Without Scram
BWR	Boiling Water Reactor
CHF	Critical Heat Flux
CHFR	Critical Heat Flux Ratio
CPR	Critical Power Ratio
DNB	Departure from Nucleate Boiling
LOCA	Loss of Coolant Accident
LWR	Light Water Reactor
MSFB	Minimum Stable Film Boiling
PWR	Pressurized Water Reactor